SISSA - International School for Advanced Studies

The Threefold Way to Cosmological Tests of Gravity

Thesis Submitted for the Degree of
"Doctor Philosophiæ"

Supervisors
Prof. Carlo Baccigalupi
Prof. Alessandra Silvestri

Candidate
Marco Raveri

June 2016

Contents

Abstract

Explaining the physical origin of cosmic acceleration still poses a challenge to modern cosmology. On one hand, observational evidence corroborating this phenomenon is compelling and continuously becoming stronger and stronger. On the other hand a physical explanation for it is still missing. Cosmic acceleration might be explained by a cosmological constant having the same effect of vacuum energy. Indeed cosmological observations point in this direction and the cosmological constant is a cornerstone of the standard cosmological model. This explanation, however, suffers from several naturalness problems that reflect the fact that, while a cosmological constant is allowed in the gravitational sector by symmetry arguments, there is no theory for the gravitational effect of quantum vacuum. To address this issue, or at least to have an intuition of the phenomenology related to the solution of this problem, one might want to add other dark fluids to the cosmic budget or modify the laws of gravity on large scales to drive the accelerated expansion of the universe.

In this thesis we develop and exploit a threefold approach to the study of the phenomenological aspects of cosmic acceleration with the aim of systematizing the investigation of models beyond the standard one.

The first path that we shall follow is that of quantifying the level of agreement of cosmological observations, within the standard cosmological model; this will allow us to determine whether there is already some indication that this model might be inappropriate in describing present day observations.

Then we shall move along the second path to study parametrized approaches to the phenomenology of Dark Energy and Modified Gravity theories. We develop the relevant tools to exploit an Effective Field Theory description for this phenomenon and we investigate some of its observational consequences.

At last we shall move along the third path that consists in testing specific non-standard models. Exploiting the unifying power of the Effective Field Theory approach, we study the cosmological implications and corresponding data constraints on two $f(R)$ models and on Hořava gravity.

Overall we find that, already at present, cosmological observations are precise enough to substantially improve our knowledge about the space of Dark Energy and Modified Gravity models. While doing so we developed the relevant tools to perform massive and systematic studies of non-standard cosmologies aiming at explaining the physical origin of Cosmic Acceleration with present data and the next generation of cosmological surveys.

Collaborations

This thesis is the result of the research done during my four years of Ph.D. and of collaborations with C. Baccigalupi, N. Frusciante, B. Hu, M. Rizzato, A. Silvestri, D. Vernieri, S.Y. Zhou. The bulk of the present work is based on the following papers published in refereed Journals:

1. Bin Hu, Marco Raveri, Matteo Rizzato, Alessandra Silvestri,
   "Testing Hu-Sawicki $f(R)$ gravity with the Effective Field Theory approach",
   Monthly Notices of the Royal Astronomical Society (in press) [arXiv:1601.07536 [astro-ph.CO]] [1].

2. Marco Raveri,
   "Are cosmological data sets consistent with each other within the Λ cold dark matter model?"
   PRD **93** (2016) 043522 [arXiv:1510.00688 [astro-ph.CO]] [2].

3. Noemi Frusciante, Marco Raveri, Daniele Vernieri, Bin Hu, Alessandra Silvestri,
   "Horava Gravity in the Effective Field Theory formalism: from cosmology to observational constraints",
   Phys. Dark Univ. **13**, 7 (2016) [arXiv:1508.01787 [astro-ph.CO]] [3].

4. Bin Hu, Marco Raveri, *"Can modified gravity models reconcile the tension between CMB anisotropy and lensing maps in Planck-like observations?"*,
   PRD **91**, (2015) 123515 [arXiv:1502.06599 [astro-ph.CO]] [4].

5. Bin Hu, Marco Raveri, Alessandra Silvestri, Noemi Frusciante, *"EFT-CAMB/EFTCosmoMC: massive neutrinos in dark cosmologies"*,
   PRD **91**, (2015) 063524 [arXiv:1410.5807 [astro-ph.CO]] [5].

6. Marco Raveri, Carlo Baccigalupi, Alessandra Silvestri, Shuang-Yong Zhou,
   "Measuring the speed of cosmological gravitational waves",
   PRD **91**, (2015) 061501 [arXiv:1405.7974 [astro-ph.CO]] [6].

7. Marco Raveri, Bin Hu, Noemi Frusciante, Alessandra Silvestri,
   "Effective Field Theory of Cosmic Acceleration: constraining dark energy with CMB data",
   PRD **90** (2014) 043513 [arXiv:1405.1022 [astro-ph.CO]] [7].

8. Bin Hu, Marco Raveri, Noemi Frusciante, Alessandra Silvestri,
"Effective Field Theory of Cosmic Acceleration: an implementation in CAMB",
PRD **89** (2014) 103530 [arXiv:1312.5742 [astro-ph.CO]] [8].

9. Noemi Frusciante, Marco Raveri, Alessandra Silvestri,
"Effective Field Theory of Dark Energy: a Dynamical Analysis",
JCAP **1402**, 026 (2014) [arXiv:1310.6026 [astro-ph.CO]] [9].

Supplementary material includes:

- EFTCAMB/EFTCosmoMC codes available at `http://www.lorentz.leidenuniv.nl/~hu/codes/`
- Bin Hu, Marco Raveri, Noemi Frusciante, Alessandra Silvestri
"EFTCAMB/EFTCosmoMC: Numerical Notes v2.0",
arXiv:1405.3590 [astro-ph.IM], (2014) [10].

Notation

Here, we provide a brief guide to the notation and a list of acronyms.

$c = 1$	the speed of light is set to be equal to one;
G	Newtonian Gravitational Constant;
m_0	Planck mass;
$(-,+,+,+)$	metric signature;
$i, j, k...$	3D spatial indices in vectors and tensors;
$\mu, \nu, \gamma...$	4D indices in vectors and tensors;
$g_{\mu\nu}$	metric tensor;
g	determinant of the metric tensor $g_{\mu\nu}$
τ	conformal time;
t	cosmic time;
$\mathcal{H}$	Hubble parameter in conformal time;
H	Hubble parameter in cosmic time $H = \mathcal{H}/a$;
$R_{\mu\nu}$, R	Ricci tensor and its trace;
$T_{\mu\nu}$, T	Stress energy tensor and its trace;
$G_{\mu\nu}$	Einstein Tensor ($G_{\mu\nu} = R_{\mu\nu} - 1/2 g_{\mu\nu} R$);
ϕ	Scalar field;
χ_m	Matter fields;
S_m	Matter action of all matter fields, χ_m;
∇_μ	Covariant derivative;
$\bar{\nabla}$	Spatial covariant derivative;
Λ	Cosmological Constant;
δ	Perturbative density field ($\delta = \rho/\overline{\rho} - 1$).

Acronyms

ΛCDM	Λ Cold Dark Matter;
CC	Cosmological Constant Λ;
DM	Dark Matter;
GR	General Relativity;
FLRW	Friedmann-Lemaître-Robertson-Walker metric;
DE	Dark Energy;
MG	Modified Gravitational Theory;
LSS	Large Scale structure;
WMAP	Wilkinson Microwave Anisotropy Probe;
SDSS	Sloan Digital Sky Survey;
2dF	Two-degree-Field Galaxy Redshift Survey;
C.L.	Confidence Level;
CMB	Cosmic Microwaves Background radiation;
BBN	Big Bang Nucleosynthesis;
EFT	Effective Field Theory for cosmic acceleration;
CAMB	Code for Anisotropies in the Microwave Background;
CosmoMC	Cosmological Monte Carlo code;
MGCAMB	Modification of Growth with CAMB;
WP	WMAP low-ℓ polarization spectra;
DoF	Degree of Freedom;
l.h.s	Left hand side;
r.h.s.	Right hand side;
w.r.t.	With respect to.

Chapter 1

Introduction

We are witnessing the dawn of a golden era in cosmology. Ongoing and upcoming experiments will map cosmic structures over a significant fraction of our Universe, providing us with extremely accurate measurements. Observational collaborations are driving the community toward this objective, working relentlessly to reach such accuracy. On the theoretical side, many questions still need to be answered and these measurements will offer a unique opportunity to tackle them. This will be possible only if we will be prepared to correctly interpret and exploit this wealth of data.

A universe described by General Relativity and filled with ordinary matter is naturally expected to decelerate, after the initial phase of rapid expansion following the Big Bang. In this respect, an important breakthrough occurred in the late 90s. Measurements of Type Ia Supernovae by the Supernova Cosmology Project [11] and the High-Z Supernova Search Team [12] provided strong evidence that the Universe has recently entered a phase of accelerated expansion. This discovery was later corroborated by many independent probes. The Wilkinson Microwave Probe satellite [13, 14] has measured the temperature fluctuations of the CMB over the full sky with high precision, offering an unprecedented ability to constrain several cosmological parameters and confirming the physical picture emerging from Supernovae observations. The Planck satellite substantially improved the accuracy of CMB measurements [15, 16], further strengthening this picture and providing the first evidence for cosmic acceleration from CMB data alone. Finally, several surveys such as SDSS [17], WiggleZ [18], CFHTLenS [19] and DES [20] are providing us with precise information about the distribution of structures in our universe. All these observations converged in confirming this description of our Universe, and nowadays cosmic acceleration is a well established fact and a cornerstone of our standard cosmological model. Yet theoretically we are struggling to find an explanation for its physical origin. To make the expansion of the Universe accelerate, we need an unnaturally small amount of vacuum energy, or an additional ingredient whose nature is unknown, Dark Energy; or we might have to change our theory of gravity on cosmological scales. In recent years, it has become increasingly clear that our best hope to unlock this mystery is to compare measurements of the expansion history of the universe with probes of the evolution of large-scale structures. This can be achieved combining data from different cosmological

surveys. A large amount of high precision measurements have been provided by several experiments and in the future the situation will further improve. The extraordinary effort of the observational community in building the next generation of cosmological probes, like the Simons Array [21], CMB-S4, Euclid [22], WFIRST [23], LSST [24] and SKA [25], will result in extremely precise measurements of the clustering of cosmic structure, the CMB and their cross correlations. Aside from helping us to discern among different candidate models of cosmic acceleration, these surveys will offer the unprecedented possibility to test general relativity, and more broadly, fundamental physics on cosmological scales.

This thesis focuses on how to exploit this wealth of data to understand the physical origin of cosmic acceleration. We develop here a threefold way to explore the space of models for this physical phenomenon. This consists in:

- Understanding the level of agreement of present data, within our fiducial model;
- Exploring the space of available alternative theories through parametrizations;
- Testing specific, physically motivated, theories;

In the space of models the first path corresponds to asking whether our present position is really motivated by experiments. If this is the case then we should proceed in our exploration of available models, to tighten our belief that the fiducial one does not only work well in explaining the data, but also works better than other models. On the other hand, if present data show substantial signs of disagreement, that cannot be attributed to some systematic effect, we have to start exploring the space of available models to search one that works better and explains these tensions on a physical basis.

The second and third ways of this threefold approach focus on how we can move away from the fiducial model. Exploring the space of available theories through parametrizations, allows to cover wide portions of model space while being agnostic about the precise physical details of the models considered. If no sign of disagreement is found, within the fiducial model, then parametrizations allow to cast constraints on model space in a general way. If they are designed to cover wide enough portions of this space, then proportionally our belief in the fiducial model will be tighten. If parametrizations relieve tensions between data, or explain the data better than the fiducial model, we can use these results to aid model building by pointing out the phenomenological signatures that are preferred by the data.

Finally the third way of the threefold approach to model exploration consists in testing specific theories. These might have a well motivated physical origin and testing them corresponds to exploring specific portions of model space.

Al the branches of this approach are complementary. If there is no sign of disagreement within the fiducial model, if general parametrizations do not favor some other phenomenological signature and none of the specific models that we know are better in explaining the data then we are sure that, at present, our fiducial model is our best description of the universe. Conversely we can

conclude that our present fiducial model is outdated if we find signs of disagreement, and these either correspond to some phenomenological signature that is caught by parametrizations or can be explained by a model. We can arrive to the same conclusion if we find some parametrization that has a phenomenological signature that is favoured by the data and we have a solid physical origin for that.

This thesis is organized as follows. It is divided into an introductory part and other three parts reflecting the structure of the threefold approach previously discussed.

In part I we review some basic concepts of Modern Cosmology. In chapter 2 we briefly introduce the notion of background cosmology; in chapter 3 we discuss the behavior of cosmological perturbations and in chapter 4 we discuss the cosmological observables that can be used to probe these two regimes.

Part II concerns the development and exploitation of statistical null test for the concordance of cosmological observations as discussed in chapter 5.

Part III of this thesis is focused on parametrized approaches and in particular on the Effective Field Theory approach to DE and MG and its implementation. In chapter 6 we introduce this framework and in chapter 7 we discuss its phenomenology at the background level. In chapter 8 we move at the perturbation level and we describe the implementation of the EFT approach in the Einstein-Boltzmann solver CAMB that can be used to study the cosmological phenomenology of models enclosed in the EFT description. At last, in chapter 9 we discuss some of the observational consequences that have been obtained by applying this framework and its corresponding code implementation.

Part IV instead, focuses on model tests that we performed by exploiting the power and flexibility of the EFT approach. In chapter 10 we discuss the cosmological phenomenology and corresponding constraints on designer $f(R)$ gravity. In chapter 11 we discuss Hu-Sawicki $f(R)$ model and in chapter 12 we discuss Horăva gravity.

We conclude in part V.

Part I

Modern Cosmology

Chapter 2

Cosmological Background

Cosmology is the study of the composition and evolution of the universe by means of mathematical and physical tools. The energy scales characterizing our description of the universe, from its birth until today, vary over a wide range, and therefore modern cosmology exploits a number of different branches of physics.

Still the main difference between cosmology and the other branches of physics is that the natural phenomenon that we are trying to understand is the universe in which we live.
This implies that we cannot perform experiments because we cannot control its parameters and we do not have different universes to consider as different realization of the same physical phenomenon. We are then limited to observe the universe and we can only collect information coming to us. We can then build physical models based upon the laws that have been studied on the Earth and compare them with the information that have been collected.
In order for this process to be meaningful we have to assume a mediocrity principle that formalizes our belief that things are quite the same throughout the universe. This is the heart of the Cosmological Principle that states the following [26]:

On sufficiently large scales the properties of the universe are the same for all fundamental observers.

Three different qualifications are implied by this principle.
The first is that observed phenomena do not depend on the quality of the observer. The second is that natural laws do not depend on the position of the observer. The third is that on sufficiently large scales the differences in the observations are negligible.
This principle legitimates the process of comparison between what we see on the earth and what we observe from the universe and gives a key to interpret them.
The problem with the Cosmological Principle (hereafter CP) is that it is a philosophical assumption that cannot be verified nor deduced from experiments. But at the present time there are some evidences that make this assumption at least reasonable. The most remarkable of these evidences is the observed isotropy

of the cosmic microwave background radiation, originated when the Universe had about the temperature of a star. In fact we see in all directions in the sky an electromagnetic radiation that has the same wavelength with deviations of order 10^{-5}. If we were living in an irregular universe we would probably see the imprint of these irregularities on this radiation. Another clue to the CP comes from the fact that our "geographical knowledge" of the universe is increasingly enlarged by new observations made possible by recent technological advances. Until the 1920s it was believed that our galaxy was the entire universe [27]. Today we have wide surveys of galaxies that tell us that the Milky Way is one in billions of galaxies.
Even if these facts do not prove the cosmological principle they make it a little harder to believe that we occupy a special position in the universe.
If we then accept general relativity as our theory of gravitation the CP has an important consequence [28].
In fact it implies that, smoothed on sufficiently large scales, the universe is spatially homogeneous and isotropic so it is a four dimensional semi-Riemannian manifold that has a family of three dimensional maximally symmetric sub spaces.
It is a well-known fact [28] that the metric is the Friedmann-Robertson-Walker (FLRW) one and the line element takes the form:

$$ds^2 = g_{\mu\nu}dx^\mu dx^\nu = -dt^2 + a^2(t)\left[\frac{dr^2}{1-kr^2} + r^2(d\theta^2 + \sin(\theta)^2 d\phi^2)\right], \quad (2.1)$$

where $k = -1, 0, 1$ indicates the curvature of the spatial slicing (flat spatial slicing corresponds to $k = 0$, negatively curved to $k = -1$ and positively curved to $k = 1$) and $a(t)$ is the *scale factor* describing the expansion of space. We have here normalized the curvature parameter to $|k| = 1$; an alternative normalization is setting the scale factor today $a_0 \equiv a(t_0) = 1$. The family of fundamental observer is then characterized by their four-velocity that in this reference frame is $u^\mu = (-1, 0, 0, 0)$ so that their spatial position does not change in time. We shall refer to these observers as comoving observers. The coordinate t is the proper time as measured by a comoving observer and is referred to as *cosmic time*. We can naturally introduce another time variable, the *conformal time* η via:

$$\eta(t) \equiv \int_0^t \frac{dt'}{a(t')}\,. \quad (2.2)$$

and this brings the FLRW metric (2.1) to:

$$ds^2 = a^2(\eta)\left[-d\eta^2 + \frac{dr^2}{1-kr^2} + r^2(d\theta^2 + \sin(\theta)^2 d\phi^2)\right], \quad (2.3)$$

where $a(\eta) \equiv a[t(\eta)]$. In the case of flat space slicings, $k = 0$, the metric defined by (2.3) is conformally equivalent to the Minkowski metric $\eta_{\mu\nu}$.

A fundamental quantity for cosmology is the *Hubble parameter* defined as

$$H \equiv \frac{\dot{a}}{a}\,, \quad (2.4)$$

where the overdot indicates a derivative with respect to the cosmic time t. The Hubble parameter describes the expansion history of the universe as it measures

the rate at which the scale factor changes. The Hubble parameter can be directly derived from the recession velocity of distant galaxies and their distance from us. Edwin Hubble (1929) was the first to find that distant galaxies recede from us and that they do so with a velocity which is proportional to their distance. This observation matched exactly what is expected in an expanding universe. Neglecting peculiar motion of the galaxies, in fact, we expect $v = Hd$.

2.1 FLRW models

In this section we shall review the cosmological models that arise from the assumption of the CP and the metric tensor (2.1). These models were developed between the 1920s and the 1930s by Alexander Friedmann, Georges Lemaître, Howard Percy Robertson and Arthur Geoffrey Walker and named FLRW after them. The metric is the fundamental object in GR, as it describes gravity in terms of curvature of the spacetime. The field equations for the metric are the Einstein equations, a set of non-linear partial differential equations relating the curvature of spacetime to its content. In the GR language these are:

$$G_{\mu\nu} = 8\pi G T_{\mu\nu}\,, \tag{2.5}$$

where the Einstein tensor is related to the metric by:

$$\begin{aligned}
&G_{\mu\nu} \equiv R_{\mu\nu} - \frac{1}{2} R g_{\mu\nu}\,,\\
&R_{\mu\nu} \equiv R^{\alpha}_{\mu\alpha\nu}\,,\\
&R \equiv g^{\mu\nu} R_{\mu\nu}\,,\\
&R^{\alpha}{}_{\mu\nu\beta} = \Gamma^{\alpha}_{\nu\beta,\mu} - \Gamma^{\alpha}_{\mu\beta,\nu} + \Gamma^{\gamma}_{\mu\beta}\Gamma^{\alpha}_{\nu\gamma} - \Gamma^{\gamma}_{\nu\beta}\Gamma^{\alpha}_{\mu\gamma}\,,\\
&\Gamma^{\alpha}_{\mu\nu} = \frac{1}{2} g^{\alpha\sigma}(g_{\sigma\mu,\nu} + g_{\sigma\nu,\mu} - g_{\mu\nu,\sigma})\,.
\end{aligned} \tag{2.6}$$

where $g^{\mu\nu}$ is the inverse matrix of $g_{\mu\nu}$, i.e. $g^{\mu\nu} g_{\mu\nu} = \delta^{\mu}_{\nu}$ and with the subscript $_{,\nu}$ we indicate a covariant derivation ∇_{ν}. R is the Ricci scalar, a contraction of the Ricci tensor $R_{\mu\nu}$, which in turn is the contraction of the Riemann tensor $R^{\alpha}{}_{\mu\nu\beta}$. Finally, $T_{\mu\nu}$ is the energy-momentum tensor of matter fields. FLRW models describe a universe filled with a homogeneous isotropic perfect fluid, and so $T_{\mu\nu}$ has the form:

$$T_{\mu\nu} = (\rho + p) u_{\mu} u_{\nu} + p g_{\mu\nu}\,, \tag{2.7}$$

where u^{μ} is the fluid four-velocity, ρ and p are respectively its rest frame energy density and pressure. The fluid elements will be comoving in the cosmological rest frame and isotropic so that the energy-momentum tensor (2.7) reads

$$\begin{aligned}
&T^{0}{}_{0} = -\rho\,,\\
&T^{i}{}_{j} = p\delta^{i}{}_{j}\,,\\
&T^{0}{}_{i} = 0\,.
\end{aligned} \tag{2.8}$$

Plugging this and the FLRW metric (2.1) into the Einstein equations, we immediately obtain the two following equations:

$$H^2 = \frac{8\pi G}{3}\sum_m \rho_m - \frac{k}{a^2}\,, \tag{2.9}$$

$$\frac{\ddot{a}}{a} + \frac{1}{2}\left(\frac{\dot{a}}{a}\right)^2 = -4\pi G\sum_m p_m - \frac{k}{2a^2}\,, \tag{2.10}$$

where m labels the different matter constituents of the universe. The first equation (2.9), is referred to as the *Friedmann equation*. It is a constraint equation for the time derivative of the scale factor $\dot{a}$, relating it to the energy density and curvature of spacetime. If we combine the second equation with the Friedmann equation we obtain the *acceleration* equation:

$$\frac{\ddot{a}}{a} = -\frac{4\pi G}{3}\sum_m(\rho_m + 3p_m)\,. \tag{2.11}$$

Notice that, according to (2.11), the universe will decelerate its expansion ($\ddot{a} < 0$) as long as it is dominated by a form of matter such that $\rho_i + 3p_i > 0$.

In order to solve the Friedmann equation, we need to close the system with equations relating the energy density and pressure of the components of the universe.

2.2 Matter Components

To close the system of Friedmann equations we need the propagation equations for the matter species. The Bianchi identity $\nabla_\mu G^{\mu\nu} = 0$ implies that the total stress energy tensor of the matter components is covariantly conserved. In addition, if the matter species are not coupled the individual stress energy tensors follow the continuity equation for the energy-momentum tensor:

$$\nabla_\mu T_m^{\mu\nu} = 0\,. \tag{2.12}$$

The time ($\nu = 0$) component of equation (2.12), enforces the continuity of energy and it determines the time evolution of energy density. In a FLRW spacetime, for a perfect fluid (2.8) it reads:

$$\dot{\rho}_m + 3H(\rho_m + p_m) = 0\,. \tag{2.13}$$

Still the system of Friedmann and continuity equations is not closed and we have to specify the equation of state for our fluids. This equation relates density and pressure as $p = p(\rho)$ and is assumed to be, either exactly or approximately:

$$p_m \equiv w_m \rho_m\,. \tag{2.14}$$

Then equation (2.13) can be solved for $\rho_m(a)$ and the solution reads:

$$\rho_m \propto \exp\left(-3\int \frac{da'}{a'}(1 + w_m)\right)\,. \tag{2.15}$$

In studying the expansion of the universe, and in particular the formation of its structures, we consider radiation and non-relativistic matter. There are different relativistic massless particles constituting the radiation component of our universe and we shall consider photons and massless neutrinos. Non-relativistic matter, in turn, comes in the form of neutrons, protons, electrons and other Standard Model particles and is commonly referred to as *baryonic matter*. Baryons, however, make up just a small fraction of the total matter, and the remaining is in an elusive form which reveals itself via gravitational interactions, and is dubbed dark matter (DM).

Non-relativistic matter is characterized by a negligible kinetic energy so we expect its energy density to scale proportionally to the volume. In the case of radiation, we expect to have an extra factor in the scaling because of the *redshift* of the wavelength as the universe expands. Indeed, radiation emitted with wavelength λ_e, in the rest frame of a comoving observer, at proper time $a(t_e) = a_e$, is observed today at wavelength λ_o, related to λ_e by:

$$1 + z \equiv \frac{\lambda_o}{\lambda_e} = \frac{1}{a}\,, \tag{2.16}$$

where z is the redshift. Therefore, we expect non-relativistic matter to be characterized by $w_m = 0$, and radiation by $w_r = 1/3$, i.e.

$$\rho_m \propto a^{-3}\,, \tag{2.17}$$

$$\rho_r \propto a^{-4}\,. \tag{2.18}$$

The Standard Cosmological Model is characterized by another, dark, component. Following the discovery that the expansion of the universe is accelerating, the cosmological constant Λ re-entered in cosmology. Originally it was introduced by Einstein, as an extra term, $\Lambda g_{\mu\nu}$, in the Einstein equations (2.5) to obtain a static cosmological solution. Soon after that, it was found that the universe is not static but rather expanding, with distant galaxies receding from us and the cosmological constant was no longer necessary.

It was not introduced again until later, when the measurements of SNeIa indicated that the expansion of the universe is accelerating. This late time acceleration can be achieved if the universe is dominated by an energy component with the equations of state $w \leq -1/3$. The cosmological constant Λ results in exactly $w = -1$ and gives a component with constant energy density (and $p = -\rho$) with an energy-momentum tensor:

$$T^{\Lambda}_{\mu\nu} = -\frac{\Lambda}{8\pi G} g_{\mu\nu}\,, \tag{2.19}$$

Therefore, it is equivalent to treat a cosmological constant as a component of the energy density of the universe that serves the purpose of fueling the accelerated expansion of the universe.

2.3 Distances and Horizons

In this section we shall review the notion of distance in an FLRW universe [29].

The FLRW metric corresponds to a system of spatial coordinates which is *comoving* with the expansion of the universe. Different points will maintain their coordinates, as the universe expands, therefore their *comoving distance* will remain unchanged. The physical distance, however, will increase, with a rate given by the Hubble parameter.

The comoving distance out to an object at scale factor a is then given by:

$$\chi(a) = \int_a^1 \frac{d\ln a'}{a' H(a')} \,. \tag{2.20}$$

Of particular relevance is the comoving distance that light could have traveled since $t = 0$, which is given by the conformal time η (2.2). Causal physical processes could not have happen at distances larger than this distance, and therefore η is called the *comoving horizon*.

In an expanding universe it is possible to define other two types of distances. A common way of determining distances, in astronomy, is the parallax method. By knowing the angle θ subtended by an object of known physical size l we can infer the distance of that object

$$d_A = \frac{l}{\theta} \,. \tag{2.21}$$

this is then commonly called the *angular diameter distance*. In a flat universe it coincides with the physical distance $d_A^{flat} = a\chi$.

A second way of determining distances is by measuring the flux from an object of known luminosity. The flux, integrated over all frequencies, that we observe from a source of luminosity L through a comoving shell at distance $\chi(a)$ is given by

$$F = \frac{La^2}{4\pi\chi^2(a)} \,, \tag{2.22}$$

hence we can define the *luminosity distance* of that object as $d_L = \chi/a$.

The luminosity distance plays a central role in the study of type Ia Supernovae (SNeIa). These objects are standardizable candles as they have nearly identical intrinsic magnitude M and small differences can be balanced by knowing the shape of their light curves. Since we observe their apparent magnitude, any difference that we observe there is related to a difference in the supernovae distance.

The relation between the apparent and intrinsic magnitude in then given by the luminosity distance of the supernova:

$$m = M + 5\log\left(\frac{d_L}{10\,pc}\right) + K \,, \tag{2.23}$$

where K is a correction for the shifting of the spectrum due to expansion.

This allows us to measure the distance from us to the supernova by measuring the difference between $m - M$, independently of their redshift. We can therefore reconstruct the relationship between redshift and luminosity distance.

At last, in this section we shall mention two crucial concepts in an FLRW universe. These are causality and the horizon. As we already seen the comoving

horizon η is the maximum distance a light ray could have traveled from $t = 0$. This then represents the maximum radial distance of a point that could have communicated with us since the Big Bang. Analogously, objects separated by a distance larger than the comoving horizon η, could never have been in causal contact. It is a common practice to define the *Hubble radius* as the integrand $1/aH$ in the comoving horizon expression as this represents the distance over which particles can travel in the course of one expansion time. Particles that are separated by a distance larger than the Hubble radius cannot communicate now but still might be in communication at a different time.

2.4 Cosmic Acceleration

In the previous section we introduced SNeIa as standardizable candles, i.e. having almost the same absolute magnitude after we correct for the differences in the shapes of their light curves. This makes them the perfect tool to measure independently distances and redshift. From the difference between the apparent magnitude m and absolute magnitude M, we can infer the luminosity distance (2.23). Then one can independently measure the redshift, and thus reconstruct the distance-redshift relation. This relation in particular is given by:

$$d_L(z) = (1+z) \cdot \int_0^z \frac{dz'}{H(z')} \,. \tag{2.24}$$

By measuring independently $d_L(z)$ and z, we can then constrain the expansion history $H(z)$ over a wide range of redshifts. This program was followed by the Supernova Cosmology Project [11, 30, 31] and the High-Z Supernova Team [12, 32, 33, 34] and the Supernova Legacy Survey (SNLS) [35], and resulted in measurements of the magnitude and redshift of distant SNeIa up to redshift $z \lesssim 1.7$.

As we increase the distance from us SNeIa appear dimmer than expected if the universe was currently matter dominated. Further combining the data from SNeIa, CMB and LSS, we have a strong evidence for a universe which is currently dominated by either a cosmological constant, or a form of energy which is smoothly distributed and makes up $\sim 70\%$ of the current energy budget. In other words the universe has then recently entered a phase of accelerated expansion.

A value of $\Omega_\Lambda^0 \approx 0.7$, corresponds to an energy density

$$\rho_\Lambda^0 \approx (10^{-3} eV)^4 \,. \tag{2.25}$$

This value, however, proves puzzling to interpret [36]. If we consider this energy as a constant contributed by quantum fluctuations in the vacuum, then we would expect it to be of order the cutoff scale of our effective theory. Hence, if we believe that our effective quantum field theory is valid up to the Planck scale, we would expect ρ_Λ to be of order M_P^4; thirty orders of magnitude (in mass scale) bigger than the observed value. In addition, the cosmological constant interpretation of cosmic acceleration presents another puzzle: the coincidence between the observed vacuum energy and the current matter density today. The ratio between these two energy densities scales as a^3. Therefore there is a brief epoch of

the universe's history during which it would be possible to witness the transition from matter domination to cosmological constant domination. This is known as the *coincidence problem*. An alternative way of achieving the desired accelerated expansion is by introducing a smoothly distributed energy component with negative equation of state, commonly referred to as *dark energy* (DE). One possibility consists of employing a slowly rolling scalar field, similar to what is done for inflation. Such an approach is known as *quintessence* [37, 38, 39, 40, 41, 42]. Unfortunately it is not trivial to constrain the shape of the potential characterizing such a field, and there is always some degree of fine-tuning required in order to obtain the right scale of the energy density. Indeed we expect such a scalar field to be quite light, $m_\phi \approx H_0 \approx 10^{-33} eV$. An interesting possibility consists in coupling the scalar field to matter fields. Indeed, linking the dynamics of the scalar field to that of matter, one may solve the coincidence problem. In such models the scalar field displays a tracking behavior, and its current energy density can be largely independent of the initial conditions. An alternative to DE consists in assuming, instead of a new energy component, new gravitational dynamics on large scales, i.e. *modifying gravity* (MG). There are several models exploring this idea in the literature and we refer the reader to [43], and references therein, for a thorough review. It is important to notice that any approach to the phenomenon of cosmic acceleration, alternative to the cosmological constant, needs to explain why the vacuum energy would be zero. With respect to the cosmological constant approach, dark energy and modified gravity models have the advantage of adding some dynamics to the theory, and this might alleviate the coincidence problem and increase the experimental testability of the models. In particular, we might expect to see some peculiar signatures of these models at the level of the growth of structure. Finally, it is important to mention another alternative approach to the phenomenon of cosmic acceleration. Instead of modifying GR or assuming new components of the energy budget, we can give up the assumption of a homogeneous and isotropic background and fit the SNeIa data with a universe that has inhomogeneities. The inferred late time acceleration could then be a result of the averaging process. Several models have been recently proposed [44, 45, 46, 47, 48, 49, 50, 51], however the effect of the inhomogeneities seems to be too small to account for the data.

Chapter 3

Cosmological Perturbations

In the previous Chapter we have briefly reviewed the homogeneous and isotropic model of the universe, studying what is commonly referred to as *background dynamics*. While the remarkable isotropy of the CMB supports this model there are fluctuations in the temperature of the CMB of the order of one part in 10^5. These were discovered in the Nineties by measurements of the COBE satellite [52, 53] and later measured to high precision by WMAP [54] and *Planck* [16]. Moreover, we do see a lot of structure in our surroundings and on smaller scales the universe is highly inhomogeneous, with matter clumped into large scale structure.

In this Chapter we shall review how primordial perturbations grow under the action of gravitational instability to form the large cosmological structures that we observe today.

3.1 Perturbing the universe

To start, we need to define the perturbations around an FLRW universe (2.1) of the gravitational field, the matter fields, including radiation, baryons and CDM.

Perturbing the energy momentum tensor of the matter fields (2.8), by introducing a space dependence in the energy density and pressure also introduces a velocity field and shear. The perturbed stress-energy tensor is then:

$$\begin{aligned} T^0{}_0 &= -\bar{\rho}\,(1+\delta)\,, \\ T^i{}_j &= (\bar{p}+\delta p)\,\delta^i{}_j + \pi^i_j\,, \\ T^0{}_i &= (\bar{\rho}+\bar{p})\,v_i\,, \end{aligned} \tag{3.1}$$

where $\bar{\rho}(\eta)$ and $\bar{p}(\eta)$ are the background energy density and pressure, $\delta(\eta,\vec{x}) \equiv \delta\rho/\bar{\rho}$ is the density contrast, $\delta p(\eta,\vec{x})$ the pressure perturbation, $v_i(\eta,\vec{x})$ the velocity field and we define the anisotropic stress $\sigma(\eta,\vec{x})$ as

$$(\bar{\rho}+\bar{p})\sigma \equiv -\left(\hat{k}^j\hat{k}_i - \frac{1}{3}\,\delta^j_i\right)\pi^i_j\,. \tag{3.2}$$

When it comes to perturbing the gravitational field we can decompose the contributions to the metric in terms of irreducible representations of the rotation

group. The most generic form of the perturbed metric will therefore contain scalar, vector and tensor perturbations. At linear order, these three types of perturbations evolve independently, thanks to the superopsition principle. As we are interested in studying the growth of structure, we will concentrate on *scalar* perturbations for the rest of this Chapter.

The most generic metric containing scalar perturbations reads

$$g_{00} = -a^2(1+2A), \tag{3.3}$$
$$g_{0i} = -a^2 B_{,i}\,, \tag{3.4}$$
$$g_{ij} = a^2\left[(1+2H_L)\,\delta_{ij} + 2H_{T,ij}\right]\,, \tag{3.5}$$

where A, B, H_L, H_T are functions of time and space, $B_{,i} \equiv \partial_i B$ and $H_{T,ij} \equiv \partial_i\partial_j H_T$ (and $\partial_i \equiv \partial/\partial x_i$). Out of these four quantities we can choose two independent quantities by means of a gauge transformation. The two most common gauge choices are the *longitudinal* or Newtonian gauge, corresponding to $B = 0 = H_T$, and the *synchronous* gauge, corresponding to $B = 0 = H_L$. While the longitudinal choice completely fixes the gauge, the synchronous gauge has some residual gauge freedom, which is typically eliminated by choosing a frame that is comoving with CDM.

Most of the work in this thesis is done in synchronous-comoving gauge, as this turns out to be a convenient gauge choice to perform numerical calculations. While we will present later the results in this gauge we shall discuss here perturbation theory in Newtonian gauge to have a clearer physical interpretation.

3.2 Jeans analysis - Newtonian perturbation theory

The focus of this chapter is describing cosmological perturbation theory and how the structure we observe today formed via gravitational instability starting from small fluctuations set up in the early universe. The main results for the collapse of matter into structures can be recovered with the classical formalism of Newton's theory. Before getting into the details of the fully general relativistic theory of linear perturbations it is thus instructive to review the Jeans analysis to gain some physical insight into the process of structure formation.

The Newtonian equations governing perfect fluid dynamics are the *continuity*, *Euler* and *Poisson* equations, respectively:

$$\frac{\partial\rho}{\partial t} + \nabla(\rho\vec{v}) = 0\,, \tag{3.6}$$
$$\frac{\partial\vec{v}}{\partial t} + (\vec{v}\cdot\nabla)\vec{v} + \frac{1}{\rho}\nabla\rho + \nabla\Phi = 0\,, \tag{3.7}$$
$$\nabla^2\Phi = 4\pi G\rho\,. \tag{3.8}$$

Notice that these can be obtained from Einstein equations in the weak field and non-relativistic limit.

The simplest solution to these equations is the static one, where the matter is at rest and uniformly distributed in space. In an expanding universe, this reads

$$\rho_0(t,\vec{r}) = \frac{\rho_0}{a^3}, \quad \vec{v}_0(t,\vec{r}) = \frac{\dot{a}}{a}\vec{r}, \quad \phi_0(t,\vec{r}) = \frac{2\pi G\rho_0}{3}r^2\,. \tag{3.9}$$

Let us now expand all the fields around this background solution:

$$\begin{aligned}
\rho(t,\vec{x}) &= \rho_0(t)[1+\delta(t,\vec{x})]\,,\\
\vec{v}(t,\vec{x}) &= \vec{v}_0(t) + \vec{v}_1(t,\vec{x})\,,\\
\phi(t,\vec{x}) &= \phi_0(t) + \phi_1(t,\vec{x})\,,
\end{aligned} \tag{3.10}$$

where $|\delta|, |\vec{v}_1|/|\vec{v}_0|, \phi_1/\phi_0 \ll 1$. If we plug this expansion into the set of equations (3.6)-(3.8), linearize the equations and Fourier transform the variables, we obtain the following second order ordinary differential equation for the density contrast δ

$$\ddot{\hat{\delta}}(\vec{k}) + 2H\dot{\hat{\delta}}(\vec{k}) + \left(\frac{v_s^2|\vec{k}|^2}{a^2} - 4\pi G\rho_0\right)\hat{\delta}(\vec{k}) = 0\,, \tag{3.11}$$

where $v_s \equiv (\partial p/\partial\rho)^{1/2}$ is the sound speed of the fluid.

This is the main evolution equation describing the clustering of matter in an expanding universe. It is clear from (3.11) that there are two competing forces: the gravitational attraction and the stabilizing effect of pressure. The scale at which the two forces balance each other is known as the *Jeans length*

$$\lambda_J \equiv v_s\sqrt{\frac{\pi}{G\rho_0}}\,. \tag{3.12}$$

On scales smaller than the Jeans scale, pressure dominates and perturbations do not grow, but oscillate. On larger scales, gravity dominates and perturbations grow monotonically until the break down of linear perturbation theory. The second term in (3.11), $2H\dot{\hat{\delta}}(\vec{k})$, plays an important role in slowing the growth of perturbations and for this reason is known as Hubble friction. On scales larger than the Jeans length, the growth of density perturbations would be exponential in the absence of this term. The presence of the friction term slows down the growth of perturbations that follows a power-law behavior instead.

3.3 Linear Equations

In the previous Chapter we used the FLRW metric (2.1) and the perfect fluid stress-energy tensor to derive Friedmann equations. Similarly in this Section we use Einstein equations, along with the perturbed FLRW metric (3.3) in Newtonian gauge and the perturbed stress-energy tensor to study the dynamics of small inhomogeneities.

This procedure consists of inserting the metric (3.3) (with $H_T = 0 = B, A = \Psi, H_L = -\Phi$, as we have chosen to work in Newtonian gauge) and energy-momentum tensor (3.1) into the Einstein equations (2.5) and expand the resulting equations up to first order in these perturbations. This procedure results in

the following linearized Einstein equations:

$$time - time$$

$$k^2\Phi + 3\mathcal{H}(\Phi' + \mathcal{H}\Psi) = -\frac{\kappa^2 a^2}{2}\bar{\rho}\delta\,, \tag{3.13}$$

$$momentum$$

$$k^2\left(\Phi' + \mathcal{H}\Psi\right) = \frac{\kappa^2 a^2}{2}(\bar{\rho} + \bar{p})ikv\,, \tag{3.14}$$

$$space - diagonal$$

$$\Phi'' + \mathcal{H}\left(\Psi' + 2\Phi'\right) + \left(2\mathcal{H}' + \mathcal{H}^2\right)\Psi + \frac{k^2}{3}\left(\Phi - \Psi\right) = \frac{\kappa^2 a^2}{2}\delta p\,, \tag{3.15}$$

$$space - off diagonal$$

$$k^2\left(\Phi - \Psi\right) = \frac{3\kappa^2 a^2}{2}(\bar{\rho} + \bar{p})\sigma\,, \tag{3.16}$$

where $\kappa^2 \equiv 8\pi G$. Out of these four equations just two of them (3.13)-(3.16) are independent. It is common to use the *anisotropy* equation (3.16) and the combination of equations (3.13) and (3.14) giving the *Poisson* equation:

$$k^2\Phi = -\frac{\kappa^2 a^2}{2}\bar{\rho}\Delta\,, \tag{3.17}$$

where

$$\Delta \equiv \bar{\rho}\delta + 3i\mathcal{H}(\bar{\rho} + \bar{p})\frac{v}{k} \tag{3.18}$$

is the energy density in comoving synchronous gauge. The advantage of the Poisson equation is that it is not dynamical, it is simply a constraint equation relating the metric potential Φ to the energy-momentum sources. Also the anisotropy equation is not dynamical, and in presence of negligible shear, $\sigma \simeq 0$, it simply sets the two gravitational potentials equal.

Notice that in eq.(3.14) we considered only the irrotational component of fluid velocity so that $\vec{v} = v\hat{k}$. Since vector velocity modes decay in time we will continue doing so in the rest of the thesis.

Let us now derive the linearized version of the energy-momentum continuity equations. For a single uncoupled fluid, the continuity equations (2.12) at linear level give the two following independent equations:

$$\delta' = -(1+w)(ikv - 3\Phi') - 3\mathcal{H}\left(\frac{\delta p}{\delta\rho} - w\right)\delta\,, \tag{3.19}$$

$$v' = -\mathcal{H}(1-3w)v - \frac{w'}{1+w}v - \frac{\delta p/\delta\rho}{1+w}ik\delta + ik\sigma - ik\Psi. \tag{3.20}$$

Usually this is enough to study the growth of structures during the matter era. However, to study in detail the evolution of perturbations through all the expansion history, it is necessary to take into account non-gravitational interactions between different species. In particular photons and baryons are non-gravitationally are tightly coupled before recombination through Compton scattering, forming a photon-baryon fluid. Therefore there are extra terms in the conservation equations representing the energy-momentum transfer between

these two components. The *Botzmann* equation formalism applied to the phase space of particles offers the necessary tools. We describe interacting fluids via their *distribution function* $f(\vec{x}, \vec{p}, \eta)$, which evolves according to the Boltzmann equation

$$\frac{df}{d\eta} = \frac{\partial f}{\partial \eta} + \frac{dx^i}{d\eta}\frac{\partial f}{\partial x^i} + \frac{dp}{d\eta}\frac{\partial f}{\partial p} + \frac{d\hat{p}^i}{d\eta}\frac{\partial f}{\partial p^i} = C[f]\,, \tag{3.21}$$

where $C[f]$ is the collision term. The distribution function will be the Fermi-Dirac one for fermions (+ sign) and the Bose-Einstein distribution for bosons (− sign). At the background level these read:

$$f_0(p, \eta) = \left[\exp\left(\frac{E(p)}{T(\eta)}\right) \pm 1\right]^{-1}\,, \tag{3.22}$$

where $E(p) = \sqrt{p^2 + m^2}$. At the perturbation level the distribution function, will have a position and momentum direction dependence in the temperature:

$$f(\vec{x}, p, \hat{p}, \eta) = \left[\exp\left(\frac{E(p)}{T(\eta)[1 + \Theta(\vec{x}, \hat{p}, \eta)]}\right) \pm 1\right]^{-1}\,, \tag{3.23}$$

where $\Theta(\vec{x}, \hat{p}, \eta)$ denotes the perturbation to the background temperature. Note that p is not the comoving momentum P_i conjugate to the comoving coordinate x^i, but rather the proper momentum measured by an observer at a fixed spatial coordinate. The magnitude of p is related to P_i via $p^2 = g^{ij}P_iP_j$, and it decreases with the expansion of the universe. The components of the energy-momentum tensor can be derived from the distribution function via

$$T^\mu_\nu(\vec{x}, \eta) = g_s \int \frac{dP_1 dP_2 dP_3}{(2\pi)^3} \frac{1}{\sqrt{-g}} \frac{P^\mu P_\nu}{P^0} f(\vec{x}, \vec{p}, \eta)\,, \tag{3.24}$$

where g_s represents the number of spin states.

Since we work in Fourier space, let us use the Fourier transformed temperature perturbation $\Theta(k, \mu, \eta)$, where $\mu \equiv \hat{k} \cdot \hat{p}$ is the angle between the direction of the gradient in the temperature and the particle motion.

For the sake of brevity we do not include the details of the derivation of the explicit linear Boltzmann equations, but limit ourselves to presenting the result and referring the reader to the literature on this topic ([55, 56, 57, 58, 59, 60] and references therein).

It is useful to expand the temperature perturbation in Legendre polynomials, defining the l-th multipole of the temperature field as

$$\Theta_l(k, \eta) \equiv \frac{1}{(-i)^l} \int_{-1}^{1} \frac{d\mu}{2} \mathcal{P}_l(\mu)\Theta(\mu)\,, \tag{3.25}$$

where $\mathcal{P}_l$ denotes the Legendre polynomial of order l.

We do not present here the calculation for the collision term $C[f]$ due to Compton scattering, but we outline the resulting Boltzmann equations for radiation and baryons. Radiation contains photons, that interact with baryons before recombination, and neutrinos that for our purposes are treated as collisionless. We will indicate with Θ the temperature perturbation of photons,

with $\mathcal{N}$ the temperature perturbation of (massless) neutrinos and with ρ_b, v_b the energy density and velocity of the baryons. The resulting equations are

photons

$$\Theta' + ik\mu\Theta = \Phi' - ik\mu\Psi - \tau'[\Theta_0 - \Theta + \mu v_b - \frac{1}{2}\mathcal{P}_2(\mu)\Pi]\,, \tag{3.26}$$

$$\Pi = \Theta_2 + \Theta_{P2} + \Theta_{P0}\,,$$

$$\Theta'_P + ik\mu\Theta_P = -\tau'[\Theta_P + \frac{1}{2}(1 - \mathcal{P}_2(\mu))\Pi]\,,$$

baryons

$$\delta'_b = -ikv_b + 3\Phi'\,, \tag{3.27}$$

$$v'_b + \mathcal{H}v_b = -ik\Psi + \frac{\tau'}{R}[v_b + 3i\Theta_1]\,, \tag{3.28}$$

neutrinos

$$\mathcal{N}' + ik\mu\mathcal{N} = \Phi' - ik\mu\Psi\,, \tag{3.29}$$

where we have distinguished among photons, with temperature perturbation Θ, baryons, with energy density and velocity ρ_b, v_b and neutrinos, with temperature perturbation $\mathcal{N}$. τ is the *optical depth* related to Compton scattering, defined as $\tau' = -n_e\sigma_T a$, where σ_T and n_e are respectively the Thomson cross section and the baryon density. Finally $R \equiv 3\bar{\rho}_b^0/4\bar{\rho}_\gamma^0$ is the baryon to photon density ratio today and Θ_P is the strength of polarization of light.

The Boltzmann equation formalism can also be applied to CDM particles. However, for non-relativistic collisionless species, the density contrast δ and velocity field v are sufficient to describe the perturbed fluid. Moreover, the equations derived through the energy-momentum conservation get us to the same result with simpler algebra. For CDM, characterized by $w = 0$ and a vanishing speed of sound we have:

$$\delta'_c = -ikv_c + 3\Phi'\,, \tag{3.30}$$

$$v'_c = -\mathcal{H}v_c - ik\Psi\,. \tag{3.31}$$

We conclude this part by pointing out that it is common to turn the differential equation (3.26) for the photon temperature perturbation into an infinite series of coupled equations for the multipoles Θ_l. The advantage of this is, as we will see, that the higher moments are small and can be neglected so that we are left with a finite number of simpler equations. The result of this decomposition is the series of equations:

$$\Theta'_0 + k\Theta_1 = \Phi'\,, \tag{3.32}$$

$$\Theta'_1 - \frac{k\Theta_0}{3} = \frac{k\Psi}{3} + \tau'\left[\Theta_1 - \frac{iv_b}{3}\right]\,, \tag{3.33}$$

$$\Theta'_l + \frac{k}{(-i)^{l+1}}\int_{-1}^{1}\frac{d\mu}{2}\mu\mathcal{P}_l(\mu)\Theta(\mu) = \tau'\Theta_l\,, \qquad l \geq 2\,, \tag{3.34}$$

From this equation we immediately see that the monopole, dipole and quadrupole can be related respectively to its density contrast, the velocity field and the anisotropic stress.

3.4 Initial conditions

In order to solve the previously outlined set of differential equations we have to set initial conditions. These are set at very early times, when all the modes of interest for cosmological observables were outside the horizon.

At these scales the inflationary model for the early universe provides a powerful mechanism to generate perturbation's initial conditions, as was realized by many authors [61, 62, 63, 64, 65, 66]. If the inflationary period of rapid expansion of the universe was driven by a scalar field, quantum fluctuations of this scalar field are stretched into super-horizon classical fluctuations which seed the primordial perturbations for the metric and matter fields. We shall not cover here any details about the way inflation generates the primordial spectrum of fluctuations. We will rather assume that some mechanism is responsible for the initial conditions and we will now analyze what are the consistency relations that we need to impose on these initial conditions. We want to stress here that the predictions of inflation for the primordial power spectrum of fluctuations have so far been in very good agreement with observations. CMB experiments in fact provided one of the cleanest measurements of this and, as shown by the latest *Planck* data release [67], the primordial fluctuations are in good agreement with a Gaussian model with an almost scale invariant power spectrum.

If we consider early enough times, scales that are of interest for cosmological observables, were all super-horizon, i.e. their wavelength was larger than the horizon. In terms of the comoving momentum k and comoving horizon η, this condition is characterized by $k\eta \ll 1$. In this limit the evolution equations for the perturbations greatly simplify. In particular, for radiation all the multipoles $l \geq 1$ are negligible. All terms in the equations multiplied by k can be neglected with respect to time derivative terms.

With these approximations the set of perturbed equations for photons, neutrinos, baryons and CDM, becomes:

$$\Theta_0' - \Phi' = 0\,, \qquad \mathcal{N}_0' - \Phi' = 0\,, \tag{3.35}$$

$$\delta_b' = 3\Phi'\,, \qquad \delta' = 3\Phi'\,. \tag{3.36}$$

While the time-time component of the Einstein equation (3.13) is

$$3\mathcal{H}(\Phi' + \mathcal{H}\Psi) = -2\kappa^2 a^2(\bar{\rho}_\gamma \Theta_0 + \bar{\rho}_\nu \mathcal{N}_0)\,. \tag{3.37}$$

Notice that we have considered only radiation sources as we are taking an early time limit. If we derive eq. (3.37) with respect to conformal time, and combine it with equations (3.35), we obtain a second order differential equation for the Newtonian potential Φ

$$\Phi'' \eta + 4\Phi' = 0\,, \tag{3.38}$$

where we have neglected the photons and neutrino quadrupole resulting in $\Psi \simeq \Phi$. Eq. (3.38) has two solutions, a constant and a decaying mode. The decaying one is not physically interesting since we can imagine to set initial conditions early enough for it to be negligible at times relevant to observables. The interesting solution is the constant one and if we plug it back into eq. (3.37), assuming $\Psi \simeq \Phi$ and $a \propto \eta$ we get:

$$\Phi = -2\left[(1 - f_\nu)\,\Theta_0 + f_\nu \mathcal{N}_0\right]\,, \tag{3.39}$$

where we have used f_ν to denote neutrinos fractional density ($f_\nu \equiv \rho_\nu/(\rho_\nu+\rho_\gamma)$). It is common to set $\Theta_0(k,\eta_i) = \mathcal{N}_0(k,\eta_i)$ at early times, so that $\Phi(k,\eta_i) = -2\Theta_0(k,\eta_i)$. Finally, by means of (3.36), we get $\delta_b = \delta = 3\Theta_0 + const.$ as initial conditions. We can now distinguish two types of initial conditions, *adiabatic* and *isocurvature* ones, according to the choice of the constant appearing in the previous equation. If we choose to have a constant ratio of density contrasts in all species everywhere, so the *const.* is zero, we are selecting adiabatic initial conditions. These correspond to fluctuations in the local spatial curvature, with all components of the energy density participating in the perturbation. Notice that the fluctuation in the local number density of any species, relative to the entropy density, vanishes $\delta(n_i/s) = 0$. On the other hand, we label isocurvature initial conditions when we are in a situation in which $\delta(n_i/s) \neq 0$. These correspond to fluctuations in the form of the local equation of state. The ratio between the density contrasts of different species depends on space and the overall effect is a cancellation of the total density perturbation and hence the spatial curvature fluctuation is zero. The distinction between these two types of fluctuations is relevant on super-horizon scales. Once a mode enters the horizon there are casual physical mechanism that can redistribute energy density via fluctuations in the local pressure and hence convert isocurvature perturbations into adiabatic ones. Conversely, since casual physics cannot act on scales larger than the horizon, a super-horizon perturbation must be characterized by $\delta\rho = 0$. It follows that adiabatic perturbations need to be created as sub-horizon modes and then be stretched to super-horizon scales. A mechanism for this is offered by inflation. A period of quasi-De Sitter expansion shrinks the Hubble radius and perturbations that were below the horizon are frozen as they are brought to super-horizon scales. Observations of CMB anisotropies nowadays point toward the fact that the initial power spectrum was made mostly of adiabatic perturbations. Hence, in the following, we shall consider only this kind of initial conditions. At last, even if, as previously discussed, the velocities and dipole moments are negligible at early times, we do need to know their initial conditions in order to evolve them properly. A procedure that is analogous to the one discussed here can be followed to find:

$$\Theta_1(k,\eta_i) = \mathcal{N}_1(k,\eta_i) = \frac{iv_b(k,\eta_i)}{3} = \frac{iv(k,\eta_i)}{3} = \frac{k\Phi(k,\eta_i)}{6aH}\,. \tag{3.40}$$

It is common to express the initial power spectrum of perturbations in terms of the primordial spectrum of the gauge invariant combination:

$$\xi \equiv H_L + \mathcal{H}(B + H_T') - \frac{i\mathcal{H}}{k}v\,, \tag{3.41}$$

that measures scalar curvature perturbations and is related to the Newtonian potential by $\xi \equiv -\Phi - \frac{i\mathcal{H}}{k}v$. This quantity has the advantage that it is conserved on super-horizon scales so that we can decouple the treatment of the initial conditions from the evolution of perturbations. Regardless of the mechanism that we think is responsible for creating primordial fluctuations, once the statistical properties of ξ are in place they are preserved by subsequent time evolution, in the radiation era so that we can start to evolve perturbations, according to these initial conditions later.

If the mechanism responsible for seeding primordial fluctuations is inflation, driven by a scalar field, the quantum fluctuations of the scalar field can be

related, at horizon crossing, to the perturbation ξ. While we shall not present here the details of this mechanism we just need to highlight that at the end of inflation, in Newtonian gauge we have $\Phi = -2/3\xi$. A key prediction of inflationary models is that the initial spectrum of curvature perturbations is nearly scale invariant, which means that $k^3 P_\xi(k)$ is nearly scale independent

$$P_\xi = \left. \frac{\kappa^2 H^2}{4\epsilon k^3} \right|_{aH=k} , \tag{3.42}$$

where ϵ is the slow roll parameter of ($\epsilon \equiv \frac{d(1/H)}{dt}$) and $\kappa^2 = 8\pi G$. A scale invariant power spectrum was firstly predicted as the appropriate primordial distribution of perturbations by Harrison-Zel'dovich-Peebles. To parametrize deviations from perfect scale invariance, it is conventional to write the primordial spectrum as:

$$\ln k^3 P_\xi \equiv \ln A_s + (n_s - 1) \ln \left(\frac{k}{k_s} \right) . \tag{3.43}$$

where A_s stands for the amplitude of primordial fluctuations and the parameter n_s encodes departures from perfect scale invariance.

Chapter 4

Cosmological Observables

In the previous Chapters we have briefly reviewed the homogeneous and isotropic model of the universe and the evolution of small inhomogeneities.

In this Chapter we will review how these translate into cosmological observables and we shall highlight the experimental efforts that, over the last decades, led to the measurements of such quantities.

4.1 Random fields

When studying the universe we are interested in the statistical properties of what we observe. If *background* cosmology can be understood as the study of the average properties of the universe, studying perturbations focuses on describing departures from the average behavior, i.e. higher momenta.

Perturbation are regarded as *random fields* $\phi(\vec{x})$ taking random values at each point in space on constant time slices. Our universe is then thought to be one specific realization in an ensemble of universes, and the observables will be defined in the ensemble rather than on the single realization. These random fields are fully characterized by their statistical properties, i.e. by the N point correlation functions $< \phi(x_1)....\phi(x_N) >$, where the averaging is performed on the ensemble.

In cosmology, these random fields are assumed to be statistically homogeneous and isotropic; i.e. their distribution functions are assumed to be respectively translationally and rotationally invariant. Another common assumption is that the probability distributions of the random fields are *Gaussian*. A nice outcome of these assumptions is that all homogeneous and isotropic Gaussian random fields are ergodic. *Ergodicty* means that the ensemble average can be replaced by a spatial average. This then legitimates us in trusting spatial averages as ensemble averages.

Since perturbations are assumed to be Gaussian to good approximation, statistically isotropic random fields which are fully characterized by their r.m.s. (root mean square) fluctuation $\sigma \equiv < \phi(\vec{x})^2 >^{1/2}$ and two point correlation function

$$\xi(x) \equiv \frac{< \phi(\vec{x_1})\phi(\vec{x_2}) >}{\sigma^2}\,, \tag{4.1}$$

where $x = |\vec{x_1} - \vec{x_2}|$.

It is common to Fourier expand the perturbations

$$\phi(\vec{x}) = \frac{1}{(2\pi^3)} \int e^{i\vec{k}\cdot\vec{x}}\, \hat{\phi}(\vec{k})\, d^3k\,, \tag{4.2}$$

and to work with the functions $\phi(\vec{k})$. The advantage is that at the linear level the evolutionary equations for perturbations reduce to ordinary differential equations in time, and, thanks to the symmetries of the background, each mode evolves independently. Notice that, in writing the expansion 4.2, we have implicitly assumed a spatially flat universe. Since there is strong evidence in favor of spatial flatness, for the rest of this thesis we shall always assume that background spatial curvature vanishes. It is then assumed that the complex numbers $\hat{\phi}(\vec{k})$ have random phases, i.e. they are uncorrelated, and the *power spectrum* is defined as:

$$< \hat{\phi}^*(\vec{k})\hat{\phi}(\vec{k'}) > \equiv (2\pi)^3 \delta(\vec{k} - \vec{k'}) P(k)\,, \tag{4.3}$$

where $P(k)$ depends just on the modulus $|\vec{k}|$ because of isotropy.

4.2 Growth of Structure: the Matter Power Spectrum

With the full set of linear equations and initial conditions outlined in the previous chapter we can go on and study the evolution of perturbations over time. In other Chapters of this thesis we will see plenty of numerical solutions of these equations so here we want to gain some physical insight by approaching analytically this set of equations. We can solve them analytically when we distinguish different regimes. The two main distinctions are: super-horizon versus sub-horizon and radiation era versus matter era. As we will shortly see, on super-horizon scales, perturbations freeze remaining constant. Once they enter the horizon, causal physics starts affecting them and they start evolving. Depending on whether they enter the horizon during radiation or matter domination, their evolution will be substantially different. This difference has observational consequences and is reflected in the turnover of the power spectrum for matter $P(k)$ at a scale k_{eq} corresponding to the mode entering the horizon at matter/radiation equality a_{eq}. We shall focus here on the growth of large scale structures. As it is clear from the linear equations, CDM density perturbations are coupled to all other species. In particular they are directly coupled to the metric potentials, and they are affected by radiation only thorough its gravitational effect. Therefore, at late times, when the universe is matter dominated, we can neglect radiation and solve simply for the Newtonian potentials and CDM perturbations. At early times, however, before recombination, we need to solve for the radiation perturbations in order to determine the evolution of the metric potentials. Before recombination photons are tightly coupled to the baryons, and they can be characterized simply by the monopole

Θ_0 and dipole Θ_1. This is not true after recombination when the higher multipole moments cannot be neglected. To derive the anisotropies of the CMB we will need to account for all the multipoles of radiation properly. By means of equation (3.16), we can immediately see that, if we neglect the radiation quadrupole, the two Newtonian potentials coincide. CDM and baryons, in fact, have a vanishing anisotropic stress and the radiation one is proportional to the quadrupole. With the two gravitational potentials reducing to one we just need one Einstein equation to solve get their evolution. We shall choose one out of (3.13)-(3.15) depending on the context. Notice that the fact that $\Phi = \Psi$ in absence of anisotropic stress is a peculiar feature of GR and in general, when considering Modified Gravity theories this is no longer the case. We shall return to this point in detail in the next chapters. Our set of equations will then include one Einstein equation, either (3.13) or its combination with (3.15), the equations for CDM, (3.30) and (3.31), and two equations for radiation (before recombination), (3.32) and (3.33) We shall start by considering the super-horizon regime. As of initial conditions, we shall use the results of the previous chapter that super-horizon modes, during radiation domination, are constant. We can repeat a similar exercise in the matter era, when $a \propto \eta^2$ to find again that the potentials and matter field perturbations remain constant. It is insightful to combine the analysis of super-horizon modes for both eras in a single equation. Following [60] we introduce:

$$y \equiv \frac{a}{a_{eq}} = \frac{\rho_c}{\rho_r}\,, \tag{4.4}$$

where where the subscript r indicates radiation (photons and massless neutrinos) and c stands for CDM. Notice that we have neglected the baryons, as we will do for the rest of this Section. We can also safely neglect the equation for velocity as it is decoupled at early times and we can trade Θ_0 in favor of δ_c since they are related by $\delta_c = -3\Theta_0$ for adiabatic perturbations. We are then left with two equations for super-horizon perturbations that read:

$$\delta_c' = 3\Phi'\,, \tag{4.5}$$

$$3\mathcal{H}\left(\Phi' + \mathcal{H}\Phi\right) = -\frac{\kappa^2 a^2}{2}\bar{\rho}_c\delta_c\left[1 + \frac{4}{3y}\right]\,. \tag{4.6}$$

Notice that in obtaining this equation we used the time-time component of the Einstein equation (3.13). With some algebra it is possible to recast this set of two equations in a second order one for the gravitational potential Φ:

$$\frac{d^2\Phi}{dy^2} + \frac{21y^2 + 54y + 32}{2y(y+1)(3y+4)}\frac{d\Phi}{dy} + \frac{\Phi}{y(y+1)(3y+4)} = 0\,. \tag{4.7}$$

that can be solved by:

$$\Phi = \frac{\Phi(0)}{10}\frac{1}{y^3}\left[16\sqrt{1+y} + 9y^3 + 2y^2 - 8y - 16\right]\,. \tag{4.8}$$

When $a \ll a_{eq}$, small y, we have a constant gravitational potential $\Phi = \Phi(0)$. For large y the y^3 term dominates in the r.h.s. of (4.8) and we have again a constant solution for the gravitational potential, with $\Phi = (9/10)\Phi(0)$. As we already knew, during these two eras the potential in constant but as it

transitions from the radiation to the matter era, it decreases by an overall factor of 9/10. We now turn to the sub horizon regime $k\eta \gg 1$. The distinction between radiation and matter domination will be important and will leave a direct imprint on observable quantities. As we shall see, the main difference is pressure. Before recombination this will not be negligible and will balance the effect of gravitational attraction, preventing the growth of perturbations. When CDM starts dominating, pressure will gradually become negligible and perturbations will be free to grow due to gravitational instability. We start bu considering modes that enter the horizon during the radiation epoch. At these times radiation is the dominant component of the energy budget, therefore we need to include it in the set of equations. It turns out to be convenient to work with the combination of space-diagonal (3.15) and time-time (3.13) Einstein equations that give:

$$\Phi'' + \frac{4}{\eta}\Phi' + \frac{k^2}{3}\Phi = 0\,, \tag{4.9}$$

where we have neglected anisotropic stress $\Psi = \Phi$. The solution to eq. (4.9) is a Bessel function of order 1. If we impose as initial conditions $\Phi = \Phi_p = const.$ we obtain:

$$\Phi = 3\Phi_p \left(\frac{\sin(k\eta/\sqrt{3}) - (k\eta/\sqrt{3})\cos(k\eta/\sqrt{3})}{(k\eta/\sqrt{3})^3} \right) . \tag{4.10}$$

At horizon crossing, when $k\eta \simeq 1$, the gravitational potential decays like $\propto \eta^2$. As we further go inside the horizon, by increasing $k\eta$, the potential starts oscillating. From the sub-horizon limit of the Einstein equation (3.13) it is clear that $\Theta_0 \propto \eta^2\Phi$. Therefore the density contrast of radiation decays as $\propto 1/\eta$ when entering the horizon and then starts oscillating for $k\eta \gg 1$. After solving for the behavior of the metric potential we can turn to CDM and solve for its evolution. It turns out to be convenient to combine the two conservation equations for CDM, (3.30) and (3.31), into a single second order differential equation for δ_c

$$\delta_c'' + \mathcal{H}\delta_c = 3\Phi'' + 3\mathcal{H}\Phi' - k^2\Phi\,. \tag{4.11}$$

The general solution to this equation contains a constant and a logarithmic growing mode. The interesting one is clearly the growing one and it indicates that, already during radiation domination CDM perturbations do grow, even if with a logarithmic rate. At last let us turn to the behavior of perturbations during the matter era, in the sub-horizon regime. Radiation becomes irrelevant, so we neglect it for this part and simply solve the CDM and Φ equations. The main phenomenological signature, that is relevant for the growth of cosmic structures, is the fact that, without pressure support, fluctuations will be free to grow through gravitational instabilities. We shall consider (4.11) and the Einstein equation (3.13). Since $k\eta \gg 1$ in the sub-horizon limit, in the source term of eq.(4.11), the time derivative terms can be safely neglected with respect to the $k^2\Phi$ term. Similarly, in (3.13) we can neglect all the time derivative terms of the potential to get

$$k^2\Phi = -\frac{\kappa^2 a^2}{2}\bar{\rho}\delta_c\,, \tag{4.12}$$

which is the sub-horizon limit of the Poisson equation (3.17) since on sub-horizon scales $\Delta \simeq \delta$. Combining this equation with the quasi-static approximation of

equation (4.11), we obtain:

$$\delta_c'' + \mathcal{H}\delta_c' - \frac{\kappa^2 a^2}{2}\bar{\rho}_c\delta_c = 0\,, \tag{4.13}$$

which is a second order differential equation for δ_c. Noticeably this equation does not depend on the scale. Every mode grows at the same rate once it is inside the horizon. This behavior is not surprising since this equation corresponds to the limit when GR reduces to classical Newtonian fluid physics (3.11), with $v_s^2 = 0$. As before this equation has two families of solutions. A growing mode and a decaying mode. The first one will be characterized by a growth rate of $D_1(a) \propto a$ while the second one by $D_2(a) \propto a^{-3/2}$. Notice here that the growing mode does not grow exponentially thanks to the Hubble friction term. Since we are interested only in the growing mode, this has the following expression:

$$D_1(a) = \frac{5\Omega_m^0}{2}\frac{\mathcal{H}(a)}{aH_0}\int_0^a \frac{da'}{(\mathcal{H}'(a')/H_0)^3}\,. \tag{4.14}$$

$D_1(a)$ is a scale-independent function describing the growth of matter perturbations at late times. It follows from (4.12) that $\Phi \propto const.$ for sub-horizon modes during matter domination, i.e. $\Phi \propto D_1(a)/a$. To summarize, in order to solve for the growth of structure in standard GR, we need to solve eq.(4.13) for cold dark matter and then use the Poisson equation (4.12) to infer the behavior of $\Phi = \Psi$.

With this analytical study of the linear equations through the expansion history, we have found that the inhomogeneities in CDM remain constant on super-horizon scales, that they grow logarithmically with the scale factor on sub-horizon scales during radiation domination and that they grow linearly in the scale factor on sub-horizon scales during matter domination. It follows that, CDM perturbations that enter the horizon before recombination have a suppressed growth until $a \simeq a_{eq}$. Therefore all modes with $k > k_{eq}$ have grown by the same factor since they entered the horizon. Conversely, modes that enter the horizon after recombination, grow at a scale-independent rate. We then expect the power spectrum to maintain its primordial shape on scales larger than $k > k_{eq}$. It is common to define the *transfer function* to describe the evolution of perturbations through horizon crossing and radiation/matter transition

$$T(k) \equiv \frac{\Phi(k, a_{late})}{\Phi_{large-scale}(k, a_{late})}\,. \tag{4.15}$$

With these definitions, the potential $\Phi(\vec{k}, a)$ and the matter perturbation $\delta_c(\vec{k}, a)$ can be written in terms of the primordial one $\Phi_p(\vec{k})$ as follows

$$\Phi(\vec{k}, a) = \frac{9}{10}\Phi_p(\vec{k})T(k)\frac{D_1(a)}{a}\,, \tag{4.16}$$

$$\delta(\vec{k}, a) = \frac{3}{5}\frac{k^2}{\Omega_m^0 H_0^2}\Phi_p(\vec{k})T(k)D_1(a)\,. \tag{4.17}$$

The analysis in this section is based on linear theory, as developed in the previous Chapter. This approximation will clearly break down on small scales. At those scales CDM perturbations are growing since a long time up to apoint where the perturbative description breaks down. In this regime, one needs to solve the full non-linear equations.

4.3 The Cosmic Microwave Background

In this Section we shall briefly review the theory of CMB anisotropies. This shall shed light on how primordial perturbations remain imprinted in anisotropies that we observe in the CMB sky. When photon decouple, at the time of recombination, CMB radiation is decoupled from baryons evolution and photons are free to stream to us. It is clear that perturbations in the photon distribution will evolve very differently before and after recombination so we have to treat these two epochs separately. First we need to study how primordial perturbations evolve until last scattering, being tightly coupled to baryons. Then we need to study how inhomogeneities on the surface of last scattering translate into the anisotropies of the CMB temperature. The surface of last scattering (SLS) is a spherical surface at a distance η_* from us. Inhomogeneities on scales k get projected into anisotropies on angular scales $l \sim k(\eta_0 - \eta_*) \sim k\eta_0$ as the electrons come to us from different points on the SLS. Pressure is always significant for photons at all epochs and therefore their fluctuations never grow much and remain always linear. This highlights the power of CMB observations. We can reliably use linear perturbation theory over a wide range of scales to probe primordial physics. As we have shown in the previous section super-horizon perturbations remain constant into the radiation epoch. The focus of this Section will therefore be on sub-horizon photon perturbations from the radiation era to the matter era. In the former era, the behavior is characterized by the baryon acoustic oscillations (BAO) of the baryon-photon fluid while after recombination the photons are characterized by free streaming. Let us start with the radiation era. Photons interact with electrons through Compton scattering and protons, with a large optical depth $\tau \gg 1$. In this limit photons behave like a fluid coupled to baryons. This is usually referred to as the photon-baryon fluid and its evolution can be characterized by the first two multipoles Θ_0 and Θ_1. In this limit equations (3.34) become:

$$\Theta_l \sim \frac{k\eta}{2\tau}\Theta_{l-1}\,. \tag{4.18}$$

Therefore, before recombination, we simply need to solve equations (3.32) and (3.33) for the monopole and dipole respectively, combined with equations (3.27) and (3.28) for the baryons. We will not present the details of the calculations, but instead give the final equation that can be obtained by combining this set of equations and which governs the behavior of the monopole Θ_0. We refer the reader to [60] for more details. The result is the following equation

$$\left[\frac{d^2}{d\eta^2} + \frac{R'}{1+R}\frac{d}{d\eta} + k^2 c_s^2\right](\Theta_0 - \Phi) = -\frac{k^2}{3}\left[\frac{1}{1+R}\Phi + \Psi\right], \tag{4.19}$$

where $c_s \equiv \sqrt{R/3(1+R)}$ is the sound speed of the photon-baryon fluid. The solution of this equation is a fluid that oscillates with a period which is determined by the baryon density. These oscillations are called the baryon acoustic oscillations, BAO. If we neglect the damping term in eq. (4.19), the general solution is

$$\begin{aligned}\Theta_0(\eta) - \Phi(\eta) &= [\Theta_0(0) - \Phi(0)]\cos(kr_s) \\ &+ \frac{k}{\sqrt{3}}\int_0^\eta d\eta'\,[\Phi(\eta') + \Psi(\eta')]\sin[k(r_s(\eta') - r_s(\eta))]\,,\end{aligned} \tag{4.20}$$

where we have defined the sound horizon as

$$r_s(\eta) \equiv \int_0^\eta d\eta' c_s(\eta') \,, \tag{4.21}$$

which represents the distance traveled by a sound wave by time η. With the CMB spectrum we therefore have a handle on two distance indicators that are the sound horizon at recombination and the distance of the surface of last scattering to us. Analogously we can derive the equation for the dipole moment and here we report its solution:

$$\begin{aligned} \Theta_0(\eta) - \Phi(\eta) &= [\Theta_0(0) - \Phi(0)] \sin(k r_s) \\ &- \frac{k}{\sqrt{3}} \int_0^\eta d\eta' \left[\Phi(\eta') + \Psi(\eta')\right] \cos[k(r_s(\eta') - r_s(\eta))] \,. \end{aligned} \tag{4.22}$$

Notice that the dipole is out of phase with the monopole, and this, as we will see, has important consequences for the final CMB anisotropy spectrum. Using the two equations (4.19) and (4.22) we can evolve the primordial perturbations to find the monopole and dipole of photons at recombination. The first peak corresponds to the modes that entered the horizon before recombination, started oscillate, growing and reaching the first maximum right at the time of recombination. Modes that entered the horizon earlier, i.e. smaller scales perturbations, already passed through their first maximum and are going through a minimum of the baryon acoustic oscillations at the time of recombination. Further, modes that have entered even earlier, went through one full oscillation by recombination and lead to the second peak of the spectrum. We can continue along these lines and recover all the peaks and troughs of the CMB angular power spectrum. The nature of the baryon acoustic oscillations is such that the height of the maxima alternate, and this can be observed in the CMB peaks. Now, let us translate these fluctuations at the SLS into the anisotropies. In order to do so, we need to solve the equations for the radiation multipoles during the matter era. We present the main results, using [59] and [60] as our main references. We can write the solution of equation (3.26) as an integral over the line-of-sight

$$\Theta(k, \mu, \eta_0) = \int_0^{\eta_0} d\eta \tilde{S}(k, \mu, \eta) e^{ik\mu(\eta - \eta_0) - \tau(\eta)} \,, \tag{4.23}$$

with the source term given by:

$$\tilde{S} \equiv \Phi' - ik\mu\Psi - \tau' \left[\Theta_0 + \mu v_b - \frac{1}{2}\mathcal{P}_2(\mu)\Pi\right] . \tag{4.24}$$

After multiplying each side of eq.(4.23) by the Legendre polynomial $\mathcal{P}_l(\mu)$ and integrating over the angle μ we obtain an expression for the l-th multipole:

$$\Theta_l(k, \eta_0) = \int_0^{\eta_0} d\eta S(k, \eta) j_l[k(\eta - \eta_0)] \,, \tag{4.25}$$

where j_l denotes the spherical Bessel function and the source $S(k, \eta)$ becomes:

$$\begin{aligned} S(k, \eta) &\equiv e^{-\tau} \left[\Phi' - \tau' \left(\Theta_0 + \frac{1}{4}\Pi\right)\right] \\ &+ \frac{d}{d\eta}\left[e^{-\tau}\left(\Psi - \frac{i v_b \tau'}{k}\right)\right] - \frac{3}{4k^2}\frac{d^2}{d\eta^2}[e^{-\tau}\tau'\Pi] \,. \end{aligned} \tag{4.26}$$

With some algebraic reshuffling and with the approximations discussed in [60] we get to the final expression for the l-th multipole of the photons temperature:

$$\begin{aligned}\Theta_l(k,\eta_0) \simeq\ & [\Theta_0(k,\eta_*) + \Psi(k,\eta_*)] j_l[k(\eta_0-\eta_*)] \\ & +3\Theta_1(k,\eta_*)\left(j_{l-1}[k(\eta_0-\eta_*)] - \frac{(l+1)j_l[k(\eta_0-\eta_*)]}{k(\eta_0-\eta_*)}\right) \\ & + \int_0^{\eta_0} d\eta e^{-\tau}\left[\Psi'(k,\eta) + \Phi'(k,\eta)\right] j_l[k(\eta_0-\eta)]\,. \end{aligned} \tag{4.27}$$

We shall now briefly discuss this solution as it is crucial for understanding the physical origin of the CMB power spectrum. The first noticeable thing is that, in order to solve this equations to get the anisotropies today we need to know the photon monopole, dipole and gravitational potential Ψ evaluated at recombination. Furthermore, the presence of the Bessel function $j_l[k[\eta-\eta_0)]$ in (4.27) determines how much anisotropy is sourced by a wave k on angular scale l. As we anticipated, the main contribution comes from $k \sim l/\eta_0$. The first term on the r.h.s. of eq. (4.27) constitutes the main contribution to the CMB power spectrum. The $\Psi(k,\eta_*)$ term, in fact, represents the gravitational potential well, at the surface of last scattering, from which photons have to climb out in order to free stream to us. This is summed to the monopole of temperature perturbations to determine the total perturbation in temperature at the SLS. The second term on the r.h.s. of eq. (4.27) encodes the effect of the dipole. As we have seen, the monopole and the dipole oscillate out of phase as a peculiar feature of baryon acoustic oscillations. In eq. (4.27) the dipole contribution is subdominant with respect to the monopole, but it has the relevant effect of raising the power in the troughs of the spectrum since as it adds incoherently with the monopole. At last, there is a contribution in eq. (4.27) that depends on the time dependence of the sum of the potentials $\Phi + \Psi$, that give rise to the ISW effect. The relevance of this term comes from the fact that it is an integral measure of the time evolution of the gravitational potentials. These are constant on super-horizon scales and during matter domination on sub-horizon scales as well. However, as the universe enters the phase of accelerated expansion, at late times, they both evolve. Therefore we expect an ISW contribution on the largest scales that enter the horizon at recent times. We shall now turn on how to connect the multipoles that we just discussed to observable quantities. We start by decomposing temperature fluctuations on the sky into a time-dependent background temperature, and fluctuations depending on time, space and photon direction:

$$T(\vec{x},\hat{p},\eta) = T(\eta)\left[1 + \Theta(\vec{x},\hat{p},\eta)\right]\,. \tag{4.28}$$

By observing CMB today on the earth we can determine the anisotropies in the microwave sky, so what we measure is the dependence of temperature on the direction in the sky $\hat{p}$. Since the temperature fluctuations are a two-dimensional function we decompose them into spherical harmonics with:

$$\Theta(\vec{x},\hat{p},\eta) = \sum_{l=1}^{\infty}\sum_{m=-l}^{l} a_{lm}(\vec{x},\eta) Y_{lm}(\hat{p})\,. \tag{4.29}$$

One then typically associates a *power spectrum* to the anisotropies (4.29), defined as the distribution average of the coefficients a_{lm}

$$C_l \equiv < |a_{lm}|^2 > \,. \tag{4.30}$$

The information contained in the temperature of the CMB are then transferred to the coefficients $a_{lm}(\vec{x},\eta)$. We shall now assume that the a_{lm}'s are Gaussian random variables, with

$$< a_{lm}a^*_{l'm'} >= \delta_{ll'}\delta_{mm'}C_l\,. \tag{4.31}$$

where C_l represents the angular power spectrum of Θ. Notice that this is a strong working assumption that can be, nevertheless, tested experimentally. The a_{lm}'s are related to the temperature multipoles by:

$$a_{lm} = (-i)^l 4\pi \int d^3k Y^*_{lm}(\hat{k})\Theta_l(\vec{k},\eta)\,. \tag{4.32}$$

Therefore the angular power spectrum C_l can be expressed as a function of the multipole Θ_l. Notice that at a given l, each a_{lm} has the same variance, as a result of the statistical isotropy. Thus there is a fundamental uncertainty in the knowledge we may get about the C_l's, known as *cosmic variance*

$$\left(\frac{\Delta C_l}{C_l}\right) = \sqrt{\frac{2}{2l+1}}\,. \tag{4.33}$$

We shall now relate the observables a_{lm} to the temperature multipoles for which we have previously solved the equations. As we saw in the previous section the initial conditions for temperature fluctuations can be written in terms of the Newtonian potential Ψ. Since the evolution of Θ_l does not depend on the direction of the wavevector $\vec{k}$, we can then write:

$$\Theta_l(\vec{k},\mu,\eta) = \Psi_i(\vec{k})\Theta_l(k,\mu,\eta)\,, \tag{4.34}$$

where $\Psi_i(\vec{k})$ is the initial perturbation and $\Theta_l(k,\mu,\eta)$ is the solution to the Boltzmann equation with initial condition equal to 1, i.e. it is the transfer function for the photons. We can then write the CMB angular power spectrum as:

$$C_l = 4\pi \int \frac{d^3k}{(2\pi)^3} P_\Psi(k)|\Theta_l(k)|^2\,. \tag{4.35}$$

4.4 Cosmological Data Sets

One of the most remarkable results of modern cosmology is the fact that the physical picture outlined in the previous chapters has found robust experimental confirmation. In this section we discuss the experiments that constitute the bulk of cosmological observations and that we shall use in the following chapters.

The first data set that we shall consider consists of the "Joint Light-curve Analysis" (JLA) Supernovae sample, as introduced in [68], which is constructed by the combination of the SNLS, SDSS and HST SNe data, together with several low redshift SNe.

The second probe that we use consists of the WiggleZ Dark Energy Survey (WZ) measurements of the galaxy power spectrum in order to exploit the constraining power of data from large-scale structures. This is inferred from $170,352$ blue emission line galaxies over a volume of $1\,\mathrm{Gpc}^3$ [69, 70] up to

$k_{\rm max} = 0.2\,h/{\rm Mpc}$. The covariance matrices, as given in [70], are computed using the method described by [71]. It has been shown that linear theory predictions are a good fit to the data regardless of non-linear corrections up to a scale of $k \sim 0.2\,{\rm h/Mpc}$ [70, 72] The WiggleZ likelihood automatically marginalises over a scale independent linear galaxy bias for each of the four redshift bins, as in [70].

The third data set that we shall use in the following Chapters consists of the measurements of the galaxy weak lensing shear correlation function as provided by the Canada-France-Hawaii Telescope Lensing Survey (CFHTLenS) [73]. This is a 154 square degree multi-colour survey, optimised for weak lensing analyses, that spans redshifts ranging from $z \sim 0.2$ to $z \sim 1.3$. Here we consider the data subdivided into 6 redshift bins and we applied ultra-conservative cuts, as in [74], that exclude ξ_- completely and cut the ξ_+ measurements at scales smaller than $\theta = 17'$ for all the tomographic redshift bins. As discussed in [74], these cuts make the CFHTLenS data insensitive to the modeling of the non-linear evolution of the power spectrum. For the *Planck* best-fit ΛCDM cosmology [16] these cuts correspond to: $k_{\rm max} = 0.18\,{\rm Mpc}^{-1}$ for the CFHTLenS bin with mean redshift $\bar{z} = 0.36$; $k_{\rm max} = 0.15\,{\rm Mpc}^{-1}$ for $\bar{z} = 0.50$; $k_{\rm max} = 0.13\,{\rm Mpc}^{-1}$ for $\bar{z} = 0.68$; $k_{\rm max} = 0.12\,{\rm Mpc}^{-1}$ for $\bar{z} = 0.87$; $k_{\rm max} = 0.11\,{\rm Mpc}^{-1}$ for $\bar{z} = 1.00$ and $\bar{z} = 1.16$.

The fourth data set that we shall employ consists of the HST [75] measurements of the local Hubble constant from optical and infrared observations of more than 600 Cepheid variables.

We include in our analysis two versions of the *Planck* measurements of CMB fluctuations. We employ the 2015 data release consisting in the measurements of the CMB fluctuations in both temperature and polarization [16, 76]. At large angular scales the *Planck* release implements a joint pixel-based Likelihood including both temperature and E-B mode polarization for the multipoles range of $\ell \leq 29$, as described in [76]. At smaller angular scales we use the `Plik` Likelihood [76] for CMB measurements of the TT, TE and EE power spectra, as extracted from the 100, 143, and 217 GHz HFI channels.

The 2013 *Planck* data release consists of the temperature-temperature power spectra considering the 9 frequency channels ranging from $30 \sim 353$ GHz for low-ℓ modes ($2 \leq \ell < 50$)and the 100, 143, and 217 GHz frequency channels for high-ℓ modes ($50 \leq \ell \leq 2500$) [77, 78]. In order to break the well-known degeneracy between the re-ionization optical depth and the amplitude of CMB temperature anisotropy, when *Planck* 2013 is used, we include WMAP low-ℓ polarization spectra ($2 \leq \ell \leq 32$) [14].

We shall also consider the CMB full-sky lensing potential measurements from the *Planck* satellite in their 2013 and 2015 versions. The 2015 one [79] covers the multipoles range $40 \leq \ell \leq 400$ as obtained with techniques developed within the Planck collaboration, capable of separating foregrounds and CMB in the Planck multi-frequency data. The reconstructed CMB lensing potential is obtained with a quadratic estimators that exploit the statistical anisotropy induced by lensing [80]. This measurements resulted in a 40σ detection of the lensing signal.

The 2013 data release of the lensing potential spectrum [81], uses the 100, 143, and 217 GHz Planck frequency bands. This data set resulted in a detection of CMB lensing with an overall significance greater than 25σ.

We shall also employ BAO measurements of: the SDSS Main Galaxy Sample at

$z_{\rm eff} = 0.15$ [82]; the BOSS DR11 "LOWZ" sample at $z_{\rm eff} = 0.32$ [83]; the BOSS DR11 CMASS at $z_{\rm eff} = 0.57$ of [83]; and the 6dFGS survey at $z_{\rm eff} = 0.106$ [84], all joined together in the data set that we shall generically dub BAO. These probes offer complementary constraining power on cosmological distances.
In addition we consider the redshift space distortion (RSD) measurements of BOSS CMASS-DR11 as analysed in [85] and [86]. When these data are used we exclude the BOSS-CMASS results of [83] from the BAO Likelihood to avoid double counting.
At last we shall use the BICEP2 [87] measurements of B-mode polarization. The BICEP2 collaboration was the first one to report a detection of B-mode polarization at large angular scales, by improving the sensitivity of B-mode observatories by orders of magnitudes. A joint analysis with measurements of the *Planck* satellite [88] later showed that this detection is consistent with polarized dust emission from our galaxy and not due to a primordial component.

Part II

Null Tests of Cosmological Models

Chapter 5

Testing the Concordance of Evidences

In this chapter we present and use a complete and rigorous statistical indicator to measure the level of concordance between cosmological data sets, without relying on the inspection of the marginal posterior distribution of some selected parameters.

Our present understanding of the universe is, in fact, based on the combination of several different cosmological observations that are joined in order to exploit their complementary sensitivities to distinct characteristics of our universe, as discussed in the previous chapter. In the future, cosmological studies are going further in this direction. Wide large scale structure surveys, like Euclid, will combine maps of galaxies at several different redshifts, that will be joined with measurements of the CMB from the *Planck* satellite [15] and sub-orbital experiments.
The observational efforts, that are driving cosmology toward a phase of extremely accurate, large scale, measurements, will all be joined together to learn all possible information about the initial conditions and the evolution of our universe.

In this program, however, a problem arises.
How can we be sure that the data sets, that we will be collecting, form a coherent picture, when interpreted within a model? How do we quantify the agreement between them, to be aware of the possible presence of unaccounted systematic effects or hints toward new physical phenomena?
Testing the agreement between data sets, in a rigorous way, that goes beyond the comparison of the marginal distribution of some parameters, is critical in answering these questions. The posterior of the model parameters is, in fact, not guaranteed to show tensions due to the marginalization procedure, that can alter discrepancies, that will be then misjudged. Assessing whether the posterior distribution of two different data sets occupy a substantially different volume in the parameter space of a model is instead crucial as it could provide a useful guidance for the future research. Answering these questions is also a useful sanity check for parameters estimation. The statistical inference on the parameters of a model should get stronger as we combine together different measurements

and should not reflect the fact that we are joining low probability tails of the model posterior.
An estimate of the tensions between different data sets, based on the marginal posterior of cosmological parameters, has shown that indeed some discrepancies arise when combining several probes [73, 89, 16, 90] that could point toward some extensions of the fiducial model [91, 92, 93, 74, 4, 94].

5.1 Bayesian Statistical Tools

In this section we shall briefly review the Bayesian statistical tools that will be used in this chapter.

If we consider a model $\mathcal{M}$ and some data D. We shall refer to the evidence as the probability of the data given the model:

$$\mathcal{E} \equiv P(D|\mathcal{M})\,. \tag{5.1}$$

Notice that this is different from the probability of the model given the data that instead reads:

$$P(\mathcal{M}|D) = \frac{P(D|\mathcal{M})P(\mathcal{M})}{P(D)}\,. \tag{5.2}$$

The evidence for a model and some data can be easily computed by means of marginalization over the model parameters θ:

$$\mathcal{E} = \int P(D|\theta|\mathcal{M})P(\theta|\mathcal{M})\,d\theta\,. \tag{5.3}$$

Following a standard convention we shall define the Likelihood and the prior to be:

$$\begin{aligned}\mathcal{L}(\theta) &\equiv P(D|\theta|\mathcal{M})\\ \Pi(\theta) &\equiv P(\theta|\mathcal{M})\,.\end{aligned} \tag{5.4}$$

The evidence can be immediately used at testing the validity of different hypotheses. Suppose that we have two competing hypotheses, $\mathcal{I}_1$ and $\mathcal{I}_2$, and we want to compare them. To do so we compute:

$$\mathcal{R} = \frac{P(\mathcal{I}_1|D)}{P(\mathcal{I}_2|D)}\,. \tag{5.5}$$

that gives us the odds ratio of the two hypotheses. Based on the result of this computation we can take decisions according to the hypothesis to use following a classification scheme like the Jeffery's scale. Using Bayes' theorem we immediately have:

$$\mathcal{R} = \frac{P(D|\mathcal{I}_1)}{P(D|\mathcal{I}_2)}\frac{P(\mathcal{I}_1)}{P(\mathcal{I}_2)}\,, \tag{5.6}$$

where we can compute $P(D|\mathcal{I})$ through marginalization and $P(\mathcal{I})$ is our prior on the hypothesis $\mathcal{I}$.

5.2 The Data Concordance Test

Bayesian hypotheses testing provides a clean way of dealing with the problem of combining data sets and we shall refer to this application as the Data Concordance Test (DCT). We have two data sets and we want to test whether we can describe them with the same set of parameters or not, within a given model. Based on the outcome of such operation we shall take a decision about combining them [95, 96, 97, 98, 99, 100, 101].
Let us now consider two data sets D_1 and D_2 and a model $\mathcal{M}$. The two competing hypotheses that we want to compare are:

- $\mathcal{I}_0$: the two data sets can be characterized, within model $\mathcal{M}$, by the same (unknown) parameters;
- $\mathcal{I}_1$: the two data sets can be described, within model $\mathcal{M}$, with different (unknown) parameters.

Then, we compare the evidences for these two statements to obtain their odds-ratio. In particular by assigning non-committal priors for the two hypotheses we immediately have:

$$\begin{aligned}\mathcal{C}(D_1, D_2, \mathcal{M}) &= \frac{P(D_1 \cup D_2 | \mathcal{I}_0, \mathcal{M})}{P(D_1 \cup D_2 | \mathcal{I}_1, \mathcal{M})} \\ &= \frac{P(D_1 \cup D_2 | \mathcal{M})}{P(D_1|\mathcal{M}) P(D_2|\mathcal{M})}\,, \end{aligned} \tag{5.7}$$

where $P(D_1 \cup D_2|\mathcal{M})$ is the evidence of the joint data sets and $P(D_1|\mathcal{M})$ and $P(D_2|\mathcal{M})$ are the evidences of the single data sets. The last equality follows from the definition of the two hypotheses and the fact that under the hypothesis $\mathcal{I}_1$, the two data sets, D_1 and D_2, pertain to distinctly different classes and knowledge of one of them tells us nothing about the other.
We can interpret the odds resulting from this calculation with a classification scheme, like the Jeffreys' scale or others, depending on the decision that we have to perform afterwards. In particular, when we have to decide if it is appropriate to combine two data sets, we can establish a threshold for the positive answer, based on the risk that we are willing to take, and act accordingly. A common choice [95] with this respect is to decide to follow the $\mathcal{I}_0$ hypothesis, combining the data, if $\log \mathcal{C} > 0$ and $\mathcal{I}_1$ otherwise.

5.3 DCT Properties

The DCT is relatively easy to evaluate, once we have at our disposal the tools to perform efficient evidence computations, and has some other advantages and properties that we shall cover in this section. First of all the DCT is a quantitative and statistically rigorous prescription. It measures the odds, within model $\mathcal{M}$, of obtaining one data set given the other one. Using $P(D_1 \cup D_2|M) = P(D_1|D_2, M)P(D_2|M)$ we can immediately write:

$$\mathcal{C}(D_1, D_2, M) = \frac{P(D_1 \cup D_2|M)}{P(D_1|M)P(D_2|M)} = \frac{P(D_1|D_2, M)}{P(D_1|M)}\,, \tag{5.8}$$

that shows that the $\mathcal{C}$ is large, within model $\mathcal{M}$, if the probability of obtaining the data set D_1, given that the data set D_2 have been collected, is large.

Other properties of the DCT can be easily understood by looking at the Gaussian approximation of $\mathcal{C}$.
We start by writing the Likelihood of the data under scrutiny as:

$$\mathcal{L}(\boldsymbol{\theta}) = \mathcal{L}_{\max}\tilde{\mathcal{L}}(\boldsymbol{\theta})\,, \tag{5.9}$$

so that we can define the evidence as:

$$\log \mathcal{E} \equiv \log\left(\frac{V_{\mathcal{L}}}{V_{\Pi}}\right) + \log \mathcal{L}_{\max}\,. \tag{5.10}$$

So far this can be taken as the definition of the Likelihood volume $V_{\mathcal{L}}$ and the prior volume V_{Π} that is completely independent of the details of the problem and holds even if the prior are not separable, or cannot be factored out of the evidence integral.
The DCT between two data sets then trivially becomes:

$$\log \mathcal{C} = \log\left(\frac{V_{12}}{V_1 V_2}\right) + \log\left(V_{\Pi}\right) + \log\left(\frac{\mathcal{L}_{12}^{\max}}{\mathcal{L}_1^{\max}\mathcal{L}_2^{\max}}\right)\,, \tag{5.11}$$

where V_{12} is the Likelihood volume for the combination of D_1 and D_2, V_i is the Likelihood volume for the data set D_i. This result can easily be generalized to a combination of N datasets with:

$$\log \mathcal{C} = + \log\left(\frac{V_{1\cdots N}}{V_1 \cdots V_N}\right) + (N-1)\log\left(V_{\Pi}\right) + \log\left(\frac{\mathcal{L}_{1\cdots N}^{\max}}{\mathcal{L}_1^{\max}\cdots\mathcal{L}_N^{\max}}\right)\,. \tag{5.12}$$

Let us now assume that the Likelihood of the data set D_i is Gaussian in the N_i data $\boldsymbol{x}$ with covariance Σ_i and thus can be written as:

$$\mathcal{L}_i = \mathcal{L}_i^{\max}\exp\left[-\frac{1}{2}\left(\chi^2 - \hat{\chi}_i^2\right)\right]\,, \tag{5.13}$$

where:

$$\mathcal{L}_i^{\max} = (2\pi)^{N_i/2}\left|\Sigma_i\right|^{-1/2}\exp\left(-\frac{1}{2}\hat{\chi}_i^2\right)\,, \tag{5.14}$$

and:

$$\hat{\chi}_i^2 = \left(\boldsymbol{x} - \hat{\boldsymbol{m}}_i\right)^T \Sigma_i^{-1}\left(\boldsymbol{x} - \hat{\boldsymbol{m}}_i\right)\,. \tag{5.15}$$

where we denoted, as in the rest of the chapter, $|A| = \det A$ and we will use the hat to represent the best fit, either in the prediction $\boldsymbol{m}$, in the χ^2 or the parameters.

If we assume that the Likelihood is Gaussian also in the M parameters $\boldsymbol{\theta}$ with inverse Fisher matrix F_i we can write:

$$\mathcal{L}_i = \mathcal{L}_i^{\max}\exp\left[-\frac{1}{2}\left(\boldsymbol{\theta} - \hat{\boldsymbol{\theta}}_i\right)^T F_i^{-1}\left(\boldsymbol{\theta} - \hat{\boldsymbol{\theta}}_i\right)\right]\,. \tag{5.16}$$

In the limit where the Likelihood is more informative than the prior we can easily compute an approximation to the Likelihood volume:

$$\begin{aligned} V_i &= (2\pi)^{M/2}|F_i|^{1/2}\,, \\ V_{12} &= (2\pi)^{M/2}|F_1+F_2|^{1/2}\,, \end{aligned} \tag{5.17}$$

and we can then easily compute the DCT that becomes:

$$\begin{aligned} \log\mathcal{C}(D_1,D_2,\mathcal{M}) = &-\frac{M}{2}\log(2\pi)+\frac{1}{2}\log\left(\frac{|F_1+F_2|}{|F_1||F_2|}\right)+\log\left(V_\pi\right) \\ &-\frac{1}{2}\log\left(\frac{|\Sigma_1\oplus\Sigma_2|}{|\Sigma_1||\Sigma_2|}\right)-\frac{1}{2}\Delta\hat{\chi}^2\,, \end{aligned} \tag{5.18}$$

where we used the notation $\Sigma_1\oplus\Sigma_2$ to denote the joint covariance of the two datasets and:

$$\Delta\hat{\chi}^2=\hat{\chi}^2_{12}-\hat{\chi}^2_1-\hat{\chi}^2_2\,, \tag{5.19}$$

In the case of multiple N datasets this becomes:

$$\begin{aligned} \log\mathcal{C} = &-\frac{M}{2}(N-1)\log(2\pi)+\frac{1}{2}\log\left(\frac{|F_1+\cdots+F_N|}{|F_1|\ldots|F_N|}\right)+(N-1)\log\left(V_\pi\right) \\ &-\frac{1}{2}\log\left(\frac{|\Sigma_1\oplus\cdots\oplus\Sigma_N|}{|\Sigma_1|\ldots|\Sigma_N|}\right)-\frac{1}{2}\Delta\hat{\chi}^2\,, \end{aligned} \tag{5.20}$$

where:

$$\Delta\hat{\chi}^2=\hat{\chi}^2_{1\ldots N}-\sum_{i=1}^{N}\hat{\chi}^2_i\,, \tag{5.21}$$

We can now consider two interesting cases. The first one is the one in which we assume that we have a broad flat prior. If we take the M parameters to have equal constant prior with a width of p, so that the prior volume is $V_\pi=p^M$, we get:

$$\begin{aligned} \log\mathcal{C} = &-\frac{M}{2}\log(2\pi)+\frac{1}{2}\log\left(\frac{|F_1+F_2|}{|F_1||F_2|}\right)+\log\left(p^M\right) \\ &-\frac{1}{2}\log\left(\frac{|\Sigma_1\oplus\Sigma_2|}{|\Sigma_1||\Sigma_2|}\right)-\frac{1}{2}\Delta\hat{\chi}^2\,, \end{aligned} \tag{5.22}$$

that in the case of multiple data sets reads:

$$\begin{aligned} \log\mathcal{C} = &-\frac{M}{2}(N-1)\log(2\pi)+\frac{1}{2}\log\left(\frac{|F_1+\cdots+F_N|}{|F_1|\ldots|F_N|}\right)+(N-1)\log\left(p^M\right) \\ &-\frac{1}{2}\log\left(\frac{|\Sigma_1\oplus\cdots\oplus\Sigma_N|}{|\Sigma_1|\ldots|\Sigma_N|}\right)-\frac{1}{2}\Delta\hat{\chi}^2\,. \end{aligned} \tag{5.23}$$

The second one consists in taking a broad Gaussian prior, centered in the best fit parameter value with covariance P. In this case the DCT reduces to:

$$\log\mathcal{C}=+\frac{1}{2}\log\left(\frac{|F_1+F_2|}{|F_1||F_2|}\right)+\frac{1}{2}\log\left(|P|\right)-\frac{1}{2}\log\left(\frac{|\Sigma_1\oplus\Sigma_2|}{|\Sigma_1||\Sigma_2|}\right)-\frac{1}{2}\Delta\hat{\chi}^2\,, \tag{5.24}$$

that for multiple data sets is:

$$\log \mathcal{C} = + \frac{1}{2} \log \left(\frac{|F_1 + \cdots + F_N|}{|F_1| \ldots |F_N|} \right) + \frac{1}{2}(N-1) \log \left(|P| \right) - \frac{1}{2} \log \left(\frac{|\Sigma_1 \oplus \cdots \oplus \Sigma_N|}{|\Sigma_1| \ldots |\Sigma_N|} \right) - \frac{1}{2} \Delta \hat{\chi}^2 \,. \tag{5.25}$$

With these results at hand we can easily comment on several interesting properties of the DCT.

While the DCT measures tensions between data sets in terms of odds of agreement or disagreement and is not based on the marginal distribution of the parameters, the latter approach might point in the right direction if the Likelihood is Gaussian, both in the data and the parameters. As we can see here, and was shown in [95, 96] the DCT reduces to the usual prescription for the marginal posterior of uncorrelated parameters. When these requirements break down, however, the inspection of the parameters posterior becomes unreliable, in assessing tensions, as it tends to be biased.

In addition, as common sense suggests, the DCT naturally favours the combination of data sets, as long as there is no strong evidence that that should not be done [95, 98]. The way in which this is automatically encoded in the computation of $\mathcal{C}$ is by weighting the prior volume with the Likelihood volume, in a manner that resembles the Occam razor common to Bayesian model selection. If we consider two independent data sets so that $|\Sigma_1 \oplus \Sigma_2| = |\Sigma_1||\Sigma_2|$ and we assume that the difference in the best fit χ^2 does not change when modifying the prior and that the two data sets have the same Fisher matrix, in the case of wide flat prior we have:

$$\log \mathcal{C} = + \frac{1}{2} M \log \left(\frac{1}{\pi} \frac{(p)^2}{|F|^{1/M}} \right) - \frac{1}{2} \Delta \hat{\chi}^2 \,, \tag{5.26}$$

while in the case of Gaussian prior:

$$\log \mathcal{C} = + \frac{1}{2} M \log \left[2 \left(\frac{|P|}{|F|} \right)^{1/M} \right] - \frac{1}{2} \Delta \hat{\chi}^2 \,. \tag{5.27}$$

In both cases we can see that the first term in both expressions measures the ratio of the prior volume over the Likelihood volume. If there is no clear indication on how to set the prior ranges, i.e. the previous knowledge of the model is vague, and the prior are consequently wide, the DCT favours the combination of data sets, as this might help in gaining knowledge of the model. Conversely if the priors are stronger than the data the DCT will disfavour the combination, as we already included in the prior choice the information that is coming from the combination of the data sets.

If we assume that the Likelihood volume is of the same order of the prior volume and that the data sets are independent we recover the frequentist rule of thumb that an increase in $\hat{\chi}^2$ is justified if the number of parameters drops by roughly the same number.

If we consider one data sets and we remove a point from it regarding it as a single data set we can see that the DCT reduces to the usual recipe for outliers detection. Taking the prior volume and the Likelihood volume of the same order

and vanishing correlation between the error on a point and the other errors we immediately get:

$$\log \mathcal{C} = -\frac{1}{2}\frac{\left(x_2 - \hat{m}_{all-2}\right)^2}{\sigma^2}\,, \tag{5.28}$$

and we see that the DCT reduces to the scatter of x_2 from the best fit prediction $\hat{m}_{all-2}$ obtained by fitting the remaining elements.

The DCT has also some disadvantages. It does not give any indication whether the model is good by itself in fitting the data. Being a comparative test, we can use it to judge if the agreement, within a given model, improves or not when combining two data sets but it is possible to have a model that fits very badly the data while the DCT might still favour their combination. Another problem, that is particularly relevant when the DCT is used more than once on some data sets, is that it is not robust against over fitting. As immediately follows from the previous points, enlarging the parameter space with the introduction of an additional parameter will not decrease $\mathcal{C}$. As a consequence, it is always possible to relax a tension between different measurements by introducing a new parameter, being it just a nuisance parameter, describing some systematic effects, or a parameter related to a different underlying physical modelling. For this reason it is critical to use other statistical tools to assess whether the introduction of the additional parameter is really justified. It is worth noticing, that as a by-product of the computation of $\mathcal{C}$, for the two different models, one has the relevant information to perform evidence based model comparison. The last source of biases in the DCT are due to unaccounted correlations between the data sets. If two data sets are assumed to have independent errors and this is not the case, $\mathcal{C}$ will be biased toward positive values if the covariance between the errors of the two experiments is positive and toward negative values in the opposite case [98].

5.4 Data Sets and Model

We use several available cosmological data sets to perform a DCT over all the possible independent data couples, within the ΛCDM model.
In particular, as outlined in Chapter 4, we use JLA Supernovae, WiggleZ measurements of the galaxy power spectrum, CFHTLenS measurements, *Planck* CMB temperature, polarization and lensing data, and several BAO and RSD measurements. By means of the DCT we perform a test of the data concordance within the 6 parameter ΛCDM model. To compute non-linear corrections to the matter power spectrum and the lensed CMB power spectra, we use the halofit approach [102] with the updates of [103]. We notice that the halofit approach gives a reliable fitting formula over a limited volume in parameter space [103] and this might result in biases in the evidence computation. We use the CAMB code [104] to compute the predictions for all cosmological observables of interest and we use the Likelihoods of the previously described data sets, as implemented in CosmoMC [105]. We compute the evidence by means of the nested sampling algorithm and its implementation in the PolyChord code [106]. The PolyChord code also outputs error estimates, intrinsic to the nested sampling evidence calculation, that are reported as well. In order to assess the agreement between the

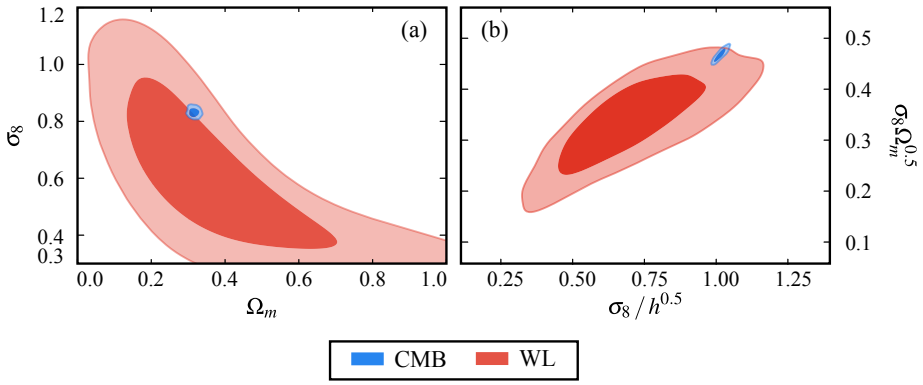

Figure 5.1: *Panel (a):* The marginalized joint posterior for Ω_m and the amplitude of the linear power spectrum on the scale of $8\,h^{-1}$ Mpc for different data sets, as shown in legend. *Panel (b):* The marginalized joint posterior for $\sigma_8\Omega_m^{0.5}$ and $\sigma_8/h^{0.5}$ for different data sets, as shown in legend. In both panels the darker and lighter shades correspond respectively to the 68% C.L. and the 95% C.L. regions. From [2].

above data sets, in the set-up commonly used for parameter estimation, we use the standard CosmoMC prior on the ΛCDM model parameters as summarized in table 5.1.

	Prior on cosmological parameters
Parameter	prior range
$\Omega_b^0\,h^2$	$[0.005\,,\,0.1]$
$\Omega_c^0\,h^2$	$[0.001\,,\,0.99]$
$100\theta_{MC}$	$[0.5\,,\,10]$
τ	$[0.01\,,\,0.8]$
n_s	$[2\,,\,4]$
$\ln(10^{10}A_s)$	$[0.8\,,\,1.2]$

Table 5.1: Prior on the six cosmological parameters of the ΛCDM model.

5.5 Results

The results of the DCT of all the independent couples of the data sets described above is shown in figure 5.2.

We can see that the combination of CMB and WL data shows evidence of substantial disagreement. It is worth noticing that the marginal distribution of the parameters is not displaying strong discrepancies. In figure 5.1, panel (a), we show the joint marginalized posterior of the parameters σ_8 and Ω_m that is commonly used [16, 107, 108, 90] to discuss tensions between these kind of

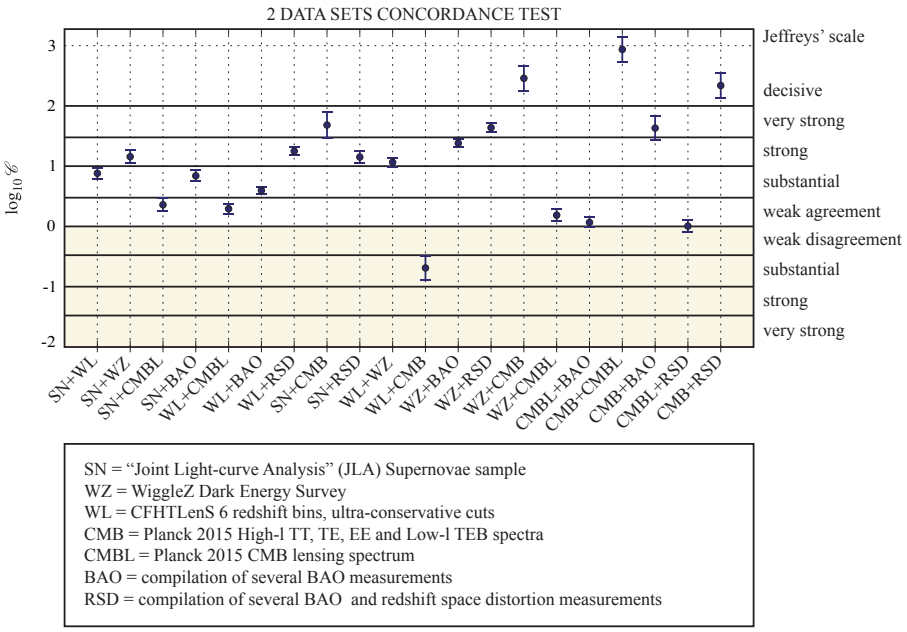

Figure 5.2: The Data Concordance Test (DCT) performed on all the independent couples of the cosmological data sets described in the text. The shaded region highlights the values of $\mathcal{C}$ that point toward disagreement between data sets. The error bars represent the uncertainty in the nested sampling computation of the evidence. From [2].

data sets. As we can see, the constraints coming from the two data sets seem consistent at 68% C.L. as in [16, 74]. In panel (b) of figure 5.1 we show the joint marginalized posterior of two combinations of cosmological parameters, $\sigma_8\Omega_m^{0.5}$ and $\sigma_8/h^{0.5}$, that can be used to discuss tensions between data sets [90]. As we can clearly see, the tension between CMB and WL seems enhanced, as they seem not to be consistent at 68%. This is a clear example where marginalising over a high dimensional non-Gaussian Likelihood to get the posterior of some parameters biases the conclusions on the possible tensions between data sets. It is clear that the DCT helps in assessing whether discrepancies, over the whole parameter space of a model, are statistically relevant and require further investigation.

The $\mathcal{C}$ values involving CMB lensing (CMBL) data are all weakly pointing toward agreement. CMBL+BAO and CMBL+RSD, in particular, are borderline between agreement and disagreement. For both data sets, this comes from some discrepancies in the determination of the background parameters. RSD data, in addition, are also penalised by some discrepancy in the determination of the amplitude of scalar perturbations. The results of the DCT involving CMB and SN, BAO, RSD and WZ are on the high end of the comparison scale, with values that range from very strong to decisive. This is largely expected as we are combining a probe that is extremely sensitive to all the cosmological parameters (CMB) with other data that probe only a sub-set of them.

Surprisingly enough, when combining CMB and CMBL the DCT reaches a very

high value, the maximum achieved in this comparison. This seems suspicious for two reasons. The first one is the known lensing amplitude tension discussed in [16, 4] and that is not found here. The second reason is the fact that CMBL was found in weak agreement with all other data sets while CMB was displaying a good agreement. It is beyond the scope of this work to investigate the possible causes of this behaviour. We can, however, have some ideas on its origin from the properties of the DCT discussed before. It seems unlikely that this discrepancy arises because of the unaccounted cross-correlation between CMB temperature fluctuations and the CMB lensing spectrum. This was indeed found to result in negligible corrections for *Planck*-like observations [109]. This leaves the factors involving the Likelihood volume and the best fit χ^2, that improve significantly with the introduction of CMB lensing, and, as shown here, are surely worth a deeper investigation. SN data show good agreement with BAO and RSD measurements, from substantial to strong on a Jeffreys' scale, as they agree on the determination of the parameters describing background evolution. The agreement between SN and RSD is slightly higher than BAO as this data set is also sensitive to some perturbations parameters. Agreement between WL and SN, BAO and RSD is also good as the DCT is rewarding the additional leverage on perturbations parameters that comes from WL measurements. For the same reason, a good agreement is found also for WZ and SN, BAO and RSD. Noticeably the values of $\mathcal{C}$ are slightly higher than the previous ones. This reflects the fact that, due to the presence of non-linear scales in WZ data, the constraints on perturbations parameters are stronger than the previous ones. Testing the combination of WL and WZ data then results in strong agreement. The two data roughly agree on the background parameters and the additional constraining power of WZ on perturbation parameters favours the combination of these two data sets.

5.6 Chapter Summary

In this chapter we have used Bayesian hypothesis testing to assess quantitatively whether there is concordance, within the ΛCDM model, between several different cosmological experiments. This test, that we dubbed DCT, allows to compute the odds that two data sets can be described by the same choice of cosmological parameters and thus gives a way of measuring the statistical significance of tensions between different measurements. We have commented some of the properties that make this test a reliable tool that extends, with statistical rigour, other commonly used approaches. We applied this test to the combinations of some of the most relevant cosmological data sets to date and found, overall, a good agreement between geometrical probes and other perturbations measurements. We showed, however, that the lensing of the CMB is only weakly in agreement with all other cosmological data sets but CMB itself. The odds of this agreement are suspiciously high, given the other results, and require further analysis. At last, we found substantial evidence for a disagreement between WL data of CFHTLenS and CMB measurements of *Planck*. We showed that a similar conclusion would not be drawn by inspecting the marginal posterior of some parameters. This tension might be a sign of new physics, pointing toward mechanisms that suppress the growth of structures in the late time universe [110, 111, 74]. It might also be a signal of the presence of

unknown systematic effects [112, 113], such as the presence of B-mode signal in weak lensing observations [114]. At last it might point toward the inadequacy of present cosmological predictions in fitting the data. A failure in modelling the evolution of perturbations on non-linear scales might bias our conclusions resulting in spurious tensions between data sets.
The investigation of these tensions, and how they are relieved in extended models, is a primary goal as these could point toward the presence of unaccounted systematic effects, an incomplete modelling of the cosmological predictions or the presence of new physical phenomena.

Part III

Parametrized Test of DE/MG Models

Chapter 6

The Effective Field Theory Approach to DE/MG Models

Anticipating a wealth of high precision large scale structure data from ongoing and upcoming surveys it is important to identify a model- independent way of testing the theory of gravity against the evolution of cosmological perturbations.

To this extent, over the past years there has been a lot of activity in the community to construct frameworks [115, 116, 117, 118, 119, 120, 121, 122, 123, 124, 125, 126, 127, 128, 129, 130, 131, 132, 133, 134, 135, 136, 137, 138, 139, 140, 141, 142, 143, 144, 145, 146, 147, 148, 149, 150, 151, 152, 153, 154, 155, 156, 157, 158, 159, 160] that would allow model-independent tests of gravity with cosmological observations. These are generally based on parametrizations of the dynamics of linear scalar perturbations, either at the level of the equations of motion, e.g. [148], of solutions of the equations, e.g. [120, 130, 145], or of the action, e.g. [161, 162, 163], with the general aim of striking a delicate balance among theoretical consistency, versatility and feasibility of the parametrization.

In this chapter we focus on a recent proposal which applies the effective field theory (EFT) formalism to the phenomenon of cosmic acceleration [162, 163, 164], inspired by the EFT of Inflation and Quintessence [165, 166, 167, 161, 168, 169, 170, 171, 172].

The formalism is based on an action constructed in unitary gauge out of all operators that are consistent with time-dependent spatial diffeomorphisms and are ordered according to the power of perturbations and derivatives. At each order in perturbations, there is a finite number of such operators that enter the action multiplied by time-dependent coefficients to which we will refer as EFT functions. The background dynamics is determined solely by three EFT functions, that are the coefficients of the three background operators; while the general dynamics of linear scalar perturbations is affected by a total of six operators, and can therefore be analyzed in terms of six time-dependent functions. From this perspective the EFT formalism can be used as a general, model-independent, framework to test the theory of gravity on large scales,

studying the effects of the different operators and the constraints that can be put by data on their coefficients.

We refer the reader to [162, 173, 174] for a detailed discussion of the assumptions and limitations of this framework. Here we shall highlight that one of the assumptions of the EFT is the validity of the weak equivalence principle, as discussed in [162, 163], which limits is range of applicability to models for which a Jordan frame, where all matter minimally couples to gravity, can be defined. Despite of the inherent limitations, the EFT framework includes most of the viable approaches to the phenomenon of cosmic acceleration that will undergo scrutiny with upcoming cosmological surveys. We shall mention, among others, the Horndeski class which includes quintessence, k-essence, $f(R)$, covariant Galileon, the effective $4D$ limit of DGP [175], Hořava gravity and more.

6.1 The EFT action in the Unitary Gauge

The EFT action is built in the Jordan frame and unitary gauge by considering the operators which are invariant under time-dependent spatial diffeomorphisms. The additional scalar DoF representing DE/MG is eaten by the metric via a foliation of space-time into space-like hypersurfaces which correspond to a uniform scalar field $\delta\phi \equiv \phi(\tau, \boldsymbol{x}) - \phi_0(\tau) = 0$. This leaves with the residual symmetries of unbroken spatial diffeomorphisms and at quadratic order, which is sufficient to study the dynamics of linear perturbations, the most general action compatible with these requirements reads:

$$\begin{aligned}\mathcal{S}_{\rm EFT} = \int d^4x\sqrt{-g}\Big\{ &+ \frac{m_0^2}{2}\left[1+\Omega(\tau)\right]R + \Lambda(\tau) - c(\tau)\, a^2\delta g^{00} \\ &+ \frac{M_2^4(\tau)}{2}\left(a^2\delta g^{00}\right)^2 - \frac{\bar{M}_1^3(\tau)}{2}\, a^2\delta g^{00}\,\delta K^\mu{}_\mu \\ &- \frac{\bar{M}_2^2(\tau)}{2}\left(\delta K^\mu{}_\mu\right)^2 - \frac{\bar{M}_3^2(\tau)}{2}\,\delta K^\mu{}_\nu\,\delta K^\nu{}_\mu \\ &+ m_2^2(\tau)\left(g^{\mu\nu}+n^\mu n^\nu\right)\partial_\mu(a^2 g^{00})\partial_\nu(a^2 g^{00}) \\ &+ \frac{\hat{M}^2(\tau)}{2}\, a^2\delta g^{00}\,\delta\mathcal{R} + \dots \Big\} + S_m[g_{\mu\nu}, \chi_m], \end{aligned} \tag{6.1}$$

where R is the four-dimensional Ricci scalar, δg^{00}, $\delta K^\mu{}_\nu$, $\delta K^\mu{}_\mu$ and $\delta\mathcal{R}$ are respectively the perturbations of the upper time-time component of the metric, the extrinsic curvature and its trace and the three dimensional spatial Ricci scalar. Finally, S_m is the matter action.

The important difference of (6.1) w.r.t. EFT of inflation [168, 169] is in the conformal factor Ω, which cannot be reabsorbed by a redefinition of the metric tensor because of the presence of matter.

Since the choice of the unitary gauge breaks time diffeomorphism invariance, each operator in the action can be multiplied by a time-dependent coefficient; in our convention, $\{\Omega, \Lambda, c, M_2^4, \bar{M}_1^3, \bar{M}_2^2, \bar{M}_2^2, \bar{M}_3^2, m_2^2, \hat{M}^2\}$ are unknown functions of the conformal time, τ, and we will refer to them as EFT functions. In particular, $\{\Omega, c, \Lambda\}$ are the only functions contributing both to the dynamics of the background and of the perturbations, while the others play a role only at level of perturbations. Let us notice that the above action includes ex-

plicitly all the operators that in ref. [163] have been considered to be relevant for linear cosmological perturbations since they can be easily related to some well known DE/MG models such as f(R), quintessence, Horndeski, or because they have been already studied in the EFT of inflation [169, 166, 168]. For such operators the corresponding field equations have been worked out [163, 8]. However, additional second order operators can also be considered, such as $(\delta\mathcal{R})^2$, $\delta\mathcal{R}^i{}_j\delta\mathcal{R}^j{}_i$ as well as operators with higher-order spatial derivatives acting on them, [162, 163, 173, 176]. In particular, as we will show in appendix .3, additional operators are needed to describe Hořava gravity in the EFT framework. For a review of higher order EFT operators see also [176, 177].

6.2 The Stückelberg field

In action (6.1) the extra dynamical scalar d.o.f. that one expects both in modified gravity and dark energy models, is hidden inside the metric. The unitary gauge is particularly suited for the construction of the most general action to describe all single field dark energy and modified gravity model. However, in order to study the dynamics of perturbations it is more practical to disentangle the scalar d.o.f from the metric ones. This can be achieved via the Stückelberg technique. Operationally, one restores the time diffeomorphism invariance by mean of an infinitesimal time coordinate transformation which introduces a scalar field, commonly referred to as the Stückelberg field, that realizes the symmetry nonlinearly. We work in conformal time, so in our case the time diffeomorphism reads:

$$\tau \to \tau + \pi(x^\mu), \tag{6.2}$$

while spatial coordinates are left unchanged. In the context of EFT of Inflation [168], the Stückelberg field is associated to the Goldstone boson, while in the effective field theory of dark energy the time translation invariance is no longer realized by the Goldstone scalar mode. Under this procedure, time-dependent functions are modified according to

$$f(\tau) \to f(\tau + \pi(x^\mu)) = f(\tau) + \dot{f}(\tau)\pi + \frac{\ddot{f}(\tau)}{2}\pi^2 + \dots \tag{6.3}$$

and are typically Taylor expanded in π. Furthermore, operators that are not fully diffeomorphism invariant transform according to the tensor transformation law, generating dynamical terms for π. For a complete description see [168, 162, 163]. To keep the resulting action at second order in perturbations, the functions multiplying the background operators, i.e. $\{\Omega, \Lambda, c\}$, are Taylor expanded up to the second order, while the functions multiplying second (and higher) order operators are expanded to zero order.

Let us illustrate how the mechanism works for the background operators, by giving the explicit form of the resulting action in terms of the Stückelberg field, up to second order in perturbations

$$S = \int d^4x\sqrt{-g}\Bigg\{ \frac{m_0^2}{2}\left[1 + \Omega(\tau+\pi)\right] R + \Lambda(\tau+\pi) \\ - c(\tau+\pi)a^2\Bigg[\delta g^{00} - 2\frac{\dot{\pi}}{a^2} + 2\mathcal{H}\pi\left(\delta g^{00} - \frac{1}{a^2} - 2\frac{\dot{\pi}}{a^2}\right) + 2\dot{\pi}\delta g^{00}$$

$$+ 2g^{0i}\partial_i\pi - \frac{\dot{\pi}^2}{a^2} + g^{ij}\partial_i\pi\partial_j\pi - \left(2\mathcal{H}^2 + \dot{\mathcal{H}}\right)\frac{\pi^2}{a^2}\Big] + \cdots \Big\} + S_m[g_{\mu\nu}], \tag{6.4}$$

where the scale factor has already been Taylor expanded according to Eq. (6.3). We give the explicit expression of the contributions to action (6.4) from second order operators in Appendix .2.1. We will use action (6.4) to derive the linearly perturbed Einstein equations in Sec. 6.4. Notice that our Stückelberg field is defined w.r.t. to conformal time, therefore there is a factor of a of difference w.r.t. the Stückelberg field of [162, 163].

6.3 Background dynamics

Varying the background part of the action (6.1) or, equivalently (6.4), with respect to the metric and assuming a flat FLRW metric one obtains the following background equations:

$$\mathcal{H}^2 = \frac{a^2}{3m_0^2(1+\Omega)}(\rho_m + 2c - \Lambda) - \mathcal{H}\frac{\dot{\Omega}}{1+\Omega}, \tag{6.5}$$

$$\dot{\mathcal{H}} = -\frac{a^2}{6m_0^2(1+\Omega)}(\rho_m + 3P_m) - \frac{a^2(c+\Lambda)}{3m_0^2(1+\Omega)} - \frac{\ddot{\Omega}}{2(1+\Omega)}, \tag{6.6}$$

where $\mathcal{H} = \dot{a}/a$ and ρ_m and P_m are, respectively, the energy density and pressure of the matter components, for which we assume a perfect fluid form with the standard continuity equation:

$$\dot{\rho}_m = -3\mathcal{H}(\rho_m + P_m). \tag{6.7}$$

Eqs. (6.5)-(6.6) can be recast in the following, more conventional, form

$$\mathcal{H}^2 = \frac{a^2}{3m_0^2(1+\Omega)}\left(\rho_m + \rho_Q\right), \tag{6.8}$$

$$\dot{\mathcal{H}} = -\frac{a^2}{6m_0^2(1+\Omega)}\left(\rho_m + 3P_m + \rho_Q + 3P_Q\right), \tag{6.9}$$

if one defines

$$\rho_Q \equiv 2c - \Lambda - \frac{3m_0^2\mathcal{H}\dot{\Omega}}{a^2},$$
$$P_Q \equiv \Lambda + \frac{m_0^2}{a^2}\left(\ddot{\Omega} + \mathcal{H}\dot{\Omega}\right). \tag{6.10}$$

The latter can be interpreted as, respectively, the energy density and pressure of the effective dark fluid. Combining Eqs. (6.7), (6.8) and Eq. (6.9) one obtains the following continuity equation for this dark component:

$$\dot{\rho}_Q = -3\mathcal{H}\left(\rho_Q + P_Q\right) + \frac{3m_0^2}{a^2}\mathcal{H}^2\dot{\Omega}, \tag{6.11}$$

which tells us that the energy density ρ_Q is conserved only in the case of $\Omega =$ const., i.e. a minimally coupled theory.

6.4 Perturbations dynamics

We shall now derive the linearly perturbed Einstein equations. We work in synchronous gauge with the line element given by

$$ds^2 = a(\tau)^2 \left[-d\tau^2 + \left(\delta_{ij} + h_{ij} dx^i dx^j\right)\right], \tag{6.12}$$

where the scalar mode of h_{ij} in Fourier space can be decomposed into

$$h_{ij} = \int dk^3 e^{i\mathbf{k}\cdot\mathbf{x}} \left[\hat{k}_i \hat{k}_j h(k,\tau) + \left(\hat{k}_i \hat{k}_j - 2\delta_{ij}\eta(k,\tau)\right)\right], \tag{6.13}$$

with h denoting the trace of h_{ij}. Unless explicitly stated otherwise, we work with Fourier transforms of all cosmological perturbations.

While the functions $\{\Omega, \Lambda, c\}$ are the only ones affecting the background dynamics in the EFT formalism, when we move to linear perturbations, more operators come into play; indeed, all the remaining functions in action (6.1), or equivalently (66), that multiply second order operators, will also affect the dynamics of linear perturbations. For the sake of brevity, here we focus on the terms contributed by background operators and we list the contributions from second order operators in Appendix .2.2.

Starting from the action in terms of the Stückelberg field (6.4), and simplifying the background terms, to linear order in scalar perturbations we have:

time-time Einstein equation:

$$\begin{aligned} k^2\eta =& -\frac{a^2}{2m_0^2(1+\Omega)}\left[\delta\rho_m + \dot{\rho}_Q\pi + 2c\left(\dot{\pi} + \mathcal{H}\pi\right)\right] + \left(\mathcal{H} + \frac{\dot{\Omega}}{2(1+\Omega)}\right) k\mathcal{Z} \\ &+ \frac{\dot{\Omega}}{2(1+\Omega)}\left[3(3\mathcal{H}^2 - \dot{\mathcal{H}})\pi + 3\mathcal{H}\dot{\pi} + k^2\pi\right], \end{aligned} \tag{6.14}$$

momentum Einstein equation:

$$\begin{aligned} \frac{2}{3}k^2\left(\sigma_* - \mathcal{Z}\right) =& \frac{a^2}{m_0^2(1+\Omega)}\left[(\rho_m + P_m)v_m + (\rho_Q + P_Q)k\pi\right] \\ &+ k\frac{\dot{\Omega}}{(1+\Omega)}\left(\dot{\pi} + \mathcal{H}\pi\right), \end{aligned} \tag{6.15}$$

space-space off-diagonal Einstein equation:

$$k\dot{\sigma}_* + 2k\mathcal{H}\sigma_* - k^2\eta = -\frac{a^2 P\Pi_m}{m_0^2(1+\Omega)} - \frac{\dot{\Omega}}{(1+\Omega)}\left(k\sigma_* + k^2\pi\right), \tag{6.16}$$

space-space trace Einstein equation:

$$\begin{aligned} \ddot{h} =& -\frac{3a^2}{m_0^2(1+\Omega)}\left[\delta P_m + \dot{P}_Q\pi + (\rho_Q + P_Q)\left(\dot{\pi} + \mathcal{H}\pi\right)\right] \\ &- 2\left(\frac{\dot{\Omega}}{1+\Omega} + 2\mathcal{H}\right)k\mathcal{Z} + 2k^2\eta \\ &- 3\frac{\dot{\Omega}}{(1+\Omega)}\left[\ddot{\pi} + \left(\frac{\ddot{\Omega}}{\dot{\Omega}} + 3\mathcal{H}\right)\dot{\pi} + \left(\mathcal{H}\frac{\ddot{\Omega}}{\dot{\Omega}} + 5\mathcal{H}^2 + \dot{\mathcal{H}} + \frac{2}{3}k^2\right)\pi\right], \end{aligned} \tag{6.17}$$

$\underline{\pi}$ field equation:

$$c\ddot{\pi} + (\dot{c} + 4\mathcal{H}c)\dot{\pi} + \left[\frac{3}{2}\frac{m_0^2\dot{\Omega}}{a^2}(\ddot{\mathcal{H}} - 2\mathcal{H}^3) - 2\dot{\mathcal{H}}c + \mathcal{H}\dot{c} + 6\mathcal{H}^2c + k^2c\right]\pi$$
$$+ ck\mathcal{Z} - \frac{m_0^2\dot{\Omega}}{4a^2}\left[\ddot{h} - 4k^2\eta + 6k\mathcal{H}\mathcal{Z}\right] = 0, \tag{6.18}$$

where $2k\mathcal{Z} \equiv \dot{h}$ and $2k\sigma_* \equiv \dot{h} + 6\dot{\eta}$ are the standard CAMB variables that will be usefull in the remaining Chapters. As we will discuss shortly in Sec. 6.5, it is important to demix the degrees of freedom in order to perform the appropriate stability analysis of perturbations in the dark sector [162]. Namely, one shall substitute for η and $\ddot{h}$ using Eq. (6.14) and (6.17), respectively, in order to obtain the following equation:

$$\left(c + \frac{3m_0^2}{4a^2}\frac{\dot{\Omega}^2}{(1+\Omega)}\right)\ddot{\pi}$$
$$+ \left[\frac{3m_0^2}{4a^2}\frac{\dot{\Omega}}{(1+\Omega)}\left(\ddot{\Omega} + 4\mathcal{H}\dot{\Omega} + \frac{(\rho_Q + P_Q)a^2}{m_0^2}\right) + \dot{c} + 4\mathcal{H}c - \frac{\dot{\Omega}}{2(1+\Omega)}c\right]\dot{\pi}$$
$$+ \left[\frac{3}{4}\frac{m_0^2}{a^2}\frac{\dot{\Omega}}{(1+\Omega)}\left(\frac{(3\dot{P}_Q - \dot{\rho}_Q + 3\mathcal{H}(\rho_Q + P_Q))a^2}{3m_0^2} + \mathcal{H}\ddot{\Omega} + 8\mathcal{H}^2\dot{\Omega} + 2(1+\Omega)(\ddot{\mathcal{H}} - 2\mathcal{H}^3)\right)\right.$$
$$\left. - 2\dot{\mathcal{H}}c + \left(\dot{c} - \frac{\dot{\Omega}}{2(1+\Omega)}c\right)\mathcal{H} + 6\mathcal{H}^2c + \left(c + \frac{3m_0^2}{4a^2}\frac{\dot{\Omega}^2}{(1+\Omega)}\right)k^2\right]\pi$$
$$+ \left[c + \frac{3}{4}\frac{m_0^2}{a^2}\frac{\dot{\Omega}^2}{(1+\Omega)}\right]k\mathcal{Z} + \frac{1}{4}\frac{\dot{\Omega}}{(1+\Omega)}(3\delta P_m - \delta\rho_m) = 0. \tag{6.19}$$

6.5 Stability of perturbations in the dark sector

In this subsection we shall focus on some requirements for theoretical stability that can be enforced on the EFT functions to ensure that the underlying gravitational theory is acceptable. For the following discussion it is more convenient to write the π field equation as follows:

$$A(\tau)\,\ddot{\pi} + B(\tau)\,\dot{\pi} + C(\tau)\,\pi + k^2\,D(\tau)\,\pi + E(\tau, k) = 0 \tag{6.20}$$

where the coefficients $\{A, \ldots, E\}$ can be easily read from Eq. (6.19) (and the results of Appendix .2.2 if second order operators are at play. In that case also A, B and D may display $k-$dependence). Relying on the discussion of [166], we place the following theoretical constraints:

- $1+\Omega > 0$: this condition on the non-minimal coupling function is required in order to ensure that the effective Newtonian constant does not change sign. Violating this condition, classically, would imply a Universe quickly becoming inhomogeneous and anisotropic [178, 179], while at the quantum level it will correspond to the graviton turning into a ghost [180];
- $A > 0$: this second condition follows from requiring that our effective scalar d.o.f. should not be a ghost, i.e. the corresponding kinetic energy

term should be positive. At the classical level there is no serious danger in this situation while at the quantum level the underlying physical theory can show instability of the vacuum [181];

- $c_s^2 \equiv D/A \leq 1$: the third condition ensures that the sound speed of π does not exceed the speed of light to prevent scalar perturbations from propagating super-luminary. This condition is no longer true when treating, for example, Lorentz violating theories [182];

- $m_\pi^2 \equiv C/A \geq 0$: last, we enforce the mass of the scalar d.o.f. to be real [183], to avoid tachyonic instabilities.

The above conditions could be relaxed in certain cases depending on the specific theory of gravity one is interested in. Let us briefly comment on this. The first two conditions are quite general and can be relaxed just in elaborated models that can associate a physical meaning to the negative branch of A and $1 + \Omega$. Furthermore, their positive and negative branches are disconnected so that no theory can allow these two quantities to cross zero as this will violate the mathematical consistency of the initial value problem for Eqs. (6.8) and (6.19). The last two conditions are milder and more strictly related to the particular theory one wants to test. Therefore, they can be relaxed in many ways if the EFT formalism is used to test some peculiar model that naturally permits their violation. In this regards, we recall, among others, cosmological models which allow for viable DE models in Lorentz violating theories [184, 185] and rolling tachyon condensates [186, 187, 188, 189, 190].

The stability conditions described in this Chapter might be modified when the coupling to matter is appreciable and the stability conditions described here should be thought to hold only when this is not the case. The full set of physical viability conditions for the general EFT action is a very complex matter that is the focus of ongoing work. Some results have been obtained in [177] and are briefly described in Appendix .2.7.

Chapter 7

A Background Dynamical Analysis

In this chapter we start tackling the phenomenological implications of the EFT of DE/MG by performing a dynamical analysis of the background cosmology.

As mentioned in the previous chapter only three functions of time contribute to the background dynamics and despite the underdetermined nature of the system, we identify a set of variables that allows us to write it as an infinite-dimensional system with an important recursive structure.

We then analyze several autonomous subsystems of increasingly higher dimension that, as we will illustrate, correspond to higher differential order for combinations of the EFT functions; in other words, we explore more and more general models of DE/MG identifying at each order conditions of cosmological viability. Furthermore, we exploit the recursive nature of the system to draw quite general conclusions on its cosmological dynamics, building on our findings at the lower orders. While we apply our method to some specific cases in order to elucidate it, the machinery we set up is general and can be used to perform dynamical analysis of models of dark energy/modified gravity within the broad and model independent EFT framework.

In this chapter only we shall extensively make use of cosmic time, as opposed to conformal time so hereafter overdots will represent derivatives with respect to cosmic time.

As outlined in the previous chapter, varying the background action with respect to the metric, assuming a spatially flat FLRW metric one obtains the following background equations:

$$3m_0^2(1+\Omega)H^2 + 3m_0^2 H\dot{\Omega} = \sum_i \rho_i - \Lambda + 2c, \tag{7.1}$$

$$3m_0^2(1+\Omega)H^2 + 2m_0^2(1+\Omega)\dot{H} + m_0^2\ddot{\Omega} + 2m_0^2 H\dot{\Omega} = -\sum_i p_i - \Lambda, \tag{7.2}$$

where ρ_i and p_i are, respectively, the background energy density and pressure of the i^{th} matter component, for which we assume a perfect fluid form. We

will consider two distinct components, i.e. dust with zero pressure (that we will indicate with a subscript 'm') and radiation with $p_r = 1/3\,\rho_r$. Their continuity equations, in cosmic time, read:

$$\dot{\rho}_m = -3H\rho_m, \tag{7.3}$$
$$\dot{\rho}_r = -4H\rho_r. \tag{7.4}$$

Deriving Eq. (7.1) w.r.t. time and combining it with Eqs. (7.2)-(7.4), one obtains what can be interpreted as a continuity equation for the effective DE component

$$2\dot{c} - \dot{\Lambda} = 3m_0^2\dot{H}\dot{\Omega} - 6Hc + 6m_0^2H^2\dot{\Omega}\,. \tag{7.5}$$

Equations (7.1)-(7.5) are all the equations we have at our disposal to study the dynamics of the background.

The covariant, background-independent approach that we adopt [162, 163], aims at offering a general framework to study the evolution of cosmological perturbations in a model independent way. In the latter context, it is common to fix the background history to the one of ΛCDM, or something close to that, and to focus on the dynamics of perturbations. This is justified by the fact that the cosmological concordance model is in very good agreement with current observables constraining the expansion history and that most alternative models are highly degenerate with it at the level of background dynamics, while predicting modifications at the level of perturbations. In the EFT framework this practice would translate into assuming that the background is given *a priori*, i.e. typically it is chosen to be close to the ΛCDM one, and one focuses on the coefficients of the higher order operators contained in $S^{(2)}_{\rm DE}$. If we were to fix the expansion history, we could use Eqs. (7.1) and (7.2) to eliminate two of the three EFT functions, typically $\Lambda(t)$ and $c(t)$. This however would still leave us with one completely undetermined function of time, $\Omega(t)$ for which we should make some arbitrary choice. In this analysis, we do not fix the expansion history, but rather we keep all the three functions free and, via a dynamical analysis of the background, we identify viable forms, as well as compatibility conditions for their time dependence in order for the model to produce an expansion history that is viable. The aim of our analysis is, given the high degree of freedom, to identify general rules of cosmological viability and compatibility for Ω, Λ, c, that can guide us in later fixing them to some form or ansätze.

7.1 Dynamical system and cosmological viability

In this Section we will set up the necessary ingredients to perform a dynamical analysis of the effective field theory of dark energy. We need to rewrite the equations for the background into an autonomous system of first ODEs, for which we can then study the stability around equilibrium points. To this purpose, we introduce the following dimensionless variables:

$$x = \frac{c}{3m_0^2(1+\Omega)H^2}, \quad y = \frac{c-\Lambda}{3m_0^2(1+\Omega)H^2}, \quad u = \frac{\rho_r}{3m_0^2(1+\Omega)H^2},$$

$$\alpha_0 = -\frac{\dot{\Omega}}{(1+\Omega)H}, \ldots, \alpha_n = -\frac{\Omega^{(n+1)}}{H\Omega^{(n)}}, \ldots,$$
$$\lambda_0 = -\frac{\dot{c}-\dot{\Lambda}}{H(c-\Lambda)}, \ldots, \lambda_m = -\frac{(c-\Lambda)^{(m+1)}}{H\,(c-\Lambda)^{(m)}}, \ldots \tag{7.6}$$

where the indices n, m are unbounded from above. Using Eqs. (7.1)-(7.5), we can write the following set of first order ODEs:

$$\frac{dx}{d\ln a} = \lambda_0 y - 6x - 2\alpha_0 + x\alpha_0 - (\alpha_0 + 2x)\frac{\dot{H}}{H^2}, \tag{7.7a}$$
$$\frac{dy}{d\ln a} = \left(\alpha_0 - \lambda_0 - 2\frac{\dot{H}}{H^2}\right) y, \tag{7.7b}$$
$$\frac{du}{d\ln a} = \left(\alpha_0 - 4 - 2\frac{\dot{H}}{H^2}\right) u, \tag{7.7c}$$
$$\frac{d\alpha_{n-1}}{d\ln a} = \left(-\alpha_n + \alpha_{n-1} - \frac{\dot{H}}{H^2}\right)\alpha_{n-1}, \quad (n \geq 1) \tag{7.7d}$$
$$\frac{d\lambda_{m-1}}{d\ln a} = \left(-\lambda_m + \lambda_{m-1} - \frac{\dot{H}}{H^2}\right)\lambda_{m-1}, \quad (m \geq 1) \tag{7.7e}$$

where

$$\frac{\dot{H}}{H^2} = -\frac{3}{2} - \frac{3}{2}x + \frac{3}{2}y + \alpha_0 - \frac{1}{2}\alpha_1\alpha_0 - \frac{1}{2}u. \tag{7.8}$$

This is a nonlinear, non-autonomous system that, however, displays a hierarchical structure in the equations for the $\alpha's$ and $\lambda's$. We will shortly describe our strategy to approach it.

Eq. (7.1) can be read as a constraint equation

$$\Omega_m = \frac{\rho_m}{3{m_0}^2(1+\Omega)H^2} = 1 - x - y - u - \alpha_0, \tag{7.9}$$

with $\Omega_m \geq 0$. When describing the cosmology of the different points, we will consider also the following parameters:

$$\Omega_{\rm DE} = x + y + \alpha_0, \qquad \Omega_{\rm r} = u,$$
$$w_{\rm eff} \equiv -1 - \frac{2}{3}\frac{\dot{H}}{H^2} = x - \frac{2}{3}\alpha_0 + \frac{1}{3}\alpha_1\alpha_0 - y + \frac{1}{3}u, \tag{7.10}$$

respectively the DE and radiation fractional energy density and the effective equation of state. Note that what we define the fractional density parameters, are the standard ones rescaled by the function $\Omega(t)$ [191].

In order to solve system (7.7) we first need to make it autonomous. The simplest option corresponds to setting α_0, λ_0 to constant and evolve only the three core equations (7.7a)-(7.7c); we refer to this case as the zero-th order one and analyze it sampling the space (α_0, λ_0) to find viable cosmologies. As we discuss in detail in Sec. 7.3, this case corresponds to assuming that Ω and $c-\Lambda$ are power laws in the scale factor. To go beyond this zero-th order analysis, we can start exploring the hierarchy of equations (7.7d) and (7.7e), by setting α_N

and λ_M constant for given $N, M \geq 1$. We are then left with a $(3+N+M)$-dimensional system formed by the three core equations for $\{x, y, u\}$, plus N equations for $\alpha_0, \ldots, \alpha_{N-1}$ and M equations for $\lambda_0, \ldots, \lambda_{N-1}$. We perform the dynamical analysis of this system sampling the space (α_N, λ_M) and determining the regions for which one can obtain viable expansion histories. What is the corresponding form of the EFT functions that we explore at this order? Let us develop the following argument in terms of Ω; it is then trivial to reproduce it for $c - \Lambda$. From the definition of the $\alpha's$, we see that fixing $\alpha_N = \text{const}$ gives

$$\Omega^{(N)}(t) = \Omega^{(N)}(t_0) a^{-\alpha_N}, \tag{7.11}$$

where t_0 is the present time. Now that we have an expression for the N^{th} derivative of Ω, we can use it to write

$$1 + \Omega(t) = \sum_{i=0}^{N-1} \frac{\Omega^{(i)}(t_0)}{i!}(t-t_0)^i + \Omega^{(N)}(t_0) \int_{t_0}^{t} \frac{(t-\tau)^{N-1}}{(N-1)!} a^{-\alpha_N}(\tau)\, d\tau, \tag{7.12}$$

that shows that the constant α_N ($N \geq 1$) parametrizes the remainder in a Taylor expansion of order $N-1$ around the present time for the function $\Omega(t)$. Notice that in order for the above argument to hold one does not necessarily need t_0 to be the present time (with $a_0 = 1$); the latter can be the desired choice in view of constraining the form of the EFT functions at recent times [162], where they are expected to have a non-trivial dynamics and where they are more likely to be probed. However, one can in principle choose any other t_0 that is suited to one's purpose, as long as a is rescaled by a_0 in (7.11) and (7.12). In the following Sections, we separately analyze the stability of the system (7.7) at different orders. In particular, after analyzing the zero-th order case in Sec. 7.3, we maintain λ_0 constant and focus on the α channel of the system, solving $3+N$ equations for the variables $\{x, y, u, \alpha_0, \ldots, \alpha_N\}$. In other words, we focus on the class of models for which $c - \Lambda$ is a power law in the scale factor, while the conformal factor Ω can be increasingly general as we go up with the order. Alternatively one could fix Ω to a constant and open the λ channel, which would correspond to exploring all minimally coupled models of DE. Finally, one could work with both channels and, for instance, explore, within this parametrized framework the full class of Horndeski theories [192].

Finally, let us point out that the structure of the system is such that the planes $y = 0$, $u = 0$, $\alpha_i = 0$, $\lambda_j = 0$ are all invariant manifolds, which implies that trajectories starting on one of these planes remain on it. This ensures that viable trajectories identified at a given order, will exist at all higher orders. We exploit this feature at the end of this Section, when we reconstruct the dynamics at a generic order $N \geq 3$.

7.2 Stability Analysis

The dynamics of system (7.7) can be studied analyzing the evolution around fixed/critical points, i.e. points p_i satisfying the equilibrium condition $dp_i/d\ln a = 0$. In the following we briefly summarize the general procedure; for an exhaustive description of the technique, and for some applications to cosmological models

we refer the reader to [193]. After determining its fixed points, one proceeds to calculate the eigenvalues μ_i of the Jacobian matrix $\mathcal{M}$ of the system in order to linearize it around each critical point. This determines the stability nature of the point, in other words it controls how the system behaves when approaching the point. We are interested in hyperbolic critical points, since around these the linearized dynamical system is a good approximation of the full nonlinear system. By definition a critical point is said to be hyperbolic if all eigenvalues of $\mathcal{M}$ have $Re(\mu_i) \neq 0$. Hyperbolic critical points are robust, in the sense that small perturbations do not change qualitatively the phase portrait near the equilibrium. For an n-dimensional system one has n eigenvalues for each point and the stability depends on the nature of these eigenvalues, according to the following classification:

- All μ_i are real and have the same sign:
  - Negative eigenvalues $\rightarrow$ Stable node/ Attractor;
  - Positive eigenvalues $\rightarrow$ Unstable node;
- All μ_i are real and at least one positive and one negative $\rightarrow$ Saddle points;
- At least one eigenvalue is real and there are pairs of complex eigenvalues:
  - All eigenvalues have negative real parts $\rightarrow$ Stable Focus-Node;
  - All eigenvalues have positive real parts $\rightarrow$ Unstable Focus-Node;
  - At least one positive real part and one negative $\rightarrow$ Saddle Focus.

A working cosmological model needs to first undergo a radiation dominated era, followed by a matter era, and then enter a phase of accelerated expansion (DE) as indicated by observations [12, 11]. In terms of critical points we need two saddle points for the radiation and the matter dominated eras, followed by a late time accelerated attractor, i.e. a stable node with $w_{\text{eff}} < -\frac{1}{3}$. In addition we impose the constraints that $\Omega_m \geq 0$ and $\Omega_r \geq 0$, given that matter and radiation energy densities should be positively defined, and $\Omega(t) > 0$ to guarantee a stable gravity [179]. On the other hand, we allow the effective dark energy density to be negative since this quantity may not correspond to the energy density of an actual fluid, and may indeed be negative in some models of modified gravity [191]. Finally, in reconstructing viable trajectories, we require that the matter era is long enough to allow for structure formation.

7.3 Zero$^{\text{th}}$ order analysis

The simplest option to make the system (7.7) autonomous is setting α_0 and λ_0 to constant and evolve only the core equations (7.7a)-(7.7c). The corresponding behavior of the EFT functions is

$$1 + \Omega(t) = \Omega_0\, a^{-\alpha_0}, \qquad c(t) - \Lambda(t) = (c - \Lambda)_0 a^{-\lambda_0}, \tag{7.13}$$

where the constants will depend on the initial conditions and their value does not affect the stability analysis.

Unless $\alpha_0 = 0$, the system (7.7a)-(7.7c) is not closed due to the dependence on α_1 through $\dot{H}/H^2$. We can use (7.7d) for $n = 1$ to get

$$\frac{\dot{H}}{H^2} = \frac{1}{2-\alpha_0}\left(2\alpha_0 - \alpha_0^2 - 3 + 3y - 3x - u\right) . \tag{7.14}$$

The resulting critical points of the system and the analysis of their stability are shown in Table 7.1. We find that the same results are still valid if $\alpha_0 = 0$. In what follows we present their eigenvalues and discuss the cosmological viability.

- P_1: *matter point*
  The eigenvalues and the relative eigenvectors of the linearized system around the first critical point are:

$$\begin{aligned} &\mu_1 = -1, && \mu_2 = \alpha_0 - 3, && \mu_3 = 3 - \lambda_0. \\ &\vec{u}_1 = \left(\frac{\alpha_0}{6-3\alpha_0}\,,\,0\,,\,1\right), && \vec{u}_2 = (1\,,\,0\,,\,0)\,, && \vec{u}_3 = \left(\frac{\alpha_0-\lambda_0}{\alpha_0+\lambda_0-6}\,,\,1\,,\,0\right). \end{aligned} \tag{7.15}$$

  This point displays a scaling solution for which matter and DE coexists with a constant ratio between their energy densities. We are primarily interested in the matter configuration, since this is the only critical point of the zero-th order system that can provide a matter dominated critical point. If we require $\Omega_m \approx 1$, then we have $\alpha_0 \approx 0$, which combined with the requirements of having a saddle, gives $\alpha_0 = 0 \wedge \lambda_0 < 3$.

- P_2: *stiff matter point*

$$\begin{aligned} &\mu_1 = 2 - \alpha_0, && \mu_2 = 3 - \alpha_0, && \mu_3 = -\alpha_0 - \lambda_0 + 6. \\ &\vec{u}_1 = (-1\,,\,0\,,\,1), && \vec{u}_2 = (1\,,\,0\,,\,0), && \vec{u}_3 = (-1\,,\,1\,,\,0). \end{aligned} \tag{7.16}$$

  This point is a DE dominated critical point; it is a stable node with accelerated expansion only if $\alpha_0 > 3 \wedge \alpha_0 + \lambda_0 > 6$. For $\alpha_0 = 0$, it has $w_{\text{eff}} = 1$, which corresponds to a stiff matter behavior that could be of interest for modeling early stages of the Universe [194].

- P_3: *DE point*

$$\begin{aligned} &\mu_1 = \lambda - 4, \\ &\mu_2 = \lambda_0 - 3, \\ &\mu_3 = \alpha_0 + \lambda_0 - 6. \\ &\vec{u}_1 = \left(\frac{\lambda_0 - 2\alpha_0}{3(\alpha_0-2)}\,,\,-\frac{\alpha_0+\lambda_0-6}{3(\alpha_0-2)}\,,\,1\right), \\ &\vec{u}_2 = \left(\frac{\alpha_0-\lambda_0}{\alpha_0+\lambda_0-6}\,,\,1\,,\,0\right), \\ &\vec{u}_3 = (-1\,,\,1\,,\,0)\,. \end{aligned} \tag{7.17}$$

  This is the second DE dominated critical point of the zero-th order system; it exhibits a correct cosmological behavior, i.e. $w_{\text{eff}} < -\frac{1}{3}$, if $(\alpha_0 \geq 3 \wedge \alpha_0 + \lambda_0 < 6) \vee (\alpha_0 < 1 \wedge \lambda_0 < \alpha_0 + 2) \vee (1 \leq \alpha_0 < 3 \wedge \lambda_0 < 3)$.

- P_4: *radiation point*

$$\begin{aligned}
&\mu_1 = 1,\\
&\mu_2 = \alpha_0 - 2,\\
&\mu_3 = 4 - \lambda_0.\\
&\vec{u}_1 = \left(\frac{\alpha_0}{6-3\alpha_0}\,,\,0\,,\,1\right),\\
&\vec{u}_2 = (-1\,,\,0\,,\,1)\,,\\
&\vec{u}_3 = \left(\frac{\lambda_0 - 2\alpha_0}{3(\alpha_0-2)}\,,\,-\frac{\alpha_0+\lambda_0-6}{3(\alpha_0-2)}\,,\,1\right).
\end{aligned} \tag{7.18}$$

  This point is characterized by $\Omega_m = 0$ and a coexistence of radiation and DE with a constant energy density ratio; in other words it is a scaling radiation point. We will focus on its radiation dominated version, since it is the only point that can supply a radiation era for the zero-th order trajectories. It can be be easily seen that it corresponds to a saddle with $w_{\text{eff}} = \frac{1}{3}$ if $\alpha_0 = 0 \wedge \lambda_0 \neq 4$.

Combining all the information above, we conclude that viable cosmological models for the zero-th order case, can be recovered setting $\alpha_0 = 0$ and $\lambda_0 < 3$, and they are characterized by the transitions $P_4 \to P_1 \to P_3$ (radiation$\to$ matter $\to$ DE attractor). One can actually further constrain the space (α_0, λ_0). Indeed, a peculiar feature of the zero-th order system is the disposition of the critical points. A careful analysis of the eigenvectors (7.15)-(7.18), shows that for any pair of critical points the heteroclinic orbits, i.e. the lines connecting the two points, are strainght lines. This is valid for any choice of (α_0, λ_0) and it allows us to put a stricter bound on λ_0 by requiring a long enough matter era for the trajectories of interest. Let us elucidate this point. The ΛCDM model corresponds to $\alpha_0 = \lambda_0 = 0$ and its trajectory is such that it starts very close to the radiation saddle point P_4, then it passes close to the matter saddle P_1 and finally it reaches the dark energy attractor P_3, always moving very close to the heteroclinic orbits that connect these three critical points. The time spent by this trajectory in the last transition gives a handle on the proper duration of the matter era for trajectories that aim to be cosmologically viable. Since after we set $\alpha_0 = 0$ the coordinates of P_1 and P_4 are fixed (i.e. independent on λ_0), we can use the constraint on the position of P_3 to put a stringent bound on λ_0; indeed if we change the latter, and hence move P_3, the duration of the matter era will change significantly. In other words, we need P_3 to be always close to its ΛCDM position, and this forces $\lambda_0 \sim 0$.
In summary, *viable cosmological models for the zero-th order case, can be recovered setting* $\alpha_0 = 0$ and $\lambda_0 \approx 0$, *and they are characterized by the transitions* $P_4 \to P_1 \to P_3$. Notice that $\alpha_0 = 0$ implies that the conformal factor $1 + \Omega(t)$ is a constant, which just rescales the Planck mass.

7.3.1 Reconstructing quintessence models

We shall now show how the results of this general dynamical analysis can be reverberated to constrain specific models of dark energy. As an example, we choose to interpret the results of the zero-th order analysis within the context

Point	$[x_c, y_c, u_c]$	Stability	$\Omega_{\rm DE}$	$w_{\rm eff}$
P_1	$\left[-\frac{1}{6}\alpha_0(1+\alpha_0), 0, 0\right]$	**Stable node:** $\lambda_0 > 3 \wedge \alpha_0 \leq 2$ **Saddle point:** $(\lambda_0 < 3 \wedge \alpha_0 \leq 2) \vee (\alpha_0 > 3 \wedge \lambda \neq 3)$	$-\frac{1}{6}(\alpha_0 - 5)\alpha_0$	$-\frac{\alpha_0}{3}$
P_2	$[1-\alpha_0, 0, 0]$	**Stable node:** $\alpha_0 > 3 \wedge \alpha_0 + \lambda_0 > 6$. **Unstable node:** $\alpha_0 < 2 \wedge \alpha_0 + \lambda_0 < 6$ **Saddle point:** otherwise	1	$1 - \frac{2\alpha_0}{3}$
P_3	$\left[\frac{1}{12}(-\alpha_0^2 - \alpha_0(\lambda_0+4) + 2\lambda_0), \frac{1}{12}(\alpha_0 - 2)(\alpha_0 + \lambda_0 - 6), 0\right]$	**Stable node:** $(\alpha_0 \geq 3 \wedge \alpha_0 + \lambda_0 < 6) \vee (\alpha_0 < 3 \wedge \lambda_0 < 3)$. **Unstable node:** $(\lambda_0 > 4 \wedge \alpha_0 \geq 2) \vee (\alpha_0 + \lambda_0 > 6 \wedge \alpha < 2)$. **Saddle point:** otherwise	1	$\frac{1}{3}(-\alpha_0 + \lambda_0 - 3)$
P_4	$\left[-\frac{\alpha_0^2}{4}, 0, \frac{1}{4}(\alpha_0 - 2)^2\right]$	**Unstable node:** $\alpha_0 > 2 \wedge \lambda_0 < 4$ **Saddle point:** $(\alpha_0 > 2 \wedge \lambda_0 > 4) \vee (\alpha_0 < 2 \wedge \lambda_0 \neq 4)$	$-\frac{1}{4}(\alpha_0 - 4)\alpha_0$	$\frac{1-\alpha_0}{3}$

Table 7.1: Hyperbolic critical points and stability analysis for the *zero-th order* system. The additional constraints $\Omega_m \geq 0$ and $\Omega_r \geq 0$ have been imposed. We have $\mathcal{D} \equiv \{\alpha_0, \lambda_0 \in \mathbb{R}\}$.

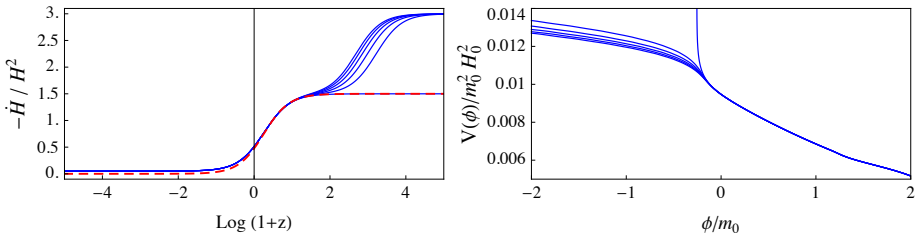

Figure 7.1: The slow roll parameter and the quintessence potential reconstructed for several trajectories of the $\alpha_0 = 0$, $\lambda_0 = 0.1$ model (blue lines). The red dashed line represents the behavior of the Planck [78] best fit ΛCDM model. From [9].

of quintessence by using the matching in [162, 163]. Given that c and Λ for quintessence models assume the following forms:

$$c = \frac{\dot{\phi}^2}{2}\,, \qquad c - \Lambda = V(\phi) = (c-\Lambda)_0 a^{-\lambda_0}, \tag{7.19}$$

one immediately notices that the bound $\alpha_0 = 0$ for the zero-th order analysis, translates into the constraint that any quintessence model with a potential which is a power law in the scale factor, cannot have a power law behavior for the conformal factor Ω, and therefore at this order is forced to be minimally coupled. Among the models selected in this way, we will choose for our example those corresponding to the value $\lambda_0 = 0.1$. For simplicity we do not include radiation in this numerical study since it will not alter much the reconstruction. We choose initial conditions so that the present day matter density matches the Planck ΛCDM best fit value [78] and we sample the trajectories that undergo a $P_1 \to P_3$ transition. Then using (7.19) we reconstruct the time evolution of the quantities of interest, i.e. the slow-roll parameter and the the potential. We show the outcome in Fig. 7.1, where one can notice that the late time DE attractor corresponds to slow roll behavior which makes the field behave approximately like a cosmological constant. On the other hand at early times the field is rolling down the potential very fast as the dark energy component behaves like stiff matter, as expected since the unstable stiff-matter point, P_2, serves as the starting point for the numerically reconstructed trajectories. The corresponding potential is monotonically decreasing and positively defined.

7.4 First order analysis

We now start exploring the hierarchy of equations for the $\alpha's$. The immediate generalization of the previous model is the one obtained by letting α_0 vary, while fixing (α_1, λ_0) to constant. As discussed at the beginning of this Section, this corresponds to setting

$$\dot{\Omega}(t) = \dot{\Omega}_0 a^{-\alpha_1}, \qquad c(t) - \Lambda(t) = (c-\Lambda)_0 a^{-\lambda_0}, \tag{7.20}$$

where again the constants will depend on the initial conditions and do not affect the stability analysis. Our system of equations is now formed by (7.7a)-(7.7c)

along with Eq. (7.7e) with $n = 1$ and the constraint (7.9). The system has nonlinear quadratic terms and, for different values of the parameters (α_1, λ_0), it can display a wide range of behaviors. The critical points of the system and the stability properties according to their eigenvalues are summarized in Table 7.2. In what follows we give a more detailed overview of each point, reporting the corresponding eigenvalues.

- P_1: *matter point*
  The linearized system around the first critical point has the following eigenvalues:
  $$\mu_1 = -3, \quad \mu_2 = \frac{3}{2} - \alpha_1, \quad \mu_3 = -1, \quad \mu_4 = 3 - \lambda_0. \tag{7.21}$$
  It corresponds to a matter dominated solution ($w_{\rm eff} = 0$) which is a saddle point for $\lambda_0 \neq 3 \wedge \alpha_1 < \frac{3}{2} \vee \lambda_0 < 3 \wedge \alpha_1 > \frac{3}{2}$.

- P_2: *stiff matter point*
  $$\mu_1 = 3, \quad \mu_2 = 3 - \alpha_1, \quad \mu_3 = 6 - \lambda_0, \quad \mu_4 = 2. \tag{7.22}$$
  This point corresponds to unstable solutions with a stiff matter equation of state, which could be relevant in the early stages of the Universe [194].

- P_3: *DE point*
  $$\mu_1 = -6 + \lambda_0, \quad \mu_2 = -3 + \lambda_0, \quad \mu_3 = -\alpha_1 + \frac{\lambda_0}{2}, \quad \mu_4 = -4 + \lambda_0. \tag{7.23}$$
  It gives a DE dominated solution which is accelerated for $\lambda_0 < 2$. For $\lambda_0 < 0$ the point has a phantom equation of state. In particular we have a late time accelerated attractor (i.e. a stable node), with $a \propto t^{2/\lambda_0}$, for $(\alpha_1 > 1 \wedge \lambda_0 < 2) \vee (\lambda_0 < 2\alpha_1 \wedge \alpha_1 \leq 1)$.

- P_4: *phantom DE point*
  $$\mu_1 = -5+2\alpha_1, \quad \mu_2 = -3+\alpha_1, \quad \mu_3 = -2+2\alpha_1-\lambda_0, \quad \mu_4 = 2(\alpha_1-3). \tag{7.24}$$
  It has a DE dominated solution with an accelerated expansion for $\alpha_1 < 3$, (with a phantom equation of state for $\alpha_1 < 2$). Furthermore, the point is a saddle for $\alpha_1 < \frac{5}{2} \wedge \lambda_0 > -2 + 2\alpha_0$ with $a \propto t^{\frac{1}{\alpha_1 - 2}}$.

- P_5: *matter scaling point*
  $$\begin{aligned}
  \mu_1 &= \frac{1}{4}\left(-21 + 13\alpha_1 - 2\alpha_1^2 - \sqrt{81 - 42\alpha_1 + 29\alpha_1^2 - 20\alpha_1^3 + 4\alpha_1^4}\right), \\
  \mu_2 &= \frac{1}{4}\left(-21 + 13\alpha_1 - 2\alpha_1^2 + \sqrt{81 - 42\alpha_1 + 29\alpha_1^2 - 20\alpha_1^3 + 4\alpha_1^4}\right), \\
  \mu_3 &= 3 - \lambda_0, \quad \mu_4 = -1.
  \end{aligned} \tag{7.25}$$
  For this critical point we have a matter scaling solution with $\Omega_m = 5 - \frac{11}{3}\alpha_1 + \frac{2}{3}\alpha_1^2$ and $\Omega_{\rm DE} = -4 + \frac{11\alpha_1}{3} - \frac{2\alpha_1^2}{3}$. The constraint on the positiveness of the matter density gives $\alpha_1 \geq 3 \vee \alpha_1 \leq \frac{5}{2}$. In this paper we do not perform a full analysis of scaling solutions, but we rather focus on the two extrema for which

Point	$[x_c, y_c, u_c, \alpha_{0,c}]$	Stability	$\Omega_{\rm DE}$	$w_{\rm eff}$
P_1	$[0,0,0,0]$	**Stable node:** $\lambda_0 > 3 \wedge \alpha_1 > \frac{3}{2}$ **Saddle point:** otherwise	0	0
P_2	$[1,0,0,0]$	**Unstable node:** $\alpha_1 < 3 \wedge \lambda_0 < 6$ **Saddle point:** otherwise	1	1
P_3	$\left[\frac{\lambda_0}{6}, 1-\frac{\lambda_0}{6}, 0, 0\right]$	**See Fig. 7.2.**	1	$\frac{1}{3}(\lambda - 3)$
P_4	$[-1,0,0,2]$	**Stable node:** $\alpha_1 < \frac{5}{2} \wedge 2 - 2\alpha_1 + \lambda_0 > 0$, **Unstable node:** $\alpha_1 > 3 \wedge 2 - 2\alpha_1 + \lambda_0 < 0$, **Saddle point:** otherwise	1	$\frac{1}{3}(-7 + 2\alpha_1)$
P_5	$\left[\frac{1}{3}(-3 + 5\alpha_1 - 2\alpha_1^2), 0, 0, -3 + 2\alpha_1\right]$	**Stable node:** $\alpha_1 < \frac{3}{2} \wedge \lambda_0 > 3$ **Saddle point:** $\alpha_1 < \frac{3}{2} \wedge \lambda_0 < 3 \ \vee \ \alpha_1 > 3 \wedge \lambda_0 > 3 \vee \alpha_1 > 3 \wedge \lambda_0 < 3 \vee \lambda_0 \neq 3 \wedge \frac{3}{2} < \alpha_1 < \frac{5}{2}$	$-4 + \frac{11\alpha_1}{3} - \frac{2\alpha_1^2}{3}$	$1 - \frac{2\alpha_1}{3}$
P_6	$\left[\frac{1}{6}[-2\alpha_1^2 + \alpha_1(\lambda_0 - 4) + 3\lambda_0], \frac{1}{6}(-3+\alpha_1)(-2+2\alpha_1-\lambda_0), 0, 2\alpha_1 - \lambda_0\right]$	**See Fig. 7.2.**	1	$\frac{1}{3}(-3 - 2\alpha_1 + 2\lambda_0)$
P_7	$[0,0,1,0]$	**Saddle point:** $\lambda_0 \neq 4 \wedge \alpha_1 \neq 2$	0	$\frac{1}{3}$
P_8	$\left[-(-2+\alpha_1)^2, 0, (-3+\alpha_1)^2, 2(-2+\alpha_1)\right]$	**Saddle point:** $\alpha_1 \neq 3 \wedge \alpha_1 \neq 2 \wedge \lambda_0 \neq 4$	$-8 + 6\alpha_1 - \alpha_1^2$	$\frac{1}{3}(5 - 2\alpha_1)$

Table 7.2: Hyperbolic critical points of the *first order* analysis ($\alpha_1, \lambda_0 =$ constant), for which we have imposed the additional constraints $\Omega_m \geq 0$ and $\Omega_r \geq 0$. We have $\mathcal{D} \equiv \{\alpha_1, \lambda_0 \in \mathbb{R}\}$.

either of the two components has fractional energy density equal to unity. We leave the full analysis of the scaling regime for future work. For this specific point it means that we consider only the case for which $\Omega_m = 1$ and the case for which $\Omega_{\rm DE} = 1$. Both points do not display the proper cosmology and therefore we do not consider P_5 any further.

- P_6: *DE point*

$$\begin{aligned}
\mu_1 =& \lambda_0 - 3, \quad \mu_2 = \lambda_0 - 4, \\
\mu_3 =& \frac{1}{4}\Big(-12 - 2\alpha_1^2 - 3\lambda_0 + \alpha_1(10 + \lambda_0) \\
& -\sqrt{-3+\alpha_1}\sqrt{-48 + 4\alpha_1^3 - 4\alpha_1^2(\lambda_0 - 1) - 8\lambda_0 + 5\lambda_0^2 + \alpha_1(32 - 12\lambda_0 + \lambda_0^2)}\Big), \\
\mu_4 =& \frac{1}{4}\Big(-12 - 2\alpha_1^2 - 3\lambda_0 + \alpha_1(10 + \lambda_0) \\
& +\sqrt{-3+\alpha_1}\sqrt{-48 + 4\alpha_1^3 - 4\alpha_1^2(\lambda_0 - 1) - 8\lambda_0 + 5\lambda_0^2 + \alpha_1(32 - 12\lambda_0 + \lambda_0^2)}\Big).
\end{aligned} \tag{7.26}$$

The point P_6 gives a DE dominated solution, with $a(t) \propto t^{\frac{1}{\lambda_0 - \alpha_1}}$, which gives an accelerated expansion for $\lambda_0 - \alpha_1 < 1$ (phantom if $\alpha_1 > \lambda_0$). The results of the stability analysis around this critical point are summarized in Fig. 7.2; one can identify regions in the space (α_1, λ_0) for which the point is a late time attractor, as well as regions for which it is a stable focus-node. The latter one is an asymptotically stable point and corresponds to the case in which the system undergoes oscillations prior to reaching the equilibrium.

- P_7: *radiation point*

$$\mu_1 = -2, \quad \mu_2 = 1, \quad \mu_3 = -\alpha_1 + 2, \quad \mu_4 = 4 - \lambda_0. \tag{7.27}$$

It corresponds to a standard radiation point with $w_{\rm eff} = \frac{1}{3}$ and can be a saddle for $\alpha_1 \neq 2$ and $\lambda_0 \neq 4$.

- P_8: *radiation scaling point*

$$\mu_1 = 1, \quad \mu_2 = 2(\alpha_1 - 3), \quad \mu_3 = -6 + 5\alpha_1 - \alpha_1^2, \quad \mu_4 = 4 - \lambda_0. \tag{7.28}$$

This point exhibits a radiation scaling behavior since $\Omega_m = 0$ while Ω_r and $\Omega_{\rm DE}$ can be both non-vanishing. However one cannot in general find values of (α_1, λ_0) that give either a proper DE or radiation dominated cosmology.

As we already discussed, a working cosmological model needs to first undergo a radiation dominated era, followed by a matter dominated era (that needs to be long enough to allow for proper structure formation) and finally it has to approach an accelerated phase. The only critical point which corresponds to a proper radiation domination in the first order system is P_7, which is a saddle for $\alpha_1 \neq 2$ and $\lambda_0 \neq 4$; a good critical point for a matter era is P_1, which can be a saddle with $a \propto t^{2/3}$. From this point the system can move to an accelerated expansion phase by going toward the late time attractors P_3, P_4 or P_6 (as well as the stable-focus version of P_6), depending on the values of α_1, λ_0. Therefore

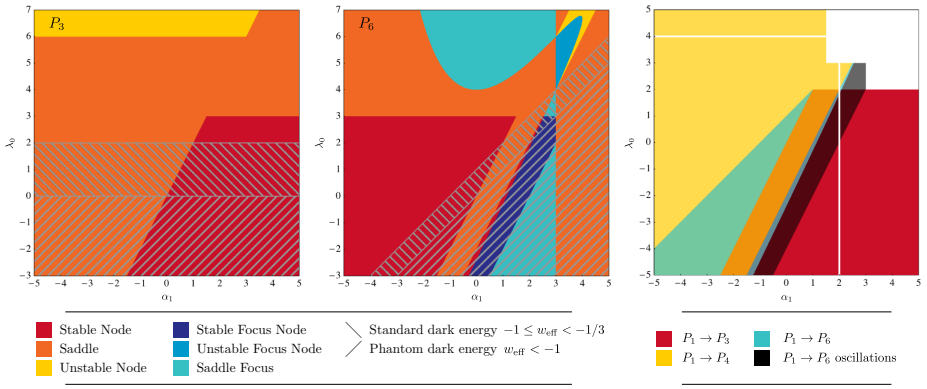

Figure 7.2: The left panel shows the results of the stability analysis of the *first order* system around P_3. The panel at the center illustrates the stability around P_6. The right panel shows the combined results of the *first order* analysis: regions in the (α_1, λ_0) plane which allow the different transitions discussed in Sec. 7.4.1 are shown in different colors. From [9].

we have three types of cosmologically viable trajectories, that can be identified by the last transition that they undergo: $P_1 \to P_3$, $P_1 \to P_4$ and $P_1 \to P_6$ (with and without oscillations). In the next subsection we investigate numerically each of these cases. Finally, we give a graphical representation of the regions in (α_1, λ_0) for which the different transitions can take place in Fig. 7.2.

7.4.1 Numerical investigation of different transitions

We shall now investigate numerically the structure of the phase space for some models that display the different types of possible transitions discussed above. In order to facilitate the visualization of the phase space, we neglect radiation. Let us briefly describe the procedure that we follow for this numerical investigation. We set initial conditions in order to reproduce the ΛCDM matter density [78] at some given initial redshift and we systematically sample trajectories that cross the plane so defined. After the integration of the equations of motion we notice that, even if nothing a priori suggests it, the trajectories that depart from constant matter density planes remain quite close to them. It is then possible to visualize the behavior of the three dimensional system by projecting the trajectories on these planes, and compactifying the latter via

$$x_P = \frac{x}{\sqrt{1+x^2+y^2}}\,, \qquad y_P = \frac{y}{\sqrt{1+x^2+y^2}}. \tag{7.29}$$

After this operation we obtain the phase space plots that are shown in Fig. 7.3. In what follows we discuss the different types of transitions recovered with the technique just described; in particular we choose four different combinations of values for (α_1, λ_0), according to the previous analysis (e.g. Fig. 7.2), to focus each time on a different type of trajectory among the cosmologically viable ones.

$P_1 \to P_3$ transition. We start with the model corresponding to $\alpha_1 = 0.1$ and $\lambda_0 = 0$. This choice of values allows us to recover trajectories that mimic very

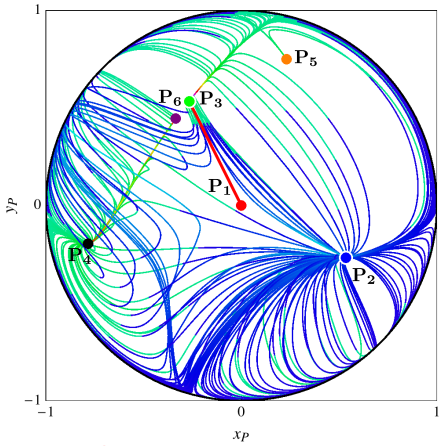

P_1: matter dominated saddle
P_2: stiff matter unstable node
P_3: dark energy stable node
P_4: dark energy attractor $w_{\rm eff} = -7/3$
P_5: stiff matter saddle
P_6: dark energy saddle

(a) The $\alpha_1 = 0.1$, $\lambda_0 = 0$ model.

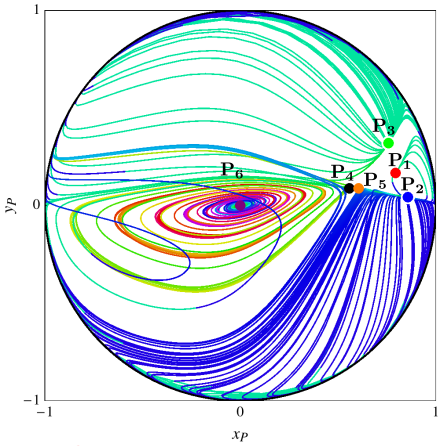

P_1: matter dominated saddle
P_2: stiff matter unstable node
P_3: dark energy attractor
P_4: dark energy saddle, $w_{\rm eff} = -0.7$
P_5: matter scaling saddle, $\Omega_m = 0.04, w_{\rm eff} = -1.7$
P_6: dark energy stable focus, $w_{\rm eff} = -1.7$

(b) The $\alpha_1 = 2.4$, $\lambda_0 = 1.3$ model.

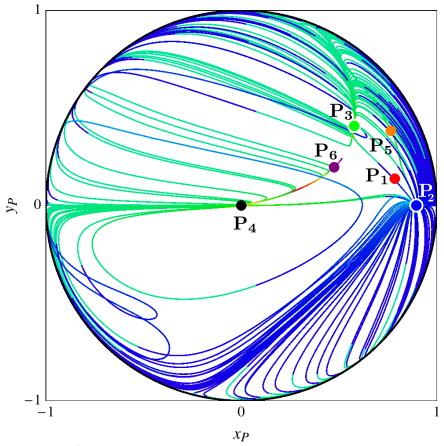

P_1: matter dominated saddle
P_2: stiff matter unstable node
P_3: dark energy attractor
P_4: dark energy attractor, $w_{\rm eff} = -2$
P_5: matter scaling saddle, $\Omega_m = 3.3, w_{\rm eff} = 0.67$
P_6: dark energy saddle, $w_{\rm eff} = -1.3$

(c) The $\alpha_1 = 0$, $\lambda_0 = -1/2$ model.

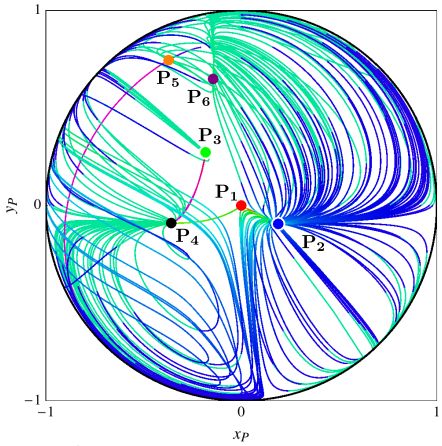

P_1: matter dominated saddle
P_2: stiff matter unstable node
P_3: dark energy saddle $w_{\rm eff} = -1.7$
P_4: dark energy attractor, $w_{\rm eff} = -3.7$
P_5: matter scaling saddle, $\Omega_m = 15, w_{\rm eff} = 2.3$
P_6: dark energy attractor, $w_{\rm eff} = -1$

(d) The $\alpha_1 = -2$, $\lambda_0 = -2$ model.

Figure 7.3: The phase space numerical investigation of different dark energy models for the *first order* system. Initial conditions are evolved both in the past (blue lines) and in the future (green lines). The red line in (a) corresponds to the ΛCDM trajectory. From [9].

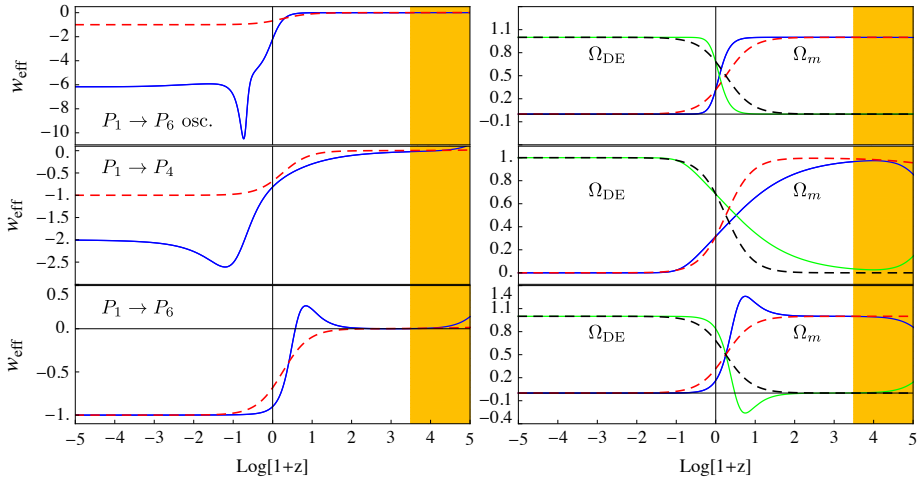

Figure 7.4: The left panel shows the behavior of the effective equation of state for ΛCDM (red dashed line) and three different DE models (blue continuous line) corresponding to different types of trajectories identified in the *first order* system and described in Sec. 7.4.1. The right panel shows the evolution of matter and dark energy densities for the ΛCDM model (respectively the red and black dashed lines) and the different DE models (respectively the blue and green solid lines). The yellow area represents the region in which we expect a non-negligible contribution from radiation which was not considered when constructing these numerical DE models. From [9].

closely the ΛCDM trajectory, shown as a red line in Fig. 7.3a. Notice that for this choice of α_1, λ_0, there is an alternative stable attractor, P_4, which gives a phantom DE. We set initial conditions to reproduce $\Omega_m^0 = 0.31$ and evolve the system to obtain the phase space plot shown in Fig. 7.3a. One can notice that the phase space is dominated in the past by trajectories moving away from the unstable point P_2. These trajectories can be divided in several groups. The first one is made by trajectories that leave P_2 and reach infinity. Obviously these correspond to unphysical solutions since the matter density and/or $w_{\rm eff}$ would go to infinity as well. The second group is made of trajectories that leave P_2 to go to P_3 and exhibit a cosmological behavior that is very similar to the ΛCDM one. The third family of trajectories leave P_2 to go to P_4 that is the phantom DE attractor, while the fourth family of trajectories is made up by solutions that leave infinity and go to P_4 and P_3. It is worth noticing that we find again the $P_2 \to P_1 \to P_3$ transition that we had found for the zero-th order system. In fact, the eigenvector that corresponds to the positive eigenvalue of P_1 is aligned with the eigenvector that corresponds to the negative eigenvalue of P_3 and the same holds for P_1 and P_2. As we already discussed, this gives rise to a family of cosmologically viable trajectories (noticeable in Fig. 7.3a) that move very close to the heteroclinic orbits connecting these points.

$P_1 \to P_6$ transition with oscillations. We now investigate numerically a model which displays a $P_1 \to P_6$ transition with oscillations (Fig. 7.3b). We obtain this behavior by setting $\alpha_1 = 2.4$ and $\lambda_0 = 1.3$. This time we impose initial conditions such that $\Omega_m = 1$ at high redshift (i.e. $z = 1000$), to evolve the

system more into the future than in the past. Doing so, we avoid the dominance of the unstable point P_2 and are able to show a richer set of trajectories in the phase space plot. The most interesting family of trajectories corresponds to trajectories that either start at P_2 or infinity at early times, then pass close to P_1 crossing the $\Omega_m = 1$ plane and then move close to P_4, and start circling toward P_6. The background cosmology of one of such trajectories is shown in Fig. 7.4.

$P_1 \to P_4$ transition. In order to numerically recover a model which displays a $P_1 \to P_4$ transition, we choose $\alpha_1 = -1/2$ and $\lambda_0 = 0$. The points P_1 and P_2 exhibit basically the same behavior as in the previous models, however for the chosen values of α_1, λ_0 both P_3 and P_4 play the role of a dark energy attractor, with different w_{eff}. This time we impose initial conditions to match the matter density today. In Fig. 7.3c we can see as a result that we obtain two different types of trajectories that go from P_1 to P_4. The first set departs from P_2 and, after passing close to the matter saddle point P_1, go to the dark energy attractor P_4. The second one starts at infinity, then passes close to P_1 and eventually moves towards P_4. We plot the cosmological behavior of a trajectory that undergoes this transition in Fig. 7.4.

$P_1 \to P_6$ transition. The last transition we want to discuss corresponds is the $P_1 \to P_6$. In order to obtain trajectories with this behavior we set $\alpha_1 = -2$ and $\lambda_0 = -2$ and impose appropriate initial conditions in order to have equivalence between dark matter and dark energy density at the same redshift as the Planck best fit ΛCDM model [78]. As we can see from the resulting phase space plot in Fig. 7.3d, the system displays a clear transition from P_1 to P_6 for the trajectories that start close to P_2. In Fig. 7.4 we show the cosmological behavior of one of these trajectories.
The selected values for α_1, λ_0, allow also different types of trajectories, as can be read off Fig. 7.2. In particular we can recognize two sets of trajectories that show a P_1 to P_4 transition. The first set of trajectories starts in P_2 and move toward P_1, but are then deviated towards P_4 instead of P_6. The second set of trajectories starts at infinity, approaches P_1 and then moves towards P_4. Noticeably in the phase space plot in consideration (Fig. 7.3d), one can observe non-trivial heteroclinic orbits joining P_1 and P_4, P_4 to P_3 and P_6 to P_5.

In summary, from the numerical investigation of the different transitions, we have learned that in general trajectories that undergo a $P_1 \to P_3$ transition are those that closely resemble the ΛCDM cosmology. Models involving other transitions, such as $P_1 \to P_4$ or $P_1 \to P_6$, display trajectories that are quite different from the ΛCDM one, but still can give viable cosmologies as can be noticed in Fig. 7.4.

7.5 Second order analysis

We now proceed to the second order by allowing both α_0 and α_1 to vary, while fixing α_2 and λ_0 to constant. The models under consideration will then be characterized by

$$\ddot{\Omega}(t) = \ddot{\Omega}_0 a^{-\alpha_2}\,, \qquad c(t) - \Lambda(t) = (c-\Lambda)_0 a^{-\lambda_0}. \tag{7.30}$$

As it can be seen from (7.7), α_2 is the first of the $\alpha's$ that does not enter the core equations (7.7a)-(7.7c); it is therefore from this order on, that we start to observe some of the effects of the recursive nature of Eqs. (7.7d). As we will shortly show, the majority of the critical points for the second order system are just trivial extensions of the critical points of the first order case; they replicate the values for the coordinates $\{x_c, y_c, u_c, \alpha_{0,c}\}$ and come in two copies distinguished by the value of α_1, being it equal or different from zero. The latter difference reflects into a different dynamics for $\Omega(t)$, which can be richer for the points with $\alpha_1 \neq 0$. To highlight this splitting of the points, we shall label with the subscript a the duplicates of the first order critical points that have $\alpha_1 = 0$, and with b the duplicates that have $(\alpha_1 \neq 0)$. This splitting trend will become regular from the next order on and it will help us in Sec. 7.6 for the classification of the points at a generic order N.
The details of all the critical points and their stability are shown in Table 3 in Appendix .1.1. In what follows we briefly comment on the characteristics of the cosmologically interesting points.

- *Matter points*
  There are two critical points that are matter dominated with $w_{\text{eff}} = 0$ and both of them represents the extension to one higher dimension of the P_1 critical point found in the first order analysis. Their coordinates and the eigenvalues of the linearized system are:

$$P_{1a} \equiv (0,0,0,0,0)$$
$$\mu_1 = -3,\ \mu_2 = -1,\ \mu_3 = \frac{3}{2},\ \mu_4 = \frac{3}{2} - \alpha_2,\ \mu_5 = 3 - \lambda_0. \tag{7.31}$$
$$P_{1b} \equiv \left(0,0,0,0,\alpha_2 - \frac{3}{2}\right)$$
$$\mu_1 = -3,\ \mu_2 = -1,\ \mu_3 = 3 - \alpha_2,\ \mu_4 = -\frac{3}{2} + \alpha_2,\ \mu_5 = 3 - \lambda_0. \tag{7.32}$$

  The first one, P_{1a}, is a viable saddle point for $\lambda_0 \neq 3 \wedge \alpha_2 \neq \frac{3}{2}$ while the second one, P_{1b}, is a saddle for $\lambda_0 \neq 0 \wedge \alpha_2 \neq \frac{3}{2} \wedge \alpha_2 \neq 3$. As we can notice the stability requirements are quite mild if compared to the constraints that we found at the previous orders. As a result the vast majority of second order models will have two cosmologically viable matter configurations distinguished by the behavior of $\Omega(t)$. When passing close to P_{1a} models will be characterized by $\ddot{\Omega} \ll \dot{\Omega} \ll \Omega$ which means that the coupling to matter will be frozen at a certain value until the model moves toward dark energy domination. On the other hand the second configuration corresponds to a matter era in which $\Omega(t)$ has a non-trivial dynamics.

- *Stiff-matter points*
  There are two P_2-like critical points with a stiff matter equation of state, $w_{\text{eff}} = 1$:

$$P_{2a} \equiv (1,0,0,0,0)$$
$$\mu_1 = 2,\ \mu_2 = 3,\ \mu_3 = 3,\ \mu_4 = 3 - \alpha_2,\ \mu_5 = 6 - \lambda_0. \tag{7.33a}$$
$$P_{2b} \equiv (1,0,0,0,-3 + \alpha_2)$$
$$\mu_1 = 2,\ \mu_2 = 3,\ \mu_3 = 6 - \alpha_2,\ \mu_4 = \alpha_2 - 3,\ \mu_5 = 6 - \lambda_0. \tag{7.33b}$$

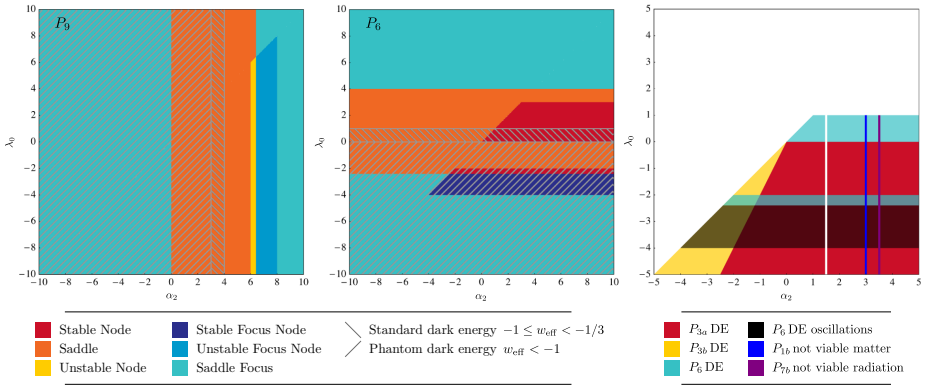

Figure 7.5: The left panel shows the results of the stability analysis of the *second order* system around P_9 (see Appendix .1.1). The panel at the center illustrates the stability of the system around P_6. The right panel shows the combined results of the *second order* analysis. Regions in the (α_2, λ_0) plane which allow the different transitions discussed in Sec. 7.5 are shown in different colors. From [9].

Their unstable configuration, which might be relevant for the early stages of the Universe, can be obtained for $\alpha_2 < 3 \wedge \lambda_0 < 6$ in the case of P_{2a}, and for P_{2b} is $3 < \alpha_2 < 6 \wedge \lambda_0 < 6$ in the case of P_1. Again the two realizations of this point correspond to different behaviors of the conformal coupling $\Omega(t)$.

- *Dark energy points*
  We have also two DE dominated points from the splitting of the first order P_3 point:

$$P_{3a} \equiv \left(\frac{\lambda_0}{6}, 1 - \frac{\lambda_0}{6}, 0, 0, 0\right)$$
$$\mu_1 = \lambda_0 - 6,\ \mu_2 = \lambda_0 - 4,\ \mu_3 = \lambda_0 - 3,\ \mu_4 = \frac{\lambda_0}{2},\ \mu_5 = \frac{1}{2}(\lambda_0 - 2\alpha_2). \tag{7.34}$$

$$P_{3b} \equiv \left(\frac{\lambda_0}{6}, 1 - \frac{\lambda_0}{6}, 0, 0, \alpha_2 - \frac{\lambda_0}{2}\right)$$
$$\mu_1 = \alpha_2 - \frac{\lambda_0}{2},\ \mu_2 = \lambda_0 - 6,\ \mu_3 = \lambda_0 - 3,\ \mu_4 = \lambda_0 - 4,\ \mu_5 = \lambda_0 - \alpha_2. \tag{7.35}$$

They both have $w_{\rm eff} = -1 + \lambda_0/3$ and are cosmologically viable late time DE attractors respectively for $(\alpha_2 \geq 0 \wedge \lambda_0 < 0) \vee (\alpha_2 < 0 \wedge \lambda_0 < 2\alpha_2)$ and for $\alpha_2 < 0 \wedge \lambda_0 > 2\alpha_2 \wedge \lambda_0 < \alpha_2$.
The other viable DE attractor is the second order equivalent of the dark energy dominated P_6 (7.26):

$$P_6 \equiv \left(\frac{\lambda_0}{2}, 1 + \frac{\lambda_0}{2}, 0, -\lambda_0, 0\right)$$
$$\mu_1 = \lambda_0 - 4,\quad \mu_2 = \lambda_0 - \alpha_2,\ \mu_3 = -3 - \frac{3}{4}\lambda_0 + \frac{1}{4}\sqrt{3}\sqrt{48 + 8\lambda_0 - 5\lambda_0^2},$$

$$\mu_4 = \lambda_0 - 3,\ \mu_5 = -3 - \frac{3}{4}\lambda_0 - \frac{1}{4}\sqrt{3}\sqrt{48 + 8\lambda_0 - 5\lambda_0^2}, \tag{7.36}$$

which is an accelerated attractor with a viable equation of state for $(\alpha_2 > 1 \wedge 0 < \lambda_0 < 1) \vee (0 < \alpha_2 \leq 1 \wedge 0 < \lambda_0 < \alpha_2)$. From the full stability graphical analysis, reported in Fig. 7.5, we can notice that this point can be an accelerated attractor for a wider range of (α_2, λ_0), however for some intervals it would have $w_{\text{eff}} < -2$, which is a value already excluded by experiments, e.g. [78], and hence we have considered a more conservative region.

- *Radiation points*
  Two radiation dominated critical points are provided by the splitting of the first order point P_7:

$$P_{7a} \equiv (0, 0, 1, 0, 0)$$
$$\mu_1 = -2,\ \mu_2 = 1,\ \mu_3 = 2,\ \mu_4 = \frac{3}{2} - \alpha_2,\ \mu_5 = 4 - \lambda_0. \tag{7.37a}$$
$$P_{7b} \equiv \left(0, 0, 1, 0, -\frac{3}{2} + \alpha_2\right)$$
$$\mu_1 = -2,\ \mu_2 = 1,\ \mu_3 = \frac{7}{2} - \alpha_2,\ \mu_4 = \alpha_2 - \frac{3}{2},\ \mu_5 = 4 - \lambda_0. \tag{7.37b}$$

  They are a saddle respectively for $\lambda_0 \neq 4 \wedge \alpha_2 \neq \frac{3}{2}$ and $\lambda_0 \neq 4 \wedge \alpha_2 \neq \frac{7}{2} \wedge \alpha_2 \neq \frac{3}{2}$. A viable radiation era can also be provided by P_{10} (see Table 3) which is a radiation-DE scaling critical point. The stability analysis of this critical point is too complicated to be shown because of the complexity of its eigenvalues; nevertheless we can deduce the stability conditions for the configurations of cosmological interest. For instance for $\alpha_2 = \frac{7}{2}$ this point supplies a good radiation dominated point which is a saddle if $\lambda_0 \neq 4$. We cannot instead identify a region of (α_2, λ_0) where this point would provide a viable DE candidate.

Combining the above results, we can see that for the second order system there is a wide variety of possible transitions between viable critical points that will give rise to a working cosmological model. This is somewhat expected given that we are moving up the α channel and allowing more and more general behaviors of the function $\Omega(t)$. The combined results of the second order dynamical analysis are shown in Fig. 7.5. In general the stability requirements for a viable radiation and matter era are much less stringent than those for the first order system. Indeed, except for a discrete set of values of α_2, λ_0, generally there are two points that can give a radiation era, i.e. P_{7a} or P_{7b}, as well as two points that can provide a matter era, i.e. P_{1a} or P_{1b}. The values of α_2 that do not allow either a viable matter or radiation critical point are shown in Fig. 7.5 as, respectively, straight blue and purple lines. A stronger selection of viable regions in the (α_2, λ_0) plane is imposed by requiring that the possible DE points, P_{3a}, P_{3b}, P_6, have a proper cosmology and stability.

7.6 N^{th} order analysis: exploiting the recursive nature of the system

In the previous Sections we performed a dynamical analysis of the system (7.7) cutting the hierarchy of equations (7.7d) at increasingly higher orders, up to the second, while keeping λ_0 constant. At each order we determined the critical points, their stability and cosmological features. The reason for treating separately the zero, first and second order is twofold. First, it allows us to study gradually more and more general models, recognizing at each order some characteristic features and cosmological viability conditions. Second, since α_2 is the first of the $\alpha's$ not to enter the core equations (7.7a)-(7.7c), we expect that from the third order up the system will display a regular pattern in the critical points that reflects the recursive structure of the equations (7.7d). We saw glimpses of this pattern already in the second order system in 7.5, but it is not until we have $N \geq 3$ that it displays fully. We will now exploit this feature to reconstruct the dynamical properties of the system at any given order $N \geq 3$, building on the findings of the lower order analyses. We neglect radiation for simplicity (our results can be easily extended to include it), so we are left with an $N+2$ dimensional system for the variables $\{x, y, \alpha_0, \alpha_1, \ldots, \alpha_{N-1}\}$. When writing the coordinates of the critical points we use the general structure $(x_c, y_c, \alpha_{0,c}, \alpha_{1,c}, \alpha_{n,c})$, with $n = 2, .., N-1$, which allows us to treat separately α_0, α_1 from α_n with $n \geq 2$, given that the former enter the core equations (7.7a)-(7.7c) and do not obey the general rules that we are about to derive.

By looking at system (7.7), one notices that the set of variables $\{x, y, \alpha_0\}$ depends on the α_n, $n \geq 2$, only through α_1. We can therefore use α_1 as a pivot variable and split the original system into two blocks: the block of equations (7.7a), (7.7b), (7.7d) with $n = 1$ and the block of equations (7.7d) with $n \geq 2$. We start by solving the equations of the first block, and determine solutions for $(x_c, y_c, \alpha_{0,c})$ as functions of α_1. We then turn to the second block and notice that one can generally distinguish two cases: those characterized by $\alpha_{1,c} = 0$ and those with $\alpha_{1,c} \neq 0$. In the former case, the two blocks are independent, while in the latter all the coordinates of the critical points will be affected by the equations of the second block. The general structure of the points for which $\alpha_1 = 0$ can then be recovered as follows. One starts solving the first block of equations, which can be done quite straightforwardly, to determine $\{x_c, y_c, \alpha_{0,c}\}$. Then one turns the attention to the second block, with $n \geq 3$ since $\alpha_{1,c} = 0$, and finds that there are three types of general solutions for this block: one in which all $\alpha_{n,c} = 0$, the second where all $\alpha_{n,c} \neq 0$ and the last case in which there will be different combinations of $\alpha's$ equal or not to zero (hence the name *combinations* in what follows). A combination is specified by the location of all the zero terms; once these are given, the values of the $\alpha's \neq 0$ are uniquely determined and can be reconstructed, after some lengthy algebra, solving the corresponding equations. Let us illustrate the general rules for the specific expressions of the non-zero $\alpha's$, by using the following representative *combination*:

$$\alpha_{n,c} \equiv (\underbrace{0, \ldots, 0}_{\text{block}=0}, \underbrace{\alpha_{q,c}, \ldots \alpha_{j,c} \ldots, \alpha_{s,c}}_{\text{block}\neq 0,\ j=q,\ldots s}, \underbrace{0, \ldots, 0}_{\text{block}=0},$$

$$\underbrace{\dots \alpha_{j,c} \dots}_{\text{block} \neq 0}, \underbrace{0, \dots, 0}_{\text{block} = 0}, \underbrace{\alpha_{k,c}, ...\alpha_{l,c}..., \alpha_{N-1,c}}_{\text{block} \neq 0,\ l=k,\dots,N-1}). \tag{7.38}$$

The elements in the non-zero blocks which are followed by a zero block have:

$$\alpha_{j,c} = (s+1-j)\frac{\dot{H}}{H^2}, \tag{7.39}$$

where $q \leq j \leq s$, with α_q being the first non-zero term in the block and α_s the last one. The particular *combination* shown in (7.38) ends with a non-zero block; the elements of such a block obeys the following specific rule:

$$\alpha_{l,c} = \alpha_N + (N-l)\frac{\dot{H}}{H^2}, \tag{7.40}$$

where $k \leq l \leq N-1$, with α_k being the first non-zero term in the block. Every time we substitute into (7.39) and (7.40) the specific value of $\dot{H}/H^2(x_c, y_c, \alpha_{0,c}, \alpha_{1,c})$ that corresponds to the point in consideration.

The solutions for which the variable α_1 assumes a non-zero value are a little trickier to treat as the components $(x_c, y_c, \alpha_{0,c})$ of the critical points will be affected by the equations of the second block, we find that also in this case the critical points can generally be separated in the three above cases based on the structure of the α_n, $n \geq 2$, block for which the general rules (7.39)-(7.40) still apply.

Using the above technique we are able to reconstruct all the critical points of system (7.7) at a given order N. In particular, we find that they can be organized in families characterized by the same cosmological behavior. These families, in most of the cases, can be directly connected to the critical points that we have analyzed in the previous Sections, as expected because of the structure of our system and its invariant manifolds (as mentioned at the end of the introductory part of Sec. 7.1). Therefore one can identify the main critical points of cosmological interest, or in other words get a good sense of the cosmologies encoded in the EFT formalism, already at the lower orders. Going to higher orders allows to analyze more and more general models.

In what follows we describe only the families of critical points that allow for a viable cosmology, leaving the discussion of the remaining critical points for Appendix .1.2. We generally indicate with s the position of the last term in a non-zero block within the combination, and with k the position of the first non-zero term in the last non-zero block that, for some cases, closes the combination.

- *Matter points:*
  This family includes 2^{N-1}, P_1-like, critical points characterized by a well defined cosmology ($\Omega_m = 1$):

$$P_{1a} \equiv (0,0,0,0,\alpha_{n,c}=0), \tag{7.41a}$$

$$P_{1b} \equiv \left(0,0,0,\alpha_N - \frac{3}{2}(N-1), \alpha_{n,c} = \alpha_N - \frac{3}{2}(N-n)\right), \tag{7.41b}$$

$$P_{1c} \equiv (0,0,0,\text{combinations}). \tag{7.41c}$$

  The latter point includes all $(2^{N-1}-2)$ possible combinations constructed via Eqs. (7.39) and (7.40) with $\dot{H}/H^2 = -1$. All critical points correspond to

matter domination, therefore, instead of performing the full stability analysis, we simply determine the intervals for which they are saddle points. The eigenvalues of the linearized system around P_{1a} and P_{1b} are:

$$P_{1a}: \mu_1 = -3,\ \mu_2 = \frac{3}{2} - \alpha_N,\ \mu_3 = 3 - \lambda_0,\ \mu_4 = \cdots = \mu_{N-1} = \frac{3}{2}, \quad (7.42a)$$

$$P_{1b}: \mu_1 = -3,\ \mu_2 = \frac{3}{2}N - \alpha_N,\ \mu_3 = 3 - \lambda_0,$$
$$\mu_4 = \cdots = \mu_{N-1} = \alpha_N - \frac{3}{2}(N-h), \quad (7.42b)$$

where $h = 1, .., N-1$. As we can see these points have only one possible stability configuration having two eigenvalues of opposite sign, therefore as long as they are hyperbolic they are saddles. The first one is hyperbolic if $\lambda_0 \neq 3$ and $\alpha_N \neq 3/2$ while for the second one we should have $\alpha_N \neq \frac{3}{2}(N-h)$, $\alpha_N \neq \frac{3}{2}N$ and $\lambda_0 \neq 3$. As for the last sub-family of critical points, P_{1c}, the analysis of the eigenvalues reveals that this is a set of saddle points regardless of the particular combination as for each combination at least two eigenvalues have opposite sign. Despite the complexity of the structure of the combinations, we are able to determine that all of them are hyperbolic if: $\lambda_0 \neq 3$ and $\alpha_N \neq \frac{3}{2}(N-h)$ with $h = 1, \ldots, N-1$.

- *Stiff-matter points:*

$$P_{2a} \equiv (1, 0, 0, 0, \alpha_{n,c} = 0), \quad (7.43a)$$
$$P_{2b} \equiv (1, 0, 0, \alpha_N - 3(N-1), \alpha_{n,c} = \alpha_N - 3(N-n)), \quad (7.43b)$$
$$P_{2c} \equiv (1, 0, 0, \text{combinations}),\ \alpha_{j,c} = -3(s+1-j)\ ,\ \alpha_{l,c} = \alpha_N - 3(N-l). \quad (7.43c)$$

The points in this family have $\Omega_{\rm DE} = 1$ and $w_{\rm eff} = 1$, therefore representing a set of 2^{N-1} stiff-matter critical points. The structure and the cosmology of these critical points suggest a similarity with the P_2 critical point we analyzed in the previous Sections. These critical points could be of interest in the early stages of the Universe as unstable critical points [194], which is the only configuration we analyze in what follows. The first two critical points have eigenvalues:

$$P_{2a}: \mu_1 = 3 - \alpha_N,\ \mu_2 = 6 - \lambda_0,\ \mu_3 = \mu_4 = \cdots = \mu_{N-1} = 3, \quad (7.44a)$$

$$P_{2b}: \mu_1 = 3,\ \mu_2 = 3N - \alpha_N,\ \mu_3 = 6 - \lambda_0,$$
$$\mu_4 = \cdots = \mu_{N-1} = \alpha_N - \frac{3}{2}(N-1-h), \quad (7.44b)$$

where $h = 1, .., N-1$. The first critical point is unstable for $\alpha_N < 3 \wedge \lambda_0 < 6$ while the unstable configuration of the second one is obtained if $3/2\,(N-2) < \alpha_N < 3N \wedge \lambda_0 < 6$. For the last sub-family, P_{2c}, there is only one combination which shows an unstable configuration and it is the one with $\alpha_1 = 0$ and $\alpha_{n,c} \neq 0$ for $n = 2, \ldots, N-1$ which is unstable if $\lambda_0 < 6 \wedge 3 < \alpha_N < 3(N-1)$. Most of the other combinations are saddle points.

- *Dark Energy points:*

$$P_{3a} \equiv \left(\frac{\lambda_0}{6}, 1-\frac{\lambda_0}{6}, 0, \alpha_{n,c}=0\right), \tag{7.45a}$$

$$P_{3b} \equiv \left(\frac{\lambda_0}{6}, 1-\frac{\lambda_0}{6}, 0, \alpha_N-\frac{\lambda_0}{2}(N-1), \alpha_{n,c}=\alpha_N-\frac{\lambda_0}{2}(N-n)\right), \tag{7.45b}$$

$$P_{3c} \equiv \left(\frac{\lambda_0}{6}, 1-\frac{\lambda_0}{6}, 0, \text{combinations}\right),$$
$$\alpha_{j,c}=-(s+1-j)\frac{\lambda_0}{2}\ ,\ \alpha_{l,c}=\alpha_N-\frac{\lambda_0}{2}(N-l). \tag{7.45c}$$

This family corresponds to a set of 2^{N-1} DE dominated critical points with $\Omega_{\text{DE}}=1$ and $w_{\text{eff}}=\frac{\lambda_0}{3}-1$. From the structure of these points we can immediately recognize a similarity with the P_3 critical point analyzed in the previous Sections. We are interested in the stable configuration for this family. The eigenvalues of the system around the first two points are:

$$P_{3a}: \mu_1=\lambda_0-6,\ \mu_2=\lambda_0-3,\ \mu_3=\frac{\lambda_0}{2}-\alpha_N,\ \mu_4=\cdots=\mu_{N-1}=\frac{\lambda_0}{2}, \tag{7.46a}$$

$$P_{3b}: \mu_1=\lambda_0-6,\ \mu_2=\lambda_0-3,\ \mu_3=\frac{\lambda_0}{2},$$
$$\mu_4=\cdots=\mu_{N-1}=\frac{\lambda_0}{2}+\alpha_N-\frac{3}{2}(N-h+1), \tag{7.46b}$$

where $h=1,\ldots,N-1$. The stability analysis reveals that P_{3a} is a stable accelerated attractor if $(\alpha_N>0\wedge\lambda_0<0)\vee(\lambda_0<2\alpha_N\wedge\alpha_N\leq 0)$ while P_{3b} displays this cosmological behavior if $(\lambda_0<0\wedge\alpha_N\leq 3)\vee(\alpha_N>3\wedge\lambda_0<6-2\alpha_N)$. The last sub-family P_{3c} does not contain any stable solution, and as a consequence will be not further considered.

The points discussed above represent all the hyperbolic, cosmologically viable, critical points of the system (7.7) at a given order $N\geq 3$ (with $\lambda_0=$ constant). Since we neglected radiation, the families of critical points which are of cosmological interest and that can be used to construct transitions from a matter era to a DE one are, respectively, the P_1-like and P_3-like family. Each family contains several critical points, therefore there are many possible specific transitions; in particular at a given order N, there are 2^{N-1} matter points and 2 DE points. Analogously to what happens in the second order case, the intervals of cosmological viability for (α_N,λ_0) are strongly influenced by the stability requirements of the DE points, while the requirements for a good matter era are significantly easier to satisfy, and only exclude some values. Once one selects the values of (α_N,λ_0) according to the intervals reported above, the trajectories of the dynamical system will generally start at early times in the neighborhood of a P_2-like unstable node then approach a P_1-like matter point, finally moving away from it heading towards a P_3-like de-Sitter attractor. Different trajectories will correspond to different behaviors of the EFT functions $\Omega(t)$ and $c(t)$. Let us conclude pointing out that viable transitions have $\lambda_0<0$, which implies that $c(t)-\Lambda(t)$ will be a growing function of time for all viable trajectories at the N^{th} order.

7.7 Chapter Summary

In this chapter we performed a thorough dynamical analysis of the background cosmology within the EFTof DE/MG formalism [162, 163]. In particular we investigated general conditions of cosmological compatibility for the three functions of time that describe the background dynamics in this formalism (EFT functions). While the system of equations is underdetermined, we identified a set of variables that allows one to transform it into an infinite-dimensional system characterized by an important recursive structure. We then studied several autonomous cases of increasingly higher dimension corresponding to more and more general models of dark energy and modified gravity within the EFT framework. Furthermore, exploiting the recursive nature of the full system of equations, as well as our findings at the lower orders, we drew some general conclusions on its dynamics and cosmological behavior.

Our set of dynamical variables contains two infinite series of variables α_n and λ_m, defined as ratios of subsequent derivatives of, respectively, the EFT functions $1+\Omega$ and $c-\Lambda$, (7.6). These variables are such that their corresponding equations assume a hierarchical structure, that we exploit throughout the paper. One can truncate these series at any desired order, and study the corresponding autonomous system. We focused on the α channel, keeping always λ_0 constant. In other words, we focused on the class of models for which $c-\Lambda$ is a power law in the scale factor, while the conformal factor Ω can be increasingly general as we go up with the order. Alternatively one could fix Ω to a constant and open the λ channel, which would correspond to exploring all minimally coupled models of DE. Finally, one could work with both channels and, for instance, explore, within this parametrized framework the full class of Horndeski theories [192]. While we leave the former for future work, we want to stress that the machinery set up in this paper is general and easily applicable to the other cases mentioned above.

As we showed in (7.12), our set up allows us to find a general expression for Ω consisting, at a given order N, of a Taylor expansion of order $N-1$ in time and the corresponding remainder that is parametrized in terms of α_N. Since we include the remainder, increasing the order of the analysis is not a matter of increasing the precision of the Taylor expansion but rather it allows the investigation of a wider class of models of dark energy and modified gravity with the most diverse coupling. An analogous argument could be repeated for $c-\Lambda$.

Focusing on the α variables, while keeping λ_0 constant, we analyzed the system at increasingly higher order. At each order we found the critical points and analyzed their stability and cosmological nature, determining regions in the plane (α_N, λ_0) which allow for viable cosmological trajectories. The simplest case we analyzed was the zero-th order one, obtained setting α_0 to constant. It corresponds to a power law behavior for the EFT functions. After finding the critical points, we performed a stability analysis and determined the cosmology of each point as function of α_0, λ_0. The general result of the zero-th order analysis is that viable cosmological models can be recovered setting $\alpha_0 = 0$ and $\lambda_0 \approx 0$ and there is really only one viable transition between cosmologically interesting critical points. Given that $\alpha_0 = 0$, the corresponding models will be characterized by a constant conformal factor Ω, which is just a rescaling of

the Planck mass. In Sec. 7.3.1 we showed how these findings, projected onto models of quintessence, imply that a quintessence model with a potential which is a power law in the scale factor, cannot have a power law behavior for Ω and therefore, at this order is forced to be minimally coupled. We then proceeded with the analysis of the first and second order systems, finding, as expected, a richer set of cosmologies. We identified respectively the (α_1, λ_0) and (α_2, λ_0) regions which result in cosmologically compatible EFT functions.

At the second order we started to notice some reflections of the recursive nature of the equations for the $\alpha's$. In particular, we found that the majority of the critical points for the second order system are just trivial extensions of the critical points of the first order case, that come in two copies with similar cosmology but a different dynamics of the conformal factor $\Omega(t)$. The recursive nature of the dynamical system fully displays when $N \geq 3$, which is part of the reason why we treated separately the zero, first and second order cases. In Sec. 7.6 we showed how to exploit this recursive feature to reconstruct the critical points, their stability and their corresponding cosmological dynamics at any given order $N \geq 3$. We identified regions in $(\alpha_N,\ \lambda_0,\ N)$ space that allow compatible forms of the EFT functions; in particular, all viable models correspond to a function $c - \Lambda$ that grows in time.

Our methodology offers a general tool to perform the dynamical analysis of dark energy and modified gravity models within the EFT language.

Chapter 8

Implementation in CAMB

We implemented the EFT approach to DE/MG in the public Einstein-Boltzmann solver CAMB: *Code for Anisotropies in the Microwave Background* [104]. The resulting code, which we dub EFTCAMB, is a powerful and versatile tool that can be used for several objectives. It can be employed to evolve the full dynamics of linear scalar perturbations of a broad range of single field dark energy and modified gravity model, once the model of interest is mapped into the EFT formalism. It offers a numerical implementation of EFT as a model-independent framework to test gravity on cosmological scales.

In this chapter we review the implementation of the EFT formalism in CAMB and we show the reliability and applicability of our code by evolving the dynamics of linear perturbations and extracting predictions for power spectra in different models. In particular we extract predictions for linear observables in some parametrized EFT models with a phantom-divide crossing equation of state for dark energy.

One of the virtue of the EFTCAMB code is that it does not rely on any quasi-static (QS) approximation but still allows for the implementation of specific single field models of DE/MG. When fitting to data or performing forecasts for upcoming surveys, one generally focuses on sub-horizon scales and neglects the time derivatives of the gravitational potentials and scalar fields w.r.t. their spatial gradients, i.e. one assumes the QS regime. In Fourier space, this brings the Einstein and scalar field equations to an algebraic form and simplifies significantly both the theoretical and the numerical setup. While the QS description of the growth of structure generally might give a good representation of the evolution on sub-horizon scales (see e.g. [195] for an analysis in $f(R)$ gravity), it might loose out on some dynamics at redshifts and scales that would leave an imprint within the reach of some ongoing and upcoming surveys [196, 197].

At the level of model-independent tests of gravity, implementations that do not employ the QS approximation are the Parametrized Post-Friedmann (PPF) modules of [119, 198] as well as MGCAMB [199, 200]. The former uses a full set of equations for all linear scales, obtained by the interpolation between the super-horizon and the QS regime and it relies on three free functions and one parameter; however, in order to study specific models, one needs to work out interpolations and fits to the these functions and parameters for each case. The

latter relies on a generic parametrization of the Poisson and anisotropy equation to form a complete and general set of equations for all linear scales, allowing for model-independent analysis of modified growth such as those of [137, 126, 147]; however, one has to restrict to the QS regime in order to study a specific model. We shall mention also ISiTGR [135, 139], which is an integrated set of modified modules for use in testing whether observational data are consistent with general relativity on cosmological scales.

Our code solves the full Klein-Gordon equation for the Stückelberg field, as opposed to macroscopic hydrodynamic/fluid treatments [141, 201, 202]. This allows us to maintain an approach which is closer to the true nature of the theory as well as to have a direct control and easier interpretation of the possible instabilities related to this d.o.f. as we discuss in Sec. 6.5. Furthermore, with our method we can easily evolve perturbations in models that cross the phantom-divide, as we will illustrate in Sec. 8.4.

In this chapter we focus on the prediction of cosmological observables of interest for ongoing and upcoming surveys, in particular showing outputs of our code for the CMB temperature-temperature auto-correlation, the CMB lensing potential auto-correlation, the cross-correlation between temperature and lensing potential for the CMB and the matter power spectrum. In particular we study cosmological predictions for a ghost-free power law parameterizations of the EFT background functions that display a phantom-divide crossing background.

We refer the reader to Part III for a discussion of the specific models that have been implemented in EFTCAMB, their phenomenology and observational constraints.

8.1 Code implementation of the background cosmology

In this section we focus on the treatment of the cosmological background for *pure* EFT models. In this approach we fix the expansion history to the desired one. We can then use Eqs. (6.5)-(6.6) to determine two of the EFT background functions $\{\Omega, \Lambda, c\}$ in terms of the third one. It turns out to be convenient to solve for c and Λ in terms of Ω:

$$c = -\frac{m_0^2\ddot{\Omega}}{2a^2} + \frac{m_0^2\mathcal{H}\dot{\Omega}}{a^2} + \frac{m_0^2(1+\Omega)}{a^2}(\mathcal{H}^2 - \dot{\mathcal{H}}) - \frac{1}{2}(\rho_m + P_m), \quad (8.1)$$

$$\Lambda = -\frac{m_0^2\ddot{\Omega}}{a^2} - \frac{m_0^2\mathcal{H}\dot{\Omega}}{a^2} - \frac{m_0^2(1+\Omega)}{a^2}(\mathcal{H}^2 + 2\dot{\mathcal{H}}) - P_m. \quad (8.2)$$

We then use the EFT designer approach discussed above to get c, Λ and either (6.10) or the prescription described below (see Eq. (8.5)) to get the Q quantities.

For the actual implementation of the *pure* EFT cases, we fix the expansion history to

$$\mathcal{H}^2 = \frac{8\pi G}{3}a^2(\rho_m + \rho_{\rm DE}), \quad (8.3)$$

with

$$\rho_{\rm DE} = 3H_0^2 M_P^2 \Omega_{\rm DE}^0 \exp\left[-3\int_1^a (1+w_{\rm DE}(a'))\, d\ln a'\right], \tag{8.4}$$

where $w_{\rm DE}$ represents the equation of state of the effective dark energy component and can be set accordingly to the model that one wants to study. In particular we will consider the following three cases:

- $w_{\rm DE} = -1$, corresponding to a ΛCDM expansion history;

- $w_{\rm DE} = \text{const} \neq -1$, we will refer to this case as wCDM;

- $w_{\rm DE}(a) = w_0 + w_a(1-a)$, i.e. the CPL parametrization [203, 204], where w_0 and w_a are constant, respectively the value and the derivative of $w_{\rm DE}$ today.

Other parametrizations for the DE EoS are available in the EFTCAMB code and are covered in Appendix .2.5.

From a comparison of (6.8), (6.9) with (8.3), (8.4), one obtains the following correspondence:

$$\begin{aligned} \rho_Q &= (1+\Omega)\,\rho_{\rm DE} + \Omega\rho_m\,, \\ P_Q &= (1+\Omega)\,P_{\rm DE} + \Omega P_m\,. \end{aligned} \tag{8.5}$$

After fixing $w_{\rm DE}$, we use (8.5) to determine the Q quantities; we then choose an $\Omega(\tau)$ and use (8.1) and (8.2) to get c and Λ. Let us note that the quantity $\rho_{\rm DE}$ represents one possible way of modeling the contribution of the dark component, alternative to the quantity ρ_Q introduced above. The Q and DE quantities coincide in the case $\Omega = 0$, i.e. when the dark sector is minimally coupled to gravity. However, when $\Omega \neq 0$, Eq. (6.10) gives a more proper representation of the effective scalar d.o.f. of the dark sector, taking into account the coupling to matter and the corresponding exchange of energy between the dark and the matter sectors. In fact, the continuity equation (6.11) and that one for (8.4) coincide when $\dot{\Omega} = 0$, while for $\dot{\Omega} \neq 0$ the density ρ_Q receives an extra contribution from the coupling to matter. We choose to formulate the designer approach for our code in terms of $(\rho_{\rm DE}, w_{\rm DE})$, which allows for a more direct implementation of the background cosmology in CAMB. However, we express the equations for linear perturbations in terms of the Q quantities, as it is usually done in the EFT framework, since those better represent the contributions to the evolution of perturbations from the EFT dark component.

While in the linearly perturbed equations of next Section we keep c and the Q quantities, we implicitly assume that once the background is fixed, those will be expressed in terms of the expansion history and Ω via a combination of (8.1), (8.2) and (8.5) for the *pure* EFT cases.

8.2 Numerically Evolving Perturbations

After the expansion history is sorted out the EFTCAMB code solves consistently perturbations around the given background, following Section 6.4.

In our numerical setup, we set the standard initial conditions for matter components and curvature perturbations in the radiation dominated epoch, at

a time when the corresponding momentum mode re-enter the horizon. For the Stückelberg field instead, we set initial conditions at a later time, corresponding to $a_\pi = 0.01$. The reasons for this choice are several. First of all, we are interested in the late time accelerating universe and we typically want our theory to reproduce standard GR at early times ($a < a_\pi$). In other words, we expect the Stückelberg field not to be excited at early times. This fact also makes initial conditions for this scalar field less motivated at deep redshift, when the other matter components initial conditions are instead well defined. Finally, from the numerical point of view, the system is more easily controlled since, not evolving the π equation at early times, we avoid some potential high frequency dynamics that would make the integration time longer, while keeping track of the underlying mode of evolution of the scalar field. Indeed, since the equation of motion for the Stückelberg field, (6.19), is coupled to metric and matter perturbations, which behaves as an external driving source, we set the π field to trace the dynamics of the source at times earlier than a_π. In this way we can get regular and proper initial conditions for the π field at a_π, while avoiding potential high frequency dynamics around the underlying growing mode which anyhow are not expected to leave imprints on physical observables.

8.3 Cosmological Observables

In view of using our code to test gravity with upcoming and future cosmological surveys, the observables of interest are all the two-point auto- and cross-correlations between Weak Lensing, Galaxy Clustering and the CMB. In this section we show outputs of our code for the temperature-temperature auto-correlation, the CMB lensing potential auto-correlation, the cross-correlation between temperature and lensing potential for the CMB and the matter power spectrum.

It is expected that the dynamics of the Stückelberg field will mainly affect the time evolution of the metric potentials and matter perturbations at late times. Therefore we expect to see the more noticeable effects in observables such as the ISW effect of the CMB and WL. The former is a secondary anisotropy induced by the time evolution of the Weyl potential ($\psi \equiv (\Phi + \Psi)/2$ in Newtonian gauge [1]) at late times. The latter involves the distortion of light rays when they pass close to clustering objects, such as galaxies and clusters; it is sourced by the spatial gradients of the Weyl potential. During the accelerated epoch, no significant polarization modes of the CMB photon are generated, therefore we will not consider them here.

The CMB temperature angular spectrum can be computed via the line of sight integration method [205]

$$C_\ell^{TT} = (4\pi)^2 \int \frac{\mathrm{d}k}{k}\, \mathcal{P}(k) \left|\Delta_\ell^{\mathrm{T}}(k)\right|^2, \tag{8.6}$$

where $\mathcal{P}(k) = \Delta^2_{\mathcal{R}}(k)$ is the primordial power spectrum and the radiation trans-

[1] where we assume the following convention for the Newtonian gauge: $\mathrm{d}s^2 = a^2(\tau)[-(1+2\Psi)\mathrm{d}\tau^2 + (1-2\Phi)\mathrm{d}x^2]$. The gauge transformations between Newtonian and synchronous gauges are given by: $\Psi = \dot{\sigma}_* /k + \mathcal{H}\sigma_*/k$, $\Phi = \eta - \mathcal{H}\sigma_*/k$.

fer function

$$\Delta_\ell^T(k) = \int_0^{\tau_0} \mathrm{d}\tau \; e^{ik\mu(\tau-\tau_0)} S_\mathrm{T}(k,\tau) j_\ell[k(\tau_0-\tau)] \tag{8.7}$$

is sourced by

$$\begin{aligned} S_\mathrm{T}(k,\tau) =& e^{-\kappa}\left(\dot\eta + \frac{\ddot\sigma_*}{k}\right) + g\left(\Delta_{\mathrm{T},0} + 2\frac{\dot\sigma_*}{k} + \frac{\dot v_\mathrm{B}}{k} + \frac{\Pi}{4} + \frac{3\ddot\Pi}{4k^2}\right) \\ &+ \dot g\left(\frac{\sigma_*}{k} + \frac{v_B}{k} + \frac{3\dot\Pi}{4k^2}\right) + \frac{3}{4k^2}\ddot g\Pi \,, \end{aligned} \tag{8.8}$$

where τ_0, μ, κ, g, $\Delta_{\mathrm{T},0}$, v_B and Π are, respectively, the present conformal time, angular separation, optical depth, visibility function, intrinsic CMB density perturbations at the last scattering surface, velocity of baryonic matter and total anisotropic stress of normal matter (which includes CMB photons, massless/massive neutrino). Since the recombination of electrons and protons happens very fast, the visibility function g peaks sharply at that early moment, so we do not expect the Stückelberg field to affect the terms proportional to the visibility function and its derivatives. As already discussed, the only relevant term of (8.8) for our analysis is the ISW one, which can be expressed as follows:

$$\begin{aligned} \ddot\sigma_* + k\dot\eta =& -2\mathcal{H}\dot\sigma_* - 2\dot{\mathcal{H}}\sigma_* + \frac{v_m}{1+\Omega}\frac{a^2(\rho_m+P_m)}{m_0^2} - \frac{1}{k(1+\Omega)}\frac{d}{d\tau}\left(\frac{a^2P}{m_0^2}\Pi\right) \\ &+ \frac{k\pi}{1+\Omega}\frac{a^2(\rho_Q+P_Q)}{m_0^2} + \frac{\dot\Omega}{1+\Omega}\left[k\mathcal{H}\pi - \dot\sigma_* + \frac{1}{k(1+\Omega)}\frac{a^2P}{m_0^2}\Pi\right]. \end{aligned} \tag{8.9}$$

(8.10)

As for WL, we calculate its angular power spectrum following the convention of [206]:

$$C_\ell^{\psi\psi} = 4\pi \int \frac{\mathrm{d}k}{k}\mathcal{P}(k)\left[\int_0^{\chi_*} \mathrm{d}\chi \; S_\psi(k;\tau_0-\chi) j_\ell(k\chi)\right]^2, \tag{8.11}$$

where the source S_ψ is given in terms of the transfer function of the Weyl potential ψ, i.e.:

$$S_\psi(k;\tau_0-\chi) = 2T_\psi(k;\tau_0-\chi)\left(\frac{\chi_*-\chi}{\chi_*\chi}\right), \tag{8.12}$$

$$\begin{aligned} T_\psi(k,\tau) =& \frac{\dot\sigma_* + k\eta}{2} \\ =& \frac{1}{2}\left[-2\mathcal{H}\sigma_* + 2k\eta - \frac{1}{k(1+\Omega)}\frac{a^2P}{m_0^2}\Pi - \frac{\dot\Omega}{1+\Omega}(\sigma_* + k\pi)\right]. \end{aligned} \tag{8.13}$$

Conventionally, the line of sight integral in the lensing source is expressed in terms of comoving distance χ. Here χ_* is the comoving distance of the source objects. Since ISW and WL are sourced by the same potential, one being

sensitive to time derivatives and the other to spatial gradients of the Weyl potential, it is expected that the two effects are strongly correlated and this correlation produces a non-zero cross-spectrum $C_\ell^{\mathrm{T}\psi}$ [207]:

$$C_\ell^{\mathrm{T}\psi} = 4\pi \int \frac{\mathrm{d}k}{k}\mathcal{P}(k)\Big\{ \int_0^{\tau_0} \mathrm{d}\tau\ e^{ik\mu(\tau-\tau_0)}e^{-\kappa}(\dot{\Phi}+\dot{\Psi})j_\ell\Big[k(\tau_0-\tau)\Big]\times \int_{\tau_*}^{\tau_0} \mathrm{d}\tau S_\psi(k;\tau)j_\ell\Big[k(\tau_0-\tau)\Big]\Big\}\,, \tag{8.14}$$

with τ_* denoting for the conformal time at recombination.

Finally, the matter power spectrum can be computed via

$$P(k) = \frac{2\pi^2}{k^3}\mathcal{P}(k)\Delta_{\mathrm{T}}(k)^2, \tag{8.15}$$

with the matter transfer function defined as [208]

$$\Delta_{\mathrm{T}}(k) = \frac{\delta_m(k,z=0)\delta_m(0,z=\infty)}{\delta_m(k,z=\infty)\delta_m(0,z=0)}\,, \tag{8.16}$$

which describes the evolution of matter density perturbations through the epochs of horizon crossing and radiation/matter transition. A proper calculation of $\Delta_{\mathrm{T}}(k)$ requires that in our code we take all types of non-relativistic matter into account, and follow the growth of each mode outside and inside the horizon.

8.4 Some Numerical Results

In this Section we showcase the reliability and scope of EFTCAMB by commenting on some numerical results. While we have all the necessary ingredients to consider models which involve also second order operators in action (6.1), for the numerical analysis of this section we focus on the cases that involve only the background operators. The examples that we present should convey the wide range of applicability of our code.

EFTCAMB can, in fact, be used to fulfill the true purpose the EFT formalism has been envisaged for, i.e. a framework for model-independent tests of gravity on cosmological scales. To this extent, presumably one fixes the expansion history as discussed in [162, 163] and briefly reviewed in Sec. 6.3, and then focuses on the dynamics of cosmological perturbations studying the effects of the different operators in action (6.1). In this case it is necessary to select some parametrization for the functions of time multiplying the operators under consideration. Restricting to the background operators, we show the outputs for power law parameterization of the remaining EFT free function $\Omega(a)$ with a phantom-divide crossing background.

Throughout this section we will always use the following cosmological parameters: $H_0 = 70\,\mathrm{Km/s/Mpc}$, $\Omega_b = 0.05$, $\Omega_c = 0.22$, $T_{\mathrm{CMB}} = 2.7255\,\mathrm{K}$.

On the lines of Sec. 6.3 for the *pure* EFT cases, we fix the desired expansion history and we make a choice for $\Omega(a)$, deriving the remaining quantities from the EFT designer procedure.

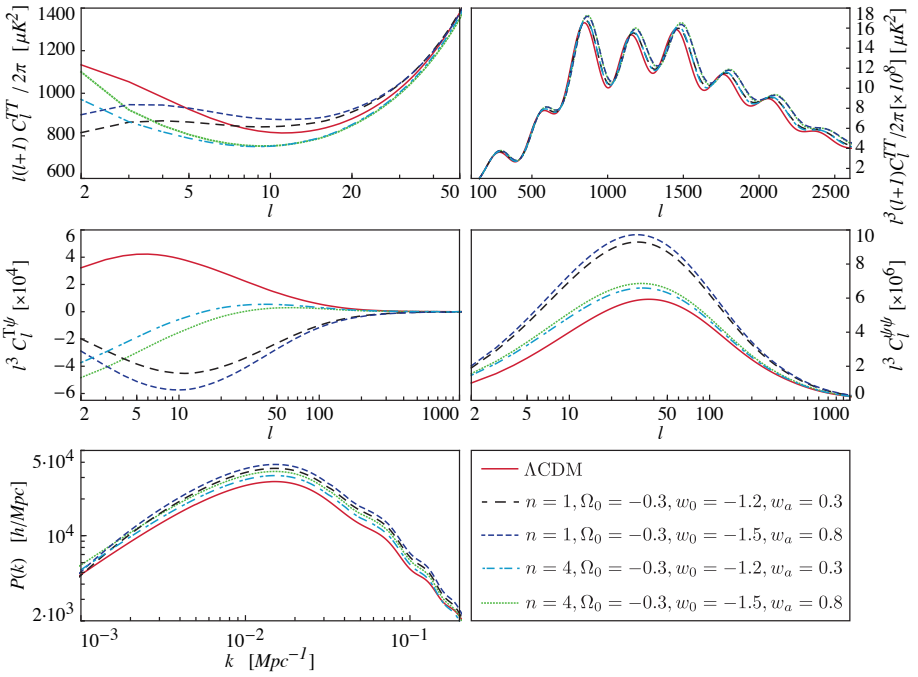

Figure 8.1: Power spectra of several cosmological observables for parametrized EFT models with a phantom-divide crossing background. The red solid line represents predictions for the ΛCDM model. Dashed lines portray models corresponding to several choices of parameters defining the function Ω. *Upper panels:* CMB temperature power spectra; *central panels:* lensing-temperature cross-correlation (left) and the lensing potential power spectra (right); *lower panels:* total matter power spectra (left). See Sec. 8.4 for a detailed explanation. From [8].

Here we consider power laws for Ω and we set:

$$\Omega(a) = \Omega_0 a^n \,, \tag{8.17}$$

which gives an Ω analogous to the one of the BZ parametrization of $f(R)$ models when $\Omega_0 = -B_0\Omega_m/2$ and $n = 3$, as we will discuss in Chapter 10. We fix the expansion history to be the one of a dark energy model displaying an extreme phantom-divide crossing which is a phenomenological feature that is naturally and consistently accounted for by the EFT approach. Let us stress that with our code we have checked that these models satisfy the stability constraints listed in Sec. 6.5. In this case, given that we are not choosing a specific model of DE/MG, but rather a form for Ω, these stability requirements acquire the meaning of a validity check on the time dependence of the EFT functions in view of the corresponding behavior of the perturbations. In particular, the stability conditions will constrain the parameter space describing the expansion history, (w_0, w_a), and Ω, in this case n, offering a complementary constraining power.

We plot the resulting power spectra in Fig. 8.1 for two ghost-free phantom model: $n = 1, 4$ and $\Omega_0 = -0.3$ in two different background specified by

$(w_0 = -1.2, w_a = 0.3)$ and $(w_0 = -1.5, w_a = 0.5)$. We shall outline here some interesting features. We can notice that the CMB power spectrum at small scales is mostly influenced by the change in the expansion history while all the other observables are more sensitive to the change in the power law exponent. Between the linear ($n = 1$) and the non-linear ($n = 4$) models we can see a pronounced qualitative difference while the different expansion histories induce just quantitative changes. This is particularly clear in the ISW part of the CMB temperature power spectrum, in the lensing potential and in the lensing-temperature cross correlation. Interestingly enough we see that the effects on the total matter power spectrum are limited even if the models that we considered are chosen to be rather extreme. At last we notice that no pathological feature arises in these spectra associated to the crossing of the phantom-divide.

8.5 Chapter Summary

In this chapter we presented an implementation of the EFT framework in the publicly available CAMB code. The resulting product, which we dubbed EFTCAMB, is a full versatile Einstein-Boltzmann code which allows a thorough investigation of linear scalar cosmological perturbations in general theories that approach the phenomenon of cosmic acceleration. Our code has several advantages.

EFTCAMB does not rely on any QS approximation, solving instead the full dynamics of scalar perturbations on all linear scales. The latter is an important feature for several reasons; it allows the exact implementation of any given single field DE/MG model that can be cast into the EFT language, without need of resorting to sub-horizon approximated expressions which often correspond to solutions of the theory. It also ensures that we do not miss out on any potential sub-horizon dynamics of the scalar d.o.f. which in some cases could be non-negligible and could leave an imprint on cosmological observables within the reach of ongoing and upcoming surveys. To this extent, we presented an example of signature on the small scales of the CMB lensing potential angular power spectrum from the sub-horizon dynamics of the scalaron in $f(R)$ models. Effects like the latter will be measured at increasing accuracy in the next years, and our code offers a way to exploit these data as complementary tests of gravity.

Our code can handle very general expansion histories, ranging from the ΛCDM one to phantom-divide crossing ones. In this paper we presented results for models with a ΛCDM, wCDM and CPL background (including phantom-divide crossing models). The time-varying case is implemented in such a way that the contribution to perturbations coming from the evolution of the dark energy equation of state, is consistently taken into account. Finally, our code has a built-in check for theoretical viability of the model under consideration. In other words, in order to ensure that the underlying theory of gravity is physically acceptable we impose on the EFT operators some stability conditions and the code automatically checks that they are satisfied before proceeding with the evolution of the equations. In particular we require: a positive Newtonian constant, absence of ghost instabilities, absence of super-luminary propagating perturbations and, finally, a positive mass of the extra scalar degree of freedom.

We used the *pure* EFT approach, i.e. we chose an expansion history and

a parametrized form for the EFT function Ω and again explored signatures on power-spectra observables. In this case we focused on backgrounds with a phantom-divide crossing demonstrating how within the EFT framework there is no special pathology arising when $w_{\rm DE} = -1$ is crossed.

Chapter 9

Observational Results

In the previous Chapter we introduced EFTCAMB, a patch which implements the EFT formalism for DE/MG models into the public Einstein-Boltzmann solver CAMB [104]. As such, the code can be used to investigate the implications of the different EFT operators on linear perturbations as well as to study perturbations in any specific DE or MG model that can be cast into the EFT language, once the mapping is worked out.

Along with EFTCAMB we have developed a modified version of the Markov-Chain Monte-Carlo code CosmoMC [105], that we dubbed EFTCosmoMC. In combination with the check for stability of the theory embedded in EFTCAMB, it allows to explore the parameter space of models of cosmic acceleration under general viability criteria that are well motivated from the theoretical point of view.

In this chapter we illustrate the use of these patches in exploring parametrized DE/MG models, obtaining constraints on different models within the EFT framework, using several cosmological data sets.

9.1 EFTCosmoMC: sampling of the parameter space under stability conditions

To fully exploit the power of EFTCAMB we equipped it with a modified version of the Markov-Chain Monte-Carlo code CosmoMC [105] that we dubbed EFTCosmoMC. The complete code now allows to explore the parameter space performing comparisons with several cosmological data sets, and it does so with a built-in stability check that we shall discuss in the following.

In the EFT framework, the stability of perturbations in the dark sector can be determined from the equation for the perturbation π, which is an inhomogeneous Klein-Gordon equation with coefficients that depend both on the background expansion history and the EFT functions [162, 163, 8]. Following the arguments of [166], in the previous Chapter and in [8] we listed general viability requirements in the form of conditions to impose on the coefficients of the equation for π; these include a speed of sound $c_s^2 \leq 1$, a positive mass $m_\pi^2 \geq 0$ and the avoidance of ghost. Furthermore we required a positive non-minimal

coupling function, *i.e.*$1+\Omega > 0$, to ensure a positive effective Newton constant.

When exploring the parameter space one needs to check the stability of the theory at every sampling point. While this feature at first might seem a drawback, however, it is one of the main advantages of the EFT framework and a virtue of EFTCAMB/EFTCosmoMC. Indeed, as we outlined in [8], checking the stability of the theory ensures not only that the dynamical equations are mathematically consistent and can be reliably numerically solved, but also, perhaps more importantly, that the underlying physical theory is acceptable. This of course is desired when considering specific DE/MG models and, even more, when adopting the *pure* EFT approach. In the latter case indeed, one makes a somewhat arbitrary choice for the functional form of the EFT functions and satisfying the stability conditions will ensure that there is an underlying, theoretically consistent model of gravity corresponding to that given choice.

Imposing stability conditions generally results in a partition of the parameter space into a stable region and an unstable one. In order not to alter the statistical properties of the MCMC sampler, like the convergence to the target distribution, when dealing with a partitioned parameter space we implement the stability conditions as priors so that the Monte Carlo step is rejected whenever it would fall in the unstable region. We call these constraints *viability priors* as they represent the degree of belief in a viable underlying single scalar field DE/MG theory encoded in the EFT framework. We would like to stress that they correspond to specific conditions that are theoretically well motivated and, hence, they represent the natural requirements to impose on a model/parametrization. One of the virtues of the EFT framework, and consequently of EFTCAMB/EFTCosmoMC, is to allow their implementation in a straightforward way.

9.2 Linear EFT Observational Results

We start our exploration of cosmological constraints on DE/MG theories with a *pure* EFT model. We adopt the designer approach choosing two different models for the expansion history, the ΛCDM one and the wCDM one (corresponding to a constant dark energy equation of state). As we explained in Section 8.1, after fixing the background expansion history one can use the Friedmann equations to solve for two of the three EFT background functions in terms of the third one; as it is common, we use this to eliminate Λ and c. We are then left with Ω as a free background function that will leave an imprint only on the behaviour of perturbations. We assume the following functional form:

$$\Omega(a) = \Omega_0^{\rm EFT}\, a\,, \tag{9.1}$$

which can be thought of as a first order approximation of a Taylor expansion in the scale factor. We set to zero the coefficients of all the second order EFT operators. In the remaining we refer to this model as the linear EFT model.

Before proceeding with parameter estimation, it is instructive to study the shape of the viable region in the parameter space of the model. As we discussed in Section 9.1, the check on the stability of any given model is a built-in feature of EFTCAMB/EFTCosmoMC, so that the user does not need to separately perform such an investigation prior to implementing the model in the code.

Nevertheless, in some cases it might be useful to look at the outcome of such analysis as one can learn interesting things about the model/parametrization under consideration. Let us briefly discuss the stability of the linear EFT model.

In the case of a ΛCDM expansion history, it is easy to show that all the stability requirements that we introduced in Section 6.5, imply the following *viability prior*:

$$\Omega_0^{\rm EFT} \geq 0\,. \tag{9.2}$$

On the other hand, the case of a wCDM expansion history can not be treated analytically so we used our EFTCAMB code along with a simple sampling algorithm to explore the stability of the model in the parameter space. We varied the parameters describing the dark sector physics while keeping fixed all the other cosmological parameters. The result is shown in Figure 9.1 and includes interesting information on the behaviour of this model. First of all, also in this case the stable region correspond to $\Omega_0^{\rm EFT} > 0$; furthermore it is possible to have a viable gravity model with $w_0 < -1$, although in this case $\Omega_0^{\rm EFT}$ needs to acquire a bigger and bigger value to stabilize perturbations in the dark sector. Finally, we see that if $\Omega_0^{\rm EFT} = 0$ we recover the result, found in the context of quintessence models [209], that $w_0 > -1$. This case corresponds, in fact, to minimally coupled quintessence models with a potential that is crafted so that the resulting expansion history mimics that of a wCDM model.

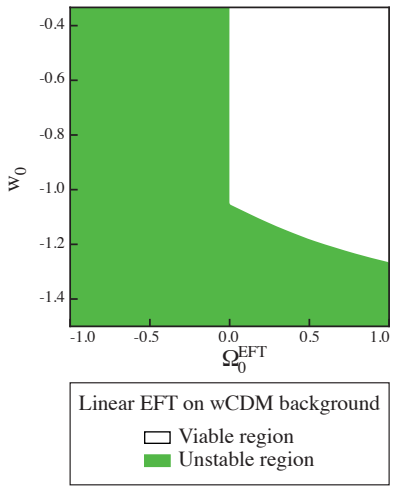

Figure 9.1: Stability regions of linear EFT model on a wCDM background. The cosmological parameters defining the expansion history are set to their CAMB default values: $H_0 = 70\,\mathrm{Km/s/Mpc}$, $\Omega_b = 0.05$, $\Omega_c = 0.22$, $T_{\rm CMB} = 2.7255\,\mathrm{K}$. From [7].

9.2.1 Results Without Massive Neutrinos

We use *Planck* 2013 CMB temperature and lensing spectrum, the WMAP (WP) CMB low-ℓ polarization spectra and several BAO measurements outlined in Chapter 4.

To explicitly show the effect of individual data sets on the different parameters that we constrain, we adopt three different combinations of data, namely: *Planck*+WP; *Planck*+WP+BAO; *Planck*+WP+BAO+lensing, where with lensing we mean the CMB lensing potential distributions as measured by *Planck*. In all cases we assume standard flat priors from CMB on cosmological parameters while we impose the *viability priors* discussed in Section 9.1 on model parameters.

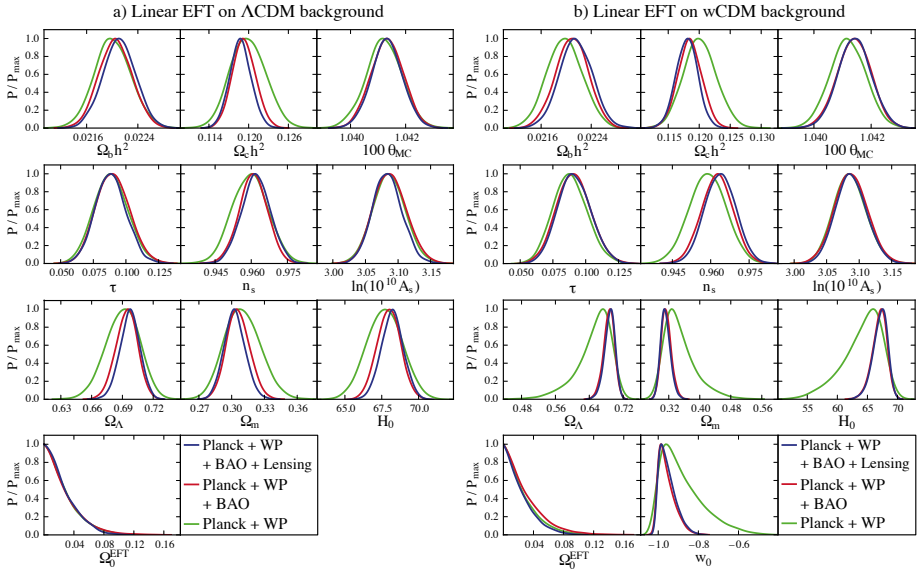

Figure 9.2: 1D Marginalized posterior distributions of cosmological and model parameters for the *pure* linear EFT model both on a ΛCDM (left) and wCDM (right) background. Different colors represent different combinations of cosmological data sets. From [7].

For the ΛCDM background case, the 1D marginalized posterior distributions, obtained with the three different data compilations discussed above, are shown in Figure 9.2 (a). The corresponding marginalized statistics are summarized in Table 9.1 (a). We find that the three different data compilations produce similar results, with *Planck*+WP+BAO+lensing giving:

$$\Omega_0^{\rm EFT} < 0.061 \quad (95\%\text{C.L.}) \, . \tag{9.3}$$

Next we consider a wCDM expansion history, characterized by an equation of state for dark energy constant in time, w_0, but different from -1. Upon inspecting Figure 9.2 (b) one can notice that the marginalized posterior distributions of $(\Omega_m, \Omega_\Lambda, H_0, w_0)$ obtained from *Planck*+WP data are significantly skewed, *i.e.*their right tail goes to zero much more sharply than the left one. The situation changes significantly when one adds BAO data. This is due to the combination of two effects. On one hand, when BAO data are not included, the constraints on $(\Omega_m, \Omega_\Lambda, H_0, w_0)$ are relatively loose since one is lacking the complementary high precision information on the expansion history. In other words, the gain/loss of likelihood value in the vicinity of best-fit points is not very significant, so the sampling points of cosmological parameters broadly spread around

their central values. In this case, the stability requirements on $\Omega_0^{\rm EFT}$ and w_0 dominate over the data constraining power. On the other hand, as shown in Figure 9.1, the viable region in the space $(\Omega_0^{\rm EFT}, w_0)$ for the linear EFT model on a wCDM background covers mostly $w_0 > -1$, *i.e.*it is highly asymmetric in the range around $w_0 = -1$. This explains the asymmetry in the posterior distribution of w_0 since the marginalized posterior distribution in Monte-Carlo integration algorithms follows the number of projected sampling points in the given volume. Furthermore, from the left panel of Figure 9.3 (green curve), one can see that $(\Omega_m, \Omega_\Lambda, H_0)$ are degenerate, as expected, with w_0 and this explains while their posterior distributions are skewed as well. As soon as complementary measurements of cosmological distances, such as BAO, are added to the data sets, the constraining power is strong enough and the posterior distributions become more symmetric; indeed BAO data significantly helps to localize the confidence regions close to $w_0 \sim -1$, making the posterior distribution less affected by the global profile of *viability priors*.

Finally, from the left panel of Figure 9.3 we can see that the degeneracy of $\Omega_0^{\rm EFT}$ with the other parameters is not very significant after adding BAO data (blue and red curves). As a result the bounds on $\Omega_0^{\rm EFT}$ remain at the same level of those obtained for a ΛCDM background. With *Planck*+WP+BAO+lensing data we obtain:

$$\Omega_0^{\rm EFT} < 0.058 \quad (95\%\text{C.L.}) \,. \tag{9.4}$$

One can notice that the addition of lensing data does not significantly improve the constraint on $\Omega_0^{\rm EFT}$ in neither the ΛCDM nor the wCDM case.

9.2.2 Results With Massive Neutrinos

The direct measurements of neutrino flavor oscillations provide evidence for non-zero neutrino masses, but give no hint on their absolute mass scale (see e.g. the reviews [210, 211]). Cosmology, on the other hand, provides a powerful, complementary way of placing constraints on the sum of the mass of neutrinos (see e.g. the reviews [212, 213]). Indeed massive neutrinos can significantly affect the distribution of large-scale structure (LSS) and the pattern of cosmic microwave background (CMB) anisotropies depending on the value of their mass. The current constraint from CMB experiments on the summed neutrino mass fixes the upper limit at $\sum m_\nu < 0.66$ eV (95%; *Planck*+WP+highL) for a flat ΛCDM cosmology [78]. Besides slightly affecting the expansion history, massive neutrinos leave an imprint on the dynamics of linear scalar perturbations. On scales smaller than their mass scale neutrinos free stream damping the structure and accordingly diminishing the weak lensing effect on those scales [214]. Furthermore, they contribute an early Integrated-Sachs Wolfe (ISW) effect because their transition from relativistic to non-relativistic happens on an extended redshift interval which, for the typical neutrino mass ($\sum m_\nu \sim 0.1$ eV), overlaps with the transition from radiation to matter [214].

Similar effects are also observed in DE and MG models. The latter generally involves an extra, dynamical massive scalar degree of freedom (d.o.f.). which mediates a fifth force between matter particles and can have a speed of sound different from unity. Besides affecting the background dynamics such as to source cosmic acceleration, on linear scales the field can modify significantly the clustering of matter as well as the sub-horizon dynamics of metric potentials on scales

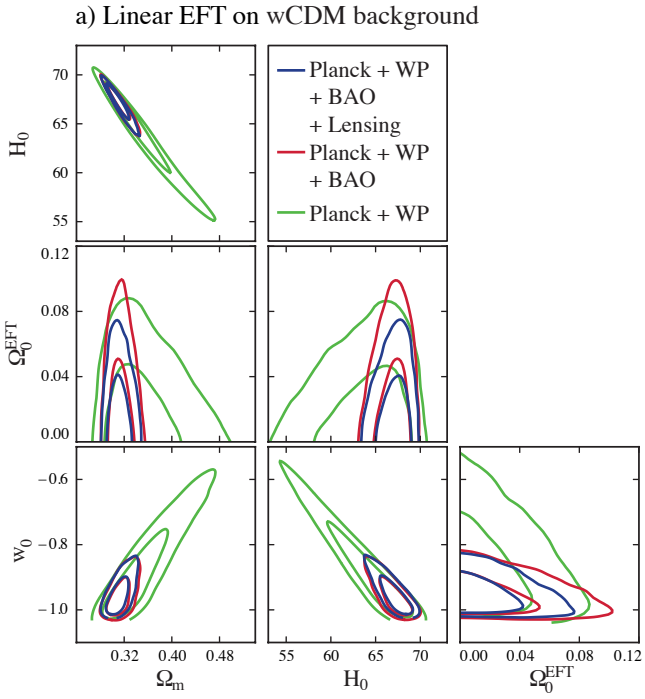

Figure 9.3: 68% and 95% confidence regions on combinations of cosmological parameters for the linear *pure* EFT model on wCDM background. Different combinations of observables are indicated with different colors. From [7].

below or above its characteristic lengthscale. Hence, structure formation, the ISW effect and weak lensing effect will be modified accordingly [215, 216, 217]. Based on these considerations, a degeneracy between massive neutrinos and the dark sector is expected, and in general neutrinos bounds depend significantly on the cosmological model within which they are analyzed. This has been investigated by several authors [200, 218, 219, 220, 72].

In this Section we investigate the degeneracy between massive neutrinos and the linear EFT model.

In our analysis we will use different combinations of the following data sets: *Planck* 2013 CMB temperature and lensing spectra, WMAP low-ℓ CMB polarization spectra, several BAO measurements and WiggleZ galaxy power spectrum data, as outlined in Chapter 4.

To test the Linear EFT model we use different combinations of these data sets and the corresponding constraints on $\Omega_0^{\rm EFT}$ and $\sum m_\nu$ are listed in Table 9.2. From there we can see that the bounds on $\Omega_0^{\rm EFT}$ do not sensibly change with respect to the results reported in 9.2.1, where neutrino masses were set to zero. In that case the bound on $\Omega_0^{\rm EFT}$ was found to be $\Omega_0^{\rm EFT} < 0.061$ (95% C.L.) when considering *Planck*+WP+BAO+lensing (for details see Table 9.1). The only exception is given by the most complete data combination which slightly improves on the previous bounds. Overall, the constraints on the sum of neutrino masses are stringent for all the data sets considered, given the lack of

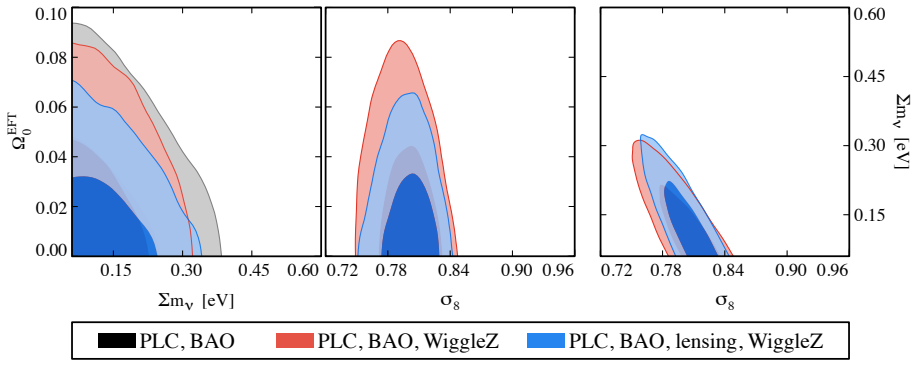

Figure 9.4: The marginalized joint likelihood for the present day value of $\Omega_0^{\rm EFT}$, the sum of neutrino masses, $\sum m_\nu$, and the amplitude of the (linear) power spectrum on the scale of $8\,h^{-1}$Mpc, σ_8. Different colors correspond to different combinations of cosmological observations as shown in the legend. The darker and lighter shades correspond respectively to the 68% C.L. and the 95% C.L.. No new significant degeneracies between these parameters are found. From [5].

degeneracy as can be noticed in Figure 9.4. In particular the bounds are close to those found in [78] in the absence of modified gravity. However, when lensing data are added one can notice some weak degeneracy between $\Omega_0^{\rm EFT}$ and $\sum m_\nu$ in the left panel of Figure 9.4, which results in this data set favoring a slightly bigger neutrino mass and a smaller value of $\Omega_0^{\rm EFT}$. From the middle and right panels of Figure 9.4, we can see that the degeneracy between σ_8 and $\Omega_0^{\rm EFT}$ is also negligible and that the interplay between neutrino masses and σ_8 is not sensibly altered, with respect to [78], by linear EFT models.

These results suggest that almost no degeneracy with massive neutrinos is present when the linear EFT model on ΛCDM cosmology is considered. One could wonder whether the same model on a different background would result in a different degeneracy. The results in 9.2.1 seem to imply that exploring the same model on wCDM would not alter so much the bounds, since no effects due to a modification of gravity would be appreciable.

9.3 Investigating Tensions with Parametrizations

Another application of parametrized DE/MG models is that of investigating the physical origin of tensions between different data sets. In this Section we show a worked example of this application.

Based on the full-mission *Planck* observations of temperature and polarization anisotropies of the cosmic microwave background (CMB) radiation, *Planck*-2015 results show that the temperature and polarization power spectra are consistent with the standard spatially-flat six-parameter ΛCDM cosmology with a primordial power-law spectrum of adiabatic scalar perturbations. On the other hand, the same data, especially the temperature-temperature (TT) spectrum reveals some tension with the CMB lensing deflection angle (d) spectrum re-

constructed from the same maps. In details, the lensing amplitude in CMB temperature and polarization spectra, $A_{\rm L} = 1.22 \pm 0.10$, is in 2σ tension with the amplitude of the CMB trispectrum reconstructed lensing deflection angle spectrum, $A_{\rm L}^{\phi\phi} = 0.95 \pm 0.04$ while it is expected that in the base-ΛCDM model both these quantities should be equal to unity.

The *Planck* collaboration finds that, compared with the base-ΛCDM model, the base-ΛCDM+$A_{\rm L}$ model can reduce the logarithmic likelihood ($\Delta\chi^2 = -6.1$) and provide a better fit to the data sets with [1] $A_{\rm L} = 1.28$ or marginalized constraint $A_{\rm L} = 1.22 \pm 0.10$ [16] . More importantly, they find that there is roughly equal preference for high $A_{\rm L}$ from intermediate and high multipoles (*i.e.*, the `Plik` likelihood; $\Delta\chi^2 = -2.6$) and from the low-ℓ likelihood ($\Delta\chi^2 = -3.1$) with a further small change coming from the priors. This means that the base-ΛCDM+$A_{\rm L}$ model can provide a better fit than base-ΛCDM model against both TT and lowP data sets. However, the increase in $A_{\rm L}$ will induce changes on the full sets of cosmological parameters as mentioned in the reference [16]. For example, compared with the base-ΛCDM fit, the scalar index, n_s, is increased by 1%, the primordial scalar spectrum amplitude, A_s, is reduced by 4% and the effective amplitude of the TT spectrum, $A_s e^{-2\tau}$, is reduced by 1%. Through the complicated relationship between parameters and their degeneracy the reionization optical depth parameter, τ, falls to 0.060, which is roughly in 2σ tension with *Planck*-2013 temperature + WMAP low-ℓ polarization data results of $\tau = 0.089^{+0.012}_{-0.014}$.

Inspired by these observations, in this Section, we investigate whether some modifications of gravity can relieve the tension between *Planck* CMB anisotropy spectra and CMB lensing results.

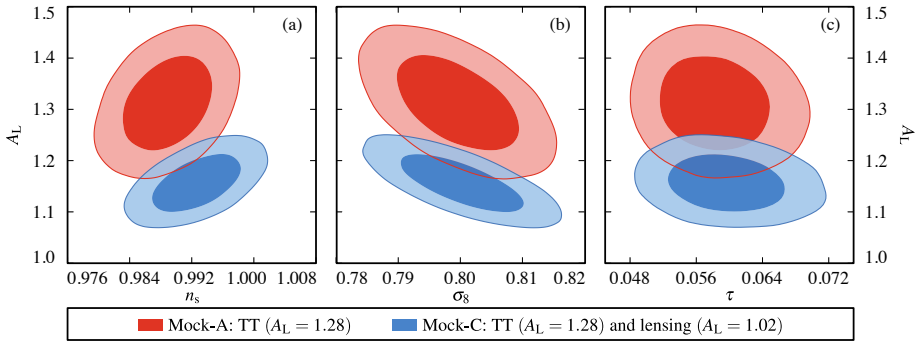

Figure 9.5: the marginalized joint likelihood for the lensing amplitude $A_{\rm L}$ and the scalar spectral index n_s *panel (a)*, the amplitude of the (linear) power spectrum on the scale of $8h^{-1}$Mpc, σ_8 *panel (b)* and the reionization optical depth τ *panel (c)*. In all three panels different colors correspond to different combination of mock data sets as shown in legend. The darker and lighter shades correspond respectively to the 68% C.L. and the 95% C.L.. From [5].

[1] From the PLA-PR2-2015 official chains `base-Alens-plikHM-TT-lowTEB` at `http://pla.esac.esa.int/pla/`.

9.3.1 Simulating Tensions in Planck Data

To investigate this tension in Planck data we will simulate a tension CMB data set that resembles the tension present in the *Planck*-2015 results and we will try to fit the resulting power spectra with different models to have a glimpse of the changes in the parameter that arise because of this tension.

We analyse a *pure* EFT modified gravity model against two sets of simulations of CMB spectra (TT,TE,EE) and CMB lensing spectra (dd and Td) with the fiducial cosmological parameter equal to the *Planck*-2015 data release best-fit values and *Planck* blue book beam and noise specifications.

We use these simulations because the cosmological parameters are degenerate with each other in a complicated way, by using simulations, we can efficiently isolate and study the effects coming from different parameters and their combinations.

To construct our simulations we use the cosmological parameters listed in Table 9.3 along with the CAMB code [104] to produce the fiducial CMB temperature and E-mode polarization power spectra. We feed these to the FuturCMB[2] package [221] to compute the noise power spectra for T, E-mode and the lensing deflection angle based on the Hu-Okamoto [80] quadratic estimator. For further details about the FuturCMB code we refer the reader to [221] while for the construction of the spectrum likelihood we refer to [222, 223, 221]. In this paper, we shall adopt the *Planck* bluebook [224] beam and noise parameters listed in Table 9.4.

After the above operations, we build two mock data sets (C_ℓ^{TT}, C_ℓ^{TE}, C_ℓ^{EE}, C_ℓ^{dd} and C_ℓ^{Td}), that we shall call Mock-A and Mock-B, whose fiducial cosmological parameter values (see Table 9.3) are, respectively, the best-fit values of base-ΛCDM+$A_{\rm L}$ to *Planck*-2015 TT+lowP and *Planck*-2015 TT+lowP+lensing data sets[3]. Since the Mock-A data set, which mimics *Planck*-2015 TT+lowP, is generated from $A_{\rm L} \sim 1.3$, we can treat it as a realization of a non-ΛCDM universe; Mock-B data, that mimics *Planck*-2015 TT+lowP+lensing, $A_{\rm L} \sim 1.0$, is closer to a realization of ΛCDM universe.

Based on Mock-A and Mock-B data sets, we build a "tension" data set, called Mock-C, by combining (C_ℓ^{TT}, C_ℓ^{TE}, C_ℓ^{EE}) from Mock-A and (C_ℓ^{dd} and C_ℓ^{Td}) from Mock-B. The resulting data set should mimic the tension present in Planck data while being free of additional complications that arise in the real situation. Before the end of this section, we would like to emphasize that the strategy of simulating data has both strong and weak points. On one hand this procedure allows to single out specific effects that in the real data could be shaded by systematics or by noise and this allows to target precisely the physical phenomena under scrutiny. On the other hand the simulated dataset is not expected to reproduce precisely the results of the real one because there are a number of details about the likelihood construction that can not possibly be mimicked. Our likelihood is built analytically at all multipoles without binning and assuming the same sky coverage in all frequency bands in temperature and polarization. In addition we adopt all the polarization data into

[2] `http://lpsc.in2p3.fr/perotto/`

[3] The best-fit values are read from the PLA-PR2-2015 official chains `base-Alens-plikHM-TT-lowTEB` and `base-Alens-plikHM-TT-lowTEB-lensing` at `http://pla.esac.esa.int/pla/`.

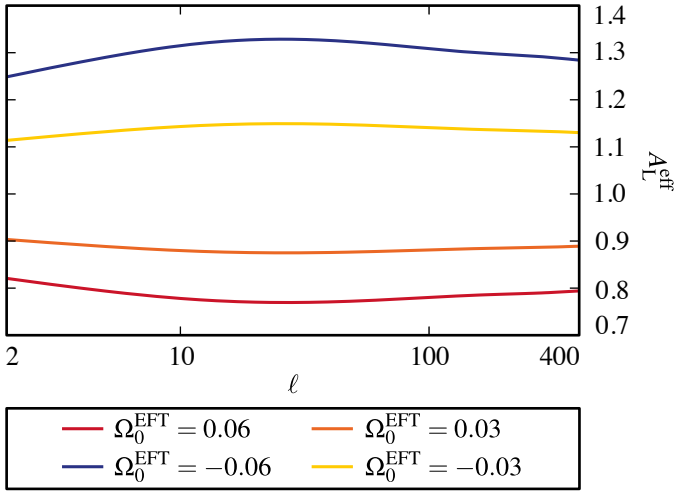

Figure 9.6: the effective lensing amplitude $A_{\rm L}^{\rm eff}(\ell) \equiv C_\ell^{\phi\phi}({\rm MG})/C_\ell^{\phi\phi}({\rm GR})$ as a function of scale in the constant Ω *pure* EFT model considered here. Different colors correspond to different values of the model parameters as shown in legend. From [5].

our numerical analysis, unlike in the lowP likelihood in which only the low-ℓ polarization data are used. The simulated lensing data is then reconstructed based on these power spectra and the relative balance between the lensing likelihood and the T and E one results in assigning more weight to the T and E likelihood (because we include high-ℓ TE and EE data) with respect to real Planck (TT+lowP+lensing) results. This procedure for building the likelihood is not the same as those adopted by the Planck collaboration and the results on specific parameters reflect this point.

9.3.2 Results

In the one extra parameter extension of the base-ΛCDM model in the *Planck*-2013 [78] and *Planck*-2015 [16] results, the collaboration studied the case of varying the lensing amplitude parameter, $A_{\rm L}$, in the CMB anisotropies, which was originally introduced in [225]. This phenomenological parameter is defined by $C_\ell^{\phi\phi} \to A_{\rm L} C_\ell^{\phi\phi}$, which simply rescales the lensing amplitude contribution to the CMB anisotropies. This parameter, however, only modulates the CMB anisotropy spectra, C_ℓ^{TT}, C_ℓ^{TE} and C_ℓ^{EE}, and rescales the lensing potential spectrum $C_\ell^{\phi\phi}$ but does not rescale the estimator of the lensing spectrum $\hat{A}_{\rm L}^{\phi\phi}$ which is computed from the CMB anisotropy trispectra [81, 79]. For a review of CMB temperature and polarization lensing we refer the reader to [206].

In the following we shall elaborate on the relationship between this phenomenological parameter and modifications of gravity.

We shall consider a model that consists in taking a constant value for the conformal coupling $\Omega(a) = \Omega_0^{\rm EFT}$ and requiring the expansion history to be

exactly that of the ΛCDM model. This requirement will then fix, through the Friedmann equations, the time dependence of the operators c and Λ.

We highlight here that the constant Ω model is not a simple redefinition of the gravitational constant. In fact the requirement of having a ΛCDM background with a non-vanishing Ω, that would change the expansion history, means that a scalar field is sourced in order to compensate this change. This scalar field will then interact with the other matter fields and modify the behaviour of cosmological perturbations and consequently the CMB power spectra and the growth of structure. For instance, it is easy to show that in the constant Ω model, $c(\tau)$, which is vanishing in general relativity, is non-zero and reads

$$c = \frac{\Omega}{2}(\rho_m + P_m) \ . \tag{9.5}$$

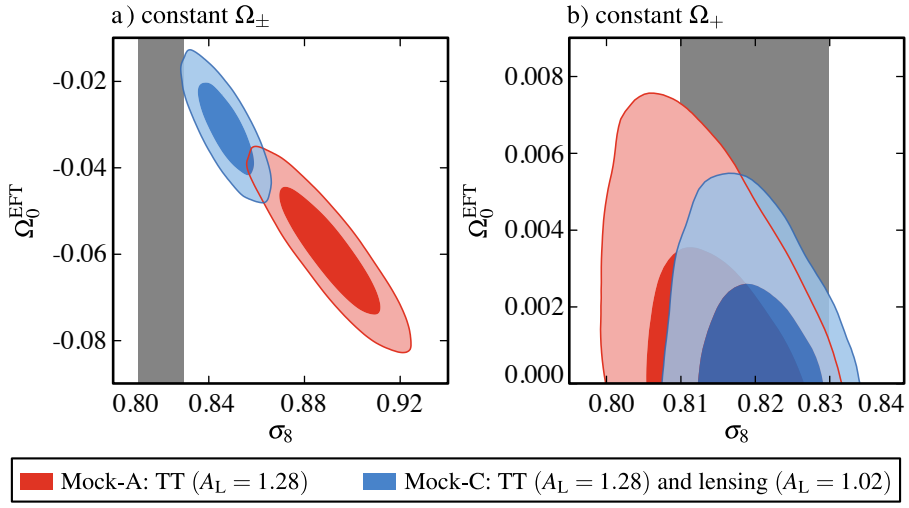

Figure 9.7: the marginalized joint likelihood for the amplitude of the (linear) power spectrum on the scale of $8h^{-1}$Mpc, σ_8 and the present day value of the conformal coupling $\Omega_0^{\rm EFT}$ in the case in which it is allowed to have positive and negative values *panel (a)* and in the case in which it is restricted to positive values *panel (b)*. In all panels different colors correspond to different combination of mock data sets as shown in legend and the grey band is the marginalized 1σ bound on σ_8 from the base-ΛCDM+$A_{\rm L}$ model. The darker and lighter shades correspond respectively to the 68% C.L. and the 95% C.L.. From [5].

Another general remark we would like to make on the models that we consider here, is that they display a radically different cosmology, as they correspond to two different behavior of the perturbation's effective gravitational constant. We consider two possibilities. If the constant Ω is positive the model will be characterized by a smaller effective gravitational constant resulting in a suppression of the growth and consequently a suppression of the CMB lensing. We shall call this case the Ω_+ model. If the constant Ω is negative, on the other hand, the model will have an enhanced effective gravitational constant. In contrast to what happens to the Ω_+ case, that respects all the usual requirements

of physical viability [8], this model is only classically stable. This means that perturbations around the FLRW background are stable and well behaved but, for example, the sign of the scalar field kinetic term is wrong. We shall call the case in which the constant Ω can be greater and smaller than zero the $\Omega_{\pm}$ model.

We firstly check the reliability of our simulations. As reported in the Table 9.3 we use the fiducial $A_{\rm L} = 1.28$ for the generation of the Mock-A data set. After going through the Markov-Chain Monte-Carlo analysis [105], we get the marginalized constraint from the Mock-A data set as

$$A_{\rm L} = 1.31 \pm 0.06 \, , (68\%\text{C.L.}) \, . \tag{9.6}$$

The consistency between the input and output values of our simulations can also be seen in the panels of Figure 9.5. In addition from panel (a) we can see that there is a relatively large positive correlation between n_s and $A_{\rm L}$. This happens because a large value of n_s will enhance the high-ℓ multipoles, while an increase in $A_{\rm L}$ will smear the peaks in the same multipole range. Panel (b) instead shows that σ_8 and $A_{\rm L}$ are anti-correlated. An increase of $A_{\rm L}$ will suppress the growth inferred from the TT power spectrum, hence we end up with lower σ_8 value. Panel (c), at last, shows that no significant degeneracy arises between $A_{\rm L}$ and the re-ionization optical depth parameter τ.

From all the panels of Figure 9.5 we can see how different cosmological parameters reacts to the use of a tension data set. The shift of blue and red contour from Mock-A and Mock-C data sets shows the tension between them. In particular in panel (a) we can see that the Mock-C data set gives a value of $A_{\rm L} \sim 1.15$ that is in the middle of the Mock-A ($A_{\rm L} \sim 1.3$) and Mock-B ($A_{\rm L} \sim 1.0$) data sets. This happens because the Mock-C likelihood is constructed from the equally weighted combination of the Mock-A and Mock-B ones while in the real Planck results [16], instead, the CMB lensing data dominates the constraint on $A_{\rm L}$.

From panel (b) and (c) we can instead see that the marginal probability distribution of σ_8 and τ does not change significantly as the tension in the data set is introduced. This happens because the constraint on these two quantities are dominated by the TT and EE power spectra. From the same panels we can notice that there is a slight bias in parameter estimation with respect to the real Planck data. This is due to differences in the construction of the likelihood that result in different weights being assigned to the temperature and polarization likelihood with respect to the lensing one. As stressed at the beginning of this Section, this simulation procedure is targeted at mimicking the tension between the data sets rather than the data sets themselves and their specific constraints on cosmological parameters therefore this effect does not affect the following analysis of the results and conclusions.

After checking the consistency of our simulations we move to their interpretation within the modified gravity models here considered.

First of all we check whether these models can reproduce the input amplitude of lensing. To do so we define an effective lensing amplitude as $A_{\rm L}^{\rm eff}(\ell) \equiv C_\ell^{\phi\phi}({\rm MG})/C_\ell^{\phi\phi}({\rm GR})$ and we plot it for several choices of the parameters defining our modified gravity model in Figure 9.6. We can see that the effective lensing amplitude is generally a function of scale so that the accuracy of using a scale

independent approximation for it is limited by the accuracy of observations. That is, if observations are not precise enough then the scale independent approximation can work while if the observations have enough sensitivity we would bias parameter estimation by considering it scale independent. This point will be more and more relevant as the experimental accuracy improves.

The constant Ω_+ and $\Omega_\pm$ models are shown in Figure 9.6. From there we can see that $A_{\rm L}^{\rm eff}(\ell)$ has a wide bump or dip around multipoles of few tenths while the scale dependence is somewhat weaker than the previous case. As expected, in the Ω_+ model the amplitude of lensing is decreased as a consequence of the suppression of growth while the opposite behavior shows when $\Omega_0^{\rm EFT}$ is smaller than zero.

We fit these models to our Mock-A and Mock-C data sets and we show the marginalized bound on parameters of interest in Figure 9.7.

From panel (a) we can see that there is a strong negative correlation between $\Omega_0^{\rm EFT}$ and σ_8 due to the fact that negative values of Ω correspond to significant deviations from GR, and consequently to stronger enhancement of CMB lensing. The bound on σ_8 from the $A_{\rm L}$ fit, shown in Figure 9.7 as a gray band, is almost compatible with the one in the $\Omega_\pm$ case. This is due to the fact that deviations from scale independence of $A_{\rm L}^{\rm eff}$, in this model, are weaker and a constant Ω is efficient at mimicking a scale independent $A_{\rm L}$. Since a weaker effective Newton constant is disfavoured by the *Planck*-2015 CMB anisotropy data, the best-fit parameter in the Ω_+ model mimic those in the base-ΛCDM model and the model result to be compatible with GR.

At last in Table 9.5 we list the best-fit χ^2 for the one parameter extensions of the base-ΛCDM model considered here.

From there we can see that the best-fit χ^2 values in the base-ΛCDM+$A_{\rm L}$, $\Omega_\pm$ models are similar and are noticeably smaller than those from base-ΛCDM or Ω_+ models with $\Delta\chi^2 \simeq -16$ from the Mock-A and $\Delta\chi^2 \simeq -11$ from the Mock-C data sets. The best-fit χ^2 in the $\Omega_\pm$ case is closer to the $A_{\rm L}$ one because of the weaker scale dependence of $A_{\rm L}^{\rm eff}$.

9.4 Observational Signatures of Modified Gravitational Waves

Another application of parametrized DE/MG models, that we will investigate in this section, is that of studying the observational signatures of a modified propagation of GWs.

In general relativity gravitational waves propagate at the speed of light, however in alternative theories of gravity that might not be the case. In this Section we study the effects of a modified speed of gravity, c_T^2, on the B-modes of the CMB anisotropy in polarisation.

Gravitational waves have been recently directly observed [90] opening a new observational window on our Universe. CMB experiments, on the other hand, have recently detected the B-modes of polarisation [87, 226], and are getting closer to offering an indirect measurement of cosmological GWs (tensor modes). While on small angular scales the BB-power spectrum is dominated by the

lensing of the CMB, on larger scales, the B-modes of polarisation are primarily produced by tensor modes and give an insight onto primordial GWs [227].

In general relativity, short-wavelength GWs follow the null geodesics of the background, thus their propagation speed equals the speed of light on a flat background. However in alternative theories addressing the phenomenon of cosmic acceleration, in Hořava-Lifshitz [228, 229] gravity and, more generally, in Lorentz-violating theories [230, 231, 182], the speed of gravity may deviate from that of light. For instance, some of the generalized scalar-tensor models within the Horndeski family [192, 232], like the covariant galileon involving certain derivative couplings, are expected to modify the tensor propagation speed [233, 234, 235, 236]; quantum gravity effects may modify the dispersion relation of GWs [237]; or the graviton may have a mass which prevents it from behaving light-like [238]. Massive gravity has the added complication that diffeomorphism invariance is explicitly broken, therefore in this paper we will focus on variations of c_T and will not consider a mass term [238, 239].

A direct measurement of the speed of GWs could be achieved comparing the arrival times of light and gravitational wave signals from a distant astronomical source [240]. This has not been possible yet, however indirect, local observations of gravitational radiation seem to suggest that its propagation speed, at the current epoch, is close to the speed of light. For instance, accurate measurements of binary pulsar timing indicate that the sound speed of GWs should not deviate from the general relativistic value by more than 1% [240]; the latter bound assumes that energy is lost via GWs; models of modified gravity might however imply also a loss of energy via scalar radiation associated to an additional d.o.f., possibly modifying this bound [241, 242, 243].

In this section we focus on the B-modes of CMB polarisation and show how they offer a novel, *independent* way to measure the propagation speed of GWs at the time of recombination. As we will show, variations of c_T affect the BB power spectrum in a unique way which makes it orthogonal with other cosmological parameters. Interestingly, as we will discuss, the B-modes are only sensitive to the modifications of the dispersion relation of the graviton around the time of recombination, therefore they are complementary to bounds from binary pulsars, allowing a combined constraint on the time variation of c_T.

On a flat Friedmann-Robertson-Walker background one can use the rotational and translational symmetries to decompose the metric perturbations into scalar, vector and tensor components. We are only interested in the tensorial part:

$$\mathrm{d}s^2 = -a(\tau)^2[\mathrm{d}\tau^2 + (\delta_{ij} + h_{ij})\mathrm{d}x^i\mathrm{d}x^j]\,, \tag{9.7}$$

where h_{ij} satisfy $\partial_i h_{ij} = 0$ and $h_{ii} = 0$. We shall consider a linear perturbation theory that also satisfies the gauge symmetry $h_{ij} \to h_{ij} + \partial_{(i}\epsilon_{j)}$, where ϵ_i is a generic function of the coordinates. Using the same EFT approach described in the previous chapters we can write down the most general quadratic action for h_{ij} that is ghost free and satisfies the symmetries mentioned above:

$$S_T^{(2)} = \frac{1}{8}\int \mathrm{d}\tau\,\mathrm{d}^3x\,a^2 M_P^2(\tau)\left(h'_{ij}h'_{ij} - c_T^2(\tau)\partial_k h_{ij}\partial_k h_{ij}\right)\,, \tag{9.8}$$

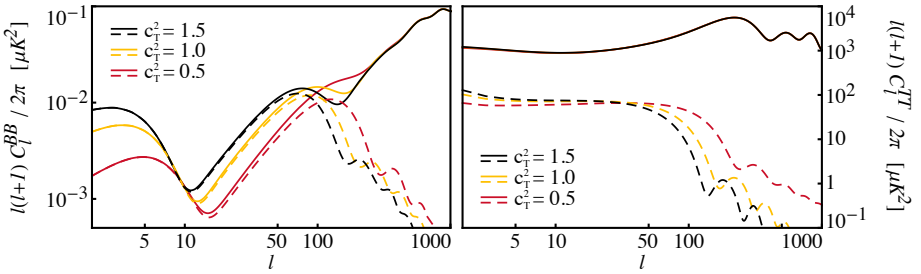

Figure 9.8: *Left:* the total B-mode polarisation power spectrum (solid lines) and its component due to tensor perturbations (dashed lines). *Right:* the total CMB temperature power spectrum (solid lines) and its tensor component (dashed lines). In both panels different colors correspond to different values of the speed of GWs. From [6].

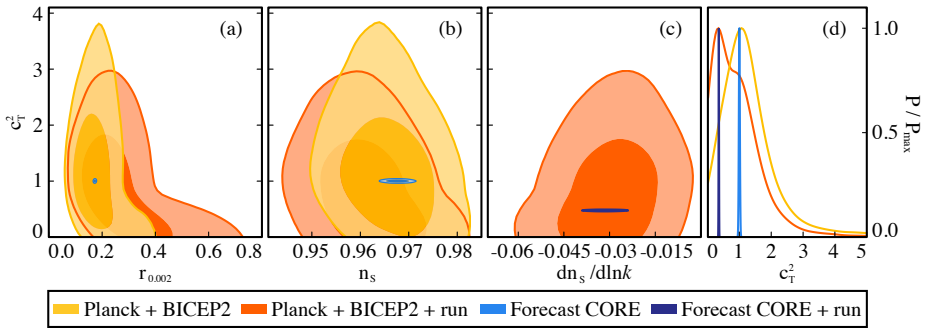

Figure 9.9: *Left:* The marginalized joint likelihood for the GWs speed of sound c_T^2 and parameters defining the primordial tensor power spectrum: the tensor to scalar ratio $r_{0.002}$, the scalar perturbations spectral index n_s and its running $dn_s/d\ln k$. Different colors correspond to different combinations of datasets and models as shown in the legend. The two different shades indicate the 68% and the 95% confidence regions. *Right:* Marginalized likelihoods of the tensor perturbations sound speed for the considered datasets and models. From [6].

where matter sources are assumed to be minimally coupled to the metric. Generally higher order gradient terms $h_{ij}\partial^{2n}h_{ij}(n > 1)$ should also be included in the action (9.8) but we have neglected them as we are interested in the low energy phenomenology [239]. The function $M_P^2(\tau)$ plays the role of the Planck mass which is allowed by the above mentioned symmetries to vary in time. We fix its value to $M_P^2 \equiv (8\pi G)^{-1}$ since time variations of this quantity are constrained by a large number of complementary observations [240, 244, 43] while polarisation observables are expected to depend weakly on this quantity. We are then left with modifications of the sound speed of tensor modes, so that the action (9.8) results in the following wave equation:

$$h_{ij}'' + 2\frac{a'}{a}h_{ij}' - c_T^2\partial_k\partial_k h_{ij} = \frac{2}{M_P^2 a^2}S_{ij}\,, \tag{9.9}$$

where S_{ij} is the transverse and traceless component of the energy momentum

tensor of the matter sector. Varying c_T^2 changes the relevant dynamical scale of tensor perturbations from the effective cosmological horizon, corresponding to the case $c_T^2 = 1$ (in units of the speed of light), to the sound horizon. For this reason the net effect on CMB spectra is an horizontal shift of the whole tensor induced component whose main peak moves at the angular scale of the GWs sound horizon at recombination as can be seen in figure 9.8. Notably the sources of the E and B-mode polarisation spectra are peaked at the recombination epoch [227] thus making them dependent on the dynamics of tensor perturbations at earlier times but limiting the impact of a later evolution. We have studied this effect numerically and found that a possible late time dependence of the GWs sound speed does not noticeably affect the polarisation observables which are in turn sensitive to its value around the recombination time. According to this result we have assumed c_T^2 to be constant throughout all cosmological epochs. Changing the speed of GWs in principle impacts also the reionization bump at large scales in the polarisation spectra. The effect is however less prominent than the shift of the recombination peak and its constraining power is also reduced by cosmic variance, which is stronger at those scales. The effect of horizontal shifting of the tensor component of the CMB spectra can in principle be mimicked by a change in the cosmological expansion history which is however tightly constrained by the scalar part of the CMB itself [78, 245] and many other observations. Other cosmological parameters, especially those defining the primordial tensor power spectrum, are not expected to be degenerate with c_T^2. The tensor to scalar ratio, for example, shifts vertically the tensor part of CMB spectra while the spectral index primarily changes its shape. More complicated models for the tensor primordial power spectrum could in principle be degenerate with c_T^2 but if inflationary consistency relations [246] are assumed then the scalar sector is expected to break this degeneracy.

From figure 9.8 we can also see that the effect of changing c_T^2 weakly influences the CMB temperature power spectrum because the tensor induced component is several orders of magnitude smaller than the scalar one for values of the tensor to scalar ratio not yet excluded by observations. We have also investigated the influence of this effect on the E-mode polarisation spectrum and found it negligible. The B-mode spectrum is instead greatly influenced by changes in the speed of GWs thus making this CMB observable the most suited for these studies.

9.4.1 A Worked Example

In this section we address the possibility of detecting such effect. At this goal we use the BICEP2, *Planck* CMB temperature power spectrum and WMAP low-ℓ CMB polarisation spectra discussed in Chapter 4. To understand how well the speed of sound of cosmological GWs can be constrained with an initial, statistically weak, detection of tensor modes we ignore the polarized dust emission modelling of *Planck* [88]. To forecast the precision at which this quantity will be measured by the next generation of CMB experiments we create simulated datasets adopting the specifications of the *Cosmic Origins Explorer* (CORE) [247] and the *Polarized Radiation Imaging and Spectroscopy Mission* (PRISM) [248] satellites. We perform a Markov Chain Monte Carlo analysis of both the data and the simulated data using the publicly available CosmoMC

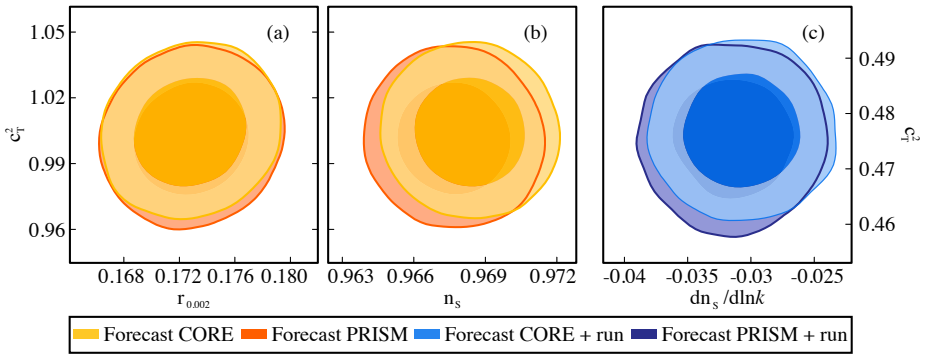

Figure 9.10: The marginalized joint likelihood for the GWs speed of sound c_T^2, the tensor to scalar ratio $r_{0.002}$, the scalar perturbations spectral index n_s and its running $dn_s/d\ln k$. Different colors correspond to different instrumental specifications used in the forecast and different models as shown in the legend. The two different shades indicate the 68% and the 95% confidence regions. From [6].

package [105]; in the case of forecast this allows us to have a good handle on the degeneracies among cosmological parameters. We allow variation of the six baseline cosmological parameters of the ΛCDM model, plus the running of the scalar spectral index and the amplitude of primordial cosmological GWs; we impose the single field inflationary scenarios to relate the spectral index of tensors to the scalar one.

The results of this analysis for both current data and forecast are shown in figure 9.9, while in figure 9.10 we provide a zoom of the forecasts of the cosmological parameters most relevant for our analysis. From panel (d) of figure 9.9 we can see that the marginalized likelihood of c_T^2 is peaked at its GR expected value, i.e. $c_T^2 = 1$ (in units of the speed of light) when considering a model without the running of the spectral index. Very high values of c_T^2 are excluded since they would move the tensor component of the B-mode spectrum to large scales, resulting in a poor fit of the measured data points. From panel (a) of figure 9.9, we can notice that there is a degeneracy between c_T^2 and the tensor to scalar ratio assumed at a pivot scale of $0.002\,\mathrm{Mpc}^{-1}$. The reason for this degeneracy is that those values of c_T^2 shift the GWs contribution to the spectrum toward smaller scales so that the only way to fit the data points is to change the spectrum amplitude. We can also see from panel (b) of figure 9.9 that c_T^2 is weakly degenerate with the spectral index due to the poor constraining power of the BICEP2 measurements. From the combination of the *Planck* and BICEP2 datasets we obtain the marginalized bound: $c_T^2 = 1.30 \pm 0.79$ and $c_T^2 < 2.85$ at 95% C.L..

If we allow a running of the primordial tensor power spectrum index the situation changes slightly. From the marginalized joint likelihood of c_T^2, $r_{0.002}$, n_s and $\mathrm{dn}_s/\mathrm{dln}\,k$ in panels (a,b,c) of figure 9.9, we can see that c_T^2 is driven toward smaller values and this is further confirmed by its marginalized distribution in panel (d). The peak of the probability distribution of c_T^2 is found not to be at its GR value which is however not excluded. From the same figure we can

see that as c_T^2 goes toward smaller values its degeneracy with $r_{0.002}$ is enhanced while it is not so pronounced with respect to the running of the spectral index, shown in panel (c), and n_s itself, shown in panel (b). Given the skewness of the marginal distribution of c_T^2 which is also cut at $c_T^2 = 0$ we report here only its upper bound: $c_T^2 < 2.33$ at 95% C.L..
We now turn to the forecasts to investigate further these degeneracies and to evaluate our capability of constraining the speed of cosmological GWs with future generation surveys. Our results do not include any forecast on de-lensing capability, and thus represent rather conservative bounds in the adopted forecast setup. Indeed the CMB lensing signal represents the main contaminant for measurement of primordial GWs from the BB spectrum and the constraining power will improve accordingly to the capability of tracing this signal. The results are shown in figure 9.10, with a fiducial model assumed to be the best fit one obtained with the *Planck* and BICEP2 datasets. We can clearly see that increasing the accuracy of B-mode polarisation observations removes all the degeneracy with the other cosmological parameters since the measurements would be able to disentangle the effect of horizontal shifting, due to changes in c_T^2, from the vertical shifting induced by varying $r_{0.002}$ or the shape changes due to n_s and the running of the spectral index. As a result we can say that the parameter c_T^2, quantifying the speed of GWs at recombination, is orthogonal to other cosmological parameters, as it is theoretically expected. We can also notice that considering an instrument with higher precision like PRISM, does not improve significantly on the determination of c_T^2 with respect to CORE, since the effect is seen at degree angular scales where both of the considered experiments are cosmic variance limited.
Overall, we see that the next generation of CMB experiments will constrain the speed of cosmological GWs with a 1% accuracy independently of the assumed shape of the primordial power spectrum.

9.5 Chapter Summary

In this chapter, we described how we equipped and used EFTCAMB with a modified version of CosmoMC, that we dubbed EFTCosmoMC, creating a bridge between the EFT parametrization of the dynamics of perturbations and observations. EFTCosmoMC allows to practically perform tests of gravity and get constraints analyzing the cosmological parameter space with several cosmological observables.

As discussed in Section 9.1, exploring the parameter space requires a step by step check of the stability of the theory. We implemented the resulting stability conditions as *viability priors* that makes the Monte Carlo step be rejected whenever it would fall in the unstable region of the parameter space. The latter procedure, in our view, represents a clean and natural way to impose priors on parameters describing the dark sector.

To illustrate the use of the EFTCAMB/EFTCosmoMC package, we have derived constraints on a *pure* linear EFT model. We used three different combinations of *Planck*, WP, BAO and CMB lensing data sets to show their different effects on constraining the parameter space. For both models we have adopted the designer approach built-in in EFTCAMB and have considered the case of a

ΛCDM as well as of a wCDM background.

For the linear EFT model, we have derived bounds on the only model parameter, i.e the present value of the conformal coupling functions $\Omega_0^{\rm EFT}$, as described in Section 9.2. In the case of a ΛCDM background, we have found that the latter needs to satisfy $\Omega_0^{\rm EFT} \geq 0$ as a viability condition and with *Planck*+WP+BAO+lensing data we get a bound of $\Omega_0^{\rm EFT} < 0.061$ (95%C.L.) (the three different data compilations give similar results). For the wCDM expansion history, the outcome of the stability analysis is shown in Figure 9.1; specifically, there is a stable region in parameter space where the dark energy equation of state can be smaller than -1 as long as the corresponding value of $\Omega_0^{\rm EFT}$ is high enough to stabilize perturbations in the dark sector; finally, the value $\Omega_0^{\rm EFT} = 0$ corresponds to a minimally coupled model and requires $w_0 > -1$, like in the case of quintessence. The combined bound on $\Omega_0^{\rm EFT}$ with *Planck*+WP+BAO+lensing data gives $\Omega_0^{\rm EFT} < 0.058$ (95%C.L.).

To further showcase the applicability of the EFT framework and EFTCAMB/EFTCosmoMC, in Section 9.2.2, we have studied how these observational bounds change when considering massive neutrinos along with a MG model.

It is well known that the addition of massive neutrinos to the standard cosmological model affects the growth of structures in the Universe. On the other hand, the same imprint on structure formation might be also a characteristic of a class of scalar tensor theories. That is why the degeneracy between the massive neutrino component and models of modified gravity has been extensively investigated.

In the case of the *pure* linear EFT model we found that there is no appreciable degeneracy between the present day value of the coupling, $\Omega_0^{\rm EFT}$, and the sum of neutrino masses for all the data set combinations that we considered. While a more extensive investigation of different non-minimally coupled pure EFT models is left for future work, we stress that the absence of degeneracy is to be considered peculiar of the specific parametrization chosen for the coupling, i.e. linear in the scale factor. As a result the constraints on $\Omega_0^{\rm EFT}$ slightly improve with respect to the one previously obtained in [7] regardless of the presence of massive neutrinos. The combination of the PLC, BAO, lensing and WiggleZ data then results in $\Omega_0^{\rm EFT} < 0.05$ and $\sum m_\nu < 0.26$ at 95% C.L..

We then investigated, in Section 9.3, the possibility of using the EFT framework to explore the physical origin of some tension between cosmological data sets. The results of *Planck*-2015, in fact, revealed some interesting tensions between CMB temperature and polarization anisotropies and CMB lensing. These tensions add to the one reported by LSS surveys, like CFHTLenS, that seem to favour a smaller σ_8. If this is not due to some unaccounted systematic effects, this might be an indication of exotic physics beyond the base-ΛCDM model and as such should be investigated in great detail.
In Section 9.3, using a simulation of the *Planck*-2015 data set, we tried to reconcile this tension with some modified gravity models. In particular we studied whether this tension can be mitigated by models characterized by a constant conformal coupling between gravitational and matter perturbations. We found that this model can mimic the role of $A_{\rm L}$ even if, generally, the amplitude of lensing, with respect to the GR case, is scale dependent. In order to provide

a good fit to the *Planck*-like CMB anisotropy spectra, however, these models predict an enhancement of the growth on smaller scales that make the tension in σ_8 even worse. From these results we can conclude that the tension between the growth of matter perturbations assessed from CMB power spectra, CMB lensing and LSS surveys can be mimicked by modified gravity models but is hardly relieved by simple models beyond the standard ΛCDM one. This in turn suggests to investigate more complicated models, possibly with different time dependencies, to allow for different regimes of growth at the times at which each of these observations is more sensitive.

At last, in Section 9.4, we have used a parametrized, EFT-like approach, to study the observational imprint of a modified speed of gravitational waves. This modification, indeed leaves an imprint on the power spectrum of B-modes of the Cosmic Microwave Background (CMB) anisotropies polarisation.

We have derived the expected constraints on this quantity from from *Planck* and the BB power spectrum on the degree angular scale as reported by the BICEP2 experiment. Since we did not account for the presence of dust polarization these results give us an hint of the expected constraining power coming from an initial detection of the tensor component of the B-mode spectrum. Moreover, we have derived the projected constraints which will be within reach of the future generation, polarisation dedicated CMB satellites.

We have found that a departure of c_T from the speed of light has an apparent projection effect on the characteristic peak of the BB power spectrum at the degree scale, which corresponds to the part produced by cosmological GWs. We have identified the origin of this feature in the effective "re-scaling" of the gradient term of the wave equation (9.9), affecting the horizon re-entry time for the tensor component, and thus the location of the BB peak in the angular domain.

Since the effect of c_T^2 is rather orthogonal with that of other cosmological parameters, we have established the ultimate constraining power by adopting the specifications of the future proposed CMB satellites. We have found that those are indeed capable of resolving the parameter space into a neat constraint on c_T, without degeneracies with other parameters, down to a percent level. We observe that such a constraining power is almost competitive with the one from observations of binary pulsar timing. These results confirm the relevance of CMB polarisation measurements in exploring fundamental physics.

	Linear EFT+ΛCDM			Linear EFT+wCDM		
	Planck+WP	*Planck*+WP+BAO	*Planck*+WP+BAO+lensing	*Planck*+WP	*Planck*+WP+BAO	*Planck*+WP+BAO+lensing
Parameters	mean ± 68% C.L.	mean ± 68% C.L.	mean ± 68% C.L.	mean ± 68% C.L.	mean ± 68% C.L.	mean ± 68% C.L.
$100\Omega_b h^2$	2.201±0.028	2.205±0.025	2.211±0.025	2.198±0.028	2.209±0.026	2.216±0.026
$\Omega_c h^2$	0.1199±0.0026	0.1193±0.0017	0.1188±0.0016	0.1201±0.0026	0.1185±0.0019	0.1180±0.0018
$100\theta_{\rm MC}$	1.04121±0.00063	1.04133±0.00058	1.04132±0.00055	1.04119±0.00062	1.04141±0.00058	1.04142±0.00058
τ	0.089±0.013	0.090±0.013	0.088±0.012	0.088±0.013	0.091±0.013	0.091±0.012
n_s	0.9596±0.0073	0.9608±0.0057	0.9619±0.0059	0.9588±0.0071	0.9625±0.0060	0.9637±0.0060
${\rm Log}(10^{10}A_s)$	3.086±0.024	3.088±0.025	3.084±0.022	3.086±0.025	3.088±0.025	3.088±0.023
$\Omega_0^{\rm EFT}$	< 0.066 (95%C.L.)	< 0.072 (95%C.L.)	< 0.061 (95%C.L.)	< 0.065 (95%C.L.)	< 0.076 (95%C.L.)	< 0.058 (95%C.L.)
w_0	–	–	–	$-0.88^{+0.21}_{-0.14}$ (95%C.L.)	$-0.96^{+0.09}_{-0.06}$ (95%C.L.)	$-0.95^{+0.08}_{-0.07}$ (95%C.L.)
Ω_m	0.310±0.016	0.306±0.010	0.3028±0.0096	0.349±0.041	0.314±0.013	0.312±0.013
H_0	67.71±1.20	67.99±0.79	68.22±0.75	64.10±3.26	66.99±1.22	67.08±1.21
$\chi^2_{\rm min}/2$	4902.799	4904.074	4908.849	4902.921	4903.957	4908.846

Table 9.1: Mean values and 68% (or 95%) confidence limits for primary/derived parameters for a linear EFT model on ΛCDM/wCDM background.

	Varying m_ν	
Data sets	$\Omega_0^{\rm EFT}$ (95% C.L.)	$\sum m_\nu$ (95% C.L.)
PLC + BAO	< 0.06	< 0.30
PLC + BAO + WiggleZ	< 0.06	< 0.25
PLC + BAO + lensing + WiggleZ	< 0.05	< 0.26

Table 9.2: Constraints on the cosmological parameter of *pure* linear EFT parametrization with varying neutrino mass, using different combinations of data sets.

CP	Mock-A	Mock-B
$10^9 A_s$	2.10745	2.14338
n_s	0.97468	0.97156
τ	0.0611	0.0664
$\Omega_b h^2$	0.022674	0.022379
$\Omega_c h^2$	0.11639	0.11748
H_0	69.02	68.39
$A_{\rm L}$	1.28	1.02
$\sum m_\nu$/eV	0.06	0.06

Table 9.3: Fiducial parameters of the mock data sets

Experiment	Frequency	$\theta_{\rm beam}$	σ_T	σ_P
Planck:	217	5.02	13.1	26.7
	143	7.30	6.0	11.4
	100	9.68	6.8	10.9

Table 9.4: *Planck* blue book instrumental specifications

$\chi^2_{\rm best-fit}$	Mock-A	Mock-C
base-ΛCDM	1967.373	3314.547
base-ΛCDM+$A_{\rm L}$	1951.122	3303.599
$f(R)$	1952.325	3305.251
Ω_+	1967.604	3314.676
$\Omega_\pm$	1951.109	3304.507

Table 9.5: The best-fit χ^2

Part IV

Test of Specific DE/MG Models

Chapter 10

Designer $f(R)$ Gravity

In this Chapter we showcase the flexibility of the EFTCAMB code in studying *mapping* models and, in particular, $f(R)$ models that mimic a given expansion history. The simplicity of its theoretical structure and the representative phenomena to which it leads at the level of growth of structure, have long made $f(R)$ gravity a popular model of modified gravity.

To start with, we focus on $f(R)$ models that reproduce a ΛCDM expansion history and we compare our outputs to those of the common implementation of these theories in MGCAMB [199, 200, 195]. This allows us to perform a consistency check of our code as well as to identify some peculiar features in the power spectra contributed by the sub-horizon dynamics of the scalaron, which is neglected by the QS implementation of $f(R)$ in MGCAMB. We then extend to designer $f(R)$ models with more general expansion histories, considering both a constant but different than -1 and a time-varying dark energy equation of state. We analyze in details all the imprints of these models on the different observables and the corresponding observational constraints.

We then investigate the degeneracy between massive neutrinos and $f(R)$ theories, with the designer approach, updating the bound on the Compton scale parameter B_0 with and without massive neutrino.

At last we explore the tensions between CMB temperature and polarization anisotropies and CMB lensing, within $f(R)$ models.

The examples that we present should highlight the versatility of our EFTCAMB code: it can be used to evolve the full dynamics of linear perturbations for any given DE/MG model that can be cast into the EFT language, without the need to resort to the QS approximation.

10.1 Introduction to Designer $f(R)$ gravity

Let us begin by briefly reviewing the theory of $f(R)$ gravity. We consider the following Lagrangian in Jordan frame

$$S = \int d^4x\sqrt{-g}\,[R + f(R)] + S_m\,, \tag{10.1}$$

where $f(R)$ is a generic function of the Ricci scalar and the matter sector is minimally coupled to gravity.

For a detailed discussion of the cosmology in $f(R)$ theories we refer the reader to [249, 250, 251, 252]. Here we will briefly review the main features that are of interest for our analysis. The higher order nature of the theory translates into having an extra scalar d.o.f. which can be identified with the field $f_R \equiv df/dR$, commonly dubbed the *scalaron* [253]. Implementing the mapping to EFT, we have that Stückelberg field for $f(R)$ theories is given by $\pi = \delta R/R$ [162], which can be easily related to the perturbation of the scalaron, δf_R.

Viable $f(R)$ models need to satisfy certain conditions of stability and consistency with local tests of gravity [251], which can be inferred from the conditions in Sec. 6.5 once the mapping (10.4) is implemented. Finally, given the higher order of the theory, it is possible to reproduce any given expansion history by an appropriate choice of the $f(R)$ function [249, 251]. In other words, $f(R)$ models can be treated with the so called *designer* approach which consists in fixing the expansion history and then using the Friedmann equation as a second order differential equation for $f[R(a)]$. As we will recap shortly, generically one finds a family of viable models that reproduce this expansion; the latter are commonly labeled by the boundary condition at present time, f_R^0. Equivalently, they can be parametrized by the present day value of the function:

$$B = \frac{f_{RR}}{1+f_R}\frac{\mathcal{H}\dot{R}}{\dot{\mathcal{H}}-\mathcal{H}^2}\,. \tag{10.2}$$

Let us recall that the heavier the scalaron the smaller B_0 and $|f_R^0|$.

10.2 Mapping $f(R)$ to the EFT framework

It is straightforward to map $f(R)$ models of gravity into the EFT formalism. In particular this has been already presented in [162, 163] and here we will briefly summarize the main steps and the final result. Starting from action (11.1), we can expand it in perturbations of the Ricci scalar around its value on a FLRW background, $R^{(0)}$. It turns out to be convenient to do so by choosing a preferred time-slicing for which the constant time hypersurfaces coincides with the uniform R hypersurfaces. This allows to truncate the expansion at linear order since all higher order terms will contribute always at least one power of δR to the equations, and the latter vanishes. Therefore, to linear order we have:

$$S = \int d^4x\sqrt{-g}\frac{m_0^2}{2}\left\{\left[1+f_R(R^{(0)})\right]R + f(R^{(0)}) - R^{(0)}f_R(R^{(0)})\right\}\,. \tag{10.3}$$

Comparing this action with the EFT one (6.1), we can easily derive the following mapping recipe:

$$\Lambda = \frac{m_0^2}{2}\left[f - Rf_R\right] \quad ; \quad c = 0 \quad ; \quad \Omega = f_R\,. \tag{10.4}$$

10.3 Comparison with MGCAMB on Cosmological Predictions

MGCAMB relies on two functions of time and scale to parametrize deviations in the Poisson and anisotropy equations, closing the system of equations for matter in conformal Newtonian gauge with the two following equations:

$$k^2\Psi \equiv -\frac{a^2}{2M_P^2}\mu(a,k)\rho_m\Delta_m, \qquad \frac{\Phi}{\Psi} \equiv \gamma(a,k)\,. \tag{10.5}$$

In order to evolve perturbations in $f(R)$ models one has to specify the corresponding forms for $\mu(a,k)$ and $\gamma(a,k)$, and this can be achieved by taking the QS limit of the linearly perturbed equations, which corresponds to neglecting time-derivatives of the metric potentials and of the scalar field, as well as focusing on sub-horizon scales $k \gg \mathcal{H}$. In this limit we have:

$$\begin{aligned} k^2\Psi &= -\frac{1}{1+f_R}\frac{1+4f_{RR}/(1+f_R)k^2/a^2}{1+3f_{RR}/(1+f_R)k^2/a^2}\frac{a^2\rho_m\Delta_m}{2M_P^2}, \\ \frac{\Phi}{\Psi} &= \frac{1+2f_{RR}/(1+f_R)k^2/a^2}{1+4f_{RR}/(1+f_R)k^2/a^2}. \end{aligned} \tag{10.6}$$

On sub-horizon scales the dynamics of linear perturbations in $f(R)$ is generally described sufficiently well by this QS approximation [195]. Eqs. (10.6) have inspired the following parametrization [120, 254, 195, 200]:

$$\begin{aligned} \mu^{\rm BZ}(a,k) &= \frac{1}{1-B_0\Omega_m a^{s-1}/2}\frac{1+2/3B_0\left(k/H_0\right)^2 a^s}{1+\frac{1}{2}B_0\left(k/H_0\right)^2 a^s}, \\ \gamma^{\rm BZ}(a,k) &= \frac{1+1/3B_0\left(k/H_0\right)^2 a^s}{1+2/3B_0\left(k/H_0\right)^2 a^s}, \end{aligned} \tag{10.7}$$

to which we will refer as the BZ parametrization that consists in assuming

$$\frac{f_{\rm RR}}{1+f_{\rm R}} \equiv \frac{B_0}{6H_0^2}a^{s+2}. \tag{10.8}$$

A standard way of extracting predictions for cosmological observables and comparing $f(R)$ models to data is the one of modeling the late time universe by inserting Eq. (10.7) into MGCAMB, leaving B_0 as a free parameter and fixing $s = 4$ [199]. Let us recall that a $f(R)$ model defined by Eq. (10.7) with a constant value for s will not in general be capable of reproducing the full ΛCDM expansion history. However, it works as a good approximation for each epoch alone [132], as can be inferred from Eq. (10.8). Indeed a reasonable value of s is given by $s \approx 5$ during radiation domination, $s \geq 4$ during matter domination and $s < 4$ during the late time phase of accelerated expansion. For small values of B_0, it is customary to fix $s = 4$ as discussed in [195], however here we will re-examine this choice in view of the precision and extent of upcoming surveys.

In order to compute observables for these theories with MGCAMB it suffices to fix the expansion history to that of ΛCDM, $s = 4$ and input (10.7) for μ and

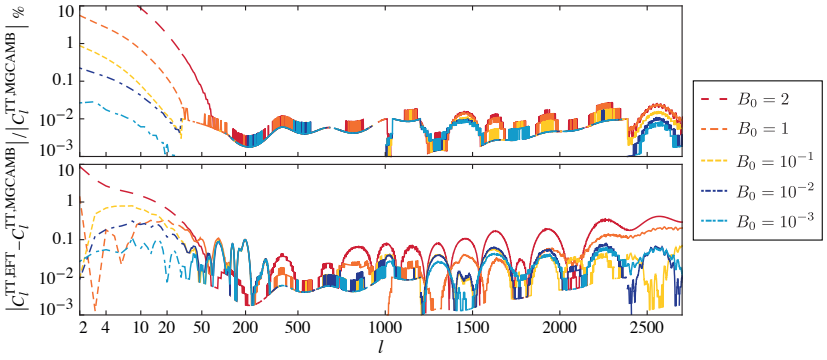

Figure 10.1: *Upper panel*: comparison between the temperature anisotropy angular power spectra of EFTCAMB and MGCAMB for $f(R)$ models with a ΛCDM expansion history but different values of B_0 and modeled via the BZ approach described in Sec. 10.3. *Lower panel*: same comparison for the case of a designer $f(R)$ model with ΛCDM background. For a detailed interpretation of the plots see Sec. 10.3. From [8].

γ for several choices of B_0. EFTCAMB, on the contrary, does not rely on the quasi-static BZ parametrization, but rather solves the full equations; therefore even after fixing the expansion history to ΛCDM we need to feed the code a form for the EFT functions. We consider two cases:

- BZ case: from Eq. (10.8) we read off the implications of the BZ parametrizations for $f(R)$ and then we reconstruct the corresponding Ω and Λ to input in the full equations for linear perturbations. We again stress that our code does not rely on any QS approximation;
- Designer case: we implement in our code the $f(R)$ designer approach to reconstruct viable $f(R)$ models that mimic the ΛCDM expansion history and determine the corresponding Ω, Λ via the mapping, Eq. (10.4).

The BZ case allows us to make a check of reliability of our code with minimal changes with respect to the way $f(R)$ theories are treated in MGCAMB. The designer case corresponds to a proper full treatment of $f(R)$ models and therefore let us fully exploit the potential of our code, avoiding spurious effects due to the BZ approximation; this will allow us to check the accuracy of the QS approximation in $f(R)$ models to a new extent. The latter case corresponds to the proper treatment of the background operators in the *mapping* EFT cases.

Let us start with the BZ case. Using the mapping formulae (10.4) we see that the BZ ansätz (10.8) can be mapped into the EFT formalism as follows:

$$\begin{aligned}
\Omega &= -1 + e^{-\frac{3B_0\Omega_m a^{s-1}}{2(s-1)}} = -\frac{3}{2}\frac{B_0\Omega_m a^{s-1}}{s-1} + O(B_0^2), \\
\frac{\Lambda}{m_0^2} &= -\frac{\rho_{\rm DE}}{m_0^2} + B_0 H_0^2 \frac{27a^4\Omega_m^2 - 9\Omega_m a^s\left(4a^3(s-4)\Omega_\Lambda + (s-1)\Omega_m\right)}{4a^4(s-4)(s-1)} + O(B_0^2).
\end{aligned} \tag{10.9}$$

As in MGCAMB, we fix $s = 4$ and we use different values of B_0 ranging from very large ones ($B_0 = 2$) to very small ones ($B_0 = 10^{-3}$). The comparison of the temperature spectra from the two codes is shown in the upper panel of Fig. 10.1. As we can clearly see the agreement on small scales is very good ($\lesssim 0.01\%$) and remains under control ($\lesssim 0.1\%$) even on very large scales for small values of B_0 ($\lesssim 0.01$). We get some tension between the two codes, (relative difference $> 1\%$), at low multipoles for large values of B_0 ($\gtrsim 0.1$). This is partially due to the way we treat the background in this case; first of all when $B_0 \gtrsim 1$ the correction term in (10.9) cannot be neglected anymore. For example, for $B_0 = 2$ this introduces an order of magnitude approximation error in Ω and Λ. Secondly, there is some fictitious dynamics of the scalar d.o.f., excited by the fact that the BZ parametrization (10.8) does not give an exact representation of the background dynamics. We also expect this discrepancy to be partially due to the fact that the QS approximation inherent in the treatment of $f(R)$ in MGCAMB does not give a full account of the ISW effect. However, in order to make meaningful statements about the latter, we need to make a comparison between the output of MGCAMB and the output of EFTCAMB with the full treatment of the background, i.e. consider the designer case mentioned above.

Let us then abandon the BZ parametrization for our background cosmology, and rather adopt the designer approach that allows us to reconstruct all the viable $f(R)$ models that reproduce a ΛCDM expansion history. As mentioned earlier, $f(R)$ models are able to reproduce any given expansion history by means of a designer approach firstly discussed in [249] and later generalized to include radiation and a time varying dark energy equation of state in [251]. The Friedmann equation for $f(R)$ theories can indeed be written as a second order differential equation for $f[R(a)]$, namely:

$$f'' - \left(1 + \frac{H'}{H} + \frac{R''}{R'}\right) f' + \frac{R'}{6H^2} f = -\frac{R'}{3M_P^2 H^2} \rho_{\rm DE}, \tag{10.10}$$

where primes denote differentiation w.r.t. $\ln a$ and $\rho_{\rm DE}$ is the energy density of the effective dark energy component. The procedure consists then in fixing the expansion history by choosing an equation of state of dark energy $w_{\rm DE}(a)$, determining the corresponding energy density like in (8.4) and solving Eq. (10.10) for f. For any given expansion history the solution will consist in a family of $f(R)$ models labeled by B_0. We implement this procedure in EFTCAMB and show the output in Fig. 10.2; for the ΛCDM and wCDM cases one can notice that the reconstructed $f(R)$ are in agreement with those of [249]. We show also the results for the case of a CPL background.

We start with a ΛCDM expansion history, consider different values of B_0 and compare our results with those of MGCAMB in the lower panel of Fig. 10.1. The overall agreement for values of $B_0 < 0.1$ is within 0.1% in the high multipoles regime and within 1% in the low multipoles regime. For larger values, i.e. $B_0 \gtrsim 1$ (which are in tension with constraints from current data [255, 155, 256, 257]) we notice that at large scales there is a better agreement, while on smaller scales we get some systematic offset. In what follows we analyze this discrepancy using $B_0 = 2$ which emphasizes the offset of the codes and facilitates the investigation.

We choose to investigate the source of the above mentioned discrepancy by comparing the functions $\mu(z, k)$ and $\gamma(z, k)$ in the BZ parametrization (10.7) to

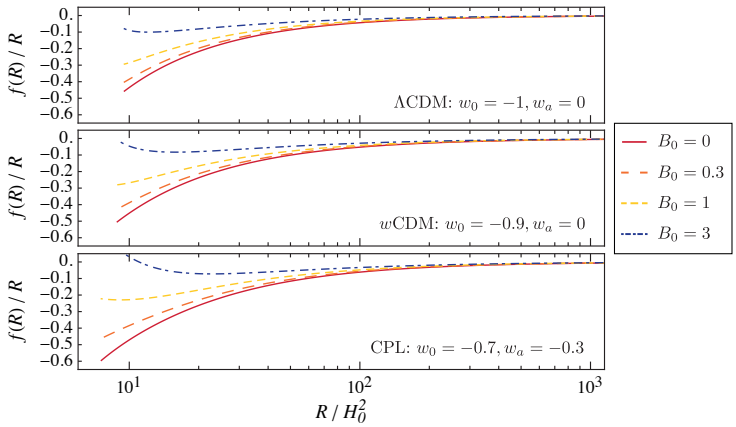

Figure 10.2: We show designer $f(R)$ models that mimic different expansion histories as reconstructed with our code: ΛCDM in the top panel, a constant $w_{\rm DE} = -0.9$ in the middle panel and a time-varying $w_{\rm DE}$ in the bottom panel. For each case we plot four curves corresponding to four different values of the boundary condition B_0. The values of $w_{\rm DE}$ in the first two panels are chosen to facilitate the comparison with [249]. See Sec. 10.3 for a detailed explanation. From [8].

those inferred from our code. The latter are obtained evolving the full dynamics for the designer $f(R)$ model in EFTCAMB and then substituting the perturbations into Eqs. (10.5), therefore we indicate them with a subscript 'des'. In Fig. 10.3 we plot all these quantities in the (z, k) space, as well as the fractional difference between the BZ and designer quantities both for μ and for γ. Overall we get good agreement between the BZ quantities and our designer ones, reproducing the known pattern of recovery of the standard GR behavior at early times on large scales, and having some significant deviations from the standard behavior on small scales at late times. After a more careful look, we see that on super-horizon scales the differences between $\mu_{\rm BZ}(\gamma_{\rm BZ})$ and $\mu_{\rm des}$ $(\gamma_{\rm des})$ are relatively small and are simply due to the fact that our full-Boltzmann code catches some well known dynamics of the scalaron at those scales, and the return to GR is not as exact as in the quasi-static BZ where it is imposed a priori. On smaller scales, in particular on scales around the Compton wavelength of the scalaron, the fractional difference plot shows some non-trivial differences between the BZ and designer quantities. In other words, at late times and on scales around the Compton one, EFTCAMB is able to catch some dynamics of the scalaron which is not entirely negligible and perhaps is the source of the discrepancies that we noticed in the CMB lensing spectrum on small scales. The latter appears especially in models for which the Compton wavelength of the scalaron is close to the horizon scale and the sub-horizon and sub-Compton regimes are not clearly distinguished.

To investigate the non-trivial sub-horizon dynamics further, we introduce

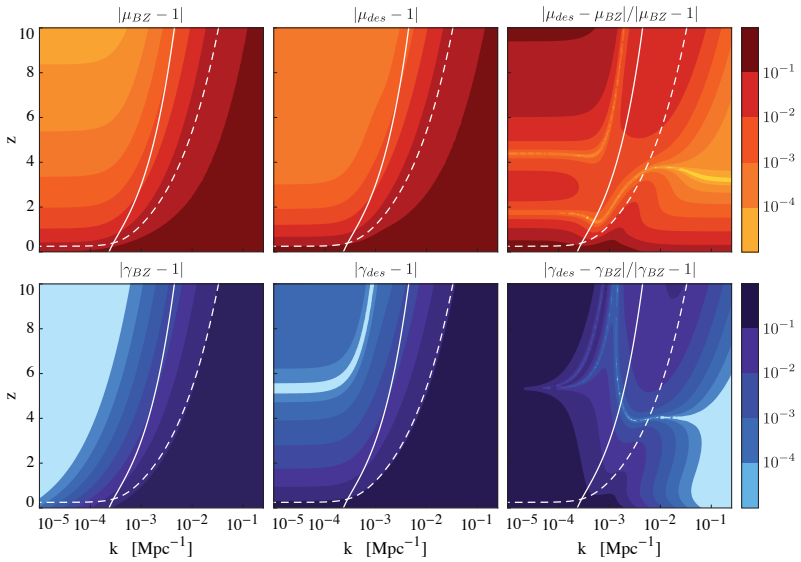

Figure 10.3: We compare the functions $\mu(z,k)$ and $\gamma(z,k)$ in Eq. (10.7), with $B_0 = 2$ and $s = 4$, to those computed in EFTCAMB evolving the full set of Einstein-Boltzmann equations for $f(R)$ models that reproduce a ΛCDM expansion history and have $B_0 = 2$. In all plots, the solid line represents the physical horizon while the dashed line represents the Compton wavelength of the scalaron (10.2). *Upper panel*: respectively $|\mu_{\rm BZ} - 1|$, $|\mu_{\rm des} - 1|$ and $|\mu_{\rm BZ} - \mu_{\rm des}|/|\mu_{\rm BZ} - 1|$. *Lower panel*: $|\gamma_{\rm BZ} - 1|$, $|\gamma_{\rm des} - 1|$ and $|\gamma_{\rm BZ} - \gamma_{\rm des}|/|\gamma_{\rm BZ} - 1|$. See Sec. 10.3 for a detailed explanation. From [8].

the following indicator:

$$\xi \equiv \frac{\dot{\pi}}{\mathcal{H}\pi}\,, \tag{10.11}$$

which quantifies deviations from quasi-staticity for the scalar degree of freedom. In this context with quasi-staticity we mean the fact that time derivaties of the quantities of interest can be neglected. We plot ξ in the left panel of Fig. 10.4; from that contour plot one can notice that the scalaron has some dynamics on super-horizon scales, it then slows on scales of the order of its Compton wavelength and finally resumes evolving in time below the latter scale, especially at low redshift. Let us stress that ξ is a good indicator of whether one can neglect the time derivatives of the scalar field, but does not necessarily carry information on the dynamics of the metric potentials and therefore on the overall validity of the QS approximation. The latter will depend on how the scalar field couples with gravity and the matter sector. In the right panel of Fig. 10.4 we plot the behavior of π as a function of redshift for four different scales, comparing it with the evolution of the source term in Eq. (6.20). The curves confirm what we inferred about the dynamics of π from the behavior of the indicator ξ; on very large scales the scalaron evolves slowly, following the source term at early times and then almost stops evolving at extremely late times. On the other hand, on smaller scales, the field evolves slowly at early times, tracking the source and

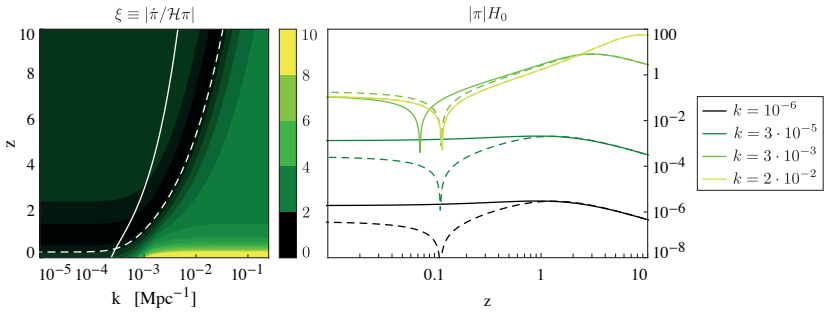

Figure 10.4: *Left:* time and scale dependence of ξ Eq. (10.11), which is the quantity we introduce as an indicator of the applicability of the QS approximation. *Right:* time evolution of the Stückelberg field $|\pi|H_0$ (solid curve) compared to that of the source $|H_0 E/(C + k^2 D)|$ (dashed curve) for four different scales (dark curves are for large scales, light curves are for smaller, but linear, scales). Notice that for $k = 2 \cdot 10^{-2}$ the source and the field coincide. In both panels we use an $f(R)$ model with a ΛCDM expansion history and $B_0 = 2$. See Sec. 10.3 for a detailed explanation. From [8].

continues to evolve even at later times eventually crossing zero at some point. At this point the QS approximation for the dark sector breaks down because the field becomes very small while its derivatives remains finite.

To summarize, we see that the strongest deviations from the BZ parametrization of $f(R)$ gravity are found close to the Compton wavelength of the scalaron. Below this scale, depending on the value of B_0, the dynamics of the scalar field might be non-negligible even if we are on sub-horizon scales; and depending on the coupling of π to gravity and dark matter, this might generate a non-standard dynamics of matter perturbations. We expect deviations from QS, parametrized predictions to show up in cosmological observables around $k_c^2 = 6H_0^2/B_0$ which is roughly the Compton scale today. For what concerns the CMB, this effect will show up, for very large values of B_0, both on very large scales due to the differences induced on the ISW effect and on small scales due to the modified evolution of perturbations that will influence the lensing of the CMB. As the value of B_0 decreases the Compton wavelength will move to scales that just contribute to the lensing, but the magnitude of the effect will decrease as well. In the end, for small values of B_0, this will just introduce some very small, negligible, discrepancies that we can see in Fig. 10.1. We however stress that ongoing experiments, such as *Planck*, and forthcoming ones, like Euclid, are expected to be much more sensitive to these effects which will have to be properly accounted for when extracting predictions for the observables of interest.

10.4 Designer $f(R)$ models on non-ΛCDM background

In this section we shall use EFTCAMB to compute the power spectra of different cosmological observables for $f(R)$ models that mimic more general expansion

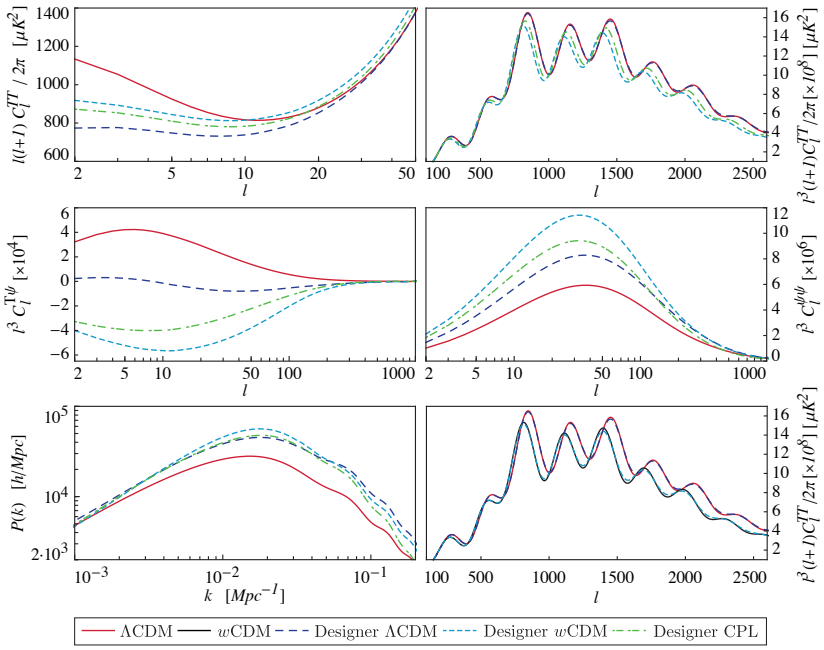

Figure 10.5: Power spectra of several cosmological observables for $f(R)$ models mimicking both ΛCDM and non-ΛCDM expansion histories. The red solid line represents predictions for the ΛCDM model while the black solid one stands for a wCDM with $w_0 = -0.7$ (shown only in the bottom right panel). Dashed lines portray designer $f(R)$ models with different expansion histories but same boundary condition $B_0 = 1$: the long-dashed dark blue line corresponds to models with a ΛCDM background, the short-dashed blue to models with a wCDM background with $w_0 = -0.7$ and the dashed-dotted light blue to models with a CPL background with $w_0 = -0.7$ and $w_a = -0.3$. *Upper panels:* CMB temperature power spectra; *central panels:* lensing-temperature cross-correlation (left) and the lensing potential power spectra (right); *lower panels:* total matter (left) and CMB temperature power spectra (right) for ΛCDM / wCDM and the corresponding designer $f(R)$ models. See Sec. 10.4 for a detailed explanation. From [8].

histories. As above, after choosing an expansion history, we reconstruct viable models via an implementation in our code of the $f(R)$ designer approach and the mapping formulae (10.4). We consider a wCDM expansion history with $w_0 = -0.7$, a CPL model with $w_0 = -0.7$, $w_a = -0.3$ and we compare the results with those of the ΛCDM models analyzed in 10.3. In all cases we fix $B_0 = 1$ in order to make the various effects clearly visible. In particular we choose the parameters of the CPL model in order to resemble a cosmological constant at high redshift while evolving toward the wCDM case at late times.

We show the power-spectra observables calculated with our code in Fig. 10.5 and in what follows we give a detailed overview of each result. The first, top left, panel shows the ISW part of the CMB temperature power spectrum. On

these angular scales we notice the effects of a modified time evolution of the gravitational potentials at late times, that results in an overall suppression of power at low multipoles. This effect will, however, be shaded by cosmic variance which lowers the statistical significance of these deviations. In fact, we expect differences from the ΛCDM behavior at small scale to acquire a primary role in testing alternative models with ongoing and upcoming surveys [258]. We zoom in on the modifications to C_ℓ^{TT} at small scales in the top right panel, where we can more clearly see the part of the temperature power spectrum which is influenced by gravitational lensing. As expected, we notice that the change in the expansion history shifts the position of the peaks and reduces their amplitudes, while the modification of gravity could further smear the acoustic peaks in the lensing part. This can be clearly seen in the lower right figure which compares explicitly the resulting temperature spectra from CAMB and our designer EFTCAMB in ΛCDM and wCDM background. The impact of modifications of gravity on the CMB lensing potential is shown in the center right figure where we plot $C_\ell^{\psi\psi}$; one can appreciate that the different expansion histories change the angular size of the lenses slightly shifting the position of the peak, while the different dynamics of perturbations greatly impact the amplitude of the spectrum. Ongoing CMB experiments like *Planck*, ACT and SPT [81, 259, 260] have directly measured this observable, and in the upcoming future they will measure it with even greater accuracy, so to this extent codes like ours, that evolve the full dynamics and capture interesting features at those scales of the CMB spectrum, will be very useful.

Another quantity which is greatly influenced by modification of gravity is the power spectrum of the cross-correlation between temperature and lensing potential, i.e. $C_\ell^{\psi T}$. As we already commented, the evolution of the Weyl potential sources both the ISW and weak lensing effect inducing a correlation between these two. From the center left panel of Fig. 10.5 one can notice that for the ΛCDM model the cross-correlation is large and positive, while for $f(R)$ models with a ΛCDM expansion history but $B_0 = 1$, the cross-correlation oscillates around zero. Interestingly, the signal can be increased by changing the expansion history while keeping $B_0 = 1$; in this case the cross-correlation will become large and negative.

Finally, we shall comment on the effects that appear in the total matter power spectrum. In the bottom left panel of Fig. 10.5 we can appreciate that as soon as B_0 is different from zero the spectrum is shifted, both in amplitude and in scale, with respect to the ΛCDM one. In addition a non-standard expansion history changes the amplitude of the spectrum at the peak and also the slope at smaller, but still linear, scales as we can see comparing the light blue lines to the dark blue ones. Interestingly, we can clearly see that the CPL model lies between the ΛCDM and the wCDM one; the amplitude of the peak, which is influenced by the early time expansion history, lies close to the ΛCDM one while the slope at smaller scales, which is affected by the late time evolution of matter perturbations, stays close to the wCDM model as w is approaching $w_0 = -0.7$.

10.5 Cosmological Constraints Without Massive Neutrinos

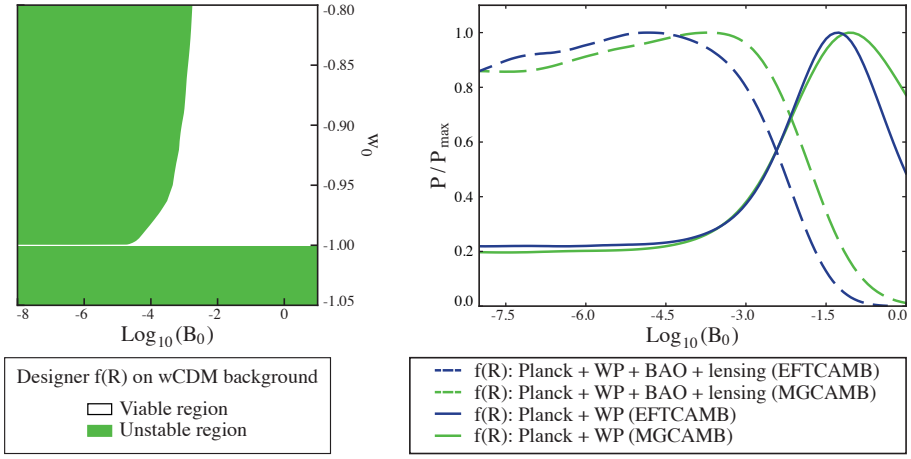

Figure 10.6: *Left panel*: stability regions of designer $f(R)$ models on a wCDM background. The cosmological parameters defining the expansion history are set to their CAMB default values: $H_0 = 70\,\mathrm{Km/s/Mpc}$, $\Omega_b = 0.05$, $\Omega_c = 0.22$, $T_{\mathrm{CMB}} = 2.7255\,\mathrm{K}$. *Right panel*: marginalized constraints on $\mathrm{Log}_{10}(B_0)$ describing designer $f(R)$ models on ΛCDM background for two data sets differing by CMB lensing and BAO. For each data set we compare the results obtained with EFTCAMB with those obtained by MGCAMB [199, 200] for the same designer $f(R)$ models. From [7].

Like in the *pure* EFT case that we treated in Section 9.2, it proves very instructive to investigate the shape of the parameter space as dictated by the stability conditions of Section 9.1. For the designer $f(R)$ model on ΛCDM background it is easy to show that the latter reproduce the known result that in order to have a positive mass of the scalaron B_0 should be greater than zero. It is much more interesting to investigate the shape of the parameter space for $f(R)$ models mimicking a wCDM background expansion history. We do it numerically, through the built-in routine of EFTCAMB, and we show the results in Figure 10.6. The first noticeable feature is that for wCDM models the value of the equation of state of dark energy can not go below -1, which is consistent with what was found in [251]. The second one is that the parameter B_0 controls the limit to GR of the theory *i.e.*when B_0 gets smaller the expansion history is forced to go back to that of the ΛCDM model in order to preserve a positive mass of the scalaron.

In what follows, we shall first investigate the constraints on B_0 in models reproducing ΛCDM background, performing also a comparison with analogous results obtained using MGCAMB [199, 200]. We will then move to study constraints on designer models on a wCDM background.

In the right panel of Figure 10.6, we compare the 1D marginalized posterior distributions of $\mathrm{Log}_{10}B_0$ from our EFTCAMB to those from MGCAMB. Overall there is good agreement between the two results. Moreover, one can notice that

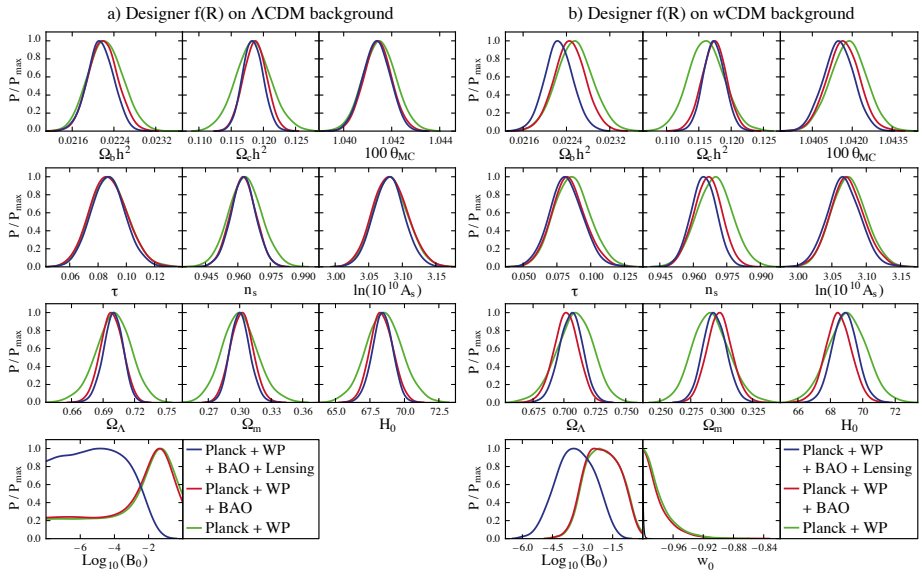

Figure 10.7: 1D Marginalized posterior distributions of cosmological and model parameters for designer $f(R)$ models both on a ΛCDM (left) and wCDM (right) background. Different colors represent different combinations of cosmological data sets. From [7].

generally the constraints obtained with EFTCAMB are a little bit tighter than those obtained with MGCAMB. This is because in the latter code $f(R)$ models are treated with the quasi-static approximation which looses out on some of the dynamics of the scalaron [195], which is instead fully captured by our full Einstein-Boltzmann solver.

The detailed 1D posterior distributions and corresponding marginalized statistics are summarized in Figure 10.7 (a) and Table 10.1 and they are consistent with previous studies employing the quasi-static approximations [72]. The right panel of Figure 10.6 and Figure 10.7 show that lensing data add a significant consrtaining power on B_0. This is because *Planck* lensing data are helpful in breaking the degeneracy between Ω_m and B_0 which affect the lensing spectrum in different ways. Indeed, in $f(R)$ gravity the growth rate of linear structure is enhanced by the modifications, hence the amplitude of the lensing potential spectrum is amplified whenever B_0 is different than zero (see our previous work [8]); however, the background angular diameter distance is not affected by B_0, so the position of the lensing potential spectrum is not shifted horizontally. On the other hand, Ω_m affects both the background and linear perturbation so that both the amplitude and position of the peaks of the lensing potential are sensitive to it.

Similarly to what happens in the linear EFT model, reviewed in Section 9.2, $f(R)$ gravity shows some novel features in the case of a wCDM background. Once again we find a non-trivial likelihood profile of $\mathrm{Log}_{10}B_0$ (see Figure 10.7) for all the three data compilations, with the shape of the marginalized posterior distribution of $\mathrm{Log}_{10}B_0$ being dominated by the shape of the stable region. In

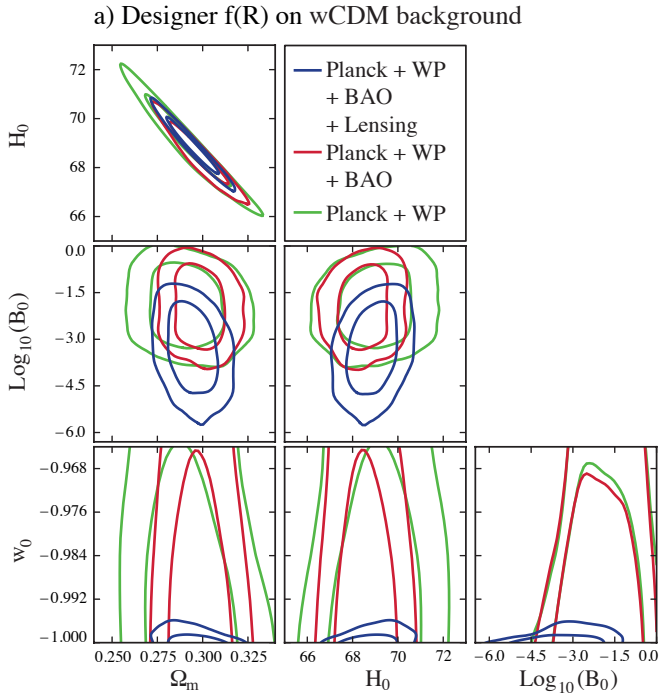

Figure 10.8: 68% and 95% confidence regions on combinations of cosmological parameters for designer $f(R)$ models on wCDM background. Different combinations of observables are indicated with different colors. From [7].

the middle panel of Figure 10.6 one can see indeed that when B_0 tends to smaller values, *i.e.*the theory tends to GR, the stable regions becomes narrower and narrower, with a tiny tip pointing to the GR limit. Since the width of this tip is so narrow compared with the current capability of parameter estimation from *Planck* data, the gains of likelihood of the sampling points inside this parameter throat are not significant, *i.e.*they are uniformly sampled in the throat. Hence, even though the full data set has a very good sensitivity to B_0, the marginalized distribution of $\mathrm{Log}_{10}B_0$ is dominated by the volume of the stable region in the parameter space. A complementary consequence of the shape of the stable region in the (B_0, w_0) space is the fact that when B_0 tends to zero, w_0 is driven to -1. In other words the stability conditions induce a strong correlation between B_0 and w_0 and, as a consequence, in $f(R)$ models, no matter in the ΛCDM or wCDM background case, the GR limit is effectively controlled by a single parameter, *i.e.*B_0.

Finally one can notice that the bound on w_0 with *Planck* lensing data is quite stringent compared to those without lensing, namely:

$$\begin{aligned} w_0 &\in (-1, -0.94)\ (95\%\text{C.L.})\ \text{without lensing}, \\ w_0 &\in (-1, -0.9997)\ (95\%\text{C.L.})\ \text{with lensing}. \end{aligned} \tag{10.12}$$

We argue that this stringent constraint actually is a consequence of the combination of the strong correlation between B_0 and w_0 induced by the viability prior, as discussed above, and the sensitivity of lensing data to B_0, that we capture

well with our code. As shown in [155] *Planck* lensing data is very sensitive to MG parameters such as B_0; indeed, in our analysis with *Planck*+WP+BAO+lensing data we get

$$\mathrm{Log}_{10}B_0 = -3.35^{+1.79}_{-1.77} \quad (95\%\mathrm{C.L.})\ . \tag{10.13}$$

Furthermore, from Figure 10.8, one can see that the ellipse in the $(\mathrm{Log}_{10}B_0, w_0)$ space corresponding to *Planck*+WP+BAO+lensing data (blue) is orthogonal to those without lensing (red and green). In other words, when lensing data is included, $\mathrm{Log}_{10}B_0$ and w_0 display a degeneracy which propagates the stringent constraint on the scalar Compton wavelength from CMB lensing data to w_0. Besides this, we do not find other remarkable degeneracies between B_0 and standard cosmological parameters.

10.6 Cosmological Constraints With Massive Neutrinos

As we discussed in Section 9.2.2, massive neutrinos are an extension of the cosmological standard model which modify the dynamics of linear scalar perturbations, leaving a characteristic imprint on the growth of structure [212]. Specifically, on linear scales smaller than the neutrino free streaming distance, the overall matter clustering is suppressed. Interestingly scalar tensor models of modified gravity leave a complementary signature on the growth of structure, enhancing the clustering on linear scales within the Compton scale of the extra scalar degree of freedom, because of the fifth force mediated by the latter. Depending on the mass of neutrinos and of the scalar field, there may be a significant degeneracy between the two effects at some redshifts and scales. The latter has been investigated to large extent in the context of $f(R)$ theories of gravity, and generally an appreciable degeneracy has been found. However, a common feature of all previous analyses is the assumption of the quasi static (QS) limit in the equations for the perturbations and the employment of the QS parametrization introduced by Bertschinger and Zukin in [120]. In this Section we revisit this degeneracy employing EFTCAMB, which has the important virtue of letting us implement exact $f(R)$ models and evolve their full dynamics. Another key feature of our analyses is the consistent treatment of the background cosmology, which is based on a designer reconstruction of $f(R)$ models with the inclusion of massive neutrinos.

In EFTCAMB massive neutrinos are implemented by numerically integrating their Fermi-Dirac distribution and adding their contribution to all the designer $f(R)$ equations, as well as the EFT perturbation equations.

Things are different in the case when MGCAMB is used. While the framework at the basis of this code is in general not restricted to the quasi static limit, the implementation of specific models like $f(R)$ relies on the parametrization introduced by Bertschinger and Zukin in [120], and later extended in [251, 254, 131], which is quasi static and introduces an approximation for the time evolution of f_R. More specifically, the background is fixed to whatever the desired one is, in this case ΛCDM plus the parameter f_ν modeling massive neutrinos. The effects of modified gravity are then taken into account via the following

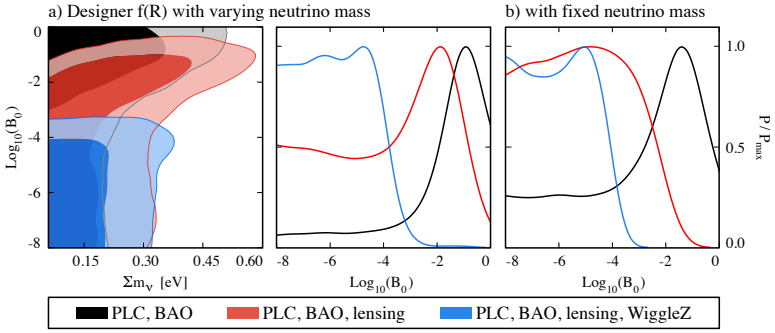

Figure 10.9: *Left:* the marginalized joint likelihood for the present day value of $\mathrm{Log}_{10}B_0$ and the sum of neutrino masses, $\sum m_\nu$. *Center and right:* the marginalized likelihood of $\mathrm{Log}_{10}B_0$ for, respectively, designer $f(R)$ models with varying (a) and fixed (b) neutrino mass. In all three panels different colors correspond to different combination of cosmological observations as shown in legend. The darker and lighter shades correspond respectively to the 68% C.L. and the 95% C.L.. From [5].

parametrization of Poisson and anisotropy equations:

$$k^2\Psi = -\mu(a,k)\frac{a^2}{2M_P^2}\left[\rho_m\Delta_m + 3\left(\rho_m + P_m\right)\sigma_m\right] ,$$
$$k^2\left[\Phi - \gamma(a,k)\Psi\right] = \mu(a,k)\frac{3a^2}{aM_P^2}\left(\rho_m + P_m\right)\sigma_m , \qquad (10.14)$$

where no QS limit has yet been taken, and σ_m is the anisotropic stress from matter, to which neutrinos are expected to contribute at high redshift.

If one wants to implement a specific model, in this case $f(R)$, one needs to reduce to the QS limit, so that Einstein equations become a set of algebraic equations and it is easy to find an analytical expression for μ and γ. In the case of $f(R)$, they assume the following form [251]:

$$\mu = \frac{1}{1+f_R}\frac{1+4\frac{f_{RR}}{1+f_R}\frac{k^2}{a^2}}{1+3\frac{f_{RR}}{1+f_R}\frac{k^2}{a^2}}, \qquad \gamma = \frac{1+2\frac{f_{RR}}{1+f_R}\frac{k^2}{a^2}}{1+4\frac{f_{RR}}{1+f_R}\frac{k^2}{a^2}}. \qquad (10.15)$$

In the current setup of MGCAMB a further simplification is applied when treating $f(R)$ models, which reduces μ and γ to the following expressions in terms of a single parameter, B_0:

$$\mu = \frac{1}{1 - B_0\Omega_m a^3/2}\frac{1+(2/3)B_0\left(k/H_0\right)^2 a^4}{1+(1/2)B_0\left(k/H_0\right)^2 a^4},$$
$$\gamma = \frac{1+(1/3)B_0\left(k/H_0\right)^2 a^4}{1+(2/3)B_0\left(k/H_0\right)^2 a^4}, \qquad (10.16)$$

which correspond to a QS approximation with a power law to describe the time evolution of the Compton wavelength of the scalar d.o.f. [195]. For the

remaining, we will refer to (10.16) as the *BZ* parametrization. Equations (10.16) are combined with the system of Boltzmann equations for matter components and the dynamics of linear scalar perturbations is evolved. They are numerically implemented in [199, 200].

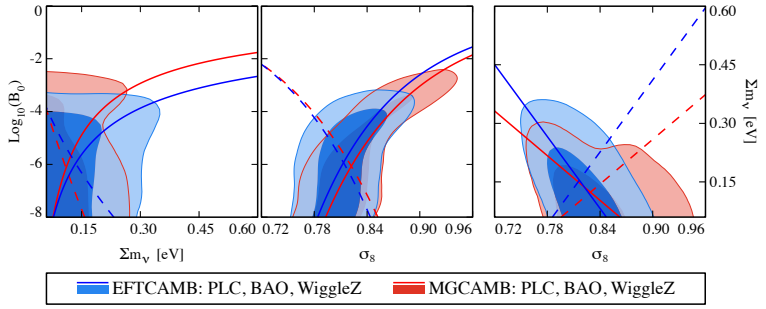

Figure 10.10: The marginalized joint likelihood for the present day value of $\mathrm{Log}_{10}B_0$, the sum of neutrino masses, $\sum m_\nu$, and the amplitude of the (linear) power spectrum on the scale of $8\,h^{-1}$Mpc, σ_8. Different colors correspond to the different codes used and, hence, a different modeling of $f(R)$ as shown in the legend. The darker and lighter shades correspond respectively to the 68% C.L. and the 95% C.L.. The solid line indicates the best constrained direction in parameter space while the dashed line indicates the worst constrained one. As we can see these directions differ noticeably for the two codes. From [5].

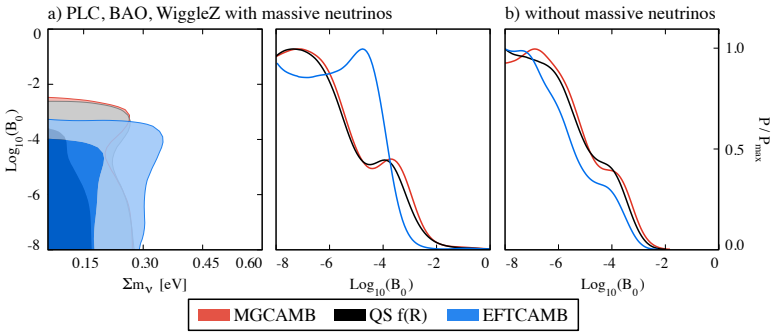

Figure 10.11: *Left:* the marginalized joint likelihood for the present day value of $\mathrm{Log}_{10}B_0$ and the sum of neutrino masses, $\sum m_\nu$. *Center and right:* the marginalized likelihood of $\mathrm{Log}_{10}B_0$ for models with varying (a) and fixed (b) neutrino mass. In all three panels different colors correspond to different numerical codes, as shown in legend and described in Section 10.6. The darker and lighter shades correspond respectively to the 68% C.L. and the 95% C.L.. From [5].

Armed with the full and consistent treatment of the background cosmology for $f(R)$ theories in the presence of massive neutrinos, we can now turn our attention to the dynamics of linear scalar perturbations. While EFTCAMB

provides a number of different parametrizations for the effective dark energy equation of state that can be used in conjunction with the $f(R)$ designer approach, in this paper we will consider only the case of a ΛCDM background. We compare our results with those obtained with the publicly available code MGCAMB [199, 200], and in particular with its adapted version of [72]. We will focus on the constraints on the mass of neutrinos and on the B_0 parameter labeling $f(R)$ theories.

Combining the different cosmological observables described in Section 9.2.2, we explore constraints on designer $f(R)$ models in the massive neutrinos scenario, both in the case of varying and fixed neutrino mass. The results are summarized in Table 10.2. From there we can see that the PLC data set combined with BAO weakly constrain $f(R)$ models so that in the range of interest there is no statistically significant upper bound on $\mathrm{Log}_{10}B_0$ both in the case of varying and fixed neutrino mass even though the mass of neutrinos is strongly constrained. This is because the constraining power of CMB temperature-temperature spectrum on $f(R)$ models is dominated by the ISW effect on the large scales. As shown in [255, 155], the tension between the observed low value of large-scale multipoles of CMB temperature-temperature spectrum and ΛCDM prediction could indeed be reconciled by a large value of B_0 because of the ISW effect. On the other hand, the summed neutrino mass is constrained better by small scale data and is affected negligibly by the tension in the low-ℓ multipoles. This is confirmed by the black line in panels (a) and (b) of Figure 10.9 that clearly shows that the posterior probability distribution of $\mathrm{Log}_{10}B_0$ is peaked at a very large value because of this effect and regardless of the mass of neutrinos. In the case of varying neutrino mass this pronounced peak results in a 2σ lower bound on $\mathrm{Log}_{10}B_0$ as can be seen from Table 10.2. This comes from the fact that models with large B_0 value fit better both the power deficit of the TT spectrum in the ISW regime and the relatively stronger lensing modulation of the TT spectrum around the 3rd and 4th peaks as found by Planck-2013. However, the inclusion of large scale structure data disfavors large values of B_0 and the peak of the posterior distribution located at a non-zero value of B_0 loses its statistical significance after including other data sets, as we will comment later. Moreover, as can be seen from Figure 10.9, the PLC and BAO data compilation are not very robust to constrain neutrino mass and the Compton wavelength at the same time due to the degeneracy between these parameters, so that when the summed neutrino mass is fixed to the vanilla model value, 0.06 eV, the tail of the distribution of $\mathrm{Log}_{10}B_0$ raises up resulting in no statistically significant lower bound on $\mathrm{Log}_{10}B_0$.

The whole picture slightly changes when CMB lensing data are added since both $f(R)$ and massive neutrinos can affect those significantly and in a degenerate way. As we already discussed, $f(R)$ models predict an enhancement of the growth on scales smaller than the Compton scale of the scalaron. Bigger values of B_0 correspond to a larger Compton scales and hence a more significant enhancement of growth on linear scales. On the other hand, massive neutrinos predict a suppression of growth via the freestreaming and a shift in the matter-radiation equality time. Therefore there is a degeneracy between B_0 and $\sum m_\nu$ when growth data are considered, with a non zero neutrino mass allowing for larger values of B_0. This degeneracy is reflected also in the lensing effect imprinted by LSS on CMB. Indeed, when lensing data are considered B_0 and $\sum m_\nu$

display a significant degeneracy which is noticeable in panel (a) of Figure 10.9. As can be seen from Table 10.2 the marginalized bounds on the parameter of interest reflect this degeneracy. On one hand, when lensing data are added the constraint on the neutrino mass gets worse with respect to the CMB and BAO case; on the other hand the constraint on $\mathrm{Log}_{10}B_0$ improves with respect to the CMB and BAO dataset combination but is worse with respect to the case in which lensing is included but the sum of neutrino masses is not allowed to vary.

Comparing the 1D likelihoods for B_0, *i.e.* the red curves, in the middle and right panels of Figure 10.9 we can see a significant difference in the bounds between the case of varying and fixed neutrino mass. The present value of the Compton scale is well constrained when the neutrino mass is kept fixed ($\sum m_\nu = 0.06\mathrm{eV}$) , with a bound of $\mathrm{Log}_{10}B_0 < -2.3$ at 95% C.L.. Instead, when the neutrino mass is varied the bound is looser. In both cases the addition of CMB lensing data rises the tail of the $\mathrm{Log}_{10}B_0$ distribution removing any statistical significance from the lower bound found in the PLC and BAO case.

Finally we can see that the addition of the WiggleZ data improves the situation. It is true that $f(R)$ and massive neutrinos leave a degenerate imprint on LSS, however the constraining power of WiggleZ, and its high sensitivity to changes in B_0 within the range that we consider are able to partially alleviate the degeneracy. Hence we obtain a stringent bound on B_0 when the mass of neutrinos is fixed and, more generally, substantial bounds on both B_0 and $\sum m_\nu$ when the mass of neutrinos is varied.

We compare our results with those obtained with MGCAMB, following the implementation described in Section 10.6. The results are in good agreement, even though there are some interesting differences that we shall discuss in the following. Form Table 10.2 we can see that the constraints obtained with EFTCAMB on $\mathrm{Log}_{10}B_0$ are a bit tighter while the bound on neutrino mass is weaker. The reason why this happens can be easily understood by looking at the marginalized joint likelihood of $\mathrm{Log}_{10}B_0$ and $\sum m_\nu$ in Figure 10.10. From there we can see that there is a change in the degeneracy between these two parameters. This conclusion is further confirmed by looking at the principal components of the two parameters. These are shown in Figure 10.10 as two lines: the continuous one corresponds to the best constrained direction in parameter space while the dashed one corresponds to the worst constrained one. The blue lines correspond to results obtained with EFTCAMB, while the red lines correspond to those obtained with MGCAMB. As we can see the principal directions for the two codes differ noticeably. The same conclusion can be drawn from the other two panels of Figure 10.10 where we can see that the degeneracies between $\mathrm{Log}_{10}B_0$, σ_8 and $\sum m_\nu$ change substantially. In particular, there is less degeneracy between σ_8 and $\sum m_\nu$ in $f(R)$ cosmologies when the analysis is performed with EFTCAMB.

These changes in the degeneracies are due to the different modeling of modified gravity physics. As discussed in Section 10.6, with respect to the complete $f(R)$ modeling of EFTCAMB the modeling of MGCAMB relies on two different assumptions, namely the QS regime for perturbation and the power law ansatz for the time dependence of the Compton wavelength of the scalaron, characteristic of the BZ parametrization (10.16). In order to disentangle the effects of these two approximations we have created a quasi-static version of EFTCAMB customized to $f(R)$ theories, which implements Eq. (10.15), here-

after we name it QS-$f(R)$; in other words it assumes QS but model properly the time-dependence of the background terms, so that at the level of the background the modeling is the same as in EFTCAMB and the differences come only from the different treatment of the dynamics of perturbations. We show a comparison of the results obtained with EFTCAMB, MGCAMB and QS-$f(R)$ in Figure 10.11. It can be noticed that, as expected, results obtained with QS-$f(R)$ lie in between those obtained with EFTCAMB and MGCAMB. Furthermore, it can be seen that in all three panels, MGCAMB and QS-$f(R)$ results are very close to each other, while those obtained with EFTCAMB differ to some extent. Comparing the 1D likelihoods of the center and right panels we can notice that the difference between EFTCAMB and the other two codes is significantly enhanced when massive neutrinos are added. From these comparisons we can infer that the discrepancy found in Figure 10.10 between EFTCAMB and MGCAMB is mostly due to a different modeling of the dynamics of perturbations; the quasi-static approximation misses out some important dynamical contributions. However, as can be noticed in the right panel of Figure 10.11, in the case with a fixed neutrino mass the QS approximation and the power-law modeling of the background contribute similarly to the difference between EFTCAMB and MGCAMB. We expect the above results to depend to some extent on the data set considered, with the differences potentially being smaller for data sets that have a weaker constraining power on $f(R)$. Nevertheless, given the accuracy and wealth of upcoming measurements it is certainly important to take into account these discrepancies.

10.7 Investigating Tensions with Designer $f(R)$

Following up the discussion in Section 9.3 we can investigate the interesting tensions between CMB temperature and polarization anisotropies and CMB lensing within designer $f(RM)$ models.

As we can see from Figure 10.12 the $f(R)$ case displays an $A_{\rm L}^{\rm eff}$ that is monotonically increasing as a function of scale. At low multipoles the agreement with a scale independent model is as good as few percent while in the high-ℓ range it is off by 40% depending on the present value of the Compton wavelength of the scalaron.

We fit with designer $f(R)$ our Mock-A and Mock-C data sets, described in 9.3, and we show the marginalized bound on parameters of interest in Figure 10.13. From there we can see that there is a strong positive correlation between the scalaron present Compton wavelength parameter B_0 and σ_8. This effect is well known and corresponds to the fact that as the effective Newton constant is increased the growth of matter perturbations is increased as well. When considering just Mock-A our results show that in order to mimic $A_{\rm L} \sim 1.3$, the marginalized constraint on B_0 have to point significantly toward large values of the scalaron Compton wavelength. The marginal bound is then $-1.15 < {\rm Log}_{10} B_0 < -0.04$ at 95% C.L..

Due to the significant degeneracy between B_0 and σ_8 such values of B_0 will lead to strong enhancement of the growth rate at relatively small scales making the σ_8 value too large so that the tension between *Planck* and and LSS surveys, such as CFHTLenS [261, 262], would become even worse. For this reason when

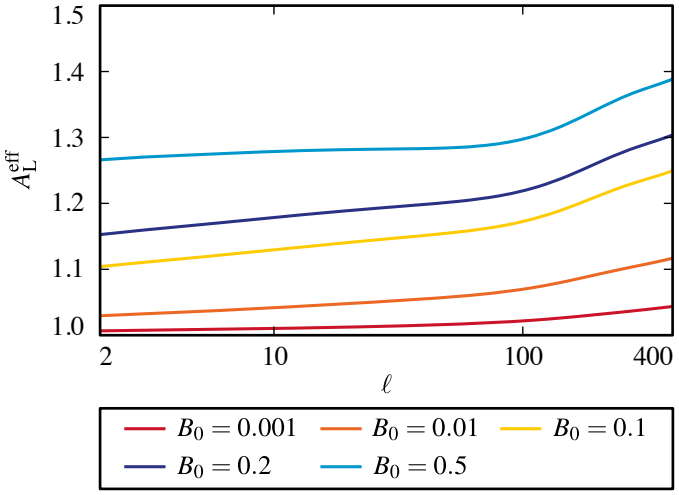

Figure 10.12: the effective lensing amplitude $A_{\rm L}^{\rm eff}(\ell) \equiv C_\ell^{\phi\phi}({\rm MG})/C_\ell^{\phi\phi}({\rm GR})$ as a function of scale in designer $f(R)$ models. Different colors correspond to different values of the model parameters as shown in legend. From [4].

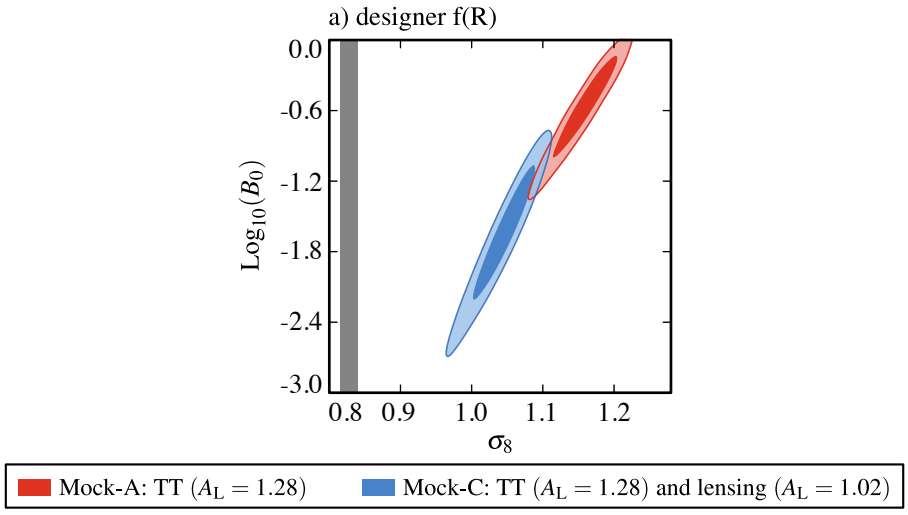

Figure 10.13: the marginalized joint likelihood for the amplitude of the (linear) power spectrum on the scale of $8h^{-1}$Mpc, σ_8 and the present day value of $\rm Log_{10}B_0$. Different colors correspond to different combination of mock data sets as shown in legend and the grey band is the marginalized 1σ bound on σ_8 from the base-ΛCDM+$A_{\rm L}$ model. The darker and lighter shades correspond respectively to the 68% C.L. and the 95% C.L.. From [4].

lensing is added in Mock-C, the tension in $A_{\rm L}$, that for the lensing data set is smaller, pushes the posterior of B_0 toward smaller values, making it closer to GR. A similar effect was also observed for the *Planck*-2015 data set [74] and in

the *Planck*-2013 data [5, 72, 155, 256].

In Table 9.5 we list the best-fit χ^2 for the one parameter extensions of the base-ΛCDM model that we investigated in this paper. From there we can see that the best-fit χ^2 values in the base-ΛCDM+$A_{\rm L}$ and $f(R)$ models are similar and are noticeably smaller than those from base-ΛCDM model with $\Delta\chi^2 \simeq -16$ from the Mock-A and $\Delta\chi^2 \simeq -11$ from the Mock-C data sets.

10.8 Chapter Summary

In this chapter, we described the implementation of designer $f(R)$ models into EFTCAMB. We presented the results that can be drawn for this model with present cosmological data and we used it as an example of the implementation of a designer mapping theory into EFTCAMB.

We started, in section 10.3, comparing our code with the outputs of MGCAMB for $f(R)$ theories in a ΛCDM background. To this extent, we focused on the CMB temperature angular spectrum and showed an agreement of the two code within 0.1% for values of the scalaron Compton wavelength consistent with existing bounds from *Planck*. For larger values of B_0 we found some tension both at the low and high multipoles; the former is due to the fact that not relying on any QS approximation, EFTCAMB gives a more accurate account of the ISW effect. To investigate the latter discrepancy instead, we considered the functions $\mu(z,k)$ and $\gamma(z,k)$ Eqs. (10.5), commonly used to parametrize deviations from GR and implemented in MGCAMB. We compared their shape in (z,k)-space as reconstructed from the full evolution of the perturbations in our code, to their form under the BZ approximation (10.7) employed to study $f(R)$ in MGCAMB. This comparison showed that EFTCAMB catches the mild dynamics of the scalaron at early times and on large scales, as well as some non-trivial dynamics on scales around and below the Compton wavelength. We confirmed this by analyzing the time- and scale-dependence of a quantity that we propose as an indicator of quasi-staticity in the dark sector, ξ Eq. (10.11). After this thorough check of consistency with MGCAMB, we moved on to fully exploit the flexibility of the EFT framework applying our code. As an example of what we called the *mapping* EFT approach, we extended the implementation of the $f(R)$ designer approach to more general expansion histories like the wCDM and CPL one, examining the effects of the combined change in the background dynamics and in the growth of structure on cosmological observables like the CMB temperature and lensing power spectra (auto- and cross-correlation), and matter power spectrum.

We then moved to deriving constraints on designer $f(R)$ with three different combinations of *Planck*, WP, BAO and CMB lensing data sets to show their different effects on constraining the parameter space. We have adopted the designer approach built-in in EFTCAMB and have considered the case of a ΛCDM as well as of a wCDM background. Constraints on the model parameter B_0, are described in Section 10.5. For the ΛCDM case we also compared our results to those that we obtained with the quasi-static treatment of these models via MGCAMB [199, 200]. The two treatments give results that are in good agreement, with bounds from EFTCAMB/EFTCosmoMC being a little tighter thanks to the full treatment of the dynamics of perturbations. On wCDM background

we have found a non-trivial likelihood profile of $\mathrm{Log}_{10}B_0$ (see Figure 10.7 (d)) for all the three data compilations and the shape of the marginalized posterior distribution in this case strongly reflects that of the viable region in parameter space. In the wCDM background, with *Planck*+WP+BAO+lensing data we get $\mathrm{Log}_{10}B_0 = -3.35^{+1.79}_{-1.77}$ (95% C.L.). The bounds on w_0 with *Planck* lensing data ($w_0 \in (-1, -0.9997)$ (95% C.L.)) are quite stringent compared to those without this data set ($w_0 \in (-1, -0.94)$ (95% C.L.)) due to the high constraining power of lensing measurements on B_0 and the strong correlation between w_0 and B_0 via the *viability prior*.

After investigating these cosmological implications we investigated the degeneracy between massive neutrinos and designer $f(R)$ models. We found that the combination of *Planck* and BAO measurements displayed a marked degeneracy between the Compton wavelength of the scalaron and the sum of neutrino masses. With the addition of large scale structure data from the WiggleZ experiment we found that this degeneracy is alleviated resulting in stronger constraints. In particular the most complete data set that we used results in $\mathrm{Log}_{10}B_0 < -4.1$ at 95% C.L. if neutrinos are assumed to have a fixed mass equal to $\sum m_\nu = 0.06\,\mathrm{eV}$ and $\mathrm{Log}_{10}B_0 < -3.8$ and $\sum m_\nu < 0.32$ at 95% C.L. if neutrino masses are allowed to vary. We compared our results to those obtained by means of MGCAMB, in which $f(R)$ models are typically treated via parametrization introduced in [120], which assumes the quasi static regime and a specific power law evolution for the characteristic lengthscale of the model. Overall there is good agreement between the two codes, finding however that due to the different modeling there is a slight change in the degeneracy between $f(R)$ models and massive neutrinos. In particular this degeneracy changes direction in parameter space resulting in the fact that EFTCAMB obtains stronger bounds on $\mathrm{Log}_{10}B_0$ but weaker constraints on $\sum m_\nu$. We observed that also other degeneracies are affected by the different physical modeling so that with EFTCAMB there is less degeneracy between $f(R)$ models and σ_8.

At last we explored the tensions between CMB temperature and polarization anisotropies and CMB lensing and we found that $f(R)$ can mimic the role of A_L even if, generally, the amplitude of lensing, with respect to the GR case, is scale dependent.

	$f(R)$+ΛCDM			$f(R)$+wCDM		
	Planck+WP	*Planck*+WP+BAO	*Planck*+WP+ BAO+lensing	*Planck*+WP	*Planck*+WP+BAO	*Planck*+WP+ BAO+lensing
Parameters	mean ± 68% C.L.	mean ± 68% C.L.	mean ± 68% C.L.	mean ± 68% C.L.	mean ± 68% C.L.	mean ± 68% C.L.
$100\Omega_b h^2$	2.224±0.033	2.220±0.027	2.214±0.025	2.255±0.033	2.246±0.029	2.226±0.026
$\Omega_c h^2$	0.1185±0.0027	0.1187±0.0017	0.1184±0.0016	0.1162±0.0027	0.1174±0.0019	0.1174±0.0016
$100\theta_{\rm MC}$	1.04149±0.00067	1.04142±0.00057	1.04136±0.00056	1.04186±0.00066	1.04166±0.00060	1.04149±0.00056
τ	0.088±0.013	0.087±0.013	0.087±0.012	0.086±0.013	0.084±0.012	0.082±0.012
n_s	0.9634±0.0076	0.9624±0.0058	0.9625±0.0057	0.9695±0.0078	0.9665±0.0062	0.9647±0.0057
$\mathrm{Log}(10^{10}A_s)$	3.083±0.025	3.082±0.025	3.080±0.022	3.075±0.025	3.072±0.024	3.067±0.024
$\mathrm{Log}_{10}B_0$	< 0.0 ([a])	< 0.0 ([a])	< -2.37 (95%C.L.)	$-1.97^{+1.61}_{-1.52}$ (95%C.L.)	$-2.01^{+1.60}_{-1.51}$ (95%C.L.)	$-3.35^{+1.79}_{-1.77}$ (95%C.L.)
w_0	–	–	–	$(-1, -0.94)$ (95%C.L.)	$(-1, -0.94)$ (95%C.L.)	$(-1, -0.9997)$ (95%C.L.)
Ω_m	0.300±0.017	0.302±0.010	0.3005±0.0092	0.291±0.015	0.2982±0.0099	0.2944±0.0093
H_0	68.51±1.30	68.35±0.81	68.41±0.72	69.04±1.18	68.50±0.80	68.89±0.75
$\chi^2_{\rm min}/2$	4900.765	4901.399	4907.901	4900.656	4901.140	4908.286

Table 10.1: Mean values and 68% (or 95%) confidence limits for primary/derived parameters for a designer $f(R)$ model on ΛCDM/wCDM background.

[a] No significant upper bound found in the parameter range we investigated.

	Varying m_ν		Fixing m_ν
Data sets	$\mathrm{Log}_{10}B_0$ (95% C.L.)	$\sum m_\nu$ (95% C.L.)	$\mathrm{Log}_{10}B_0$ (95% C.L.)
PLC + BAO	> -6.35	< 0.37	none
PLC + BAO + lensing	< -1.0	< 0.43	< -2.3
PLC + BAO + lensing + WiggleZ	< -3.8	< 0.32	< -4.1
PLC + BAO + WiggleZ (EFTCAMB)	< -3.8	< 0.30	< -3.9
PLC + BAO + WiggleZ (QS $f(R)$)	< -3.2	< 0.24	< -3.7
PLC + BAO + WiggleZ (MGCAMB)	< -3.1	< 0.23	< -3.5

Table 10.2: *Second column*: joint constraints on the B_0 parameter of designer $f(R)$ models and a varying neutrino mass. *Third column*: constraints on B_0 in the case of a fixed neutrino mass ($\sum m_\nu = 0.06$eV). In both cases, we use different combinations of the data sets described in Section 9.2.2 and the EFTCAMB code. The last three rows report the comparison between EFTCAMB, MGCAMB and a quasi-static designer $f(R)$ code. These results are reported for the specific combinations of data used in [72] both considering the case of a varying and fixed neutrino mass.

Chapter 11

Hu-Sawicki $f(R)$ Gravity

While in the previous Chapter we focused on a designer model, in this chapter we show how to fully map a specific model of modified gravity into EFTCAMB. This approach consists in few steps and allows to obtain the cosmological phenomenology of a model with minimal effort. Here we discuss all these steps, from the solution of the dynamical equations for the cosmological background of the model to the use of the mapping relations to cast the model into the effective field theory language and use the latter to solve for perturbations. The model that we choose for this purpose is the popular Hu-Sawicki $f(R)$ gravity, that was introduced in [263] and represents one of the few known viable functional forms of $f(R)$ with the interesting feature of being able to satisfy solar system tests of gravity. The non-linear structure formation via N-body simulations of this model has been studied in [264, 219, 265, 266, 267]. Finally, a generic No-Go theorem of the screening mechanism for chameleon-like models has been studied in [268]. After solving the background and performing the mapping, we interface the algorithm with EFTCAMB and take advantage of the effective field theory framework to integrate the full dynamics of linear perturbations, returning all quantities needed to accurately compare the model with observations. We discuss some observational signatures of this model, focusing on the linear growth of cosmic structures. In particular we present the behavior of $f\sigma_8$ and E_G that, unlike the ΛCDM scenario, are generally scale dependent in addition to redshift dependent. Finally, we study the observational implications of the model by comparing its cosmological predictions to the Planck 2015 data, including CMB lensing, the WiggleZ galaxy survey and the CFHTLenS weak lensing survey measurements.

As anticipated, the dynamics of linear perturbations in $f(R)$ models of gravity can be studied exactly through the EFT framework working only with two EFT functions: Ω and Λ. In figure. 11.1, we demonstrate the logical steps of the implementation of a full-mapping module in EFTCAMB. Our algorithms only asks for a few steps to interface the model parameters with EFTCAMB, such as the background equation of state of the dynamical dark energy field (or the modified Hubble parameter) and the corresponding EFT functions. The modules of the code will automatically calculate the derivatives and integrals of these quantities numerically. In the following we will show how to determine the time-dependence of these functions, which is all is needed in order to have EFT-

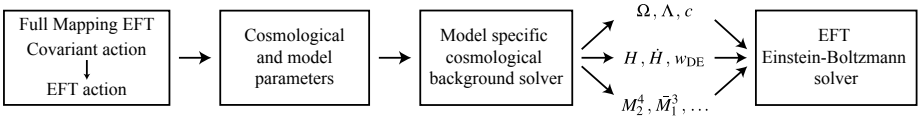

Figure 11.1: Diagram illustrating the logical steps of the implementation of a full-mapping module in EFTCAMB. At first a specific theory needs to be mapped to the EFT framework. These mapping relations, along with the cosmological and model parameters are fed to a module that solves the cosmological background equations, for the specific theory, and outputs the time evolution of the EFT functions. These functions are then used to evolve the full perturbed Einstein-Boltzmann equations and compute cosmological observables. From [1].

CAMB solve for the dynamics of cosmological perturbations, in $f(R)$ models, through the full mapping procedure.

While we specialized to the Hu-Sawicki model as a working example in this Chapter, the steps presented here also constitute the necessary ingredients to map other modified gravity models into EFTCAMB. Indeed, in a similar way one has to write a model specific module that solves the background equations for the model of interest. Then one has to work out and use the mapping relations between the model and the EFT framework to get the specific time dependence of the EFT functions (e.g. [177] offers a complete guide on the mapping). Once these functions are fed to EFTCAMB, the code will automatically calculate derivatives and integrals numerically and finally output all the cosmological observables of interest.

11.1 Introduction to Hu-Sawicki $f(R)$

The Hu-Sawicki model of $f(R)$ gravity was introduced in [263] and represents one of the few known viable functional forms of $f(R)$ with the interesting feature of being able to satisfy solar system tests of gravity. It corresponds to the following action:

$$S = \int d^4x\sqrt{-g}\frac{m_0^2}{2}\left[R + f(R)\right] + S_m[g_{\mu\nu}, \chi_m], \tag{11.1}$$

where

$$f(R) = -m^2\frac{c_1(R/m^2)^n}{c_2(R/m^2)^n + 1}\,, \tag{11.2}$$

with

$$m^2 \equiv H_0^2\Omega_m = (8315\text{Mpc})^{-2}\left(\frac{\Omega_m h^2}{0.13}\right)\,. \tag{11.3}$$

The non-linear terms in $f(R)$ introduce higher-order derivatives acting on the metric, making explicit the higher order nature of the theory. It is possible to cast the theory into a second order one with an extra scalar degree of freedom represented by $f_R \equiv \mathrm{d}f/\mathrm{d}R$, *i.e.* the *scalaron*.

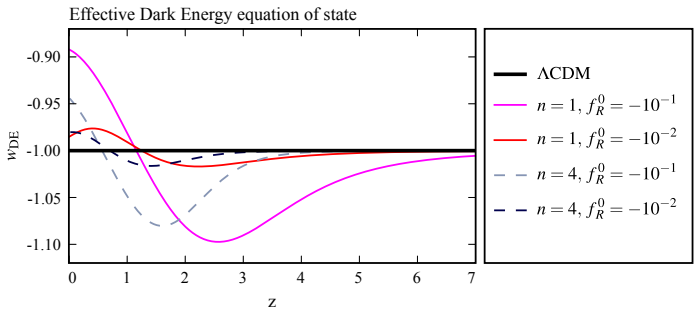

Figure 11.2: Effective Dark Energy Equation of State for the Hu-Sawicki $f(R)$ model as a function of redshift. Different colors and ticks represent different values of model parameters, as shown in legend. From [1].

In the high curvature regime, $R \gg m^2$, the action (11.2) can be expanded in m^2/R:

$$\lim_{m^2/R\,0} f(R) \approx -\frac{c_1}{c_2}m^2 + \frac{c_1}{c_2^2}m^2\left(\frac{m^2}{R}\right)^n + \cdots \,. \tag{11.4}$$

This limit can be applied up to $z = 0$ if the parameter m^2 is properly chosen. In particular it can be applied for the value given in (11.2), as discussed in [263]. Furthermore one can notice that the first term corresponds to a cosmological constant and the second term to a deviation from it, which becomes more important at low curvature. It is possible to closely mimic a ΛCDM evolution if the value of c_1/c_2 is fixed by:

$$\frac{c_1}{c_2} \approx 6\frac{\Omega_\Lambda}{\Omega_m} \,. \tag{11.5}$$

which is valid as long as the high curvature regime holds. Using the latter relation, the number of free model parameters can be reduced to two. In addition, the parameter c_2 can be expressed in terms of $f_R^0 \equiv \mathrm{d}f/\mathrm{d}R(z=0)$ so that the two free parameters of the Hu-Sawicki model, that we shall discuss in the next sections, are f_R^0 and n.

11.2 HS $f(R)$ Background Cosmology

We shall now focus on solving the background dynamics of the Hu-Sawicki model, with the goal of deriving the time-dependence of the EFT functions in (10.4). Let us start from the modified Friedmann equations in conformal time:

$$\begin{aligned} &\left(1+f_R\right)\mathcal{H}^2 + a^2\frac{f}{6} - \frac{\ddot{a}}{a}f_R + \mathcal{H}\dot{f}_R = \frac{1}{3m_0^2}a^2\rho_m \,, \\ &\frac{\ddot{a}}{a} - \left(1+f_R\right)\mathcal{H}^2 + \frac{a^2}{6}f + \frac{\ddot{f}_R}{2} = -\frac{1}{6m_0^2}a^2\left(\rho_m + 3P_m\right) \,. \end{aligned} \tag{11.6}$$

The trace of Einstein equations provides a dynamical equation for the additional scalar degree of freedom of the theory

$$\Box f_R = \frac{1}{3}\left(-\frac{\rho_m}{m_0^2} + R - f_R R + 2f\right) \,. \tag{11.7}$$

From a closer look at (11.7), it can be realized that in the high curvature regime the solution of this equation displays highly oscillatory modes when $f_{RR} > 0$, [249, 253]. These oscillations have an amplitude that decays in time and eventually fades away as the curvature decreases. Nevertheless, one needs extra care to cope with these oscillations when solving the background dynamics, as we will discuss later.

Starting from (11.6) it is possible to recast the Friedmann equations in their general relativistic form, incorporating the effects of the modifications of gravity into an effective dark fluid with the following equation of state:

$$w_{\rm DE} = -\frac{1}{3} - \frac{2}{3}\frac{\left(\mathcal{H}^2 f_R - \frac{a^2 f}{6} - \frac{1}{2}\ddot{f}_R\right)}{\left(-\mathcal{H}^2 f_R - \frac{a^2 f}{6} - \mathcal{H}\dot{f}_R + \frac{a^2 f_R R}{6}\right)} \,. \tag{11.8}$$

Following [263], we can then define two auxiliary variables:

$$y_h = \left(\frac{\mathcal{H}^2}{m^2} - a^{-1}\right) a^{-2}, \quad y_r = \frac{R}{m^2} - 3a^{-3}, \tag{11.9}$$

to recast the first equation in (11.6) and the geometrical relation between R and H into a first order system of non-linear ordinary differential equations:

$$\begin{aligned} y_h' &= \frac{1}{3} y_r - 4 y_h \\ y_r' &= 9a^{-3} - \frac{1}{y_h + a^{-3}} \frac{m^2}{f_{RR}} \left[y_h - f_R\left(\frac{1}{6} y_r - y_h - \frac{1}{2} a^{-3}\right) + \frac{1}{6}\frac{f}{m^2} \right] \end{aligned} \tag{11.10}$$

where the prime stands for the derivative w.r.t. the number of efolds $\ln a$. As we already discussed, the solution of this system of differential equations is expected to display high frequency oscillations at high redshift. In order to ensure an accurate and efficient approach, we shall determine the particular solution of it around which oscillations happen. This is defined by the smooth evolution of the minimum of the potential defined by the r.h.s. of equation (11.7). Requiring the field to seat at the bottom of its potential, immediately results in:

$$R = \frac{k^2 \rho_m - 2f}{1 - f_R}. \tag{11.11}$$

We can then linearize the initial system around the evolution of the minimum of the effective potential. At the leading order in the high curvature expansion (11.4), the evolution for $\mathcal{H}^2$ can be described by:

$$\mathcal{H}^2 \approx m^2 a^{-1} + \frac{c_1}{6c_2} m^2 a^2 \,. \tag{11.12}$$

Then, the variable that can be safely used for our linearization at high redshift, is:

$$\bar{y}_h \equiv \frac{\mathcal{H}^2 - m^2 a^{-1} - \frac{c_1}{6c_2} m^2 a^2}{m^2 a^{-1}} = \frac{\mathcal{H}^2 - \mathcal{H}^2_{\Lambda\rm CDM}}{m^2 a^{-1}} \,, \tag{11.13}$$

where $\mathcal{H}^2_{\Lambda\rm CDM}$ is the Hubble parameter for the ΛCDM model. Once (11.10) has been linearized, the evolution of its stable solution is well approximated by

the ratio of the non-homogeneous term and the mass term of the corresponding linearized system.

The strategy that we shall use to solve the background equations, for the Hu-Sawicki $f(R)$ model, consists in the following steps: we will start deep in radiation domination, when the system (11.10) shows extreme stiffness, and we approximate its solution with the stable solution of the linearized system; when the stiffness of the system becomes tractable by standard numerical methods the particular solution introduced before, is used as the initial condition for the numerical solution of (11.10). After solving the background equations, we can reconstruct the effective DE equation of state (11.8):

$$w_{\rm DE} = -1 - \frac{y_h'}{3y_h}\,. \tag{11.14}$$

Figure 11.2 shows the time evolution of this quantity as a function of redshift, for some selected values of model parameters. As we can see the Hu-Sawicki model is never exactly mimicking a cosmological constant. Differences, with respect to the ΛCDM expansion history, are however decreasing as we decrease the value of f_R^0 and we increase the value of the exponent n, as expected.

The numerical algorithm to solve (11.10), along with the mapping (10.4), constitute all the ingredients that the user needs to supply in order to have EFTCAMB solve for the full dynamics of linear perturbations in the Hu-Sawicki model. All these operations can then be implemented in a model specific module of EFTCAMB that is simply interfaced with the part that solves Boltzmann-Einstein equations.

11.3 Scale Dependence of the Growth of Structures

After we implement the background solver, EFTCAMB solves consistently the full perturbed Einstein-Boltzmann equations to compute all cosmological quantities of interest. We shall not review the matter and cosmic microwave background spectra but rather refer the reader to [10], where such observables have been outputted using EFTCAMB for designer $f(R)$ models. In this section we will focus instead on some specific combinations of observables that capture interesting phenomenological signatures, namely the growth rate $f\sigma_8$ and the E_G statitstics, defined below. For some other interesting features see also [276].

We shall first consider the observational effects imprinted in the time and scale dependence of $f\sigma_8$. Within General Relativity and the ΛCDM model, on linear scales, the combination of $f(z,k) = {\rm d}\log\delta_m(z,k)/{\rm d}\log a$ and the amplitude of the linear power spectrum on the scale of $8\,h^{-1}\,$Mpc does not depend on the scale at which this quantity is computed. This does not hold in generic modified gravity models. In particular, in $f(R)$ models, the growth rate is enhanced at scales that are smaller than the Compton wavelength of the scalaron field, resulting in specific scale-dependent patterns [249, 251].

In figure 11.3 we show the effect of this scale dependence in $f\sigma_8$, at two different scales. It can be noticed that in Hu-Sawicki $f(R)$ gravity, the growth rate of short wavelength modes is enhanced with respect to that of long wave-

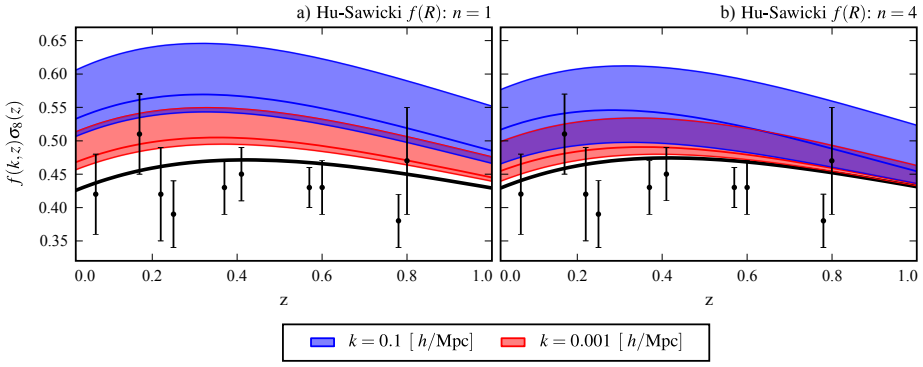

Figure 11.3: The linear growth rate, $f\sigma_8$, in Hu-Sawicki $f(R)$ gravity, at different redshifts and scales. Different panels correspond to different values of the Hu-Sawicki exponent n. The black thick line corresponds to ΛCDM cosmology. Different colors indicate different scales at which $f\sigma_8$ is computed, as shown in the legend. The colored thick lines show the behavior of $f\sigma_8$ for the mean value of cosmological parameters of the corresponding model, as obtained from the most complete data set combination discussed in section 11.4. The color bands denote the 1σ uncertainties on the f_R^0 parameter from the data compilation of Planck15+BAO+JLA+WiggleZ+CFHTLenS. Specifically this means that in the $n = 1$ case the mean/lower/upper bound values of f_R^0 are, -3×10^{-5}, -1×10^{-5} and -6×10^{-4}. In the $n = 4$ case the mean/lower/upper bound values of f_R^0 are -4×10^{-5}, -3×10^{-6} and -2×10^{-2}. The black points with error bars are 10 redshift space distortion measurements from: 6dFGRS [269], 2dFGRS [270], WiggleZ [271], SDSS LRG [272], BOSS CMASS [273] and VIPERS [274]. From [1].

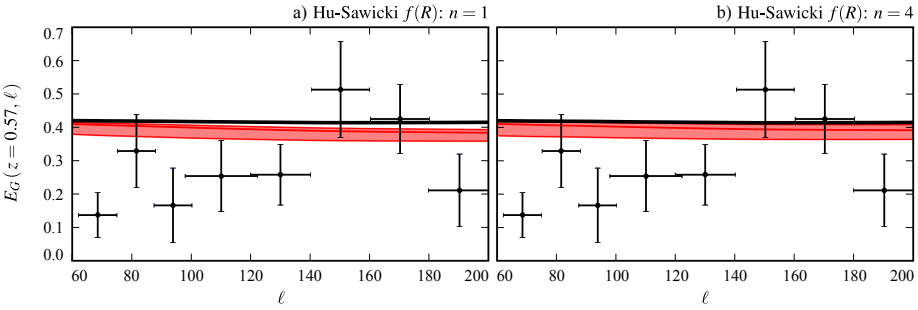

Figure 11.4: E_G for Hu-Sawicki $f(R)$ gravity for a BOSS-CMASS-like survey with average redshift $\bar{z} = 0.57$ and different angular scales. Different panels correspond to different values of the Hu-Sawicki exponent n. The black thick line corresponds to ΛCDM cosmology. The red thick line shows the behavior of E_G for the mean value of cosmological parameters of the corresponding model, as obtained from the most complete data set combination discussed in section 11.4. The color bands denote the 1σ uncertainties on the f_R^0 parameter from the data compilation of Planck15+BAO+JLA+WiggleZ+CFHTLenS. In the $n = 1$ case the mean/lower/upper bound values of f_R^0 are, -3×10^{-5}, -1×10^{-5} and -6×10^{-4}. In the $n = 4$ case the mean/lower/upper bound values of f_R^0 are -4×10^{-5}, -3×10^{-6} and -2×10^{-2}. The black points with error bars measurements of E_G from BOSS-CMASS [275]. From [1].

length modes and also as compared to the scale-independent rate of the ΛCDM model. This behavior is consistent with the picture emerging from the matter power spectra, as those shown in [8]. While being mild, this scale dependence cannot certainly be neglected and the plots in figure 11.3 warn about the possibility of biasing cosmological inference by not properly accounting for it. From figure 11.3, by comparing the two panels, we can also see how this scale dependence changes with the value of the parameter n. The smaller the value of n, the stronger the enhancement of the growth with respect to ΛCDM and hence the bigger the overall scale dependence of $f\sigma_8$. The second observable that we shall consider is the modified gravity statistic, E_G, [118] that was proposed to constrain or detect deviations from a ΛCDM cosmology. In order to do so, different observables are combined into a single one that is free from the modeling of other unknown quantities like bias. We refer to [277] for the complete derivation of the observationally-motivated definition of E_G in modified gravity scenarios. Here we consider the following definition, given by [278, 275]:

$$E_G = \Gamma \frac{C_\ell^{\kappa g}}{C_\ell^{\theta g}}, \qquad \Gamma = \frac{\mathcal{H}(z) f_g(z)}{3 H_0^2 W_\kappa(z)(1+z)^2}\ , \tag{11.15}$$

where $C_\ell^{\kappa g}$ is the cross correlation between galaxy lensing convergence and galaxy number counts fluctuations; $C_\ell^{\theta g}$ is the cross correlation between galaxy peculiar velocity and galaxy number counts fluctuations; $W_\kappa(z)$ is the lensing convergence window function; $f_g(z)$ is the normalized galaxy redshift distribution as in [279].

The particular combination of observables in (11.15), is scale independent on linear scales for the ΛCDM model. In general, when we consider modified gravity

Model	Data set	$\log_{10}(-f_R^0)$	σ_8	H_0
$n=1$	D_1	< -2.7	$0.87^{+0.12}_{-0.08}$	$67.7^{+0.9}_{-0.9}$
	D_1 + WiggleZ	$-3.4^{+1.4}_{-1.2}$	$0.95^{+0.07}_{-0.07}$	$67.7^{+0.9}_{-0.9}$
	D_1 + CFHTLenS	< -4.5	$0.83^{+0.07}_{-0.04}$	$67.8^{+0.9}_{-0.9}$
	All	< -3.2	$0.90^{+0.07}_{-0.10}$	$67.7^{+0.9}_{-0.9}$
$n=4$	D_1	$-$	$0.87^{+0.06}_{-0.07}$	66^{+2}_{-4}
	D_1 + WiggleZ	> -5.2	$0.90^{+0.04}_{-0.08}$	66^{+2}_{-4}
	D_1 + CFHTLenS	< -2.8	$0.84^{+0.07}_{-0.04}$	$67.8^{+0.9}_{-0.9}$
	All	$-4.4^{+2.9}_{-4.2}$	$0.87^{+0.06}_{-0.07}$	67^{+1}_{-1}
n free	D_1	$-$	$0.86^{+0.08}_{-0.07}$	67^{+2}_{-3}
	D_1 + WiggleZ	> -5.2	$0.93^{+0.09}_{-0.11}$	67^{+2}_{-2}
	D_1 + CFHTLenS	< -2.3	$0.84^{+0.06}_{-0.04}$	67^{+1}_{-1}
	All	< -1.9	$0.88^{+0.08}_{-0.08}$	67^{+1}_{-1}

Table 11.1: The 95% C.L. marginalized bounds, from the used data set combinations, on Hu-Sawicki models. In the case where the parameter n is allowed to vary, within its prior range $n \in [0, 10]$, no statistically significant constraint on n is found.

scenario, this does not hold anymore and E_G acquires a scale dependence. This is shown for the Hu-Sawicki model in figure 11.4. While the ΛCDM behavior is clearly scale independent the Hu-Sawicki case shows a slight scale dependent suppression. This suppression is due to an enhancement of the galaxy velocity field in $f(R)$ gravity with respect to the ΛCDM case. As in the previous case we can notice that the scale dependence and deviation from the ΛCDM behavior is stronger in the $n = 1$ case and weaker in the $n = 4$ case.

11.4 Cosmological constraints

We shall now use different cosmological data to place constrain on the Hu-Sawicki model via EFTCAMB/EFTCosmoMC. Cosmological constraints on this model have been already explored in [250, 255, 280, 281, 282, 150, 153, 283, 284] (see [252, 285] for review). Let us stress that most of the previous approaches have relied on the quasi-static approximation and often assumed a ΛCDM background, while we evolve the full dynamics of perturbations and use the specific background expansion history of the model. In our analysis we use several geometrical and dynamical probes, combining them progressively. The baseline data set combination employed, hereafter "D1", consists of: the *Planck* 2015 temperature and polarization CMB spectra, JLA Supernovae and several BAO measurements. We shall add to the D1 data set compilation the WiggleZ galaxy number density power spectrum. The third data set combination, that we dub "D1+CFHTLenS", consists of D1 joined with CFHTLenS weak lensing measurements. Finally we shall refer to "All" to indicate the data set combination obtained by joining D1, WiggleZ and CFHTLenS. For a detailed discussion of these data sets we refer the reader to Chapter 4. We shall consider three different Hu-Sawicki models: a model with the exponent $n = 1$, a model with the exponent $n = 4$ and a model in which n is free to vary in the range $[0, 10]$. In all the cases, there is another model parameter which is left free to vary, i.e. f_R^0.

We sample it logarithmically within the range $\log_{10}(-f_R^0) \in (-9, 0)$.

The marginalized bounds on the model parameters, that we obtain for all cases are summarized in table 11.1. One can notice that bounds on $\log_{10}(-f_R^0)$ from the D1 data set are weak for the $n = 1$ model, and do not result in statistically significant constraints in the $n = 4$ and n free cases. On the other hand the WiggleZ data set clearly favors a high value of $\log_{10}(-f_R^0)$ driving the parameter bound away from the ΛCDM limit as far as:

$$\log_{10}(-f_R^0) = -3.4^{+1.4}_{-1.2} \ , \text{ at } 95\% \text{ C.L. } (n = 1, \ \text{“D1 + WiggleZ''}) \qquad (11.16)$$

A similar result was found, for another type of $f(R)$ model, in [72, 5]. We can estimate the Compton wavelength, λ_c, of the scalaron corresponding to the above results, using $B_0 \simeq -6f_R^0$, where B_0 gives the square of the Compton wavelength in Hubble units. We get $\lambda_c \in (172, 3429)$ Mpc at 95% confidence level, which is safely inside the linear regime. This results is thus consistent with the linear cut off that we adopted for the WiggleZ survey. The CFHTLenS data set on the contrary pushes the bounds on $\log_{10}(-f_R^0)$ toward the ΛCDM limit. This behavior is caused by the fact that, in $f(R)$ gravity, the growth of cosmic structures, on scales below the Compton wavelength of the scalar field, is enhanced with respect to the ΛCDM scenario. The combination of *Planck* and WiggleZ data seems to prefer this enhancement of the growth, while the CFHTLenS weak lensing data, favors the opposite behavior, *i.e.* a suppression of the amplitude of the matter power spectrum. This is also reflected in the σ_8 bounds. If we consider the $n = 1$ case we can immediately read from table 11.1 that the combination of D1 with WiggleZ results in a statistically significant enhancement of the σ_8 value while the opposite holds for D1 joined with the CFHTLenS data set. Furthermore, we can also see that the estimated Hubble parameter H_0 is weakly dependent on the data set and model considered. However, even if the mean value does not change significantly, the 95% C.L. bounds are, instead, significantly dependent on the model considered.

All these conclusions about the parameters bounds are further confirmed by the inspection of the marginalized posterior of several parameters. In figure 11.5 we can clearly see the degeneracy between the present day amplitude of scalar perturbations, σ_8, and the present day value of f_R. Through this degeneracy, WiggleZ data set favors a high value of both parameters, while CMB and CFHTLenS measurements favor a smaller value. This degeneracy changes as we change the value of the Hu-Sawicki model exponent. With this respect, figure 11.6, shows the $n = 4$ case. Noticeably, we can see that as soon as $\log_{10}(-f_R^0) > -2$, the degeneracy between σ_8 and $\log_{10}(-f_R^0)$ has an abrupt change in direction. This change in direction clearly shows up also in the posterior distribution of σ_8 and H_0, in panel (b) of figure 11.6. The reason for this behavior can be understood by looking at panel (c) of the same figure. As we can clearly see, for $\log_{10}(-f_R^0) < -2$, the parameter describing $f(R)$ is not degenerate with the Hubble parameter but, as soon as $\log_{10}(-f_R^0) > -2$, a marked degeneracy arises. This means that when $\log_{10}(-f_R^0) < -2$ the model is constrained through its effect on perturbations while in the regime $\log_{10}(-f_R^0) > -2$ the effect of this modification of gravity at the background level is not negligible. On the contrary, in this parameter range, background observables play an important role in constraining the model. To further support this conclusion we notice that such a degeneracy does not arise in designer $f(R)$ models, where

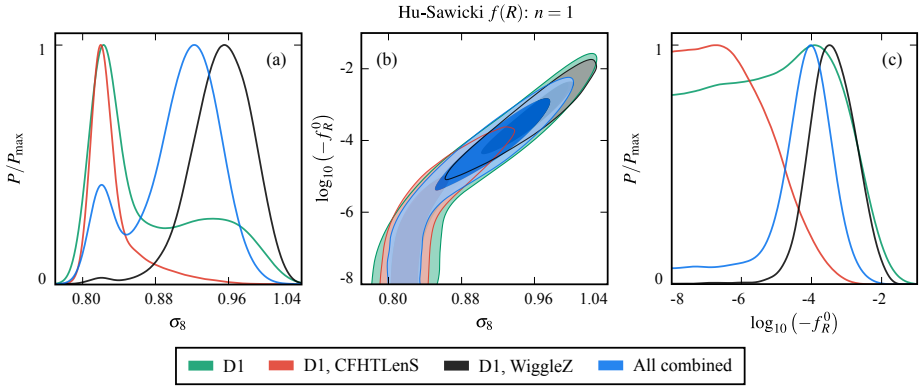

Figure 11.5: Results of the analysis of Hu-Sawicki $f(R)$ with $n = 1$. *Panel (a):* The marginalized posterior of σ_8. *Panel (b):* The marginalized joint posterior of σ_8 and $\log_{10}(-f_R^0)$. The darker and lighter shades correspond respectively to the 68% C.L. and the 95% C.L.. We can see the strong degeneracy between these two parameters. The WiggleZ data set drives the joint posterior toward high values of $\log_{10}(-f_R^0)$ and σ_8. *Panel (c):* The marginalized posterior of $\log_{10}(-f_R^0)$. As we can see the WiggleZ data set favors a large value of $\log_{10}(-f_R^0)$. In all panels different colors correspond to different data set combinations as shown in legend. From [1].

the cosmological background mimics exactly the ΛCDM one, as in [5]. When n is allowed to vary the situation slightly changes. As we can see from figure 11.7 there is a significant degeneracy between n and $\log_{10}(-f_R^0)$ and, being n weakly constrained, the bound on $\log_{10}(-f_R^0)$ gets weaker.

Finally, in figure 11.8, for different data set combinations we can see how the degeneracy between the growth of structure and modifications of gravity induced by the Hu-Sawicki model depends on the value of the exponent n. The general trend is that the degeneracy is stronger for small values of n and weaker for high values on n, as can be seen clearly from the $n = 1$ and $n = 4$ posterior. The case with n free obviously covers these two sub-cases and noticeably enough, in this case, the degeneracy is not that different from the other two cases.

11.5 Chapter Summary

In this chapter, we have presented in detail the procedure at the basis of the full mapping of a specific model of modified gravity into the linear Einstein-Boltzmann solver EFTCAMB. We chose the Hu-Sawicki $f(R)$ model as an example, demonstrating how to set up its background solver and how to implement it in EFTCAMB, mapping between the model parameters and the relevant EFT functions. Once the mapping of the model into the EFT language is worked out, from the numerical point of view all the user needs for this model is to interface EFTCAMB with the background equation of state of the dynamical dark energy field (or the modified Hubble parameter) and the EFT functions. The relevant modules of the code will automatically calculate their derivatives and integrals

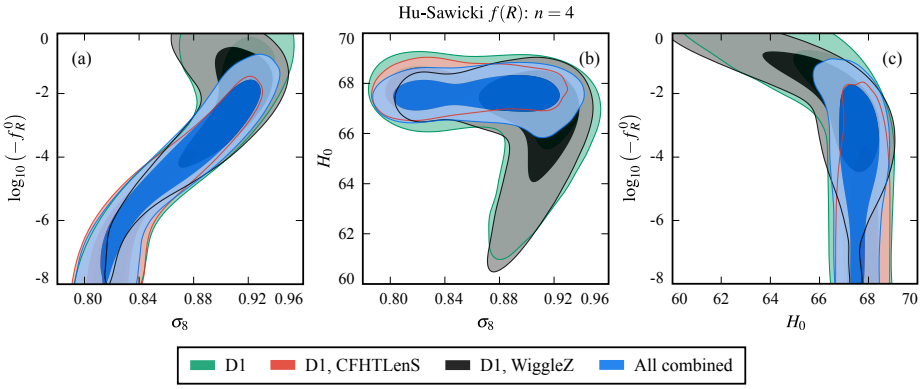

Figure 11.6: Results of the analysis of Hu-Sawicki $f(R)$ with $n = 4$. *Panel (a):* The marginalized joint posterior of $\log_{10}(-f_R^0)$ and σ_8. We can see the well known degeneracy between $\log_{10}(-f_R^0)$ and the growth of structure. *Panel (b):* The marginalized joint posterior of H_0 and σ_8 displaying a marked degeneracy between the two parameters. *Panel (c):* The marginalized joint posterior of $\log_{10}(-f_R^0)$ and H_0. We can see a strong degeneracy between the two parameters for large values of $\log_{10}(-f_R^0)$. This is introduced by the modification of the background equations. In all panels different colors correspond to different data set combinations as shown in legend. From [1].

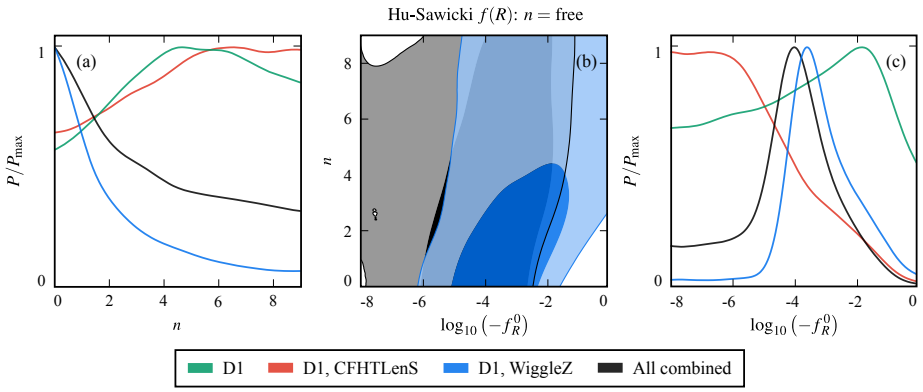

Figure 11.7: Results of the analysis of Hu-Sawicki $f(R)$ varying both model parameters, i.e. the index n and the boundary condition f_R^0. *Panel (a):* The marginalized posterior of n. As we can see there is no statistically significant bound on this parameter. *Panel (b):* The marginalized joint posterior of n and $\log_{10}(-f_R^0)$. The darker and lighter shades correspond respectively to the 68% C.L. and the 95% C.L.. It is the first time were the significant correlation between these two parameters is shown. *Panel (c):* The marginalized posterior of $\log_{10}(-f_R^0)$. As in the previous cases the WiggleZ data set drives the posterior of $\log_{10}(-f_R^0)$ away from the ΛCDM limit. In all panels different colors correspond to different data set combinations as shown in legend. From [1].

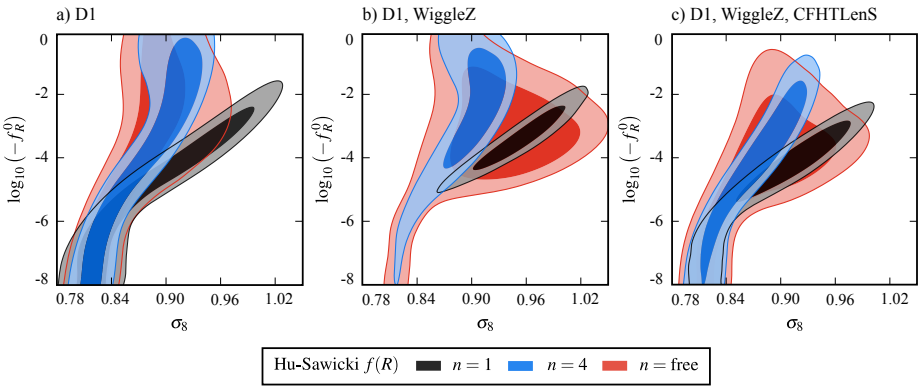

Figure 11.8: All panels show the marginalized joint posterior of σ_8 and $\log_{10}\left(-f_R^0\right)$ for different data set combinations. The darker and lighter shades correspond respectively to the 68% C.L. and the 95% C.L.. Different colors correspond to different Hu-Sawicki models as shown in legend. We can see the change in the degeneracy direction depending on the value of n that is used, with a weak dependence on the data set. From [1].

numerically. More generally, one will need to interface EFTCAMB with the time evolution of the EFT functions corresponding to the given model. The advantage of this mapping algorithm is that it allows the users to implement a specific model within a few steps without going to the details of the complicated perturbation equations. The EFTCAMB background and perturbation solvers will solve the coupled system consistently.

In order to display the full potential of this implementation, which treats fully and in a model specific way the dynamics of both the background and the perturbations, we discussed some linear structure growth rate estimators, such as $f\sigma_8$ and E_G, and studied the constraints on the Hu-Sawicki $f(R)$ model with current cosmological data. As for the growth estimators, unlike in the ΛCDM scenario, at the linear regime, both $f\sigma_8$ and E_G are *scale-dependent* in DE/MG models, and this was clearly visible for the Hu-Sawicki model. For this reason, we showed the $f\sigma_8$ growth in different wavenumber and the E_G angular distribution at some fixed averaged redshift snapshot. The former, as expected, showed quite significant scale-dependent profiles against the present redshift space distortion data. However, since there are a lot of residual systematics in the E_G estimator pipeline, the scale-dependent angular distribution in $f(R)$ case is still inside of the scattering of the current data points.

Finally, we run a Markov-Chain Monte-Carlo analysis and estimated the model and cosmological parameters against Planck CMB, including CMB lensing, WiggleZ galaxy number density counts as well CFHTLenS weak lensing surveys. We found some degeneracy between σ_8 and $|f_R^0|$, through which, the WiggleZ data set, favors a high value of both parameters, while CMB and CFHTLenS measurements favor a smaller value. Furthermore, when $n = 4$ and $\log_{10}(-f_R^0) > -2$, this degeneracy has an abrupt change in direction. This change in the degeneracy direction clearly showed up also in the posterior distribution of σ_8 and H_0. For the small value of the scalaron Compton wavelength,

such as $\log_{10}(-f_R^0) < -2$, the parameter describing $f(R)$ is not degenerate with the Hubble parameter but, as soon as $\log_{10}(-f_R^0) > -2$, a marked degeneracy arises. It is because when $\log_{10}(-f_R^0) < -2$ the model is constrained through its effect on perturbations, while in the regime $\log_{10}(-f_R^0) > -2$ the effect of this modification of gravity at the background level is not negligible. Hence, the background kinematics play an important role in constraining the model in this parameter range. This degeneracy was fully displayed for the first time since with our procedure we have solved the specific background for the model, without approximating it to a ΛCDM one.

Chapter 12

Hořava Gravity

In their quest to find a quantum theory of gravity that could describe physical phenomena at the Planck scale ($\sim 10^{19}$ GeV/c^2), relativists have recently started to explore Lorentz violating theories (LV) (see [182] and references therein). Indeed, even though Lorentz invariance (LI) is considered a cornerstone of our knowledge of reality, the challenge presented by physics at Planck energy is forcing us to question also our firmest assumptions. In the cosmological context, LV theories represent interesting candidates for cosmic acceleration, since in their low-energy limit they generally predict a dynamical scalar degree of freedom (DoF) which could provide a source for the late time acceleration, in alternative to the cosmological constant.

Interestingly, LV theories typically break LI at all scales, and are therefore constrainable with many different measurements and data sets over a vast range of energies. Constraints and measurements on the parameters of a general realistic effective field theory for Lorentz violation [286], usually referred to as the Standard Model Extension [287, 288], support LI with an exquisite accuracy. Furthermore, LI has been tested to high accuracy on solar system scales, and stringent bounds have been placed on the Post Newtonian parameters (PPN), in particular on those corresponding to the preferred frame effects, since such effects are typical of LV theories [240]. Phenomena on astrophysical scales, and in particular tests of gravity in the strong regime, such as those of binary pulsars [289, 290], provide further bounds on LV [240]. On the contrary, the exploration of cosmological bounds on LV theories is still in its infancy [291, 292, 185, 293, 294].

In this chapter, we focus on the class of LV theories known as Hořava gravity [295, 228] which modifies the gravitational action by adding higher order spatial derivatives without adding higher order time derivatives, thus modifying the graviton propagator and achieving a power-counting renormalizability. This is possible if one considers that space and time scale differently. Such a prescription is implemented through a breaking of full diffeomorphism invariance, which leads to LV at all scales. The resulting theory propagates a new dynamical scalar DoF, i.e. the spin-0 graviton. As a candidate for quantum gravity, Hořava theory is expected to be renormalizable and also unitary. Nevertheless, at the moment there is no evidence for renormalizability beyond the power-counting arguments.

Hořava gravity shows a rich phenomenology on cosmological scales, e.g. the higher curvature terms in the action lead to a matter bouncing cosmology [296, 297]; it also shows different mechanisms by which it is possible to explain the nearly scale invariant spectrum of cosmological perturbations without introducing an inflationary phase [298, 299, 300, 301, 302], finally, cosmological perturbations at late time have been investigated in refs. [291, 303, 304, 305, 306, 307, 308].

Here we consider Hořava gravity within the framework of the EFT of DE/MG, that has been recently considered and investigated in refs. [176, 309]. We work out a complete mapping of the theory into the EFT language for an action including all the operators which are relevant for linear perturbations with up to sixth order spatial derivatives, which is the minimal prescription to achieve power counting renormalizability. We focus on the part of this action that contributes to linear order in perturbations [310]. For this action we work out a complete mapping to the EFT framework deriving also the generalization of the original EFT action used in refs. [8, 311]. When we compare the predictions of the theory to the observations, we consider only the low-energy operators of Hořava gravity, since those are the relevant ones to describe the large scale cosmology associated to the observables that we employ. We work out the contribution of these operators to the equations of motion for linear scalar and tensor perturbations.

We then employ EFTCAMB/EFTCosmoMC to study the cosmology of the low-energy limit of Hořava gravity and derive constraints on its parameters using several cosmological data sets We get improved upper bounds, with respect to those from Big Bang Nucleosynthesis, on the deviation of the cosmological gravitational constant from the local Newtonian one. At the level of the background phenomenology, we find a relevant rescaling of the Hubble rate at all epoch, which has a strong impact on the cosmological observables; at the level of perturbations, we discuss in details all the relevant effects on the observables and find that in general the quasi-static approximation is not safe to describe the evolution of perturbations. Overall we find that the effects of the modifications induced by the low-energy Hořava gravity action are quite dramatic and current data place tight bounds on the theory parameters.

12.1 Introduction to Hořava Gravity

Hořava gravity has been recently proposed as a candidate for an ultraviolet completion of GR [295, 228]. The basic idea is to modify the graviton propagator by adding to the action higher-order spatial derivatives without adding higher-order time derivatives, in order to avoid the presence of Ostrogradski instabilities [312]. The theory is constructed in such a way to be compatible with a different scaling of space and time, i.e.

$$[dt] = [k]^{-z}\,, \qquad [dx] = [k]^{-1}\,, \tag{12.1}$$

where z is a positive integer and k is the momentum. In order to accommodate such a different scaling between space and time, the action of Hořava gravity cannot still be invariant under the full set of diffeomorphisms as in GR, but it

can be invariant under the more restricted foliation-preserving diffeomorphisms

$$t \to \tilde{t}\,(t)\,, \qquad x^i \to \tilde{x}^i\left(t, x^i\right). \tag{12.2}$$

Therefore, within this approach, space and time are naturally treated on different footing leading to Lorentz violations at all scales. The emergence of LV is reflected in modified dispersion relations for the propagating DoFs. From a practical point of view, the different behavior of space and time is achieved by picking a preferred foliation of spacetime, geometrically described within the Arnowitt-Deser-Misner (ADM) formalism.

It has been shown that the theory is power-counting renormalizable if and only if $z \geq d$, where d indicates the number of spatial dimensions, which means that the action has to contain operators with at least $2d$ spatial derivatives [313, 314]. Hence, in a four-dimensional spacetime, $d = 3$, power-counting renormalizability arguments request at least sixth-order spatial derivatives in the action.

Considering the above arguments, the action of Hořava gravity can be written as follows [310]

$$\begin{aligned}\mathcal{S}_H =& \frac{1}{16\pi G_H}\int d^4x\sqrt{-g}\left(K_{ij}K^{ij} - \lambda K^2 - 2\xi\bar{\Lambda} + \xi\mathcal{R} + \eta a_i a^i + L_4 + L_6\right)\\ &+ S_m[g_{\mu\nu}, \chi_i],\end{aligned} \tag{12.3}$$

where g is the determinant of the metric $g_{\mu\nu}$, $\mathcal{R}$ is the Ricci scalar of the three-dimensional space-like hypersurfaces, K_{ij} is the extrinsic curvature, and K is its trace. $\{\lambda, \xi, \eta\}$ are dimensionless running coupling constants, $\bar{\Lambda}$ is the "bare" cosmological constant, $a_i = \partial_i \ln N$ where as usual N is the lapse function of the ADM metric. L_4 and L_6 denote the Lagrangians associated to the higher-order operators, that contain, respectively, fourth and sixth-order spatial derivatives (see appendix .3 for the explicit expressions of their parts that contribute to linear order perturbations). These Lagrangians constitute the high-energy (HE) part of the action (12.3), while the operators preceding them represent the low-energy (LE) limit of the theory and are the ones of relevance on large scale. S_m is the matter action for all matter fields, χ_i. Finally, G_H is the coupling constant which can be expressed as

$$G_H = \xi G \tag{12.4}$$

where G is the "bare" gravitational constant. As demonstrated in ref. [310], the solution of the static point-like mass in the Newtonian limit gives the relationship between the "bare" gravitational constant (G) and the Newtonian one (G_N), i.e.

$$G = G_N\left(1 - \frac{\eta}{2\xi}\right). \tag{12.5}$$

Then, the coupling in front of the action reads

$$\frac{1}{16\pi G_H} = \frac{m_0^2}{(2\xi - \eta)}, \tag{12.6}$$

where $m_0^2 = 1/8\pi G_N$ is the Planck mass defined locally.

Notice that the action of GR is recovered when $\lambda = 1$, $\xi = 1$ and $\eta = 0$, and the higher order operators in L_4 and L_6 are not considered.

The symmetry of the theory allows for a very large number of operators $\sim \mathcal{O}(10^2)$ in L_4 and L_6. In order to limit the huge proliferation of couplings in the full theory, in the first proposal Hořava imposed some restrictions, i.e. projectability and detailed balance (for the details see refs. [315, 316, 317, 318, 319, 320, 321]). In the following we will not impose any of these limitations to the action (12.3) and we will consider for L_4 and L_6 all the operators which contribute to the dynamics of linear perturbations [310].

12.2 Mapping Hořava Gravity into EFT

In this section we will work out explicitly the mapping of the low-energy (LE) part of action (12.3) into the EFT formalism. This is the part of the action for which we will explore cosmological constraints. We show the mapping for the high-energy (HE) part (L_4 and L_6) in the appendix .3.

We define a time-like unit vector, n_μ as :

$$n_\mu = \frac{\partial_\mu t}{\sqrt{-g^{\alpha\beta}\partial_\alpha t \partial_\beta t}}, \qquad \text{with} \qquad n_\mu n^\mu = -1, \tag{12.7}$$

which corresponds to the convention that we use for the normal vector to the uniform-field hypersurfaces in the EFT construction of the action (6.1) [163, 8]. In conformal time and at second order in perturbations, one has

$$n_\mu = \delta^0_\mu \left(1 + \frac{1}{2}a^2\delta g^{00} + \frac{3}{8}(a^2\delta g^{00})^2\right), \tag{12.8}$$

$$n^\mu = g^{0\mu} \left(1 + \frac{1}{2}a^2\delta g^{00} + \frac{3}{8}(a^2\delta g^{00})^2\right). \tag{12.9}$$

In the following, these relations will be often employed.

Let us first recall the low-energy action, which can be rewritten as:

$$\begin{aligned}\mathcal{S}_{H,LE} =& \frac{m_0^2}{(2\xi-\eta)}\int d^4x\sqrt{-g}\Big[K_{ij}K^{ij} - \lambda K^2 + \xi\mathcal{R} - 2\xi\bar{\Lambda} + \eta a_i a^i\Big] \\ =& \frac{m_0^2}{(2\xi-\eta)}\int d^4x\sqrt{-g}\Big[\xi R + (1-\xi)K^{ij}K_{ij} + (\xi-\lambda)K^2 \\ & - 2\xi\bar{\Lambda} + \eta a_i a^i\Big] + \text{boundary terms}\,,\end{aligned} \tag{12.10}$$

where the second line has been obtained by using the Gauss-Codazzi relation [322].
In the following, we show how to rewrite every single term of the above action in the EFT formalism described by the action (6.1), providing the mapping of the Hořava gravity parameters into the EFT functions.

- $\frac{m_0^2\xi}{(2\xi-\eta)}\left(R - 2\bar{\Lambda}\right)$
  Comparing the above expression with the EFT action (6.1), it is straightforward to deduce that these two terms contribute to the following EFT

functions

$$(1+\Omega)=\frac{2\xi}{(2\xi-\eta)},\qquad \Lambda=-2\frac{m_0^2\xi}{(2\xi-\eta)}\bar{\Lambda}. \tag{12.11}$$

- $\frac{m_0^2}{(2\xi-\eta)}(\xi-\lambda)K^2$

In order to identify the relation between the EFT functions and the Hořava gravity parameters we have to expand K^2 up to second order in perturbations as

$$K^2=2K^{(0)}K+(\delta K)^2-K^{(0)2}, \tag{12.12}$$

by using $K=K^{(0)}+\delta K$. Comparing the above relation with the action (6.1), it is straightforward to see that the last term gives contribution to $\Lambda(\tau)$ and the second one to $\bar{M}_2^2(\tau)$. The first term can be computed as follows [162]

$$\begin{aligned}\int d^4x\sqrt{-g}2K^{(0)}K &= 2\int d^4x\sqrt{-g}K^{(0)}\left(\nabla_\mu n^\mu\right)\\ &= -2\int d^4x\sqrt{-g}\nabla_\mu K^{(0)}n^\mu\\ &= 2\int d^4x\sqrt{-g}\frac{\dot{K}^{(0)}}{a}\left[1-\frac{1}{2}(a^2\delta g^{00})-\frac{1}{8}(a^2\delta g^{00})^2\right],\end{aligned} \tag{12.13}$$

where we have integrated by parts the second line and we have used eq. (12.9). The last line will give respectively its contribution to $\Lambda(\tau)$, $c(\tau)$ and $M_2^4(\tau)$. Then summarizing, the corresponding contributions to the EFT functions from the K^2 term are

$$\begin{aligned}&\Lambda(\tau)=-\frac{m_0^2(\xi-\lambda)}{(2\xi-\eta)}\left(K^{(0)2}-2\frac{\dot{K}^{(0)}}{a}\right),\qquad c(\tau)=\frac{m_0^2(\xi-\lambda)}{(2\xi-\eta)}\frac{\dot{K}^{(0)}}{a},\\ &M_2^4(\tau)=-\frac{m_0^2(\xi-\lambda)}{2(2\xi-\eta)}\frac{\dot{K}^{(0)}}{a},\qquad \bar{M}_2^2(\tau)=-\frac{2m_0^2}{(2\xi-\eta)}(\xi-\lambda).\end{aligned} \tag{12.14}$$

- $\frac{m_0^2(1-\xi)}{(2\xi-\eta)}K_{ij}K^{ij}$

As before, we can expand up to second order in perturbations the above operator and it can be written as

$$K_{ij}K^{ij}=2K^{(0)}_{ij}\delta K^{ij}+K^{ij(0)}K^{(0)}_{ij}+\delta K_{ij}\delta K^{ij}, \tag{12.15}$$

where we have used the spatial metric to raise the indices and the extrinsic curvature has been decomposed into its background and first order perturbation parts, i.e. $K_{ij}=K^{(0)}_{ij}+\delta K_{ij}$. Moreover, the first term can be written as

$$2K^{(0)}_{ij}\delta K^{ij}=-2\frac{\mathcal{H}}{a}\delta K=-2\frac{\mathcal{H}}{a^2}\left(aK+3\mathcal{H}\right), \tag{12.16}$$

where the term proportional to K can be treated as in eq. (12.13). Finally, in terms of the EFT functions this operator can be written as

$$\Lambda(\tau) = -\frac{m_0^2(1-\xi)}{(2\xi-\eta)}\left[K^{ij(0)}K_{ij}^{(0)} + \frac{2}{a^2}\left(\dot{\mathcal{H}}-\mathcal{H}^2\right)\right],$$
$$c(\tau) = -\frac{m_0^2(1-\xi)}{(2\xi-\eta)a^2}(\dot{\mathcal{H}}-\mathcal{H}^2)$$
$$M_2^4(\tau) = \frac{m_0^2(1-\xi)}{2a^2(2\xi-\eta)}(\dot{\mathcal{H}}-\mathcal{H}^2), \qquad \bar{M}_3^2 = -2\frac{m_0^2(1-\xi)}{(2\xi-\eta)}. \tag{12.17}$$

- $\frac{m_0^2}{(2\xi-\eta)}\eta\, a_i a^i$

Let us first write explicitly a_i in terms of perturbations up to second order

$$a_i = \frac{\partial_i N}{N} = -\frac{1}{2}\frac{\partial_i(a^2 g^{00})}{a^2 g^{00}} = \frac{1}{2}\partial_i\delta(a^2 g^{00}) + \mathcal{O}(2), \tag{12.18}$$

where in the last equality we have used $a^2 g^{00} = -1 + a^2\delta g^{00}$ and then we have expanded in Taylor series. Then we get

$$\frac{m_0^2}{(2\xi-\eta)}\eta a_i a^i = \frac{m_0^2}{4(2\xi-\eta)}\eta\frac{\tilde{g}^{ij}}{a^2}\partial_i(a^2\delta g^{00})\partial_j(a^2\delta g^{00}), \tag{12.19}$$

where $\tilde{g}^{ij}$ is the background value of the spatial metric. In the EFT language the above expression corresponds to

$$m_2^2 = \frac{m_0^2\eta}{4(2\xi-\eta)}. \tag{12.20}$$

Summarizing, we can map the low-energy action (12.10) of Hořava gravity in the EFT language at the basis of EFTCAMB as follows:

$$(1+\Omega) = \frac{2\xi}{(2\xi-\eta)},$$
$$c(\tau) = -\frac{m_0^2}{a^2(2\xi-\eta)}(1+2\xi-3\lambda)\left(\dot{\mathcal{H}}-\mathcal{H}^2\right),$$
$$\Lambda(\tau) = \frac{2m_0^2}{(2\xi-\eta)}\left[-\xi\bar{\Lambda} - (1-3\lambda+2\xi)\left(\frac{\mathcal{H}^2}{2a^2}+\frac{\dot{\mathcal{H}}}{a^2}\right)\right],$$
$$\bar{M}_3^2 = -\frac{2m_0^2}{(2\xi-\eta)}(1-\xi),$$
$$\bar{M}_2^2 = -2\frac{m_0^2}{(2\xi-\eta)}(\xi-\lambda),$$
$$m_2^2 = \frac{m_0^2\eta}{4(2\xi-\eta)},$$
$$M_2^4(\tau) = \frac{m_0^2}{2a^2(2\xi-\eta)}(1+2\xi-3\lambda)\left(\dot{\mathcal{H}}-\mathcal{H}^2\right),$$
$$\bar{M}_1^3 = \hat{M}^2 = 0, \tag{12.21}$$

where we have explicitly written the value of the extrinsic curvature and its trace on a flat FLRW background [1]. The mapping of the high-energy part of the action can be found in appendix .3.

12.3 Degrees of freedom: dynamics and stability

After the full diffeomorphism invariance is restored by means of the Stückelberg mechanism, at the level of perturbations we have a dynamical equation for the scalar DoF represented by the Stückelberg field π. In the case of the low-energy limit of Hořava gravity that we are considering, this equation reads

$$\eta\ddot{\pi} + 2\eta\mathcal{H}\dot{\pi} + \left[(3\lambda - 2\xi - 1)(\mathcal{H}^2 - \dot{\mathcal{H}}) + \eta(\mathcal{H}^2 + \dot{\mathcal{H}})\right]\pi + k^2\xi(\lambda - 1)\pi + \xi(\lambda - 1)k\mathcal{Z} + \frac{(\xi - 1)(2\xi - \eta)}{2k}\left[\frac{a^2(\rho_i + p_i)}{m_0^2}v_i\right] = 0, \quad (12.22)$$

where $\mathcal{Z}$ is the standard CAMB variable [104, 105] ρ_i, p_i are the background density and pressure of matter components, and v_i is the velocity perturbation of matter components. The above equation is coupled with the following perturbative field equations:

- time-time (t) field equation

$$2\mathcal{H}\left[k^2\pi(\eta - 3\lambda + 2\xi + 1) + (1 - 3\lambda)k\mathcal{Z}\right] + 2k^2\left(2\xi\bar{\eta} + \eta\dot{\pi}\right) + a^2\frac{2\xi - \eta}{m_0^2}\delta\rho_m = 0\,, \quad (12.23)$$

- space-space (s) field equation

$$-4\mathcal{H}\left[k^2(3\lambda - 2\xi - 1)\pi + (3\lambda - 1)k\mathcal{Z}\right] + (1 - 3\lambda)\ddot{h} + 4k^2\xi\bar{\eta} + 2k^2(-3\lambda + 2\xi + 1)\dot{\pi} + 3a^2\frac{(\eta - 2\xi)}{m_0^2}\delta P_m = 0\,, \quad (12.24)$$

where $h, \bar{\eta}$ are the usual scalar perturbations of the metric in synchronous gauge (notice that we have added a bar to the standard metric perturbation in order to do not confuse it with the Hořava gravity parameter, η). EFTCAMB evolves the above set of coupled differential equations along with the usual matter perturbation equations and the initial conditions are set following ref. [8]. Let us notice that by using the mapping (12.21) worked out in the previous section, it is straightforward to deduce the above equations following the general prescription in ref. [8].

We shall now determine the dispersion relation of the scalar DoF, computing the determinant of the matrix of the coupled system eqs. (12.22)- (12.24). Since

[1] For the low-energy action it is possible to obtain part of the mapping by following the method in ref. [173]. However, one has to consider that our formalism and notation differ from the one in ref. [173] because we are using conformal time, a different signature for the normal unit vector, a different notation for the EFT functions and one more operator is included in our low-energy action: $a_\mu a^\mu$.

the number counting of dynamical DoFs will not be changed by neglecting the couplings with standard matter species, for simplicity, for the purpose of this calculation we neglect them. After taking the Fourier transform $\partial_\tau \to -i\omega$, we can rewrite the system (12.22)- (12.24) in the following matrix form:

$$\begin{pmatrix} \gamma_{\pi\pi} & \gamma_{\pi \mathrm{h}} & \gamma_{\pi\bar{\eta}} \\ \gamma_{\mathrm{s}\pi} & \gamma_{\mathrm{sh}} & \gamma_{\mathrm{s}\bar{\eta}} \\ \gamma_{\mathrm{t}\pi} & \gamma_{\mathrm{th}} & \gamma_{\mathrm{t}\bar{\eta}} \end{pmatrix} \begin{pmatrix} \pi \\ h \\ \bar{\eta} \end{pmatrix} = 0\,, \tag{12.25}$$

where the term γ_{ab} with $a, b = \{\pi, h, \bar{\eta}\}$ corresponds to the coefficient of b in equation a and they can be easily deduced from the above equations. Finally we set the determinant to zero and get

$$k^4\omega(\omega + i\mathcal{H})\Big[\omega^2 + i2\mathcal{H}\omega - \frac{(\lambda-1)\xi(2\xi-\eta)}{\eta(3\lambda-1)}k^2 \\ - \frac{\xi}{\eta}\left((\dot{\mathcal{H}} - \mathcal{H}^2)(\eta - 3\lambda + 2\xi + 1) + (6\lambda - 4\xi - 2)\mathcal{H}^2\right)\Big] = 0\,, \tag{12.26}$$

which can be written in a compact form as

$$k^4\omega\left(\omega + i\frac{\alpha}{2}\right)\left[\omega^2 + i\alpha\omega - k^2c_s^2 + \beta\right] = 0\,. \tag{12.27}$$

From the above equation we deduce that only one extra dynamical DoF exists, which corresponds to the scalar graviton (π field in EFT language), as expected. Furthermore, one can identify the terms in the squared bracket as follows: α is a friction term, β is the dispersion coefficient and c_s^2 can be identified with the canonical speed of sound defined in vacuum, when no friction or dispersive terms are present. Let us notice that both the friction and dispersive terms are related to the nature of the dark energy component through the dependence of the Hubble rate on the latter (12.37). The procedure to compute the dispersion relation (12.26) follows the one in ref. [163], but here we include also friction and dispersive terms.

In order to ensure that a given theory is viable, we enforce a set of physical and mathematical viability conditions. The mathematical conditions prevent exponential instabilities from showing up in the solution of the π-field equation, and the physical ones correspond to the absence of ghosts and gradient instabilities for both scalar and tensor modes. In particular, in our analysis of Hořava gravity, for the scalar DoF they correspond to

$$\frac{2m_0^2\eta(1-3\lambda)k^2}{(\eta-2\xi)\left(2(3\lambda-1)\mathcal{H}^2 + \eta(\lambda-1)k^2\right)} > 0\,, \qquad \frac{\xi(2\xi-\eta)(\lambda-1)}{\eta(3\lambda-1)} > 0, \tag{12.28}$$

where the first condition corresponds to a positive kinetic term and it has been obtained from the action by integrating out all the non dynamical fields, while the second one ensures that the speed of sound is positive. Let us note that the ghost condition reduces to the one in the Minkowski background by setting the limit $a \to 1$.

Additional conditions to be imposed comes from the equation for the propagation of tensor modes h_{ij},

$$A_T(\tau)\ddot{h}_{ij} + B_T(\tau)\dot{h}_{ij} + D_T(\tau)k^2h_{ij} + E_{Tij} = 0. \tag{12.29}$$

where δT_{ij} generally contains the matter contributions coming from the neutrino and photon components and, for Hořava gravity, the remaining coefficients read:

$$A_T = \frac{2}{2\xi - \eta}\,, \qquad B_T = \frac{4\mathcal{H}}{2\xi - \eta}\,, \tag{12.30}$$

$$D_T = \frac{2\xi}{2\xi - \eta}\,, \qquad E_{Tij} = \frac{a^2}{m_0^2}\delta T_{ij}\,. \tag{12.31}$$

The viability conditions require $A_T > 0$ and $D_T > 0$ to prevent respectively a tensorial ghost and gradient instabilities [10].

It is easy to show that the above conditions translate into the following constraints on the parameters of Hořava gravity:

$$0 < \eta < 2\xi\,, \qquad \lambda > 1 \qquad \text{or} \qquad \lambda < \frac{1}{3}, \tag{12.32}$$

which are compatible with the viable regions identified around a Minkowski background [310]. In the following we will not explore the $\lambda < 1/3$ branch since along it the cosmological gravitational constant on the FLRW background becomes unacceptably negative [178, 179] and the branch does not have a continuous limit to GR. The conditions that we have discussed are naturally handled by EFTCAMB/EFTCosmoMC in the form of *viability priors* that are automatically enforced when the parameter space is being sampled.

Besides the above theoretical viability conditions, there are observational constraints on the Hořava gravity parameters coming from existing data. In particular:

- Big Bang Nucleosynthesis (BBN) constraints [291], which set an upper bound on $|G_{cosmo}/G_N - 1| < 0.38$ (99.7% C.L.)[2], where G_{cosmo} is the cosmological gravitational constant as defined in section 12.4;

- Solar system constraints, where the parametrized post Newtonian parameters (PPN) are bounded to be[3]:

$$\alpha_1 < 3.0 \cdot 10^{-4}\ (99.7\%\text{C.L.})\,, \quad \alpha_2 < 7.0 \cdot 10^{-7}\ (99.7\%\text{C.L.})\,. \tag{12.33}$$

  where α_1 and α_2 are two of the parameters appearing in the PPN expansion of the metric around Minkowski spacetime, more precisely those associated with the preferred frame effects [240, 323]. Here we consider only these two parameters sice they are the only ones of relevance for constraining LV. It has been shown in refs. [324, 325, 326], that the PPN parameters for the low-energy action of Hořava gravity, read

$$\begin{aligned}\alpha_1 &= 4(2\xi - \eta - 2)\,,\\ \alpha_2 &= -\frac{(\eta - 2\xi + 2)(\eta(2\lambda - 1) + \lambda(3 - 4\xi) + 2\xi - 1)}{(\lambda - 1)(\eta - 2\xi)}\,.\end{aligned} \tag{12.34}$$

[2]The original bound in ref. [291] is reported at 68% C.L. and we convert it to 99.7% C.L. by assuming a Gaussian posterior distribution of $G_{cosmo}/G_N - 1$.

[3]The original bounds in ref. [323] (and references therein) are reported at 90% C.L. and we convert it to 99.7% C.L. by assuming a Gaussian posterior distribution of the relevant parameters.

It is easy to show that combining the above relations, the above mentioned PPN bounds result in a direct constraint on λ that reads:

$$\log_{10}(\lambda - 1) < -4.1 \ (99.7\%\text{C.L.}), \tag{12.35}$$

while the bound on α_1 provides a degenerate constraint on the other two parameters $\{\xi, \eta\}$.

- Čherenkov constraints from the observation of high-energy cosmic rays [327] are usually imposed as a lower bound on the propagation speed of the scalar DoF and the propagation speed of tensor modes. In the case of LV theories we will refer the reader to Refs. [327, 328], for further details. However, since these bounds have not been worked out specifically for Hořava gravity we decided not to impose them *a priori*.

For the present analysis we consider two specific cases of Hořava gravity:

1. Hořava 3, hereafter H3, where we vary all three parameters $\{\lambda, \eta, \xi\}$ appearing in the low-energy Hořava gravity action;
2. Hořava 2, hereafter H2, where we choose the theory parameters in order to evade the PPN constraints (12.34) by setting exactly $\alpha_1 = \alpha_2 = 0$. This implies:
$$\eta = 2\xi - 2, \tag{12.36}$$
so that the number of free parameters reduce to two, $\{\lambda, \eta\}$. This case has the quality of systematically evading solar system PPN constraints, meaning that it is not possible to build a local experiment, with arbitrary precision, to distinguish it from GR. Therefore it can only be constrained with cosmological observations.

For both cases we impose the physical and mathematical viability conditions in the form of *viability priors* as discussed in ref. [7]. The portion of the parameter space excluded by the *viability priors* can be seen as a dark grey contour in figure 12.6 for the H3 case and in figure 12.7 for the H2 case. For both cases we also derive the bounds on $G_{cosmo}/G_N - 1$ and for the H3 case we provide cosmological bounds on the PPN parameters. These results are shown and discussed in detail in section 12.6.

12.4 Hořava Background Cosmology

The first step toward testing a theory against cosmological observations, is to investigate the behaviour of its cosmological background. In this section, we discuss the background evolution equation for Hořava gravity, its implementation in EFTCAMB, and review the definitions that we adopt for the cosmological parameters.

The Hořava gravity field equations for a flat FLRW background read:

$$\frac{3\lambda - 1}{2}\mathcal{H}^2 = \frac{8\pi G_N(2\xi - \eta)}{6}a^2\sum_i \rho_i + \xi\frac{\bar{\Lambda}}{3}a^2, \tag{12.37}$$

$$-\frac{3\lambda - 1}{2}\left[\dot{\mathcal{H}} + \frac{1}{2}\mathcal{H}^2\right] = -\frac{\xi\bar{\Lambda}}{2}a^2 + 4\pi G_N\frac{(2\xi - \eta)}{2}a^2\sum_i p_i, \tag{12.38}$$

where ρ_i and p_i are respectively the density and the pressure of the matter fluid components, i.e. baryons and dark matter (m), radiation and massless neutrino (r) and massive neutrinos (ν). Here we consider that all massive neutrino species have the same mass and we set the sum of their masses to be 0.06 eV. In addition to the Friedmann equations, we have the standard continuity equations for matter and radiation:

$$\dot{\rho}_i + 3\mathcal{H}(1+w_i)\rho_i = 0, \tag{12.39}$$

while for massive neutrinos we refer the reader to ref. [5] for a detailed discussion.

Starting from the Friedmann eq. (12.37), we can define the cosmological gravitational constant as:

$$G_{\rm cosmo} = \frac{(2\xi-\eta)}{3\lambda-1} G_N, \tag{12.40}$$

where it is clear that $G_{\rm cosmo}$ differs from G_N, which is obtained with local experiments, as already pointed out in ref. [310]. This definition allows us to write the Friedmann equation (12.37) in another way:

$$\mathcal{H}^2 = 8\pi G_{\rm cosmo} a^2 \left(\frac{\sum_i \rho_i}{3} + \frac{1}{8\pi G_N} \frac{2\xi}{2\xi-\eta} \frac{\bar{\Lambda}}{3} \right) . \tag{12.41}$$

From this equation it is straightforward to see that in general, once the theory parameters have been properly set, the modification that Hořava gravity induces at the level of the background is a global rescaling of $\mathcal{H}$ [294].

In order to properly identify the parameters that we should fit to data, we have to pay special attention to the working definition of all the relevant quantities. In particular in the definition of the relative density abundance. For the matter fields, we define $\Omega_i(a)$ in terms of the locally measured gravitational constant, G_N, and the present time Hubble parameter, H_0. We then derive the abundance of the effective dark energy, describing the modifications to the Friedmann equations, by means of the flatness condition, i.e. $\sum_i \Omega_i(a) + \Omega_{DE}(a) = 1$. To this extent, we rewrite the Friedmann eq. (12.37) as

$$\mathcal{H}^2 = 8\pi G_N \frac{\sum_i \rho_i}{3} a^2 + \frac{2\xi}{2\xi-\eta} \frac{\bar{\Lambda}}{3} a^2 + \left(1 - \frac{3\lambda-1}{2\xi-\eta} \right) \mathcal{H}^2 , \tag{12.42}$$

so that it is straightforward to identify

$$\begin{aligned} \Omega_i(a) &= 8\pi G_N \frac{\rho_i}{3} \frac{a^2}{\mathcal{H}^2} , \\ \Omega_{DE}(a) &= \frac{2\xi}{2\xi-\eta} \frac{\bar{\Lambda}}{3} \frac{a^2}{\mathcal{H}^2} + 1 - \frac{3\lambda-1}{2\xi-\eta}. \end{aligned} \tag{12.43}$$

At present time ($a_0 = 1$), we can immediately see that $\Omega^0_{\rm DE} = 1 - \sum_i \Omega^0_i$ with:

$$\Omega^0_{DE} = \frac{2\xi}{2\xi-\eta} \frac{\bar{\Lambda}}{3H_0^2} + 1 - \frac{3\lambda-1}{2\xi-\eta}. \tag{12.44}$$

This allows us to rewrite the Friedmann eq. (12.37) in terms of the parameters that we are going to sample as:

$$\mathcal{H}^2 = \frac{(2\xi-\eta)}{3\lambda-1} a^2 H_0^2 \left[\frac{\Omega^0_m}{a^3} + \frac{\Omega^0_r}{a^4} + \rho_\nu + \left(\Omega^0_{DE} - 1 + \frac{3\lambda-1}{2\xi-\eta} \right) \right] . \tag{12.45}$$

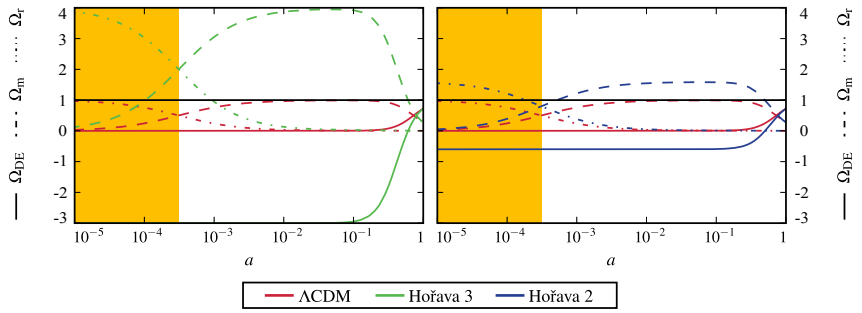

Figure 12.1: The figure shows the evolution of the densities parameters for baryons and dark matter (m, dashed line), radiation, neutrino and massive neutrinos (r, dot dashed line) and dark energy (DE, solid line). In the left panel we compare the density parameters of the H3 case (green lines) with the ones in the ΛCDM model (red lines). In the right panel the comparison is between the H2 case (blue lines) and ΛCDM. The yellow area highlights the radiation dominated era. For this figure the standard cosmological parameters are chosen to be $\Omega_b^0 h^2 = 0.0226$, $\Omega_c^0 h^2 = 0.112$, $\Omega_\nu^0 h^2 = 0.00064$ and $H_0 = 70\,\mathrm{Km/s/Mpc}$. In the H3 case the Hořava gravity parameters are $\lambda = 1.4$, $\xi = 0.9$, $\eta = 1.0$ while in the H2 case they are fixed to $\lambda = 1.4$, $\eta = 1.0$. From [3].

This is the background equation that EFTCAMB evolves, along with its time derivatives. For details about how the code treats ρ_ν see ref. [5]. Finally, one can use eq. (12.44), to substitute the "bare" cosmological constant with Ω_{DE}^0, therefore in the following we use the latter as one of the Hořava parameters that we fit to data instead of $\bar{\Lambda}$.

We shall now specialize to some choices of the Hořava parameters, and derive the corresponding expansion history in order to visualize and discuss the effects of Hořava gravity, in particular for the H3 and H2 cases, on background cosmology. We choose the background values of the cosmological parameters to be $\Omega_b^0 h^2 = 0.0226$ for baryons, $\Omega_c^0 h^2 = 0.112$ for cold dark matter, $\Omega_\nu^0 h^2 = 0.00064$ for massive neutrinos and $H_0 = 70\,\mathrm{Km/s/Mpc}$, accordingly to the default CAMB parameters. Additionally, the parameters of the H3 case are chosen to be: $\lambda = 1.4$, $\xi = 0.9$, $\eta = 1.0$; while in the H2 case we set $\lambda = 1.4$ and $\eta = 1.0$. While the general trend of the modifications does not depend on the magnitude of the theory parameters, the above values are selected in order to enhance the effects and clearly display the changes with respect to the standard cosmological model, ΛCDM. Thus they have to be considered as illustrative examples because the values involved are significantly bigger than the observational bounds that we will derive in section 12.6. However, in both cases the choices of parameters respect the viability criteria discussed in section 12.3.

In figure 12.1 we can see the behaviour of the relative densities for matter (dark matter and baryons), radiation (photons and relativistic neutrinos), and effective dark energy, as defined in eqs. (12.43). One can notice that at early times the matter species display density values that are generally bigger than one, on the contrary the dark energy component assumes negative values. This can be explained as follows. The matter components are well behaved, with positively defined densities with a time evolution that is exactly the standard

one (eq. (12.39)), as expected when working in Jordan frame. However, the expansion history changes as it is rescaled by a constant (eq. (12.45)), altering the time behaviour of the relative abundances. The effective dark energy balances this effect in order to respect the flatness condition. We argue that in this specific case the interpretation of the modification of gravity in terms of a fluid-like component is not well justified/posed, representing instead a genuine geometrical modification of the gravitational sector. This kind of behaviour for the effective dark energy component is commonly encountered in dynamical analysis studies of modified gravity models where the flatness condition is used as a constraint equation [191, 9]. From figure 12.1, we can also notice that Hořava gravity does not affect the time of radiation-matter equality as the continuity equations for these species are not changed, as it is clearly highlighted by the yellow region in the figure. Indeed Ω_m and Ω_r for all the models cross at the same value of the scale factor. On the other hand, the time of equality between matter and dark energy is slightly modified depending on the model parameters. Finally, let us notice that, once the parameters of the theory are chosen to be compatible with the observational constraints, all these effects that we have discussed are quite mitigated and become hardly noticeable by eye in the plots. Indeed, values of the parameters consistent with the bounds that we derive in section 12.6 would induce a less negative DE density at earlier times.

12.5 Cosmological Perturbations in Hořava Gravity

In this section, we proceed to study the dynamics of cosmological perturbations. Once we have worked out the background equations of Hořava gravity (12.45), as well as the mapping of this theory into the EFT language (12.21), we have all the ingredients required by EFTCAMB to perform an accurate analysis of the perturbations. For technical details on the actual implementation, as well as the full set of perturbative equations that are evolved by EFTCAMB, we refer the reader to ref. [10].

As we will see, the behaviour of perturbations in Hořava gravity displays an interesting and rich phenomenology, allowing to investigate the theory and to constrain its parameters with the available data. In the following, we perform an in depth analysis of the dynamics of linear perturbations and the corresponding observables, specializing to a choice of parameters for the case H3 and one for the case H2, in order to visualize and quantify the modifications. In all cases, we set the values of the cosmological parameters to the one used in the previous section, which are the default CAMB parameters, while for the Hořava parameters we use: in the H3 case, $(\xi - 1) = -0.01$, $(\lambda - 1) = 0.004$, $\eta = 0.01$; in the H2 case, $(\lambda - 1) = 0.02$, $\eta = 0.05$. As it will be clear in the next section, these are noticeably bigger than the observational constraints that we will derive, but they facilitate the visualization of the effects on the observables. Let us stress that, while the direction and entity of the modifications that will be described in the remaining of this section are specific to the choice of parameters, we have found an analogous trend for several choices of parameters that we have sampled in the region allowed by the *viability priors*.

Let us now focus on the time and scale evolution of cosmological perturba-

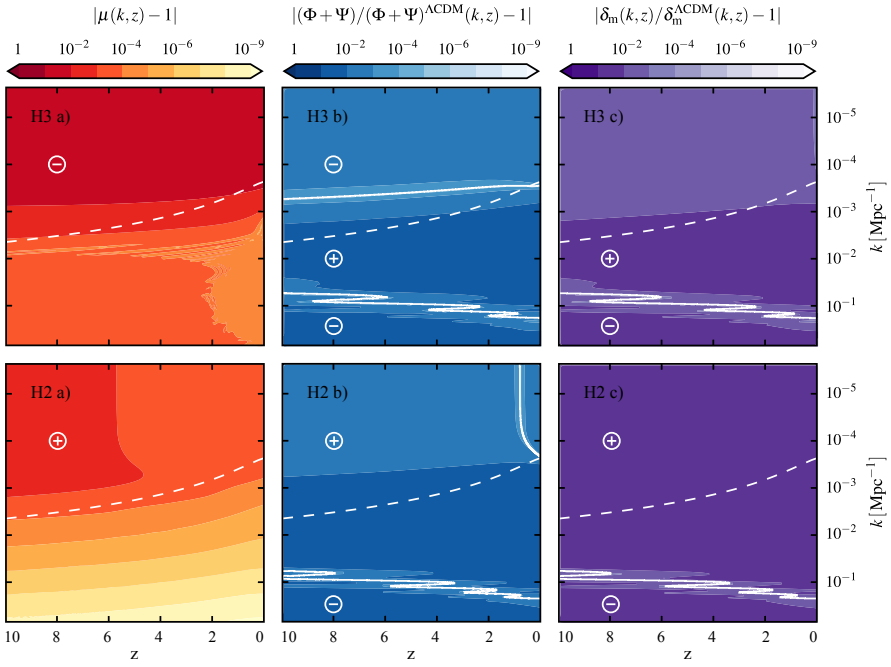

Figure 12.2: We show the relative comparison of the modification of the Poisson equation μ, the source of gravitational lensing $\Phi + \Psi$ (whose derivative sources the ISW effect on the CMB), and $\delta_{\rm m} \equiv \sum_m \rho_{\rm m}\Delta_{\rm m}/\sum_m \rho_{\rm m}$ with their ΛCDM values for the H3 (upper panel) and H2 (lower panel) models. In all panels, the dashed white line represents the physical horizon while the solid white line shows where the relative comparison changes sign. For this figure the standard cosmological parameters are chosen to be $\Omega_b^0 h^2 = 0.0226$, $\Omega_c^0 h^2 = 0.112$, $\Omega_\nu^0 h^2 = 0.00064$ and $H_0 = 70\,\mathrm{Km/s/Mpc}$. In the H3 case the additional parameters are $(\xi - 1) = -0.01$, $(\lambda - 1) = 0.004$, $\eta = 0.01$ while in the H2 case they are fixed to $(\lambda - 1) = 0.02$, $\eta = 0.05$. For a detailed explanation of this figure see section 12.5. From [3].

tions and the growth of structure. In order to discuss the deviations of Hořava gravity from ΛCDM, we study the behaviour of the $\mu(k, a)$-function, which is defined in Newtonian gauge as [145]

$$k^2\Psi \equiv -\mu(k,a)\frac{a^2}{2m_0^2}\rho_m\Delta_m\,, \tag{12.46}$$

where Δ_m is the comoving matter density contrast and Ψ is the scalar perturbation describing fluctuations in the time-time component of the metric. As it is clear from eq. (12.46), μ parametrizes deviations from GR in the Poisson equation. In the standard cosmological model, ΛCDM, this function is constant and $\mu = 1$. Let us notice that EFTCAMB does never evolve the above quantity (12.46), but it can easily output μ as a derived quantity. Moreover, we also analyse the behaviour of the quantity $\Phi + \Psi$, where Φ is the scalar perturbation of the space-space component of the metric in Newtonian gauge. This quantity is important as it allows to identify possible modifications in the lensing potential

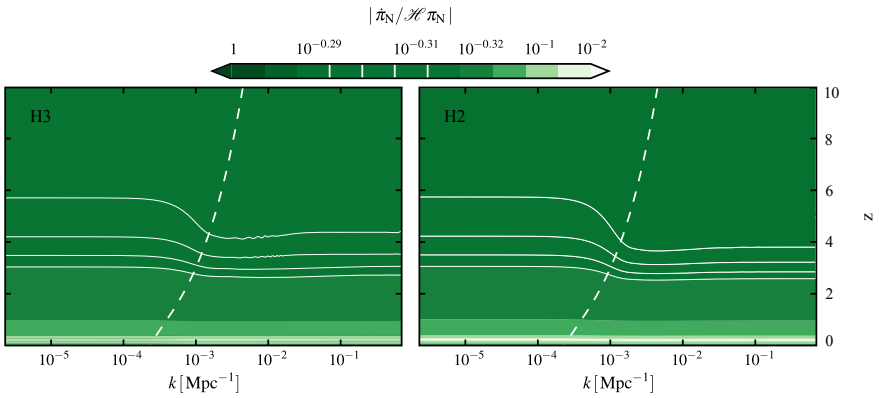

Figure 12.3: We show the quantity $\xi_N = \dot{\pi}_N/\mathcal{H}\pi_N$ that we introduce as an indicator of the goodness of the quasi-static approximation for the H3 (left panel) and H2 (right panel) cases. In both panels, the dashed white line represents the physical horizon, while the solid white lines highlight the scale dependence of this quantity. For this figure the standard cosmological parameters are chosen to be $\Omega_b^0 h^2 = 0.0226$, $\Omega_c^0 h^2 = 0.112$, $\Omega_\nu^0 h^2 = 0.00064$ and $H_0 = 70\,\mathrm{Km/s/Mpc}$. In the H3 case the Hořava gravity parameters are $(\xi - 1) = -0.01$, $(\lambda - 1) = 0.004$, $\eta = 0.01$ while in the H2 case they are fixed to $(\lambda - 1) = 0.02$, $\eta = 0.05$. For a detailed explanation of this figure see section 12.5. From [3].

and in the low multipole of the cosmic microwave background (CMB) radiation through the Integrated Sachs-Wolfe (ISW) effect. Finally, we explore the fluctuations in the total matter distribution defined as $\delta_\mathrm{m} \equiv \sum_m \rho_\mathrm{m} \Delta_\mathrm{m} / \sum_m \rho_\mathrm{m}$.

In figure 12.2 we show the time and scale behaviour of these three quantities. In order to facilitate the visualization of the deviations from the ΛCDM behaviour, we show the logarithmic fractional comparison between these quantities in the two Hořava gravity cases considered and the ΛCDM model.

- *H3 case*: from the top left panel of figure 12.2 we can see that μ significantly deviates from one at large scales and all redshift with fractional differences that are around unity (100%). Small deviations of the order of 10^{-4} can be also seen at small scales and high redshift. At small scales and low redshift, in the bottom right part of the H3 a) panel, one can notice small features due to the fact that the π field oscillates while being coupled to the other species. From the top central panel of the same figure we can see that gravitational lensing is modified as well. On large, super-horizon, scales deviations from the ΛCDM behaviour are not significant, staying below 10^{-2} at all the times shown. In general at these scales the lensing is suppressed. On sub-horizon scales in turn the enhancement of the lensing potential with respect to the ΛCDM case becomes relevant. A similar behaviour can be seen in the total matter density contrast. Although on super-horizon scales, as well as just below the horizon, the density contrast is enhanced compared to the ΛCDM one, on very small scales it is suppressed. Noticeably the oscillations that we see in μ do not reflect on $\Phi + \Psi$ and δ_m, which look rather regular. The physical interpretation of this is that even if the additional scalar DoF is introducing fluctuations in the

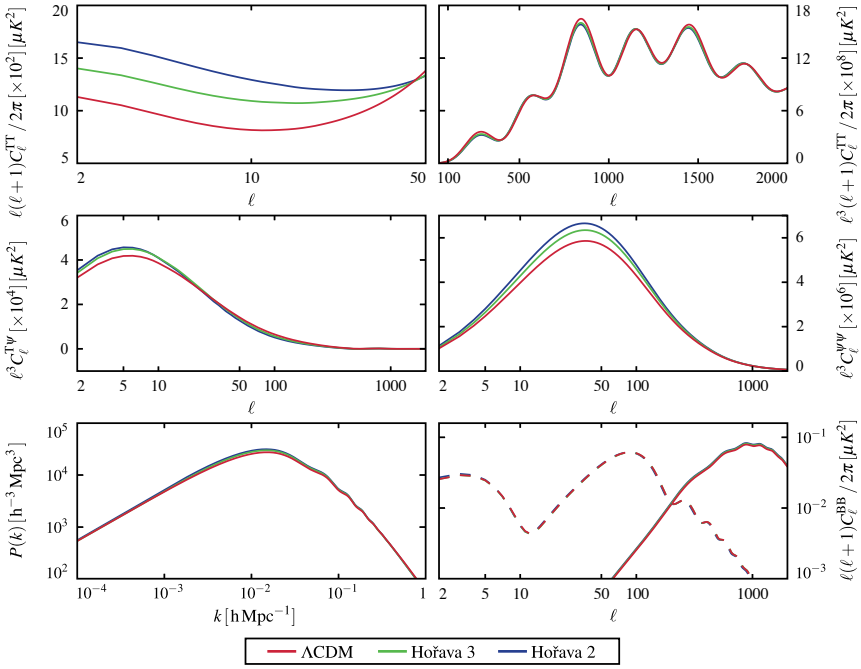

Figure 12.4: Power spectra of different cosmological observables in the ΛCDM, H2 and H3 cases. *Upper panel*: CMB temperature-temperature power spectrum at large (left) and small (right) angular scales. *Central panel*: lensing potential and CMB temperature cross correlation power spectrum (left), lensing potential auto correlation power spectrum (right). *Lower panel*: matter power spectrum (left) and B-mode polarization power spectrum (right). In this last panel the solid line corresponds to the scalar induced B-mode signal while the dashed one shows the tensor induced component. For this figure the standard cosmological parameters are chosen to be $\Omega_b^0 h^2 = 0.0226$, $\Omega_c^0 h^2 = 0.112$, $\Omega_\nu^0 h^2 = 0.00064$ and $H_0 = 70\,\mathrm{Km/s/Mpc}$. The Hořava gravity parameters in H3 case are chosen to be: $(\xi - 1) = -0.01$, $(\lambda - 1) = 0.004$, $\eta = 0.01$; in the H2 case they are: $(\lambda - 1) = 0.02$, $\eta = 0.05$. From [3].

structure of the Poisson equation the field is not coupled strongly enough to introduce fast fluctuations in the matter and metric fields themselves.

- *H2 case*: from the lower left panel of figure 12.2 we can notice that, in the H2 case, the behaviour of μ is rather different from the H3 case. In particular on small scales its value returns to the GR one. This is compatible with the extra constraint that we have imposed in this case (12.36), making the theory indistinguishable from GR on solar system scales. On large scales and high redshift, similarly to the H3 case, deviations from the ΛCDM behaviour are of the order 10^{-2} (1%). Panels H2 b) and H2 c) in figure 12.2 show that the lensing effects and the growth of matter perturbations do not follow the trend of μ. Indeed, in the case of lensing, in panel H2 b), around and below the horizon the model displays significant deviations from the ΛCDM behaviour that are similar to the H3 ones. From panel H2 c) we notice that the growth of matter perturba-

tions deviates significantly from the ΛCDM one (around 10^{-2}) at almost all redshifts and scales. Finally, in the same panel it can be noticed that the density contrast is enhanced for $k \lesssim 10^{-1}$ h/Mpc while it is suppressed at very small scales and all redshift.

After considering the cosmological evolution of metric and matter perturbations we now turn to the study of the dynamics of the additional scalar DoF that propagates in Hořava gravity. In particular we study the quantity introduced in ref. [8] to quantify the deviations from quasi-staticity for the dynamical scalar DoF, π, i.e.

$$\xi_N = \frac{\dot{\pi}_N}{\mathcal{H}\pi_N}\,, \tag{12.47}$$

where with the index N we indicate that we are working with the π-field in Newtonian gauge. This quantity compares the evolutionary time-scale of the additional scalar DoF with the Hubble time scale, thus quantifying how many times the π-field changes significantly in a Hubble time. Small values of this quantity imply that the π field is slowly evolving and that time derivatives of the field can be neglected when compared to the value of the scalar field itself. On the contrary large values mean that the time derivative of the field is playing a major dynamical role, and hence QS would not be a safe assumption.

The time and scale behaviour of ξ_N can be seen, for the H3 and H2 cases, in figure 12.3. We can notice that, roughly for both cases, the π-field is slowly evolving at low redshift ($0 < z < 1$), on the other hand, at higher redshift we can see that its dynamics becomes relevant and deviations from a QS behavior are order 30%. We can also notice that, at all scales and times, the evolutionary time scale of π_N is smaller than the Hubble rate. From the same figure we can see that this evolutionary rate does not significantly depend on scale. The white lines in figure 12.3 show some residual scale dependence at early times and clearly show that this scale dependence gets weaker at late times.

Finally, we discuss how the modified dynamics of perturbations in Hořava gravity affects the observables that we later use to constrain this theory. In figure 12.4, we compare several power spectra for the H2 and H3 cases in comparison to the ΛCDM model. We identify the following effects on the observables:

- *Differences in the late time Integrated Sachs-Wolfe (ISW) effect.* For the two cases that we explore, we find an enhancement of the amplitude of the low-ℓ temperature power spectrum, as it can be seen from the top left panel of figure 12.4 which is related to an increase of the late-time ISW effect [329]. The latter is sourced by the time derivative of $\Phi + \Psi$ and, as we can see from figure 12.2, for the two Hořava gravity cases the time evolution of this quantity is modified. This change also affects the CMB temperature-lensing cross correlation (central left panel), as discussed below.

- *Differences in the gravitational lensing.* As we already discussed, in the specific cases that we explore, gravitational lensing results to be enhanced as we can see in the central panel of figure 12.2. This reflects on the CMB lensing power spectrum as shown in the central right panel of figure 12.4, where we can notice that fluctuations of this observable are enhanced for both H3 and H2 cases with respect to the ΛCDM model. This modification

also has an effect on the high multipole of the lensed CMB temperature power spectrum as highlighted in the top-right panel of figure 12.4. At first glance we can see that, compared to the ΛCDM model, the profile of the high-ℓ peaks is less sharper in the H3 and H2 cases because of the lensing enhancement. We can also notice that there is a slight asymmetry between peaks and troughs due to a combined effect of the lensing modification with the modified Hubble rate discussed in section 12.4, thus leading to a small change in the angular scale of the CMB peaks. From the central left panel, we can see that the CMB temperature-lensing cross correlation spectrum is influenced by both the ISW and lensing modifications. In particular, this spectrum results to be enhanced at low-ℓ because of the lensing and ISW enhancements but it is suppressed for $50 < \ell < 100$ following the trend of the temperature power spectrum. Indeed, we can notice, from the top right panel of figure 12.4, that at these scales the spectra are suppressed due to the lensing effect as previously mentioned. Finally, the enhancement of the lensing potential also affects the component of the CMB B-mode power spectrum that is sourced by the lensing of the E-mode of polarization. This situation is highlighted in the lower right panel of figure 12.4. The solid lines representing this component of the B-mode spectrum are enhanced proportionally to the enhancement in the lensing potential.

- *Differences in the growth of matter perturbations and the distribution of the large scale structure.* For the two cases under analysis (H3 and H2), we observe a slight enhancement of the growth of structure in the total matter power spectrum, at intermediate scales, as well as a slight suppression on small scales, as it is clearly depicted in the lower left panel of figure 12.4, and in agreement with our previous analysis of the density contrast, see figure 12.2. The matter power spectrum, for both H2 and H3, follows the ΛCDM one on large scales ($k \lesssim 10^{-3}$ h/Mpc) while for $10^{-3} \lesssim k \lesssim 10^{-1}$ h/Mpc it is slightly enhanced, particularly for the H2 case. At very small scales, both the H2 and H3 matter spectra follow the ΛCDM behaviour.

- *Differences in the propagation of tensor modes.* As previously discussed in section 12.3, the tensor dynamical equation is modified in Hořava gravity. This change is usually reflected in the tensor induced component of the B-modes of CMB polarization [330, 6]. In particular, in the H3 case, the parameter ξ controls directly the propagation speed of gravitational waves, while the combination $2\xi - \eta$ is responsible for the strength of coupling between tensor modes and matter. Instead, in the H2 case the tensor speed of sound is controlled by η, while there is no effect on the coupling with matter. The choice of parameters we made for figure 12.4, displays a significant effect on the scalar component of the B-mode spectrum as shown in the lower right panel of figure 12.4 as solid lines, but the effect on the tensor component (dashed line) of the B-mode power spectrum for the same parameters is much smaller and not visible in the figure. In figure 12.5 we change the Hořava gravity parameters to better display the effect of the change in the tensor sector. Therefore only for this figure we choose the Hořava gravity parameters in H3 case to be $(\xi - 1) = -0.3, (\lambda - 1) = 4 \times 10^{-4}, \eta = 10^{-3}$ and in the H2 case they are $(\lambda - 1) = 1, \eta = 0.6$. As we can see from that figure, the leading effect is due

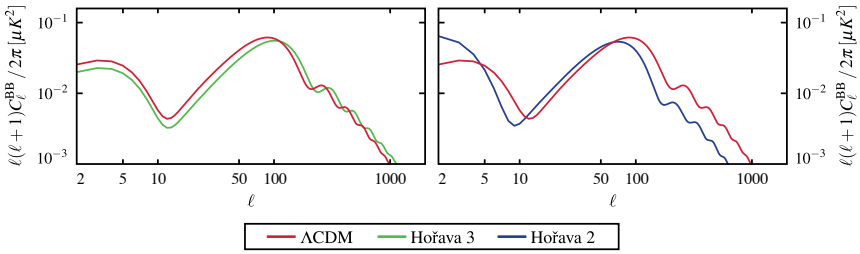

Figure 12.5: The tensor induced component of the B-mode CMB polarization power spectrum in the ΛCDM, H2 and H3 cases. For this figure the standard cosmological parameters are chosen to be $\Omega_b^0 h^2 = 0.0226$, $\Omega_c^0 h^2 = 0.112$, $\Omega_\nu^0 h^2 = 0.00064$, $r = 1$ and $H_0 = 70\,\mathrm{Km/s/Mpc}$. The Hořava gravity parameters in H3 case are chosen to be: $(\xi - 1) = -0.3, (\lambda - 1) = 4 \times 10^{-4}, \eta = 10^{-3}$ in the H2 case they are: $(\lambda - 1) = 1, \eta = 0.6$. From [3].

to the modification of the speed of gravitational waves [6]. In the next section we will find that due to a combination of viability requirements and data constraints, for the H3 case, $\xi \leq 1$, therefore the spectrum results to be shifted to the right with respect to the ΛCDM one, since tensor modes propagate sub-luminally. On the other hand, in the H2 case, tensor modes propagate super-luminally ($\eta > 0$) and the whole spectrum is shifted to the left. Finally, a modification of the coupling to matter leaves an observational imprint that is much smaller that the previous one as cosmological gravitational waves propagate almost in vacuum. We can also conclude, on the basis of the results we will present in the next section, that in the H3 case since the tensor sound speed is less than one, the Čherenkov constraints are not always satisfied but only in a very tiny range [327, 328]. On the contrary, in the H2 case the tensor sound speed is always super-luminal, then the Čherenkov constraints are evaded.

12.6 Cosmological constraints

In this section we derive and discuss the observational constraints on Hořava gravity coming from cosmological probes.

In our analysis we use several geometrical and dynamical probes, combining them progressively. The first data set employed, hereafter PLC, consists of the *Planck* 2013 CMB temperature spectrum measurements along with the WMAP large scale CMB polarization spectra. The second data set considered, denoted as BG, is a combination of background measurements that helps to break the degeneracies between background parameters and the ones describing the behaviour of perturbations. We use: HST data, JLA Supernovae and several BAO measurements. The third data set that we use, consists of the *Planck* 2013 CMB lensing potential power spectrum measurements. We refer to this data set as the lensing one, hereafter CMBL. Finally, we use the measurements of the WiggleZ galaxy power spectrum. For the details of these data sets we refer the reader to Chapter 4. However, as we will show in the next section, the cosmological

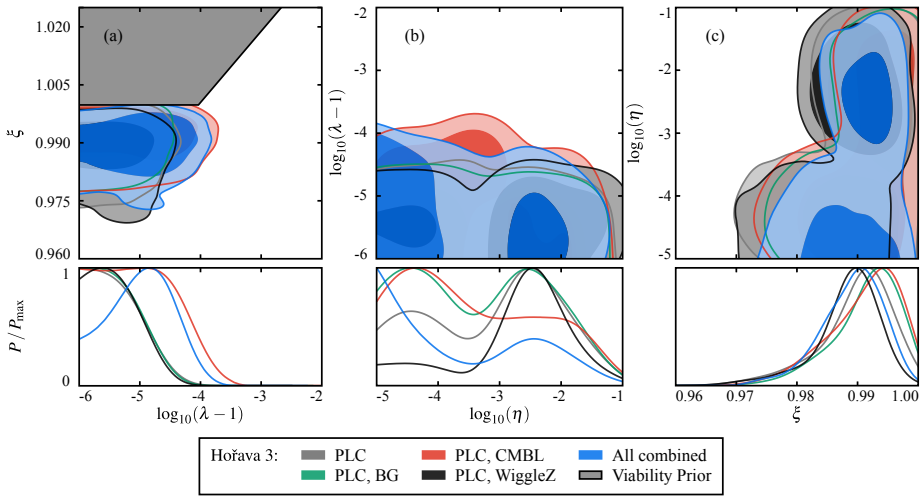

Figure 12.6: Results of our analysis of the H3 case. *Upper panel*: The marginalized joint likelihood for combinations of the parameters of low-energy Hořava gravity. The darker and lighter shades correspond respectively to the 68% C.L. and the 95% C.L.. *Lower panel*: The marginalized likelihood of the parameters of low-energy Hořava gravity. In both panels different colours correspond to different data set combinations as shown in legend. The dark grey shade corresponds to the marginalized region of parameter space excluded by *viability priors*. From [3].

	H3 case					
Parameters	Prior	PLC	PLC+BG	PLC+CMBL	PLC+WiggleZ	all combined
$\xi - 1$	$[-0.1, 0.1]$	$-0.01^{+0.01}_{-0.02}$	$-0.01^{+0.01}_{-0.02}$	$-0.01^{+0.01}_{-0.02}$	$-0.01^{+0.01}_{-0.02}$	$-0.01^{+0.01}_{-0.02}$
$\log_{10}(\lambda - 1)$	$[-8, -2]$	< -4.56	< -4.68	< -4.24	< -4.68	< -4.31
$\log_{10}\eta$	$[-5, -1]$	$--$	$--$	$--$	$--$	$--$
Ω^0_{DE}	derived	$0.69^{+0.06}_{-0.07}$	0.69 ± 0.02	$0.70^{+0.04}_{-0.05}$	0.66 ± 0.06	0.69 ± 0.02
α_1	derived	< 0.283	< 0.240	< 0.263	< 0.322	< 0.220
$\log_{10}\alpha_2$	derived	< 5.05	< 4.83	< 5.04	$2.70^{+2.52}_{-2.41}$	< 4.72
$G_{\rm cosmo}/G_N - 1$	derived	< 0.035	< 0.030	< 0.033	< 0.040	< 0.028

Table 12.1: The 99.7% C.L. marginalized posterior bounds on the H3 case parameters and relevant derived parameters.

constraints are mainly driven by CMB and background observables toward the ΛCDM limit. Therefore, we do not expect that a scale dependent bias will dominate the results in Hořava gravity when considering WiggleZ data.

12.6.1 H3 case: results

The first case we compare to cosmological observations is the low-energy limit of Hořava gravity, H3, for which the parameters of the theory are $\{\xi, \lambda, \eta\}$.

We sample λ and ξ shifting them by one so that the GR limit of the new

parameters, i.e. $\lambda-1$ and $\xi-1$, corresponds to a zero value. In addition, we use a logarithmic sampler for the parameters η and $\lambda-1$ as they are constrained to be positive by physical viability, as discussed at length in section 12.3. Instead, ξ is allowed to change sign, hence we sample $\xi-1$ linearly.

When combining the *viability priors* discussed in section 12.3, with cosmological data, we notice that the requirement of physical viability has a strong effect on the posterior distribution of the parameter ξ. This is shown in panel (a) of figure 12.6. Even though ξ is not constrained to be above or below 1 a priori, the magnitude of λ, draws the posterior of the model into a region where only values of $\xi \leq 1$ are viable. Let us notice that there is a very small viable region in the parameter space above one ($1 < \xi \lesssim 10^{-6}$), which due to the scale adopted in the plot cannot be seen by eye; however, since this is significantly smaller than the region below $\xi = 1$, it is not picked up when sampling linearly the parameter ξ. As we can see from the other two panels of figure 12.6, the *viability priors* do not have a strong impact on λ and η in the region where the posterior of the model is peaked.

From the top panels of figure 12.6, we can notice that the different parameters specifying Hořava gravity do not have sizable degeneracies between them over all the range explored (which spans several orders of magnitude). From the lower panel of the same figure we can notice that different data sets contribute differently to the parameter bounds. In particular we can see that PLC strongly constrains the λ parameter, while preferring a bigger value for η and ξ. The addition of background probes pushes these two parameters closer to the ΛCDM limit of the theory. Noticeably the addition of CMB lensing strongly degrades the bounds on λ while being consistent with PLC+BG for the other two parameters. This behavior is expected considering the known tension between the *Planck* 2013 and the *Planck* 2015 data and the CMB lensing power spectrum as reconstructed from the CMB trispectrum [78, 16, 4]. These results are confirmed by the marginalized bounds on the H3 parameters reported in table 12.1. In particular the 99.7% C.L. bounds on the ξ and η parameters weakly depend on the data set used and in particular for the η parameter no 99.7% C.L. bounds are found. As discussed in section 12.4, the "bare" cosmological constant $\bar{\Lambda}$ has been replaced in this analysis by Ω^0_{DE}, and the latter has been included in table 12.1. The most relevant result that can be drawn from table 12.1 is that low-energy Hořava modifications of gravity are severely constrained, with the corresponding parameters bounded to be orders of magnitude below unity. In particular, we find that cosmological data have a strong constraining power on λ. Here we summarize the bounds, at 99.7% C.L, that we get from the combination of all data sets:

$$\begin{aligned} &\xi - 1 = -0.01^{+0.01}_{-0.02}\,, \\ &\log_{10}(\lambda - 1) < -4.31\,, \\ &\Omega^0_{DE} = 0.69 \pm 0.02 \end{aligned} \tag{12.48}$$

Let us notice that the *viability priors* give also an upper bound on ξ, i.e. $\xi \leq 1$. All the marginalized constraints on standard and derived cosmological parameters for the H3 case are shown in appendix .4.

In table 12.1 we report also the marginal bounds on the PPN parameters $\{\alpha_1, \alpha_2\}$ and $G_{\rm cosmo}/G_N - 1$. From the first two, we can notice the extreme

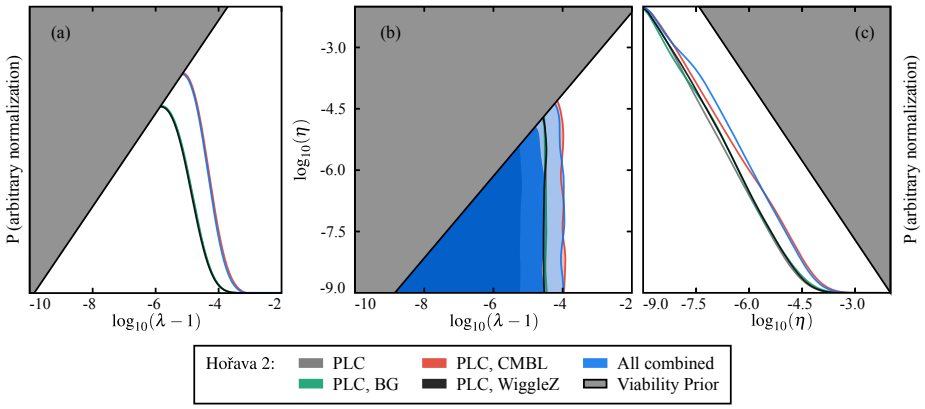

Figure 12.7: Results of our analysis of the H2 case. *Panel (a)*: The marginalized likelihood of $\log_{10}(\lambda-1)$; *Panel (b)*: The marginalized joint likelihood of $\log_{10}(\lambda-1)$ and $\log_{10}\eta$. The darker and lighter shades correspond respectively to the 68% C.L. and the 95% C.L.. The theoretical viability condition is roughly $(\lambda-1) > \mathcal{O}(2\eta/9)$; *Panel (c)*: The marginalized likelihood of $\log_{10}\eta$. In all panels different colours correspond to different data set combinations as shown in legend. The dark grey shade corresponds to the marginalized region of parameter space excluded by *viability priors*. The arbitrary normalization of the posterior is chosen to better display the effect of the *viability priors*. From [3].

complementarity of cosmological and solar system experiments in constraining Hořava gravity. The cosmological observations lead to an upper bound on α_1 that is $\alpha_1 < 0.220$, while PPN bounds on this parameter are three orders of magnitude stronger. Cosmological observations are, however, sensitive to ξ and weakly sensitive to η, while solar system probes constrain just a degenerate combination of the two. On the other hand the cosmological bounds on the parameter α_2 are worst than the PPN ones by several orders of magnitude. That is due to the fact that in the limit in which λ is constrained to be smaller than the other parameters by cosmological data, the α_2 parameter goes to infinity as it is clear from its definition (12.34). If we compare the cosmological constraint on λ with the one that is derived from α_2 in eq. (12.35), we see that our bounds are compatible with the solar system constraints. Finally, we can see that the bound on $G_{\rm cosmo}/G_N - 1 < 0.028$ (99.7% C.L., all combined) is improved by one order of magnitude with respect to previous results [291].

12.6.2 H2 case: results

The second case we consider, is a sub-case of the previous one obtained by restricting to the plane of the parameter space corresponding to $\eta = 2\xi - 2$. For this choice, the solar system constraints are automatically evaded as shown by studies of the PPN limit of Hořava gravity (see section 12.3). We refer to this as the H2 case. The free parameters of the theory are now $\{\eta, \lambda\}$ and, as discussed in the previous section, we sample the parameter space of the logarithm of η and $\lambda - 1$ since both these quantities are constrained by the *viability priors* to be positive. Unlike for the H3 case, where the *viability priors* had a strong

influence only on the parameter ξ, in the H2 case they have a strong influence on the marginalized posterior for both η and λ, as one can see in figure 12.7. In particular one can notice in panel (b) of figure 12.7 that the viable region is a triangle corresponding roughly to the condition $(\lambda - 1) > \mathcal{O}(2\eta/9)$. This triangle shape of the marginalized joint posterior of the model parameters has a strong influence on the marginalized 1D posterior of the two parameters. In particular, as we can see in panel (a) of figure 12.7 , the low tail of λ is cut by the *viability priors* and, in panel (c), the posterior of η becomes markedly non-gaussian. Apart from the degeneracy induced by this prior cut, no other degeneracy between the Hořava gravity parameters is present.

In panel (a) of figure 12.7, we can see that different data sets contribute differently to the cosmological bounds. In particular, the PLC, PLC+BG and PLC+WiggleZ data sets are pushing the posterior of λ to smaller values. The constraints become slightly weaker when considering CMB lensing for the same reasons explained in the previous section and it dominates the bounds coming from the total data set combination. Because of the degeneracy induced by the *viability priors*, in the H2 case we are able to set bounds also on η. These are shown in table 12.2. In this table we can notice that the 99.7% C.L. confidence bounds on λ are comparable to the previous ones and the bounds on η are considerably stronger. Indeed the bounds for all combination of data sets for the H2 case are:

$$\begin{aligned} &\log_{10}(\lambda - 1) < -4.39\,, \\ &\log_{10}(\eta) < -4.51\,, \\ &\Omega^0_{DE} = 0.69 \pm 0.02\,. \end{aligned} \tag{12.49}$$

As in the previous case Ω^0_{DE} and all the standard derived cosmological parameters are reported in appendix .4.

Noticeably in the H2 case, the bounds on $G_{\rm cosmo}/G_N - 1$ are more stringent than in the H3 case. In particular this bound is several orders of magnitude stronger than the BBN bound.

The H2 case studied in this section has been already investigated in ref. [294]. Indeed, our H2 case is the khronometric model in ref. [294] when the LV in matter is switched off and a precise mapping between the different notations adopted is worked out. In this respect, a comparison between our results and the one in ref. [294] is not straightforward. We find an overall good agreement in the cosmological predictions by comparing the output of the code used by [294] to EFTCAMB. The stronger bound on $G_{\rm cosmo}/G_N - 1$ is then due to the different choices of cosmological parameters that we sample and the different priors that we impose on them.

12.7 Chapter Summary

In this chapter we have performed a thorough investigation of the cosmology of Hořava gravity, which is a Lorentz violating theory proposed as a candidate for quantum gravity [295, 228]. The emergence of Lorentz violations at all scales, makes the theory power-counting renormalizable at very high energies ($\sim 10^{19}$ GeV/c^2). However, since at low energies we do not experience LV

	H2 case					
Parameters	Prior	PLC	PLC+BG	PLC+CMBL	PLC+WiggleZ	all combined
$\log_{10}(\lambda-1)$	$[-10,-2]$	< -4.62	< -4.62	< -4.38	< -4.59	< -4.39
$\log_{10}\eta$	$[-10,-2]$	< -4.68	< -4.58	< -4.40	< -4.73	< -4.51
Ω^0_{DE}	derived	$0.68^{+0.04}_{-0.06}$	0.69 ± 0.02	0.69 ± 0.04	$0.66^{+0.05}_{-0.06}$	0.69 ± 0.02
$G_{\rm cosmo}/G_N - 1$	derived	$< 3.6 \times 10^{-5}$	$< 3.6 \times 10^{-5}$	$< 6.3 \times 10^{-5}$	$< 3.9 \times 10^{-5}$	$< 6.1 \times 10^{-5}$

Table 12.2: The 99.7% C.L. marginalized posterior bounds on the H2 case parameters and $G_{\rm cosmo}/G_N - 1$.

effects, we expect large scales tests to place important constraints on the theory. In particular, we have analysed Hořava gravity at cosmological scales, to see whether there is any room for LV at these energies. As we will summarize in details in the following, we have found that cosmological data severely constrain Hořava gravity.

We have performed our analysis within the EFT framework for dark energy and modified gravity [162, 163]. We have focused on the dynamics of the background and linear perturbations, and considered the power-counting renormalizable action for Hořava gravity which includes all the *quadratic* operators with up to sixth spatial derivatives [310]. For this action, we have worked out a complete mapping into the EFT language, in section 12.2, finding that its low-energy part is completely mapped in the most commonly used EFT action (6.1). While the high-energy part requires the inclusion of additional operators, that we have identified in appendix .3. After working out the full mapping, when exploring the cosmology and corresponding observational bounds, in sections 12.4 and 12.6, we have restricted to the low-energy part of the action which is sufficient for a first exploration of the large scale phenomenology of the theory.

For our analysis we have made use of the powerful EFTCAMB/EFTCosmoMC package [8, 7, 10]. For the first time, we have implemented in EFTCAMB a *full mapping* case, solving the Hořava equations for the background, instead of using a *designer* approach to the expansion history. We have included a detailed discussion of this procedure in section 12.4. After solving the background and before proceeding to the evolution of the perturbations, EFTCAMB runs a check on the viability of the selected theory, enforcing some stability requirements such as the absence of ghosts and gradient instabilities. The latter conditions become *viability priors* when using EFTCosmoMC to constrain the parameters of the theory by means of cosmological data. Finally, we have proceeded to evolve linear scalar perturbations with the general EFT equations [10], specializing their coefficients to the corresponding expressions in the Hořava case through the mapping worked out in section 12.2.

Let us notice that besides the physical stability requirements, Lorentz violations can also be constrained via BBN and solar system tests, as discussed at length in section 12.3. In our analysis we have not imposed the BBN experimental bounds a priori, rather we have compared them to our finding for cosmological constraints. Nevertheless, we have investigated two cases: a first one, H3, where the low-energy Hořava gravity parameters $\{\lambda, \xi, \eta\}$ were allowed to vary freely; the second case, H2, where we enforced a relationship between the parameters that allows the theory to evade PPN constraints, reducing the

number of free parameters to two, $\{\lambda, \eta\}$.

In sections 12.4 and 12.5, we have studied in details the cosmology of Hořava gravity. At background level, we have found a constant rescaling of the Hubble rate which reflects in the behaviour of the density parameters. Indeed, as shown in figure 12.1, the fractional matter density exceeds unity at all times and the fractional density of the effective dark energy (12.43) correspondingly becomes negative, so that the flatness condition is satisfied at all times. This behaviour signals that the modifications of gravity in this theory should be considered as a purely geometrical effect, rather than be interpreted in terms of a dark fluid. At the level of linear perturbations we have identified modifications in the ISW effect, the gravitational lensing, the rate of growth of structure and the B-modes spectrum, which translated into stringent bounds on the Hořava parameters when we fit them to cosmological data. In order to facilitate a in depth visualization of characteristic features of Hořava gravity at the level of perturbations, we have specialized to two choices of parameters, one for the H3 case and one for the H2 case, and have performed a thorough analysis of the dynamics of perturbations and the corresponding cosmological observables. In both cases, we have found a general enhancement of the growth of matter perturbations and the lensing potential. The first modifies the shape of the matter power spectrum, which we have found to be enhanced for $10^{-3} < k < 10^{-1}$ h/Mpc; the second one impacts the CMB temperature power spectrum at high-ℓ and the CMB lensing power spectrum. In particular in the latter case the effect is of a general enhancement of power in the lensing potential auto spectrum. A modification of the lensing potential also alters the scalar perturbation induced component of the B-mode power spectrum, leading to an enhancement in that signal. On the other hand, we found an enhancement of the CMB temperature power spectrum at large angular scales and its cross-correlation with the lensing potential. This effect can be traced back to an enhancement of the ISW effect at late times. Finally, the tensor power spectrum is also modified as the speed of sound of the tensor modes depends on the parameters of the theory. In particular the tensor BB-power spectrum is shifted on the right with respect to the ΛCDM one for the H3 case as the tensor propagation is sub-luminal and on the left for H2 because the propagation is super-luminal. Noticeably, we have determined that in general the quasi-static approximation is not safe to describe the evolution of sub-horizon perturbations in Hořava gravity if we want an accuracy better than 30%. Let us stress that while the direction and entity of these modifications is dependent on the specific choice of parameters, we have found a general enhancement of the growth rate, lensing potential, and an enhancement of the ISW effect for several choices of parameters that we have sampled in the region allowed by the *viability priors*.

In section 12.6, we have moved on to perform a global fit of the two cases of low-energy Hořava gravity, H3 and H2, to progressive combinations of cosmological data sets: the CMB temperature-temperature and lensing power spectra by *Planck* 2013, WMAP low-ℓ polarization spectra, the WiggleZ galaxy power spectrum, the local Hubble measurements and Supernovae data from SNLS, SDSS and HST and the BAO measurements from BOSS, SDSS and 6dFGS.

In the case of H3, we have set upper bounds on λ and a lower bound on ξ, while for $\Omega_{DE}^{(0)}$ (which through eq. (12.44) replaces $\bar{\Lambda}$) we found a mean value and errors that are close to the ones of the ΛCDM model. Specifically we

obtained $\xi - 1 = -0.01^{+0.01}_{-0.02}$, $\log_{10}(\lambda - 1) < -4.31$ and $\Omega^0_{DE} = 0.69 \pm 0.02$ at 99.7% C.L. for the combination of all the data sets considered. For all the other data set combinations see table 12.1. As a general result we have found that the values of the Hořava gravity parameters are constrained to be close to their values in the GR limit. For both cases we reported the constraints on the standard cosmological parameters in tables 4-5. Moreover, for the H3 case we get an improved bound on $G_{cosmo}/G_N - 1 < 0.028$ (99.7% C.L., for the combination of all data sets) which outruns the BBN one. On the other hand PPN experiments are three orders of magnitude stronger in constraining the α_1 parameter that we find to be $\alpha_1 < 0.220$ (99.7% C.L., for the combination of all data sets), while our cosmological bound on λ is compatible with the one derived from solar system tests.

For the H2 case, we were able to set upper bounds on $\log_{10}(\lambda - 1) < -4.39$ and $\log_{10}(\eta) < -4.51$ and constraints on $\Omega^0_{DE} = 0.69 \pm 0.02$ at 99.7% C.L. with all data sets. Noticeably for this model we get a quite stringent bound on $G_{cosmo}/G_N - 1 < 6.1 \times 10^{-5}$ at 99.7% C.L. by combining all the considered data sets.

The full mapping of the low-energy limit of Hořava gravity has been publicly released as part of an update of EFTCAMB/EFTCosmoMC. As part of future work, it would be certainly of interest to explore the phenomenology associated to the high-energy part of the Hořava gravity action to see whether additional operators can affect significantly linear perturbations. Future analysis could also include the study of LV in the dark matter sector.

Part V

Conclusions and Outlook

Cosmic acceleration still poses a challenge for modern cosmology. While current cosmological data strikingly present observational evidence for this phenomenon its theoretical understanding is still lacking. To explain this effect one might resort to a cosmological constant, as it is done in the standard cosmological model; this, however, still does not have a deep theoretical motivation. On the other hand, one might want to add other dark fluids to the cosmic budget or modify the laws of gravity on large scales to drive this accelerated expansion.

In this thesis we presented and exploited a threefold approach to the study of the phenomenology of cosmic acceleration to perform systematic explorations of models beyond the standard one.

Within this threefold path, the first way that we followed in this thesis was to quantify the level of agreement of cosmological observations, within the standard cosmological model, to see whether there is already some tension between data that motivates us to move away from the fiducial model. We have built a statistical estimator of tensions between data sets and used it on state of the art cosmological measurements. We have found that, while most of the cosmological observations agree, within the standard ΛCDM model, there is a statistically significant tension between weak lensing measurements from the CFHTLenS survey and Planck CMB observations. This tension can be due to residual systematic effects in the data, but if this explanation is eventually excluded, it will be a first indication of the presence of physical phenomena beyond the ΛCDM ones.

The second path that we followed was to study parametrizations that would allow to explore the phenomenology of alternatives to the fiducial ΛCDM model, i.e. DE/MG models. Generally these models amount to adding a single scalar propagating degree of freedom to our gravitational theory. We thus exploited an Effective Field Theory approach to describe the cosmological phenomenology of such a scalar field.
After briefly reviewing the construction of the EFT we dived into its phenomenological applications. We started with the behavior of the cosmological background and, using dynamical systems techniques, we got some general results concerning the compatibility of the functions describing the EFT with a viable cosmological expansion history. After investigating the background we moved to the evolution of perturbations. To do so we built a modification of the Einstein-Boltzmann solver CAMB, to obtain numerical predictions for all cosmological observables of interest. The resulting tool, that we called EFTCAMB, fully exploits the power of the EFT approach when performing investigation of DE/MG models. In particular it automatically implements a check of the physical viability of a theory at any step in its parameter space. Moreover our implementation does not rely on any approximation for the DE/MG dynamics, solving the full hierarchy of modified Einstein-Boltzmann equations.
With this tool at hand we studied the observational consequences of some parametrized models investigating their phenomenological signatures. We started with the constraints on a time dependent conformal coupling between gravity and the scalar field, showing the bounds on theory parameters coming from several cosmological probes. With the same model we have investigated the degeneracy between DE/MG effects and massive neutrinos. The latter usually enhances the growth of cosmic structures while the former suppresses it. The two effects might balance each other resulting in degenerate constraints. We

have found that, if the conformal coupling between gravity and the scalar field depends linearly on the scale factor, the growth of structure is suppressed, and the corresponding degeneracy with massive neutrinos is alleviated.
Another phenomenological signature of DE/MG models that we investigated, following the results of the *Planck* satellite in its 2015 data release, concerns the gravitational lensing of the CMB. By considering a time independent change in the cosmological gravitational constant we showed that the amplitude of the CMB lensing spectrum is altered in a scale dependent way. We then tried to investigate whether we can relieve the tension between Planck CMB Temperature data and Planck CMB lensing measurements, finding that it is hardly alleviated.
Finally, we used a parametrized approach to investigate the phenomenology of a modified speed of gravitational waves. We showed that a modification of the speed of tensors leaves a distinct imprint on the CMB B-mode polarization spectrum, shifting the angular position of its peak. We then showed that the next generation of cosmological experiments will be capable of tightly constraining this quantity to an accuracy comparable with that of binary pulsar systems.

The third path that we followed, in our threefold approach to the phenomenology of DE/MG models, consisted in testing specific models. This corresponds to looking at specific positions in model space, motivated by the physical origin of models. We used the full power of the EFT approach in doing so. This can, in fact, be used to test specific models once they are mapped to the EFT framework with appropriate mapping relations between the EFT functions and the model functions. In particular, we investigated the cosmological implications of designer $f(R)$ models. These are built to reproduce exactly a given expansion history and we studied the cosmological constraints on these models when we require a ΛCDM and a wCDM expansion history. We found significant constraints on the theory parameters and, especially in the wCDM case, we found that the constraints are strongly affected by the requirements of physical viability. Using EFTCAMB allowed us to study the validity of the quasi-static approximation for these models. At this goal we built a modified version of MGCAMB to study the same designer models with this approximation. We found a negligible difference in cosmological constraints when considering designer $f(R)$ on a ΛCDM background. However, when we add to the $f(R)$ model massive neutrinos we found a noticeable change in the degeneracy direction in parameter space. These results highlight the relevance of the full treatment of perturbations in light of the accuracy of upcoming experiments.
We then moved to cosmological tests of Hu-Sawicki $f(R)$ models, that we used as an example of a model significantly changing the background expansion history. We showed that cosmological constraints are significant and the full treatment of EFTCAMB allowed us to appreciate the degeneracy between background parameters and perturbation parameters.
Finally we tested the cosmological implications and data constraints for Hořava gravity. This is an example of a Lorentz violating theory that can still be mapped to the EFT framework thanks to its flexibility. We mapped the full theory to EFT, including both high-energy and low-energy contributions. We then studied the cosmology emerging from its low energy part. We found significant constraints on the theory parameters. In particular, if the Hořava theory parameters are tuned to avoid solar system constraints, we found that cosmo-

logical observations are already at a precision stage that allows to cast powerful bounds on this model.

In conclusion, in this thesis, we have developed and applied a threefold approach to the exploration of models beyond the standard cosmological one. We have explored all the three branches constituting this approach and significantly developed them. We have shown that already at present, cosmological observations are precise enough to substantially improve our knowledge about DE/MG models. We developed the relevant tools that will allow us to perform massive ans systematic studies of DE/MG models with the next generation of cosmological surveys by following the threefold path described in this thesis.

The work presented in this thesis can be extended in several ways, that will be directly relevant and useful for the interpretation of data from contemporary and future experiments.
The first extension of this work consists in developing and exploiting robust statistical tools. It is of primary relevance to develop the relevant statistical proxies to distinguish between different scenarios, to ensure that we are using at best the power of present and future cosmological probes. The ones discussed in this thesis can be extended and applied to the process of model selection and to forecasting.
A second relevant extension is to move toward systematic studies of the cosmological constraints of several theories, including Galileon and massive gravity models. This can be pursued by extending the range of models implemented in EFTCAMB. This line should be aided by advancements in the study of agnostic parametrizations, that will allow to learn how we can optimally extract information, about gravitational theories, from different cosmological probes.
Finally, to complete the range of scales that we can use to test gravitational theories with future surveys, we have to understand what happens on small, non-linear, scales. The additional interaction that is included to source cosmic acceleration is strongly constrained by solar system tests. Viable models of DE/MG successfully develop a screening mechanism to hide the presence of this force on such scales. Generally these mechanisms rely on non-linear interactions or self-interactions between the scalar field, sourcing the fifth force, gravity and matter. The development of tools aimed at studying screening mechanisms will allow the design of laboratory experiments to test the presence of additional forces by looking at the objects for which these mechanisms are less effective. On the long run this will also help in making the connection with large scale modelling, completing the range of scales over which we will perform cosmological tests of gravity.

Part VI

Appendix

.1 Dynamical Analysis Continued

.1.1 Second Order

In this Appendix we complete the analysis of the critical points of the second order system. In particular, all critical points (including those already discussed in Sec. 7.5) and their stability analysis are reported in Table 3; while in the following we present the eigenvalues and discuss the cosmology of the points that were not considered in Sec. 7.5.

- *Phantom DE points*
  From the splitting of the first order point P_4, we have two critical points characterized by a phantom effective equation of state:

$$P_{4a}: \quad \mu_1 = -6,\ \mu_2 = -5,\ \mu_3 = -3,\ \mu_4 = -2-\alpha_2,\ \mu_5 = -2-\lambda_0. \tag{50a}$$

$$P_{4b}: \quad \mu_1 = \frac{1}{2}(\alpha_2 - 4),\ \mu_2 = \alpha_2 - 4,\ \mu_3 = \alpha_2 - 3,\ \mu_4 = \alpha_2 + 2,\ \mu_5 = \alpha_2 - \lambda_0. \tag{50b}$$

  The first one has $w_{\rm eff} = -\frac{7}{3}$ and is a stable attractor for $\alpha_2 > -2 \wedge \lambda_0 > -2$, while the second one is an accelerated stable node for $\alpha_2 < \lambda_0 \wedge \alpha_2 < -2$ with $w_{\rm eff} < -\frac{7}{3}$. We do not consider these points viable as such values of $w_{\rm eff}$ have been already excluded by experiments (e.g. [78]).

- *ϕ-MDE and ϕ-RDE points*
  There are two critical points characterized by, respectively, matter and radiation domination with a non-negligible DE density:

$$P_5: \qquad \mu_1 = -\frac{15}{2},\ \mu_2 = -3,\ \mu_3 = -1,\ \mu_4 = 3-\alpha_2,\ \mu_5 = 3-\lambda_0. \tag{51}$$

$$P_8: \qquad \mu_1 = -6,\ \mu_2 = -6,\ \mu_3 = 1,\ \mu_4 = -\frac{1}{2}-\alpha_2,\ \mu_5 = 4-\lambda_0. \tag{52}$$

  The first point has $\Omega_m = 5$, $\Omega_{\rm DE} = -4$ and a stiff matter equation of state, while the second one has $\Omega_r = 9$ and $\Omega_{\rm DE} = -8$ with $w_{\rm eff} = \frac{5}{3}$. Both these points are not considered cosmologically relevant.

- P_9: *unstable DE point*

$$\mu_1 = \alpha_2 - 4,\ \mu_2 = \alpha_2 - 3,\ \mu_3 = \alpha_2 - \lambda_0,$$
$$\mu_4 = 6 - \frac{3}{4}\alpha_2 - \frac{1}{4}\sqrt{3}\sqrt{-\alpha_2(-32+5\alpha_2)},\ \mu_5 = 6 - \frac{3}{4}\alpha_2 + \frac{1}{4}\sqrt{3}\sqrt{-\alpha_2(-32+5\alpha_2)}. \tag{53}$$

  This point corresponds to a DE dominated configuration, albeit one that is always unstable.

- P_{11}: *radiation scaling point*
  The stability analysis of this point is too complicated to be reported, nevertheless we are able to deduce something about its cosmological behavior. From Table 3 one can see that the point corresponds to a scaling solution for radiation and DE with $\Omega_{DE} = 2\alpha_2 - 7$. However, the constraint $\Omega_r \geq 0$ imposes $\alpha_2 < 4$, and for this range of values the point cannot be neither a proper DE or radiation dominated point.

.1.2 N^{th} order analysis continued

In this Appendix we continue with the analysis of the critical points for the N^{th} order system giving an overview of the points that were not presented in Sec. 7.6 since they either did not have the desired cosmological characteristics or stability. The general structure of the critical points for the N^{th} order system was explained in detail in Sec. 7.6, however here we will give a brief review. Critical points belonging to the same family can be of three types: $(x_c, y_c, \alpha_{0,c}, \alpha_{1,c}, \alpha_{n,c} = 0)$ with $n \geq 2$, $(x_c, y_c, \alpha_{0,c}, \alpha_{1,c}, \alpha_{n,c} \neq 0)$ with $n \geq 2$ or $(x_c, y_c, \alpha_{0,c}, \alpha_{1,c}, \text{combinations})$, where 'combinations' correspond to all the different combinations of $\{\alpha_{2,c}, \ldots, \alpha_{N-1,c}\}$ for which a different A thorough description of how to build all the combinations is given in Sec. 7.6. Here we simply remind the reader that we use the index j for the $\alpha_{n,c}$ in non-zero blocks that are followed by a zero-block (rule (7.39)); while we use the index l for the $\alpha_{n,c}$ of the non-zero block that closes the combination, when it exists (rule (7.40)). Every time we substitute into (7.39) and (7.40) the specific value of $\dot{H}/H^2$ that corresponds to the point in consideration.

- *Phantom DE points:*
  There are different families of critical points which are DE dominated but give rise to cosmological behaviors which are in tension with current observations (i.e. $w_{\text{eff}} \lesssim -2$). However, their stable node configuration gives an attractor that, in principle, could be reached in the far future, provided that the duration of the matter era would remain long enough to allow for structure to form ([190] and references therein). The first family that we shall consider is P_{4a}-like, which is a set of DE dominated critical points with $w_{\text{eff}} = -\frac{7}{3}$.

$$P_{4a,1} \equiv (-1, 0, 2, 0, \alpha_{n,c} = 0), \tag{54a}$$

$$P_{4a,2} \equiv (-1, 0, 2, 0, \alpha_{n,c} = \alpha_N + 2(N - n)), \tag{54b}$$

$$P_{4a,c} \equiv (-1, 0, 2, 0, \text{combinations}),$$
$$\alpha_{j,c} = 2(s + 1 - j),\ \alpha_{l,c} = \alpha_N + 2(N - l). \tag{54c}$$

  From an investigation of the eigenvalues, one finds that the first point is a stable node for $\lambda_0 > -2$ while the second one exhibits this behavior for $\lambda_0 > -2 \wedge \alpha_N < -2\,(N - 2) \wedge \alpha_N > 3N - 8$. The last sub-family of critical points $P_{4a,c}$ also displays stable configurations for some combinations. In that case we have $\lambda_0 > -2 \wedge \alpha_N < -2$ and $\lambda_0 > -2 \wedge \alpha_N > -2$. The second family that we shall consider does not have a unique cosmological behavior, though in all the cases the critical points are DE dominated and resemble the P_{4b} point of the second order analysis.

$$P_{4b,1} \equiv (-1, 0, 2, 1, \alpha_{n,c} = 0), \tag{55a}$$

$$P_{4b,2} \equiv \left(-1, 0, 2, \frac{2N - 2 + \alpha_N}{N + 1}, \frac{-2n + 2N + n\,\alpha_N}{N}\right), \tag{55b}$$

$$P_{4b,c} \equiv \left(-1, 0, 2, \frac{2s_1}{1 + s_1}, \text{combinations}\right),$$
$$\alpha_{j,c} = \frac{2(s + 1 - j)}{s + 1},\ \alpha_{l,c} = \frac{\alpha_N + 2(N - l) + s\alpha_N}{s + 1}, \tag{55c}$$

  where s_1 is the value of s for the first non-zero block. The first critical point $P_{4b,1}$ has a well defined cosmology. It is a DE dominated point with a phantom equation of state, $w_{\text{eff}} = -\frac{5}{3}$, and it resembles the point P_{4b} of

the second order with $\alpha_2 = 0$. We can infer its stability from Table 3, which shows that it is a saddle, therefore it does not have the desired nature for a DE point and we do not analyze it further. The second critical point $P_{4b,2}$ can be written as

$$\left(-1, 0, 2, 1 + \frac{\alpha_{2,c}}{2}, \alpha_{n,c} = \frac{4 - 2n + n\alpha_{2,c}}{2}\right), \tag{56}$$

where we have used the solution of α_2 to substitute for α_N in terms of $\alpha_{2,c}$; comparing it with Table 3 we can see a clear connection with the P_{4b} critical point. As expected the equation of state for the effective fluid equation can be written as

$$w_{\text{eff}} = \frac{-3N - 4 + 2\alpha_N}{3N} = -\frac{5 - \alpha_{2,c}}{3}, \tag{57}$$

which is equivalent to the one found at second order for the point P_{4b}, and shows an accelerated behavior for $\alpha_{2,c} < 4$. For this critical point is very difficult to calculate explicitly the eigenvalues but looking at Table 3 we can infer that for $\alpha_2 < 4$ it will be a saddle, therefore we do not consider it cosmologically viable. In the latter case the critical points $P_{4b,c}$ has $w_{\text{eff}} = -\frac{7+3s}{3(s+1)}$, which for all the combinations is ≈ -1. The stability analysis, however, reveals that this is a set of saddle points, thus preventing them from being viable accelerated attractors.

The third family of DE dominated critical points is P_6-like with $w_{\text{eff}} = \frac{2}{3}\lambda_0 - 1$:

$$P_{6a} \equiv \left(\frac{\lambda_0}{2}, 1 + \frac{\lambda_0}{2}, -\lambda_0, 0, \alpha_{n,c} = 0\right), \tag{58a}$$

$$P_{6b} \equiv \left(\frac{\lambda_0}{2}, 1 + \frac{\lambda_0}{2}, -\lambda_0, 0, \alpha_{n,c} = \alpha_N - \lambda_0\ (N - n)\right), \tag{58b}$$

$$P_{6c} \equiv \left(\frac{\lambda_0}{2}, 1 + \frac{\lambda_0}{2}, -\lambda_0, 0, \text{combinations}\right),$$
$$\alpha_{j,c} = -(s + 1 - j)(3 + \lambda_0),\ \alpha_{l,c} = \alpha_N - (N - l)(3 + \lambda_0). \tag{58c}$$

The eigenvalues of the linearized system around these critical points are too complicated to be reported. However it can be shown that the first one is an accelerated attractor for $(-\frac{12}{5} < \alpha_N \leq -2 \wedge -\frac{12}{5} \leq \lambda_0 < \alpha_N) \vee (\alpha_N > -2 \wedge -\frac{12}{5} \leq \lambda_0 < -2)$ while the second one displays the same cosmological behavior for $(\alpha_N < \frac{1}{5}(24 - 12N) \wedge -\frac{12}{5} \leq \lambda_0 < -2) \vee (\alpha_N = \frac{1}{5}(24 - 12N) \wedge -\frac{12}{5} < \lambda_0 < -2) \vee (\frac{1}{5}(24 - 12N) < \alpha_N < 4 - 2N \wedge \frac{\alpha_N}{-2+N} < \lambda_0 < -2)$. Both these points, as well as P_{6c} have $w_{\text{eff}} < -2.3$, therefore we do not consider them cosmologically viable.

The last family of, P_9-like, DE dominated critical points contains configurations which all have a different effective equation of state.

$$P_{9a} \equiv (-5, 0, 6, 3, \alpha_{n,c} = 0), \tag{59a}$$

$$P_{9b} \equiv \left(\frac{-1 - 2N + \alpha_N}{(N-1)}, 0, \frac{3N - \alpha_N}{(N-1)}, 3, \frac{3N + n(\alpha_N - 3) - \alpha_N}{(N-1)}\right)$$
$$= (\alpha_2 - 5, 0, 6 - \alpha_2, 3, \alpha_{n,c} = 6 + n(\alpha_2 - 3) - \alpha_2), \tag{59b}$$

$$P_{9c} \equiv \left(-2 - \frac{3}{s_1}, 0, 3 + \frac{3}{s_1}, 3, \text{combinations}\right),$$
$$\alpha_{j,c} = \frac{3(s + 1 - j)}{s},\ \alpha_{l,c} = \frac{3(N - l) + s\alpha_N}{s}, \tag{59c}$$

where s_1 is the value of s for the first non-zero block. The equation of state parameter in these three configurations is, respectively:

$$w_{\rm eff}(P_{9a}) = -3,\ w_{\rm eff}(P_{9b}) = -\frac{3+3N-2\alpha_N}{3\,(N-1)} = -3+\frac{2}{3}\alpha_2,\ w_{\rm eff}(P_{9c}) = -\frac{2+s_1}{s_1}. \tag{60}$$

The stability analysis reveals that all the points of this family are saddles in the range for which they are accelerated and therefore we do not investigate them further.

- *Scaling solutions:*
This family of critical points is characterized by a scaling between matter and DE:

$$P_{sc1} \equiv \Big(\frac{-3-6\,(N-1)^2+5\alpha_N-2\alpha_N^2+(N-1)\,(-9+7\alpha_N)}{3(N-2)^2}, 0, \frac{3N-2\alpha_N}{N-2}, \\ , \frac{3\,(N-1)-\alpha_N}{N-2}, \alpha_{n,c} = \frac{3N+n(-3+\alpha_N)-2\alpha_N}{N-2}\Big), \tag{61a}$$

$$P_{sc2} \equiv \left(-\frac{(s_1+1)(2s_1+1)}{(s_1-1)^2}, 0, \frac{3(s_1+1)}{s_1-1}, \frac{3s_1}{s_1-1}, \text{combinations} \right), \\ \alpha_{j,c} = \frac{3(s+1-j)}{s-1},\ \alpha_{l,c} = \frac{-\alpha_N+3(N-l)+s\alpha_N}{s-1}, \tag{61b}$$

where s_1 is the value of s for the first non-zero block. These configurations correspond to a matter density and equation of state parameter:

$$\Omega_m(P_{sc1}) = -\frac{(4+N-2\alpha_N)(-3+\alpha_N)}{3(N-2)^2},\ w_{\rm eff}(P_{sc1}) = \frac{3N-2\alpha_N}{6-3N}, \\ \Omega_m(P_{sc2}) = \frac{5+s_1}{(s_1-1)^2},\ w_{\rm eff}(P_{sc2}) = \frac{s_1+1}{1-s_1}. \tag{62}$$

The study of the stability for these critical points is very complicated due to the unknown value of N. It is, however, simple to determine that, for both points, neither of the two configurations in which they are, respectively, matter ($\Omega_m = 1$) and DE dominated ($\Omega_{\rm DE} = 1$) is cosmologically viable.

In this paper we choose not to perform a full analysis of the scaling configurations, but rather focus on the two extrema for which either of the two components has fractional energy density equal to unity. While we leave a thorough investigation of the scaling regime for future work, we want to stress that this family of critical points is expected to display all the late-time scaling cosmologies that can offer a dynamical solution to the coincidence problem [194, 331, 332].

- *DE points:*
The last family of critical points is made of DE dominated configurations

$$P_{d1} \equiv \Big(\frac{-2\alpha_N^2-\lambda_0(-3+(N-1)^2\,(\lambda_0+1)+(N-1)\,(\lambda_0+2))+\alpha_N(-4+\lambda_0+(N-1)\,(4+3\lambda_0))}{6(N-2)^2}, \\ , \frac{(\alpha_N-3)(-2+2\alpha_N-\lambda_0)+(N-1)^2\,(6-5\lambda_0+\lambda_0^2)+(N-1)\,(-12+\alpha_N(8-3\lambda_0)+2\lambda_0+\lambda_0^2)}{6(N-2)^2}, \\ , \frac{\lambda_0+(N-1)\,\lambda_0-2\alpha_N}{N-2}, \frac{(N-1)\,\lambda_0-\alpha_N}{N-2}, \alpha_{n,c} = \frac{(n-2)\alpha_N+(N-n)\lambda_0}{N-2}\Big), \tag{63a}$$

$$P_{d2} \equiv \Bigg(-\frac{\lambda_0(-3+s_1^2(\lambda_0+1)+s_1(\lambda_0+2))}{6(s_1-1)^2},$$
$$\frac{3(2+\lambda_0)+s_1^2(6-5\lambda_0+\lambda_0^2)+s_1(-12+2\lambda_0+\lambda_0^2)}{6(s_1-1)^2},$$
$$\frac{\lambda_0(s_1+1)}{s_1-1}, \frac{s_1\lambda_0}{s_1-1}, \text{combinations}\Bigg),$$
$$\alpha_{j,c} = \frac{(s+1-j)\lambda_0}{s-1},\ \alpha_{l,c} = \frac{\alpha_N(s-1)+(N-l)\lambda_0}{s-1}, \tag{63b}$$

with different values of the equation of state, respectively

$$w_{\rm eff}(P_{d1}) = \frac{6-3N+2\alpha_N-2\lambda_0}{3(N-2)}, \quad w_{\rm eff}(P_{d2}) = \frac{3-3s_1-2\lambda_0}{3(s_1-1)}, \tag{64}$$

where s_1 is the value of s for the first non-zero block. The first point has a viable cosmological behavior for $\alpha_N < N-2+\lambda_0$ and would have $w_{\rm eff} = -1$ if $\lambda_0 = \alpha_N$; however we are not able to analyze its stability. The second point gives a viable cosmological behavior for $s_1+\lambda_0 > 1$; however requiring $w_{\rm eff} = -1$ gives $\lambda_0 = 0$ and the stability analysis reveals that the point is non-hyperbolic for such a value.

- *ϕ-MDE:*
  This family contains the following P_5-like:

$$P_{5a} \equiv (-1,0,-3,0,\alpha_{n,c}=0), \tag{65a}$$
$$P_{5b} \equiv (-1,0,-3,0,\alpha_{n,c}=\alpha_N-3(N-n)), \tag{65b}$$
$$P_{5c} \equiv (-1,0,-3,0,\text{combinations}),\ \alpha_{j,c}=-3(s+1-j),\ \alpha_{l,c}=\alpha_N-3(N-l), \tag{65c}$$

  which are characterized by $\Omega_m = 5$, $\Omega_{\rm DE} = -4$ and $w_{\rm eff} = 1$, therefore we do not consider them further.

.2 EFTCAMB Implementation Details

In this Appendix we review some of the details of the EFT formalism and its implementation in CAMB.

.2.1 EFT Action from Second Order Operators

The effective field theory of dark energy action in conformal time with the π field manifest through the Stückelberg trick, up to second order operators, read:

$$S = \int d^4x\sqrt{-g}\Bigg\{ \frac{m_0^2}{2}\left[1+\Omega(\tau+\pi)\right]R + \Lambda(\tau+\pi)$$
$$- c(\tau+\pi)a^2\left[\delta g^{00} - 2\frac{\dot\pi}{a^2} + 2\mathcal{H}\pi\left(\delta g^{00} - \frac{1}{a^2} - 2\frac{\dot\pi}{a^2}\right) + 2\dot\pi\delta g^{00}\right.$$
$$\left. +2g^{0i}\partial_i\pi - \frac{\dot\pi^2}{a^2} + g^{ij}\partial_i\pi\partial_j\pi - \left(2\mathcal{H}^2+\dot{\mathcal{H}}\right)\frac{\pi^2}{a^2} + ...\right]$$
$$+\frac{M_2^4(\tau+\pi)}{2}a^4\left(\delta g^{00} - 2\frac{\dot\pi}{a^2} - 2\frac{\mathcal{H}\pi}{a^2} + ...\right)^2$$

$$
\begin{aligned}
&- \frac{\bar{M}_1^3(\tau+\pi)}{2} a^2 \left(\delta g^{00} - 2\frac{\dot{\pi}}{a^2} - 2\frac{\mathcal{H}\pi}{a^2} + ...\right) \cdot \\
&\qquad \left(\delta K^{\mu}{}_{\mu} + 3\frac{\dot{\mathcal{H}}}{a}\pi + \frac{\bar{\nabla}^2\pi}{a^2} + ...\right) \\
&- \frac{\bar{M}_2^2(\tau+\pi)}{2} \left(\delta K^{\mu}{}_{\mu} + 3\frac{\dot{\mathcal{H}}}{a}\pi + \frac{\bar{\nabla}^2\pi}{a^2} + ...\right)^2 \\
&- \frac{\bar{M}_3^2(\tau+\pi)}{2} \left(\delta K^{i}{}_{j} + \frac{\dot{\mathcal{H}}}{a}\pi\delta^{i}{}_{j} + \frac{1}{a^2}\bar{\nabla}^i\bar{\nabla}_j\pi + ...\right) \cdot \\
&\qquad \left(\delta K^{j}{}_{i} + \frac{\dot{\mathcal{H}}}{a}\pi\delta^{j}{}_{i} + \frac{1}{a^2}\bar{\nabla}^j\bar{\nabla}_i\pi + ...\right) \\
&+ \frac{\hat{M}^2(\tau+\pi)}{2} a^2 \left(\delta g^{00} - 2\frac{\dot{\pi}}{a^2} - 2\frac{\mathcal{H}}{a^2}\pi + ...\right) \cdot \\
&\qquad \left(\delta R^{(3)} + 4\frac{\mathcal{H}}{a}\bar{\nabla}^2\pi + ...\right) \\
&+ m_2^2(\tau+\pi)\left(g^{\mu\nu} + n^\mu n^\nu\right)\partial_\mu\left(a^2 g^{00} - 2\dot{\pi} - 2\mathcal{H}\pi + ...\right) \\
&\qquad \partial_\nu\left(a^2 g^{00} - 2\dot{\pi} - 2\mathcal{H}\pi + ...\right) \\
&+ ...\Big\} + S_m[g_{\mu\nu}], \qquad (66)
\end{aligned}
$$

where $\bar{\nabla}$ indicates three dimensional spatial derivatives. Note that the conformal scale factor has been already Taylor expanded in π according to Eq. 6.3.

.2.2 Cosmological Perturbations from Second Order Operators

In what follows we list the contributions to the linearly perturbed equations of Sec. 6.4 from the second order operators in (66). Let us make an itemized list where for each operator we list its contributions to the r.h.s. of Eq. (6.14) by Δ_{00}, to the r.h.s. of Eq. (6.15) by Δ_{0i}, to the r.h.s. of Eq. (6.16) by $\Delta_{ij,i\neq j}$, to the r.h.s of Eq. (6.17) by Δ_{ii} and to the l.h.s. of Eq. (6.18) by Δ_π. Notice that in order to perform a correct stability analysis on the equation for π, along the lines of Sec. 6.5, it is important to demix the degrees of freedom; specifically, *once the contributions from all operators have been taken into account*, one needs to use the Einstein equations to subsistute for any $\ddot{h}, \eta, \sigma_*$ appearing in the final form of the equation for π.

$\underline{(\delta g^{00})^2}$:

$$
\begin{aligned}
&\Delta_{00} = -\frac{2M_2^4 a^2}{m_0^2(1+\Omega)}\left(\dot{\pi} + \mathcal{H}\pi\right), \\
&\Delta_{0i} = 0, \\
&\Delta_{ij,i\neq j} = 0,
\end{aligned}
$$

$$\Delta_{ii} = 0\,,$$
$$\Delta_\pi = 2M_2^4\left[\ddot{\pi} + 4\left(\mathcal{H} + \frac{\dot{M}_2}{M_2}\right)\dot{\pi} + \left(3\mathcal{H}^2 + \dot{\mathcal{H}} + 4\frac{\mathcal{H}\dot{M}_2}{M_2}\right)\pi\right]. \quad (67)$$

$\underline{\delta g^{00}\delta K^\mu_\mu}$:

$$\Delta_{00} = \frac{a\bar{M}_1^3}{2m_0^2(1+\Omega)}\left[k\mathcal{Z} - 3\left(\dot{\mathcal{H}} - 2\mathcal{H}^2 - \frac{k^2}{3}\right)\pi + 3\mathcal{H}\dot{\pi}\right],$$
$$\Delta_{0i} = \frac{a\bar{M}_1^3 k}{m_0^2(1+\Omega)}\left(\dot{\pi} + \mathcal{H}\pi\right),$$
$$\Delta_{ij,i\neq j} = 0\,,$$
$$\Delta_{ii} = -\frac{3a\bar{M}_1^3}{m_0^2(1+\Omega)}\left[\ddot{\pi} + \left(4\mathcal{H} + 3\frac{\dot{\bar{M}}_1}{\bar{M}_1}\right)\dot{\pi} + \left(3\mathcal{H}^2 + \dot{\mathcal{H}} + 3\frac{\mathcal{H}\dot{\bar{M}}_1}{\bar{M}_1}\right)\pi\right],$$
$$\Delta_\pi = \frac{\bar{M}_1^3}{2a}\Bigg[\left(3\mathcal{H} + 3\frac{\dot{\bar{M}}_1}{\bar{M}_1}\right)\left(-k\mathcal{Z} + 3(\dot{\mathcal{H}} - \mathcal{H}^2)\pi - k^2\pi\right)$$
$$- \frac{\ddot{h}}{2} + \mathcal{H}k\mathcal{Z} + 2\mathcal{H}k^2\pi + 3(\ddot{\mathcal{H}} - 4\mathcal{H}\dot{\mathcal{H}} + 2\mathcal{H}^3)\pi\Bigg]. \quad (68)$$

$\underline{(\delta K)^2}$:

$$\Delta_{00} = \frac{3\mathcal{H}\bar{M}_2^2}{2m_0^2(1+\Omega)}\left[k\mathcal{Z} - 3(\dot{\mathcal{H}} - \mathcal{H}^2)\pi + k^2\pi\right],$$
$$\Delta_{0i} = \frac{\bar{M}_2^2 k}{m_0^2(1+\Omega)}\left[k\mathcal{Z} - 3(\dot{\mathcal{H}} - \mathcal{H}^2)\pi + k^2\pi\right],$$
$$\Delta_{ij,i\neq j} = 0\,,$$
$$\Delta_{ii} = -\frac{3\bar{M}_2^2}{m_0^2(1+\Omega)}\left(2\mathcal{H} + \partial_\tau + 2\frac{\dot{\bar{M}}_2}{\bar{M}_2}\right)\left[k\mathcal{Z} - 3(\dot{\mathcal{H}} - \mathcal{H}^2)\pi + k^2\pi\right],$$
$$\Delta_\pi = \frac{\bar{M}_2^2}{2a^2}\left(3(\dot{\mathcal{H}} - \mathcal{H}^2) - k^2\right)\left[-k\mathcal{Z} + 3(\dot{\mathcal{H}} - \mathcal{H}^2)\pi - k^2\pi\right]. \quad (69)$$

$\underline{\delta K^\mu_\nu \delta K^\nu_\mu}$:

$$\Delta_{00} = \frac{\mathcal{H}\bar{M}_3^2}{m_0^2(1+\Omega)}\left[k\mathcal{Z} - 3\left(\dot{\mathcal{H}} - \mathcal{H}^2 - \frac{k^2}{3}\right)\pi\right],$$
$$\Delta_{0i} = \frac{\bar{M}_3^2 k}{m_0^2(1+\Omega)}\left[\frac{k\mathcal{Z}}{3} + \frac{2}{3}k\sigma_* - (\dot{\mathcal{H}} - \mathcal{H}^2 - k^2)\pi\right],$$

$$\Delta_{ij,i\neq j} = \frac{\bar{M}_3^2}{m_0^2(1+\Omega)}\left(2\mathcal{H} + 2\frac{\dot{\bar{M}}_3}{\bar{M}_3} + \partial_\tau\right)\left(k\sigma_* + k^2\pi\right),$$
$$\Delta_{ii} = \frac{\bar{M}_3^2}{m_0^2(1+\Omega)}\left(2\mathcal{H} + 2\frac{\dot{\bar{M}}_3}{\bar{M}_3} + \partial_\tau\right)\left[-k\mathcal{Z} + 3\left(\dot{\mathcal{H}} - \mathcal{H}^2 - \frac{1}{3}k^2\right)\pi\right],$$
$$\Delta_\pi = \frac{\bar{M}_3^2}{a^2}\Bigg[\left(\frac{k^4}{2} - k^2(\dot{\mathcal{H}} - \mathcal{H}^2) + \frac{3}{2}(\dot{\mathcal{H}} - \mathcal{H}^2)^2\right)\pi$$
$$+ \left(\frac{k^2}{2} - \frac{\dot{\mathcal{H}} - \mathcal{H}^2}{2}\right)k\mathcal{Z} + \frac{k^3}{3}(\sigma_* - \mathcal{Z})\Bigg]. \quad (70)$$

$\underline{\delta g^{00}\delta R^{(3)}}$:

$$\begin{aligned}
&\Delta_{00} = -\frac{2\hat{M}^2}{m_0^2(1+\Omega)}k^2\left(\eta+\mathcal{H}\pi\right)\,,\\
&\Delta_{0i} = 0\,,\\
&\Delta_{ij,i\neq j} = 2\frac{\hat{M}^2}{m_0^2(1+\Omega)}k^2\left(\dot{\pi}+\mathcal{H}\pi\right)\,,\\
&\Delta_{ii} = \frac{4\hat{M}^2}{m_0^2(1+\Omega)}k^2\left(\dot{\pi}+\mathcal{H}\pi\right)\,,\\
&\Delta_{\pi} = \frac{2k^2}{a^2}\left[\hat{M}^2\frac{k}{3}(\sigma_*-\mathcal{Z})+\left(\mathcal{H}\hat{M}^2+2\hat{M}\dot{\hat{M}}\right)\eta+\left(2\mathcal{H}\hat{M}\dot{\hat{M}}+\dot{\mathcal{H}}\hat{M}^2\right)\pi\right].
\end{aligned} \tag{71}$$

$\underline{(\mathrm{g}^{\mu\nu}+\mathrm{n}^{\mu}\mathrm{n}^{\nu})\partial_\mu\delta\mathrm{g}^{00}\partial_\nu\delta\mathrm{g}^{00}}$:

$$\begin{aligned}
&\Delta_{00} = -\frac{4m_2^2}{m_0^2(1+\Omega)}k^2\left(\dot{\pi}+\mathcal{H}\pi\right)\,,\\
&\Delta_{0i} = 0\,,\\
&\Delta_{ij,i\neq j} = 0\,,\\
&\Delta_{ii} = 0\,,\\
&\Delta_{\pi} = 4m_2^2\left(2\mathcal{H}+\frac{\dot{m}_2}{m_2}+\partial_\tau\right)k^2\left(\dot{\pi}+\mathcal{H}\pi\right)\,.
\end{aligned} \tag{72}$$

.2.3 EFTCAMB Notation

In this Appendix and the following Sections we shall follow the notation of the EFTCAMB Numerical Notes [10].

This has been developed to ensure maximum compatibility with CAMB notation while being suitable for the numerical implementation of the EFT framework.

- The overdot represents derivation with respect to conformal time τ while the prime represents derivation with respect to the scale factor a, unless otherwise specified.
- In what follows we define a new dimensionless Stückelberg field: $\widetilde{\pi}$, *i.e.*the π-field in the action (66) multiplied by H_0 and divided by a. For the rest of the notes we will suppress the tilde to simplify the equations so $\widetilde{\pi}$ is written as π, if there is no confusion.
- We redefine all the second order EFT functions to make them dimensionless and to facilitate their inclusion in the code:

$$\begin{aligned}
&\gamma_1 = \frac{M_2^4}{m_0^2H_0^2}, \quad \gamma_2 = \frac{\bar{M}_1^3}{m_0^2H_0}, \quad \gamma_3 = \frac{\bar{M}_2^2}{m_0^2},\\
&\gamma_4 = \frac{\bar{M}_3^2}{m_0^2}, \quad \gamma_5 = \frac{\hat{M}^2}{m_0^2}, \quad \gamma_6 = \frac{m_2^2}{m_0^2}.
\end{aligned} \tag{73}$$

Let us notice that in the last EFTCAMB released version (v2.0) we have slightly changed the definition of the second order EFT functions w.r.t. the convention used in v1.0 and v1.1. These new definitions do not change the general structure and physics in the code, but they allow for a more direct and cleaner implementation of Horndeski models [192, 333]. For the sake of clarity let us list the explicit correspondence between this new convention and that one used in the previous releases (v1.0 and v1.1), in terms of the α's:

$$\gamma_1 = \alpha_1^4, \quad \gamma_2 = \alpha_2^3, \quad \gamma_3 = \alpha_3^2, \quad \gamma_4 = \alpha_4^2, \quad \gamma_5 = \alpha_5^2, \quad \gamma_6 = \alpha_6^2. \tag{74}$$

- We define all the EFT functions Ω, c, Λ and the γ-functions as function of the scale factor a .

.2.4 Structure and Evolution of the EFTCAMB code

In parallel with the flexibility of the EFT approach to DE and MG models we need a complicated logical structure to control its numerical implementation. This structure changed from version to version growing in complexity while the model coverage increased. The structure corresponding to different releases is shown in Figures 8, 9 and 10. In this section we shall briefly outline the structure of the latest version (2.0) as in Figure 10.

There is a number associated to each model selection flag; such number is reported in Figure 10 and it controls the behaviour of the code. The main code flag is `EFTflag`, which is the starting point after which all the other sub-flags, can be chosen according to the user interests.

- The number `EFTflag` = 0 corresponds to the standard CAMB code. Every EFT modification to the code is automatically excluded by this choice.

- The number `EFTflag` = 1 corresponds to *pure* EFT models. The user needs then to select a model for the background expansion history via the `EFTwDE` flag. Various common parametrizations for the DE equation of state are natively included in the code. The implementation details of the dark energy equations of state can be found in Section .2.5. Finally, to fully specify the *pure* EFT model, one has to fix the EFT functions behaviour as functions of the scale factor a. The corresponding flags for the model selection are: `PureEFTmodelOmega` for the model selection of the EFT function $\Omega(a)$ and `PureEFTmodelGammai`, with i = 1, .., 6 for the $\gamma_i(a)$ EFT functions. Some built-in models are already present in the code and can be selected with the corresponding number, see Flowchart 10. The details about these models can be found in Section .2.9. There is also the possibility to use the flag `PureEFTHorndeski` to restrict *pure* EFT models to Horndeski one. The code will then internally set the behaviour of the EFT functions γ_4, γ_5, γ_6 according to eq. (126) in order to cancel high order derivatives, at this point choices made for these functions will be ignored (see Section .2.9 for more details). After setting these flags the user has to define the values of the EFT model parameters for the chosen model. Every other value of parameter and flag which do not concern the chosen model is automatically ignored.

- The number `EFTflag` = 2 corresponds to the designer *mapping* EFT procedure. Also in this case the `EFTwDE` flag controls the background expansion history which works as in the previous case.
  For the *mapping* case the user can investigate a particular DE/MG model once the matching with the EFT functions is provided and the background evolution has been implemented in the EFT code.
  The model selection flag for the *mapping* EFT procedure is `DesignerEFTmodel`. Various models are already included in the code (see the blue lines in the Flowchart 10) and their implementation details are presented in Section .2.10. Models corresponding to the grey lines in the Flowchart 10 are some of the models that can be cast into the EFT formalism and that will be gradually implemented in future code releases.

- The number `EFTflag` = 3 corresponds to the implementation of alternative model-independent parametrizations in terms of EFT functions. A lot of alternative parametrizations already present in literature can be completely described by using the versatility of the EFT approach allowing to preserve all the advantages of EFTCAMB. See Section .2.11 for details.

- The number `EFTflag` = 4 corresponds to the full *mapping* EFT procedure. In this case the background expansion history is not set by a choice of $w_{\rm DE}$ and a model has to be fully specified. The code will then solve the background equations for the given model to map it into the EFT framework. Low energy Hořava gravity has been included as the first example of the implementation of full mapping models. More models will be gradually filled in the near future. See Section .2.12 for details.

In addition EFTCAMB takes advantage of the feedback mechanism of CAMB with the following modifications:

- `feedback level=0` no feedback from EFTCAMB nor from EFTCosmoMC;
- `feedback level=1` basic feedback, no feedback from EFTCAMB when called from EFTCosmoMC;
- `feedback level=2` advanced feedback, no feedback from EFTCAMB when called from EFTCosmoMC;
- `feedback level=3` debug feedback also when EFTCAMB is called from EFTCosmoMC;

In order to implement the EFT formalism in the CAMB and CosmoMC codes we had to modify several files. We list them in this Section.
To further help the user in understanding our part of code and/or applying the EFT modification to an already modified version of CAMB/CosmoMC we enclosed every modification that we made inside the following commented code lines:

```
! EFTCAMB MOD START
...
! EFTCAMB MOD END
```

for the CAMB part and:

```
! EFTCOSMOMC MOD START
...
! EFTCOSMOMC MOD END
```

for the CosmoMC part.

The step by step guide to the EFTCAMB modification v1.0 and v1.1 will still be available at `http://www.lorentz.leidenuniv.nl/~hu/codes/guide_EFTCAMB.html` and the EFTCosmoMC one at `http://www.lorentz.leidenuniv.nl/~hu/codes/guide_EFTCosmoMC.html`.

We also provide a developers version of the code at `https://github.com/EFTCAMB/EFTCAMB`. The tools provided by Github to visualize the history of the modifications of the code will, from now on, supersede the guides to the EFTCAMB/EFTCosmoMC modifications.

Structure of the EFTCAMB modification

The modification to the CAMB code is mainly implemented by modifying or adding the following files:

- `EFT_def.f90`: this file contains all the compile time EFTCAMB options and the definition of the parametrizations for the dark energy equation of state.
- `EFT_designer.f90`: this file contains the module for designer models.
- `EFT_Horndeski.f90`: this file contains all the code regarding implementation of Horndeski models.
- `EFT_functions.f90`: this file contains the definition of the EFT functions for the chosen model, in particular it contains the definitions of the *pure* EFT parametrizations.
- `EFT_main.f90`: this file contains a module that evaluates whether the considered DE/MG model is stable or not and a module that finds the time (if it exists) at which the considered model is so close to GR that it is pointless to evolve the DE equation.
- `EFTstabilitySpace.f90`: this file contains a program that can be compiled with the directive `make eftstability` to serve the purpose of making simple explorations of the stability region in parameter space for the theory of interest. This proves extremely helpful to understand and visualize the shape of the parameter space of a theory before exploring it with CosmoMC.
- `equations_EFT.f90`: this is a modified version of the standard CAMB equations file. It contains all the equations that the code needs to solve to get the full behaviour of perturbations in DE/MG models. These equations are reported in Section .2.6 and being written in terms of the EFT functions there is no need for the user to modify this file to include new DE/MG models in CAMB.

- `cmbmain.f90`: it includes modification of the standard CAMB file to run the designer code, the stability check and the return to GR detection just after EFTCAMB is launched. It also contains an optional code that will print the behaviour of perturbations in the DE/MG model that is considered. The latter part of code is not controlled by the parameter file so the user has to search for it in the code and manually activate it. It is also possible to use it at debug purposes.

Several other files have to be marginally modified to complete the integration between CAMB and EFTCAMB. We encourage the user to inspect the released code for more details.

Structure of the EFTCosmoMC modification

To interface CosmoMC with EFTCAMB we had to modify the following files:

- `params_CMB_EFT.ini`: to specify the EFT model parameters that are sampled in the MCMC run and their priors.
- `common_batch1_EFT.ini` and `common_batch2_EFT.ini`: to read cosmological parameters from `params_CMB_EFT.ini`.
- `EFT_params.ini`: to let the user choose the model via the selection flags.
- `params_CMB.paramnames`: to add the names of the EFT model parameters.
- `Makefile`: to compile the whole program with the EFTCAMB/EFTCosmoMC files.
- `settings.f90`: to increase the number of theory parameters.
- `CosmologyTypes.f90`: to add the EFT model parameters into the set of CosmoMC parameters and read the values of the model selection flags.
- `CalcLike_Cosmology.f90`: to perform the stability check on the considered model for the specific choice of cosmological parameters that are being considered by the MCMC sampler and reject them if the theory is found to be unstable.
- `Calculator_CAMB.f90`: to pass the EFT model parameters and the values of the model selection flags to EFTCAMB.
- `Calculator_Cosmology.f90`: to make the stability module works with the newest version of CosmoMC.
- `CosmologyParameterizations.f90`: to increase the number of CosmoMC parameters and associate the EFT parameter name to the one in the parameters files.

As of now the EFTCosmoMC_Oct15 code does not enforce automatically the compatibility between the model selection flags and the parameters that are included in the MCMC run. This means that the user has to do the following to properly launch a run:

- At first the proper values for the EFT model selection flags have to be chosen in the file `EFT_params.ini` according to the scheme in Figure 10.
- Then the user has to modify `params_CMB_EFT.ini` to select the parameters to include in the run, their center values and priors.
  In order to exclude unwanted EFT parameters from the run, their `start width` and `propose width` have to be set to zero while for the parameters related to the previously selected model these two have to be chosen different from zero.
  Since EFTCAMB enforces *viability priors* it is then sufficient that the standard CosmoMC priors are set to a value that reasonably includes the stable region in parameter space.
  We then suggest to set the center of a parameter relatively far from its GR limit as the parameter space of a given model might be not well behaved in the vicinity of that point.
- After these two steps the run can be launched in the standard way.

.2.5 EFTCAMB Background Equations: Code Notation

Given the high degree of freedom already at the level of background, and since the focus will be on the dynamics of linear perturbations, it is common to adopt a designer approach as described in [162, 163]. First of all one writes the background equations as follows:

$$\begin{aligned}
\mathcal{H}^2 =& \frac{8\pi G}{3}a^2(\rho_m+\rho_{\rm DE}+\rho_\nu)\,,\\
\dot{\mathcal{H}} =& -\frac{4\pi G}{3}a^2\left(\rho_m+\rho_{\rm DE}+\rho_\nu+3P_m+3P_{\rm DE}+3P_\nu\right)=-\frac{\mathcal{H}^2}{2}-\frac{8\pi G a^2 P_{\rm tot}}{2}\,,\\
\ddot{\mathcal{H}} =& 8\pi G a^2\rho_m\mathcal{H}\left(\frac{1}{6}+w_m+\frac{3}{2}w_m^2\right)+8\pi G a^2\rho_{\rm DE}\mathcal{H}\left(\frac{1}{6}+w_{\rm DE}+\frac{3}{2}w_{\rm DE}^2-\frac{1}{2}aw'_{\rm DE}\right)\\
&+8\pi G a^2\left(\frac{\mathcal{H}}{6}\rho_\nu-\frac{\mathcal{H}}{2}P_\nu-\frac{1}{2}\dot{P}_\nu\right)
\end{aligned}\tag{75}$$

where the prime stands for derivative w.r.t. the scale factor a, $\{\rho_m, P_m\}$ are the energy density and pressure of matter (e.g. dark matter, radiation and massless neutrinos) and $\{\rho_{\rm DE}, P_{\rm DE}\}$ encode the contributions from the extra scalar field into the form of an energy density and pressure of dark energy. For the matter components, one has the following continuity equations, and corresponding solutions:

$$\begin{aligned}
&\dot{\rho}_m+3\mathcal{H}\left(\rho_m+P_m\right)=0\,,\\
&\qquad\rho_m=\frac{3H_0^2}{8\pi G}\,\Omega_m^0\,a^{-3(1+w_m)}\,,\\
&\dot{\rho}_{\rm DE}+3\mathcal{H}\rho_{\rm DE}\left[1+w_{\rm DE}(a)\right]=0\,,\\
&\qquad\rho_{\rm DE}=\frac{3H_0^2}{8\pi G}\,\Omega_{\rm DE}^0\,\exp\left[-3\int_1^a\frac{\left(1+w_{\rm DE}(a)\right)}{a}\,da\right],
\end{aligned}\tag{76}$$

where $\Omega^0_{m,{\rm DE}}$ is the energy density parameter today, respectively of matter sector and dark energy, and H_0 is the present time Hubble parameter. Finally,

$\{\rho_\nu, P_\nu\}$ are the density and pressure contributions due to massive neutrinos. The equation of state of massive neutrinos has a complicated, time dependent expression, hence the code computes directly $\dot{P}_\nu$. As the treatment of massive neutrinos in EFTCAMB is exactly the same as CAMB we refer the user to [59]. However, let us stress that in EFTCAMB the indirect interaction (via gravity) of massive neutrino and DE/MG sectors has been consistently taken into account both at the background and perturbations level, see also [5]. With this setup, *a background is fixed specifying* $w_{\rm DE}$. We illustrate in the next Section .2.5 the models that are currently implemented in the code. After the expansion history has been chosen one can then determine c, Λ in terms of $\mathcal{H}$ and $\Omega(a)$; namely, combining eq. (75) and eq. (76) with the EFT background eqs. (12,13) in [8] one has:

$$\frac{ca^2}{m_0^2} = \left(\mathcal{H}^2 - \dot{\mathcal{H}}\right)\left(\Omega + \frac{a\Omega'}{2}\right) - \frac{a^2\mathcal{H}^2}{2}\Omega'' + \frac{1}{2}\frac{a^2\rho_{\rm DE}}{m_0^2}(1+w_{\rm DE})\,, \ [{\rm Mpc}^{-2}] \tag{77}$$

$$\frac{\Lambda a^2}{m_0^2} = -\,\Omega\left(2\dot{\mathcal{H}} + \mathcal{H}^2\right) - a\Omega'\left(2\mathcal{H}^2 + \dot{\mathcal{H}}\right) - a^2\mathcal{H}^2\Omega'' + w_{\rm DE}\frac{a^2\rho_{\rm DE}}{m_0^2}\,, \ [{\rm Mpc}^{-2}] \tag{78}$$

$$\begin{aligned}\frac{\dot{c}a^2}{m_0^2} =& \frac{\mathcal{H}}{2}\left(-3\left(1+w_{\rm DE}\right)^2 + aw'_{\rm DE}\right)\frac{\rho_{\rm DE}a^2}{m_0^2} - \Omega\left(\ddot{\mathcal{H}} - 4\mathcal{H}\dot{\mathcal{H}} + 2\mathcal{H}^3\right)\\ &+ \frac{a\Omega'}{2}\left(-\ddot{\mathcal{H}} + \mathcal{H}\dot{\mathcal{H}} + \mathcal{H}^3\right) + \frac{1}{2}a^2\mathcal{H}\Omega''\left(\mathcal{H}^2 - 3\dot{\mathcal{H}}\right)\\ &- \frac{1}{2}a^3\mathcal{H}^3\Omega'''\,, \ [{\rm Mpc}^{-3}]\end{aligned} \tag{79}$$

$$\begin{aligned}\frac{\dot{\Lambda}a^2}{m_0^2} =& -2\Omega\left(\dddot{\mathcal{H}} - \mathcal{H}\ddot{\mathcal{H}} - \mathcal{H}^3\right) - a^2\Omega''\mathcal{H}\left(2\mathcal{H}^2 + 3\dot{\mathcal{H}}\right) - a^3\mathcal{H}^3\Omega'''\\ &- a\Omega'\left(4\mathcal{H}\dot{\mathcal{H}} + \ddot{\mathcal{H}}\right) + \frac{\rho_{\rm DE}a^2}{m_0^2}\mathcal{H}\left[aw'_{\rm DE} - 3w_{\rm DE}(1+w_{\rm DE})\right]. \ [{\rm Mpc}^{-3}]\end{aligned} \tag{80}$$

As discussed in the Sections .2.9 and .2.10, depending on whether one wants to implement a *pure* or *mapping* EFT model, the choice for Ω changes. After fixing the expansion history, in the former case one selects an ansätz for $\Omega(a)$, while in the latter case one determines via the matching the $\Omega(a)$ corresponding to the chosen model. In this case one has to separately solve the background equations for the given model, which might be done with a model-specific designer approach. In fact, this is the methodology we adopt for $f(R)$ models (see Section .2.10).

Finally, for the purposes of the code, it is useful to compute the following EFT dark fluid components that can be derived from eq. (10) of [8]:

$$\frac{\rho_Q a^2}{m_0^2} = 2\frac{ca^2}{m_0^2} - \frac{\Lambda a^2}{m_0^2} - 3a\mathcal{H}^2\Omega'\,, \ [{\rm Mpc}^{-2}] \tag{81}$$

$$\frac{P_Q a^2}{m_0^2} = \frac{\Lambda a^2}{m_0^2} + a^2\mathcal{H}^2\Omega'' + a\dot{\mathcal{H}}\Omega' + 2a\mathcal{H}^2\Omega'\,, \ [{\rm Mpc}^{-2}] \tag{82}$$

$$\frac{\dot{\rho}_Q a^2}{m_0^2} = -\,3\mathcal{H}\left(\frac{\rho_Q a^2}{m_0^2} + \frac{P_Q a^2}{m_0^2}\right) + 3a\mathcal{H}^3\Omega'\,, \ [{\rm Mpc}^{-3}] \tag{83}$$

$$\frac{\dot{P}_Q a^2}{m_0^2} = \frac{\dot{\Lambda} a^2}{m_0^2} + a^3\mathcal{H}^3\Omega''' + 3a^2\mathcal{H}\dot{\mathcal{H}}\Omega'' + a\Omega'\ddot{\mathcal{H}} + 3a\mathcal{H}\dot{\mathcal{H}}\Omega' + 2a^2\mathcal{H}^3\Omega'' - 2a\mathcal{H}^3\Omega' \,. \; [\mathrm{Mpc}^{-3}] \tag{84}$$

Effective Dark Energy equation of state parametrizations

Several models for the background expansion history have been implemented in the code:

- The ΛCDM expansion history:

$$\begin{aligned} w_{\rm DE} &= -1 \,, \\ \rho_{\rm DE} &= m_0^2\Lambda \,; \end{aligned} \tag{85}$$

- The wCDM model:

$$\begin{aligned} w_{\rm DE} &= w_0 = \text{const} \neq -1 \,, \\ \rho_{\rm DE} &= 3m_0^2H_0^2\Omega^0_{\rm DE}a^{-3(1+w_0)} \,; \end{aligned} \tag{86}$$

In code notation: $w_0 =$ `EFTw0`.

- The CPL parametrization [203, 204]:

$$\begin{aligned} w_{\rm DE}(a) &= w_0 + w_a(1-a) \,, \\ \rho_{\rm DE} &= 3m_0^2H_0^2\Omega^0_{\rm DE}a^{-3(1+w_0+w_a)}\exp\left(-3w_a(1-a)\right) \,; \end{aligned} \tag{87}$$

where w_0 and w_a are constant and indicate, respectively, the value and the derivative of $w_{\rm DE}$ today.
In code notation: $w_0 =$ `EFTw0` and $w_a =$ `EFTwa`.

- The generalized Jassal-Bagla-Padmanabhan parametrization [334, 335]:

$$\begin{aligned} w_{\rm DE} &= w_0 + (1-a)a^{n-1}w_a \,, \\ \rho_{\rm DE} &= 3m_0^2H_0^2\Omega^0_{\rm DE}a^{-3(1+w_0)}\exp\left(\frac{3w_a\left((a(n-1)-n)a^n+a\right)}{a(n-1)n}\right) \,; \end{aligned} \tag{88}$$

where w_0 is the value of $w_{\rm DE}$ for $a = 1$ and $n = 1$, while n encodes the time of maximum deviation from w_0 and w_a the extent of this deviation. For $n = 1$ this reduces to the usual CPL parametrization.
In code notation: $w_0 =$ `EFTw0`, $w_a =$ `EFTwa` and $n =$ `EFTwn`.

- The *turning point* parametrization [336]:

$$\begin{aligned} w_{\rm DE} &= w_0 + w_a\left(a_t - a\right)^2 \,, \\ \rho_{\rm DE} &= 3m_0^2H_0^2\Omega^0_{\rm DE}a^{-3\left(1+w_0+a_t^2w_a\right)}\exp\left(-\frac{3}{2}w_a(a-1)\left(1+a-4a_t\right)\right) \,, \end{aligned} \tag{89}$$

here w_0 is $w_{DE}(a = a_t)$ where a_t is the value of the scale factor at the turning point, and w_a is its time derivative. In code notation: $w_0 =$ `EFTw0`, $w_a =$ `EFTwa` and $a_t =$ `EFTwat`.

- The Taylor expansion around $a = 0$:

$$w_{\rm DE} = w_0 + w_a a + \frac{1}{2} w_2 a^2 + \frac{1}{6} w_3 a^3 \,,$$
$$\rho_{\rm DE} = 3 m_0^2 H_0^2 \Omega_{\rm DE}^0 a^{-3(1+w_0)} \cdot \exp\left((1-a)\left(3 w_a + \frac{3}{4} w_2 (a+1) + \frac{1}{6} w_3 (a^2+a+1) \right) \right) \,, \quad (90)$$

where w_2 and w_3 are respectively the 2nd and 3rd time derivatives of w_{DE}. In code notation: $w_0 =$ `EFTw0`, $w_a =$ `EFTwa`, $w_2 =$ `EFTw2` and $w_3 =$ `EFTw3`.

- User defined: the EFTCAMB code includes the possibility for the user to define his/her own DE equation of state parametrization and it will properly account for it in any calculation. Let us notice that this option can be safely chosen without any modification in the structure of the code if the parametrized form of $w_{\rm DE}$ is given as a function of the scale factor $a(\tau)$.

These definitions of $w_{\rm DE}$ are shared by the pure EFT and designer EFT modules and can be consistently used for both choices of model.

.2.6 EFTCAMB Perturbations Equations: Code Notation

Linear Scalar Perturbations

In this Section we write the relevant equations that EFTCAMB uses [59]. We write them in a compact notation that almost preserves the form of the standard equations simplifying both the comparison with the GR limit and the implementation in the code.
The dynamical equations that EFTCAMB evolves can be written[4] as:

$$A(\tau,k)\,\ddot{\pi} + B(\tau,k)\,\dot{\pi} + C(\tau)\,\pi + k^2\,D(\tau,k)\,\pi + H_0 E(\tau,k) = 0 \,, \quad (91)$$
$$k\dot{\eta} = \frac{1}{X}\left[\frac{1}{1+\Omega} \frac{a^2(\rho_{m,\nu} + P_{m,\nu})}{m_0^2} \frac{v_{m,\nu}}{2} + \frac{k^2}{3H_0} F + (U - X)\frac{\mathcal{Z} k^2}{3} \right] \,, \quad (92)$$

while constraint equations take the form:

$$\sigma = \frac{1}{X}\left[\mathcal{Z} U + \frac{1}{1+\Omega} \frac{3}{2k^2} \frac{a^2(\rho_{m,\nu} + P_{m,\nu})}{m_0^2} v_{m,\nu} + \frac{F}{H_0} \right] \,, \quad (93)$$
$$\dot{\sigma} = \frac{1}{X}\left[-2\mathcal{H}\,[1+V]\,\sigma + k\eta - \frac{1}{k} \frac{a^2 P_{m,\nu}}{m_0^2} \frac{\Pi_{m,\nu}}{1+\Omega} + \frac{N}{H_0} \right] \,, \quad (94)$$
$$\ddot{\sigma} = \frac{1}{X}\Bigg[-2\,(1+V)\left(\dot{\mathcal{H}}\sigma + \mathcal{H}\dot{\sigma} \right) - 2\mathcal{H}\sigma\dot{V} + k\dot{\eta} + \frac{1}{k} \frac{a\mathcal{H}\Omega'}{(1+\Omega)^2} \frac{a^2 P_{m,\nu}}{m_0^2} \Pi_{m,\nu} - \frac{1}{k(1+\Omega)} \frac{d}{d\tau}\left(\frac{a^2 P_{m,\nu}}{m_0^2} \Pi_{m,\nu} \right) - \dot{X}\dot{\sigma} + \frac{\dot{N}}{H_0} \Bigg] \,, \quad (95)$$

[4] Notice that working in the Jordan frame ensures that the energy-momentum conservation equations will not change with respect to their GR form. For this reason the evolution equations for density and velocity are not reported here.

$$\mathcal{Z} = \frac{1}{G}\left[\frac{k\eta}{\mathcal{H}} + \frac{1}{2\mathcal{H}(1+\Omega)k}\frac{a^2\delta\rho_{m,\nu}}{m_0^2} + \frac{L}{kH_0}\right], \tag{96}$$

$$\begin{aligned}\dot{\mathcal{Z}} =& \frac{1}{U}\left[-2\mathcal{H}\left[1+Y\right]\mathcal{Z} + k\eta - \frac{1}{1+\Omega}\frac{3}{2k}\frac{a^2\delta P_{m,\nu}}{m_0^2} - \frac{3}{2k(1+\Omega)}\frac{M}{H_0}\right], \\ =& \frac{1}{U}\Bigg[-2\mathcal{H}\mathcal{Z}\left(1+Y-\frac{G}{2}\right) - \frac{1}{2(1+\Omega)k}\frac{a^2\delta\rho_{m,\nu}}{m_0^2} - \frac{3}{2(1+\Omega)k}\frac{a^2\delta P_{m,\nu}}{m_0^2} \\ & - \frac{\mathcal{H}L}{H_0 k} - \frac{3}{2(1+\Omega)k}\frac{M}{H_0}\Bigg],\end{aligned} \tag{97}$$

where $2k\mathcal{Z} \equiv \dot{h}$ and $2k\sigma_* \equiv \dot{h} + 6\dot{\eta}$ are the standard CAMB variables. In these expressions we wrote the same prefactor, X, in eqs. (93) and (94), and U, in eqs. (93) and (97), but we have to stress that they might be different if other second order EFT operators are considered. In addition the last expression (97) has two forms: the first is the standard one while the second one is used when the CAMB code uses the RSA approximation.
At last, to compute the observable spectra we had to define two auxiliary quantities:

$$\begin{aligned}\texttt{EFTISW} =& \ddot{\sigma} + k\dot{\eta} \\ =& \frac{1}{X}\Bigg[-2\left[1+V\right]\left(\dot{\mathcal{H}}\sigma + \mathcal{H}\dot{\sigma}\right) - 2\mathcal{H}\sigma\dot{V} \\ & + \frac{(1+X)}{2(1+\Omega)X}\frac{a^2(\rho_{m,\nu}+P_{m,\nu})}{m_0^2}v_{m,\nu} + \frac{1}{k}\frac{a\mathcal{H}\Omega'}{(1+\Omega)^2}\frac{a^2P_{m,\nu}}{m_0^2}\Pi \\ & - \frac{1}{k(1+\Omega)}\frac{d}{d\tau}\left(\frac{a^2P_{m,\nu}}{m_0^2}\Pi_{m,\nu}\right) + \frac{(1+X)k^2}{3H_0X}F \\ & + \frac{(1+X)k^2}{3X}\mathcal{Z}(U-X) - \dot{X}\dot{\sigma} + \frac{\dot{N}}{H_0}\Bigg],\end{aligned} \tag{98}$$

$$\begin{aligned}\texttt{EFTLensing} =& \dot{\sigma} + k\eta \\ =& \frac{1}{X}\left[-2\mathcal{H}\left(1+V\right)\sigma + (1+X)k\eta - \frac{1}{k(1+\Omega)}\frac{a^2P_{m,\nu}}{m_0^2}\Pi_{m,\nu} + \frac{N}{H_0}\right].\end{aligned} \tag{99}$$

The coefficients for the π field equation, once a complete de-mixing is achieved, can not be divided into contributions due to one operator at a time so we write here their full form:

$$A = \frac{ca^2}{m_0^2} + 2a^2H_0^2\gamma_1 + \frac{3}{2}a^2\frac{\left(\mathcal{H}\Omega' + H_0\gamma_2\right)^2}{2(1+\Omega)+\gamma_3+\gamma_4} + 4\gamma_6k^2, \tag{100}$$

$$\begin{aligned}B =& \frac{\dot{c}a^2}{m_0^2} + 4\mathcal{H}\frac{ca^2}{m_0^2} + 8a^2\mathcal{H}H_0^2\left(\gamma_1 + a\frac{\gamma_1'}{4}\right) + 4k^2\mathcal{H}\left(2\gamma_6 + a\gamma_6'\right) \\ & + ak^2\frac{\gamma_4+2\gamma_5}{2(1+\Omega)-2\gamma_4}\left(\mathcal{H}\Omega' + H_0\gamma_2\right) \\ & - a\frac{\mathcal{H}\Omega' + H_0\gamma_2}{4(1+\Omega)+6\gamma_3+2\gamma_4}\Bigg[-3\frac{a^2(\rho_Q+P_Q)}{m_0^2} - 3a\mathcal{H}^2\Omega'\left(4 + \frac{\dot{\mathcal{H}}}{\mathcal{H}^2} + a\frac{\Omega''}{\Omega'}\right) \\ & - 3a\mathcal{H}H_0\left(4\gamma_2 + a\gamma_2'\right) - \left(9\gamma_3 - 3\gamma_4\right)\left(\dot{\mathcal{H}} - \mathcal{H}^2\right) + k^2\left(3\gamma_3 - \gamma_4 + 4\gamma_5\right)\Bigg]\end{aligned}$$

$$+\frac{1}{1+\Omega+2\gamma_5}\left(a\mathcal{H}\Omega'+2\mathcal{H}\left(\gamma_5+\gamma_5'\right)-(1+\Omega)\frac{a\mathcal{H}\Omega'+aH_0\gamma_2}{2(1+\Omega)+3\gamma_3+\gamma_4}\right)\cdot$$
$$\cdot\left[-\frac{a^2c}{m_0^2}+\frac{3}{2}a\mathcal{H}^2\Omega'-2a^2H_0\gamma_1-4\gamma_6k^2+\frac{3}{2}a\mathcal{H}H_0\gamma_2\right], \tag{101}$$

$$\begin{aligned}C=&\mathcal{H}\frac{\dot{c}a^2}{m_0^2}+\left(6\mathcal{H}^2-2\dot{\mathcal{H}}\right)\frac{ca^2}{m_0^2}+\frac{3}{2}a\mathcal{H}\Omega'\left(\ddot{\mathcal{H}}-2\mathcal{H}^3\right)+6\mathcal{H}^2H_0^2\gamma_1a^2\\
&+2a^2\dot{\mathcal{H}}H_0^2\gamma_1+8a^3\mathcal{H}^2H_0^2\frac{\gamma_1'}{4}+\frac{3}{2}\left(\dot{\mathcal{H}}-\mathcal{H}^2\right)^2(\gamma_4+3\gamma_3)\\
&+\frac{9}{2}\mathcal{H}H_0a\left(\dot{\mathcal{H}}-\mathcal{H}^2\right)\left(\gamma_2+a\frac{\gamma_2'}{3}\right)+\frac{a}{2}H_0\gamma_2\left(3\ddot{\mathcal{H}}-12\dot{\mathcal{H}}\mathcal{H}+6\mathcal{H}^3\right)\\
&-a\frac{\mathcal{H}\Omega'+H_0\gamma_2}{4(1+\Omega)+6\gamma_3+2\gamma_4}\Bigg[-3\frac{a^2\dot{P}_Q}{m_0^2}-3\mathcal{H}\left(\frac{a^2\rho_Q}{m_0^2}+\frac{a^2P_Q}{m_0^2}\right)\\
&-3a\mathcal{H}^3\left(a\Omega''+6\Omega'+2\frac{\dot{\mathcal{H}}}{\mathcal{H}^2}\Omega'\right)+3\left(\ddot{\mathcal{H}}-2\mathcal{H}\dot{\mathcal{H}}\right)(\gamma_4+3\gamma_3)\\
&+6\mathcal{H}\left(\dot{\mathcal{H}}-\mathcal{H}^2\right)\left(3\gamma_3+3a\frac{\gamma_3'}{2}+\gamma_4+a\frac{\gamma_4'}{2}\right)\\
&-3aH_0\left(3\mathcal{H}^2\gamma_2+\dot{\mathcal{H}}\gamma_2+a\mathcal{H}^2\gamma_2'\right)\Bigg]\\
&+\frac{1}{1+\Omega+2\gamma_5}\left(a\mathcal{H}\Omega'+2\mathcal{H}\left(\gamma_5+a\gamma_5'\right)-(1+\Omega)\frac{a\mathcal{H}\Omega'+aH_0\gamma_2}{2(1+\Omega)+3\gamma_3+\gamma_4}\right)\cdot\\
&\cdot\left[-\frac{1}{2}\frac{a^2\dot{\rho}_Q}{m_0^2}-\mathcal{H}\frac{a^2c}{m_0^2}+\frac{3}{2}a\mathcal{H}\Omega'\left(3\mathcal{H}^2-\dot{\mathcal{H}}\right)-2a^2\mathcal{H}H_0^2\gamma_1\right.\\
&\left.-\frac{3}{2}aH_0\gamma_2\left(\dot{\mathcal{H}}-2\mathcal{H}^2\right)-3\mathcal{H}\left(\dot{\mathcal{H}}-\mathcal{H}^2\right)\left(\frac{3}{2}\gamma_3+\frac{\gamma_4}{2}\right)\right],\end{aligned}$$

$$\begin{aligned}D=&\frac{ca^2}{m_0^2}-\frac{1}{2}a\mathcal{H}H_0\left(\gamma_2+a\gamma_2'\right)+\left(\mathcal{H}^2-\dot{\mathcal{H}}\right)(3\gamma_3+\gamma_4)+4\left(\dot{\mathcal{H}}\gamma_6+\mathcal{H}^2\gamma_6+a\mathcal{H}^2\gamma_6'\right)\\
&+2\left(\dot{\mathcal{H}}\gamma_5+a\mathcal{H}^2\gamma_5'\right)\\
&-a\frac{\mathcal{H}\Omega'+H_0\gamma_2}{4(1+\Omega)+6\gamma_3+2\gamma_4}\left[-2a\mathcal{H}\Omega'+4\mathcal{H}\gamma_5-2\mathcal{H}\left(3\gamma_3+3a\frac{\gamma_3'}{2}+\gamma_4+a\frac{\gamma_4'}{2}\right)\right]\\
&+\frac{1}{1+\Omega+2\gamma_5}\left(a\mathcal{H}\Omega'+2\mathcal{H}\left(\gamma_5+a\gamma_5'\right)-(1+\Omega)\frac{a\mathcal{H}\Omega'+aH_0\gamma_2}{2(1+\Omega)+3\gamma_3+\gamma_4}\right)\cdot\\
&\cdot\left[\frac{1}{2}a\mathcal{H}\Omega'-2\mathcal{H}\gamma_5+\frac{1}{2}aH_0\gamma_2+\frac{3}{2}\mathcal{H}\gamma_3+\mathcal{H}\frac{\gamma_4}{2}-4\mathcal{H}\gamma_6\right]\\
&+\frac{\gamma_4+2\gamma_5}{2(1+\Omega)-2\gamma_4}\left[\frac{a^2\left(\rho_Q+P_Q\right)}{m_0^2}+a\mathcal{H}^2\Omega'-\gamma_4\left(\dot{\mathcal{H}}-\mathcal{H}^2\right)\right.\\
&\left.+a\mathcal{H}H_0\gamma_2+3\gamma_3\left(\mathcal{H}^2-\dot{\mathcal{H}}\right)\right]+k^2\left[\frac{\gamma_3}{2}+\frac{\gamma_4}{2}+\frac{\gamma_4+2\gamma_5}{2(1+\Omega)-2\gamma_4}\left(\gamma_3+\gamma_4\right)\right],\end{aligned}$$

$$
\begin{aligned}
E =& \Bigg\{ \frac{ca^2}{m_0^2} - \frac{3}{2}a\mathcal{H}^2\Omega' - \frac{1}{2}a\mathcal{H}H_0\left(2\gamma_2 + a\gamma_2'\right) + \frac{1}{2}\gamma_3\left(k^2 - 3\dot{\mathcal{H}} + 3\mathcal{H}^2\right) \\
&+ \frac{1}{2}\gamma_4\left(k^2 - \dot{\mathcal{H}} + \mathcal{H}^2\right) - a\frac{\mathcal{H}\Omega' + H_0\gamma_2}{4(1+\Omega) + 6\gamma_3 + 2\gamma_4}\Bigg[- 2\mathcal{H}\left(a\Omega' + 2(1+\Omega)\right) \\
&- 2\mathcal{H}\left(3\gamma_3 + 3a\frac{\gamma_3'}{2} + \gamma_4 + a\frac{\gamma_4'}{2}\right)\Bigg] \\
&+ \frac{1}{1+\Omega+2\gamma_5}\left(a\mathcal{H}\Omega' + 2\mathcal{H}\left(\gamma_5 + a\gamma_5'\right) - (1+\Omega)\frac{a\mathcal{H}\Omega' + aH_0\gamma_2}{2(1+\Omega) + 3\gamma_3 + \gamma_4}\right)\cdot \\
&\cdot\left[\mathcal{H}\left(1 + \Omega + \frac{a\Omega'}{2}\right) + \frac{1}{2}aH_0\gamma_2 + \frac{3}{2}\mathcal{H}\gamma_3 + \frac{\mathcal{H}\gamma_4}{2}\right] \\
&+ \frac{\gamma_4 + 2\gamma_5}{2(1+\Omega) - 2\gamma_4}k^2\left(\gamma_4 + \gamma_3\right)\Bigg\} k\mathcal{Z} \\
&+ 3a\frac{\mathcal{H}\Omega' + H_0\gamma_2}{4(1+\Omega) + 6\gamma_3 + 2\gamma_4}\left(\frac{a^2\delta P_{m,\nu}}{m_0^2}\right) \\
&+ \frac{\gamma_4 + 2\gamma_5}{2(1+\Omega) - 2\gamma_4}k\left(\frac{a^2\left(\rho_{m,\nu} + P_{m,\nu}\right)v_{m,\nu}}{m_0^2}\right) \\
&- \frac{1}{2}\frac{1}{1+\Omega+2\gamma_5}\Bigg(a\mathcal{H}\Omega' + 2\mathcal{H}\left(\gamma_5 + a\gamma_5'\right) \\
&- (1+\Omega)\frac{a\mathcal{H}\Omega' + aH_0\gamma_2}{2(1+\Omega) + 3\gamma_3 + \gamma_4}\Bigg)\left(\frac{a^2\delta\rho_{m,\nu}}{m_0^2}\right) . \qquad (102)
\end{aligned}
$$

On the other hand the non-zero contributions to be added to the Einstein equations can be written for each operator separately and are listed in the following as $\Delta F, \Delta G, \Delta N, ...$ respectively.
We adopt the following convention: $F = \sum \Delta F$ and the same applies to all the other terms.

Background operators:

$$
\begin{aligned}
\Delta F =& \frac{3}{2k(1+\Omega)}\left[\frac{(\rho_Q + P_Q)a^2}{m_0^2}\pi + a\mathcal{H}\Omega'\left(\dot{\pi} + \mathcal{H}\pi\right)\right], \ [\mathrm{Mpc}^{-1}], \\
\Delta G =& \left(1 + \frac{a\Omega'}{2(1+\Omega)}\right), \ [\,] \\
\Delta L =& -\frac{3}{2}\frac{a\Omega'}{1+\Omega}(3\mathcal{H}^2 - \dot{\mathcal{H}})\pi - \frac{3}{2}\frac{a\Omega'}{1+\Omega}\mathcal{H}\dot{\pi} - \frac{1}{2}\frac{a\Omega'}{1+\Omega}k^2\pi \\
&+ \frac{\pi}{2\mathcal{H}(1+\Omega)}\frac{a^2\dot{\rho}_Q}{m_0^2} + \frac{\dot{\pi} + \mathcal{H}\pi}{\mathcal{H}(1+\Omega)}\frac{a^2 c}{m_0^2}, \ [\mathrm{Mpc}^{-2}] \\
\Delta M =& \frac{\dot{P}_Q a^2}{m_0^2}\pi + \frac{(\rho_Q + P_Q)a^2}{m_0^2}\left(\dot{\pi} + \mathcal{H}\pi\right) + a\mathcal{H}\Omega'\left[\ddot{\pi} + \left(\frac{\dot{\mathcal{H}}}{\mathcal{H}} + 4\mathcal{H} + a\mathcal{H}\frac{\Omega''}{\Omega'}\right)\dot{\pi}\right. \\
&\left. + \left(2\dot{\mathcal{H}} + 6\mathcal{H}^2 + a\mathcal{H}^2\frac{\Omega''}{\Omega'} + \frac{2}{3}k^2\right)\pi\right], \ [\mathrm{Mpc}^{-3}] \\
\Delta N =& -\frac{a\mathcal{H}\Omega'}{1+\Omega}k\pi, \ [\mathrm{Mpc}^{-2}] \\
\dot{N} =& -\frac{a\dot{\mathcal{H}}\Omega'}{1+\Omega}k\pi - \frac{a\mathcal{H}\Omega'}{1+\Omega}k\dot{\pi} - \frac{a\mathcal{H}^2}{(1+\Omega)}\left[\Omega' + a\Omega'' - \frac{a\Omega'^2}{1+\Omega}\right]k\pi, \ [\mathrm{Mpc}^{-3}] \\
\Delta X =& 1, \qquad \Delta\dot{X} = 0, \ [\,,\,]
\end{aligned}
$$

$$
\begin{aligned}
\Delta Y =& \frac{a\Omega'}{2(1+\Omega)}\,, \ [\,] \\
\Delta U =& 1, \ [\,] \\
\Delta V =& \frac{1}{2}\frac{a\Omega'}{1+\Omega}\,, \qquad \Delta\dot{V} = \frac{a\mathcal{H}}{2(1+\Omega)}\left[\Omega' + a\Omega'' - \frac{a\Omega'^{\,2}}{1+\Omega}\right] . \ [\,, \mathrm{Mpc}^{-1}]
\end{aligned}
\tag{103}
$$

$\underline{(\delta g^{00})^2}$:

$$
\Delta L = \frac{2a^2 H_0^2 \gamma_1}{\mathcal{H}\,(1+\Omega)}\,(\dot{\pi} + \mathcal{H}\pi)\ . \qquad [\mathrm{Mpc}^{-2}] \tag{104}
$$

$\underline{\delta g^{00}\delta K^\mu_\mu}$:

$$
\begin{aligned}
\Delta G =& \frac{aH_0\gamma_2}{2\mathcal{H}(1+\Omega)}\,, \ [\,] \\
\Delta F =& \frac{3}{2}aH_0\gamma_2\frac{\dot{\pi}+\mathcal{H}\pi}{k(1+\Omega)}\,, \ [\mathrm{Mpc}^{-1}] \\
\Delta L =& \frac{3}{2}\frac{aH_0\gamma_2}{1+\Omega}\left[\left(\frac{\dot{\mathcal{H}}}{\mathcal{H}} - 2\mathcal{H} - \frac{k^2}{3\mathcal{H}}\right)\pi - \dot{\pi}\right], \ [\mathrm{Mpc}^{-2}] \\
\Delta M =& aH_0\left[\gamma_2\ddot{\pi} + \left(4\gamma_2 + a\gamma_2'\right)\mathcal{H}\dot{\pi} + \left(3\mathcal{H}^2\gamma_2 + \dot{\mathcal{H}}\gamma_2 + a\mathcal{H}^2\gamma_2'\right)\pi\right] . \ [\mathrm{Mpc}^{-3}]
\end{aligned}
\tag{105}
$$

$\underline{(\delta K)^2}$:

$$
\begin{aligned}
\Delta G =& \frac{3}{2}\frac{\gamma_3}{1+\Omega}\,, \qquad [\,] \\
\Delta F =& +\frac{3}{2}\frac{\gamma_3}{1+\Omega}\left[k - 3\frac{\dot{\mathcal{H}}-\mathcal{H}^2}{k}\right]\pi\,, \ [\mathrm{Mpc}^{-1}] \\
\Delta L =& -\frac{3}{2}\frac{\gamma_3}{1+\Omega}\left[k^2 - 3\left(\dot{\mathcal{H}}-\mathcal{H}^2\right)\right]\pi\,, \ [\mathrm{Mpc}^{-2}] \\
\Delta M =& \gamma_3\left(3\mathcal{H}^2 - 3\dot{\mathcal{H}} + k^2\right)\dot{\pi} + \gamma_3\left(6\mathcal{H}^3 - 3\ddot{\mathcal{H}}\right)\pi \\
& + 2\mathcal{H}k^2\pi\left(\gamma_3 + a\frac{\gamma_3'}{2}\right) - 6a\mathcal{H}(\dot{\mathcal{H}}-\mathcal{H}^2)\frac{\gamma_3'}{2}\pi\,, \ [\mathrm{Mpc}^{-3}] \\
\Delta Y =& \frac{3}{2(1+\Omega)}\left(\gamma_3 + a\frac{\gamma_3'}{2}\right), \ [\,] \\
\Delta U =& \frac{3}{2}\frac{\gamma_3}{1+\Omega}\cdot[\,]
\end{aligned}
\tag{106}
$$

$\underline{\delta K^\mu_\nu \delta K^\nu_\mu}$:

$$
\begin{aligned}
\Delta G =& \frac{\gamma_4}{2(1+\Omega)}\,, \ [\,] \\
\Delta F =& +\frac{3\gamma_4}{2(1+\Omega)}k\pi - \frac{3\gamma_4}{2(1+\Omega)}\frac{\dot{\mathcal{H}}-\mathcal{H}^2}{k}\pi\,, \ [\mathrm{Mpc}^{-1}] \\
\Delta X =& -\frac{\gamma_4}{1+\Omega}\,, \qquad \Delta\dot{X} = -\frac{a\mathcal{H}}{1+\Omega}\left[\gamma_4' - \frac{\gamma_4\Omega'}{1+\Omega}\right], \ [\,, \mathrm{Mpc}^{-1}]
\end{aligned}
$$

$$
\begin{aligned}
\Delta L =& \frac{3\gamma_4}{2(1+\Omega)}\left(\dot{\mathcal{H}}-\mathcal{H}^2-\frac{k^2}{3}\right)\pi\,,\ [\mathrm{Mpc}^{-2}]\\
\Delta N =& \frac{2\mathcal{H}}{1+\Omega}\left(\gamma_4+a\frac{\gamma_4'}{2}\right)k\pi+\frac{\gamma_4}{1+\Omega}k\dot{\pi}\,,\ [\mathrm{Mpc}^{-2}]\\
\Delta \dot{N} =& \frac{\gamma_4 k\ddot{\pi}}{1+\Omega}+\frac{a\mathcal{H}k\dot{\pi}}{1+\Omega}\left[\gamma_4'-\frac{\gamma_4\Omega'}{1+\Omega}\right]+\frac{2k}{1+\Omega}\left(\gamma_4+a\frac{\gamma_4'}{2}\right)\left(\dot{\mathcal{H}}\pi+\mathcal{H}\dot{\pi}\right)\\
&+\frac{2a\mathcal{H}^2k\pi}{1+\Omega}\left[a\frac{\gamma_4''}{2}+3\frac{\gamma_4'}{2}-\frac{\Omega'}{1+\Omega}\left(\gamma_4+a\frac{\gamma_4'}{2}\right)\right]\,,\ [\mathrm{Mpc}^{-3}]\\
\Delta V =& -\frac{1}{1+\Omega}\left(\gamma_4+a\frac{\gamma_4'}{2}\right)\,,\ [\,]\\
\Delta \dot{V} =& -\frac{a\mathcal{H}}{1+\Omega}\left[a\frac{\gamma_4''}{2}+3\frac{\gamma_4'}{2}-\frac{\Omega'}{1+\Omega}\left(\gamma_4+a\frac{\gamma_4'}{2}\right)\right]\,,\ [\mathrm{Mpc}^{-1}]\\
\Delta Y =& \frac{1}{2(1+\Omega)}\left(\gamma_4+a\frac{\gamma_4'}{2}\right)\,,\ [\,]\\
\Delta M =& -\gamma_4\left(\dot{\mathcal{H}}-\mathcal{H}^2-\frac{k^2}{3}\right)\dot{\pi}-2\mathcal{H}\left(\gamma_4+a\frac{\gamma_4'}{2}\right)\left(\dot{\mathcal{H}}-\mathcal{H}^2-\frac{k^2}{3}\right)\pi\\
&-\gamma_4\left(\ddot{\mathcal{H}}-2\mathcal{H}\dot{\mathcal{H}}\right)\pi\,,\ [\mathrm{Mpc}^{-3}]\\
\Delta U =& \frac{\gamma_4}{2(1+\Omega)}\,.\,[\,]
\end{aligned}
\tag{107}
$$

$\underline{\delta g^{00}\delta R^{(3)}}$:

$$
\begin{aligned}
\Delta M =& -\frac{4\gamma_5 k^2}{3}\left(\dot{\pi}+\mathcal{H}\pi\right)\,,\ [\mathrm{Mpc}^{-3}]\\
\Delta N =& \frac{2\gamma_5 k}{1+\Omega}\left(\dot{\pi}+\mathcal{H}\pi\right)\,,\ [\mathrm{Mpc}^{-2}]\\
\Delta \dot{N} =& \frac{2\gamma_5 k}{1+\Omega}\left(\ddot{\pi}+\mathcal{H}\dot{\pi}+\dot{\mathcal{H}}\pi\right)+\frac{2ak\mathcal{H}}{1+\Omega}\left(\dot{\pi}+\mathcal{H}\pi\right)\left[\gamma_5'-\frac{\gamma_5\Omega'}{1+\Omega}\right]\,.\,[\mathrm{Mpc}^{-3}]
\end{aligned}
\tag{108}
$$

$\underline{(\mathrm{g}^{\mu\nu}+\mathrm{n}^{\mu}\mathrm{n}^{\nu})\partial_\mu\delta\mathrm{g}^{00}\partial_\nu\delta\mathrm{g}^{00}}$:

$$
\Delta L = \frac{4\gamma_6 k^2}{\mathcal{H}(1+\Omega)}\left(\dot{\pi}+\mathcal{H}\pi\right)\,.\,[\mathrm{Mpc}^{-2}] \tag{109}
$$

Linear Tensor Perturbations

The tensor component of the B-mode polarization of the CMB can be used to further constrain modifications of gravity [330, 6]. In this Section we write the relevant equation that EFTCAMB uses to build the tensor component of the CMB spectra. Since we are working in the Jordan frame only the propagation equation for tensor perturbations needs to be modified into:

$$
A_T(\tau)\ddot{h}_{ij}+B_T(\tau)\dot{h}_{ij}+D_T(\tau)k^2h_{ij}+E_{Tij}=0, \tag{110}
$$

where:

$$\begin{aligned} A_T =& 1+\Omega-\gamma_4\,, \\ B_T =& 2\mathcal{H}\left(1+\Omega-\gamma_4+\frac{a\Omega'}{2}-a\frac{\gamma_4'}{2}\right)\,, \\ D_T =& 1+\Omega\,, \\ E_{Tij} =& \frac{a^2}{m_0^2}\delta T_{ij}\,, \end{aligned} \tag{111}$$

and δT_{ij} contains the neutrinos and photons contribution to the tensor component of anisotropic stress.

.2.7 Viability Conditions

In this Section we list the viability priors that EFTCAMB naturally enforces on the EFT functions in order to ensure that the theory under consideration is stable. We separate these conditions in a set of physical ones and a set of mathematical ones, as described in the following. The full set of physical conditions for the general EFT action is a part of ongoing work. Here we report a preliminary version of them that contains the ghost and gradient stability for the subset of the EFT corresponding to GLPV theories [337], for which the mixing between the matter and gravity perturbations has been considered [176]. The full class of Horndeski models is included in these theories. Specifically, when $\gamma_3 = -\gamma_4$ and $\gamma_6 = 0$ (i.e. we consider GLPV theories) the kinetic and gradient stability conditions reduce respectively to

$$\tilde{W}_2\left[4\tilde{W}_1\tilde{W}_2-\tilde{W}_3^2\right]>0, \tag{112}$$

$$\begin{aligned} &\tilde{W}_0\tilde{W}_3^2+a\mathcal{H}\left(\tilde{W}_2\tilde{W}_3\tilde{W}_6'+\tilde{W}_6\tilde{W}_3\tilde{W}_2'-\tilde{W}_6\tilde{W}_2\tilde{W}_3'\right)+2\mathcal{H}\tilde{W}_3\tilde{W}_2\tilde{W}_6> \\ &\qquad \frac{9}{2}\tilde{W}_6^2\frac{a^2}{m_0^2}(\rho_m+P_m), \end{aligned} \tag{113}$$

where

$$\tilde{W}_0 = -(1+\Omega), \tag{114}$$

$$\tilde{W}_1 = \frac{ca^2}{m_0^2}+2H_0^2a^2\gamma_1-3\mathcal{H}^2(1+\Omega)-3a\mathcal{H}^2\Omega'+3\mathcal{H}^2\gamma_4-3aH_0\mathcal{H}\gamma_2, \tag{115}$$

$$\tilde{W}_2 = -3[(1+\Omega)-\gamma_4], \tag{116}$$

$$\tilde{W}_3 = 6\mathcal{H}(1+\Omega)+3a\mathcal{H}\Omega'-6\mathcal{H}\gamma_4+3aH_0\gamma_2, \tag{117}$$

$$\tilde{W}_6 = -4\left[\frac{1}{2}(1+\Omega)+\gamma_5\right], \tag{118}$$

$$\tilde{W}_2' = -3[\Omega'-\gamma_4'] \tag{119}$$

$$\begin{aligned} \tilde{W}_3' =& 6\frac{\dot{\mathcal{H}}}{a\mathcal{H}}(1+\Omega)+9\mathcal{H}\Omega'+3\frac{\dot{\mathcal{H}}}{\mathcal{H}}\Omega'+3a\mathcal{H}\Omega''-6\mathcal{H}\gamma_4' \\ &-6\frac{\dot{\mathcal{H}}}{a\mathcal{H}}\gamma_4+3aH_0\gamma_2'+3H_0\gamma_2 \end{aligned} \tag{120}$$

$$\tilde{W}_6' = -4\left[\frac{1}{2}\Omega'+\gamma_5'\right]. \tag{121}$$

Let us notice that for models characterized by $\gamma_3 \neq -\gamma_4$ and/or $\gamma_6 \neq 0$ the stability conditions need to be derived separately; while, the full set of perturbative equations evolved by EFTCAMB is still valid and can be used for a thorough investigation of linear perturbations, the derivation of the corresponding stability conditions is work in progress. Therefore, for these cases the user has to be careful in setting appropriate stability conditions for the chosen model. Hořava gravity belongs to this class of theories and in the current version of the code we implement specific stability conditions as explained in Section .2.12.

Along with the physical stability conditions discussed above, and that are work in progress, we have a set of mathematical stability conditions which guarantee that the perturbations in the dark sector are stable. They are turn off by default, but can be turned on by the user providing a second layer of protection from unhealthy models. They are imposed via the $\pi-$equation and we call them mathematical (or classical) stability conditions. Rewriting the π field equation as follows:

$$\begin{aligned}\left[A_1(\tau)+k^2A_2(\tau)\right]\,\ddot{\pi}+\left[B_1(\tau)+k^2B_2(\tau)\right]\,\dot{\pi}+C(\tau)\,\pi\\ +k^2\,\left[D_1(\tau)+k^2D_2(\tau)\right]\,\pi+H_0E(\tau,k)=0\,,\end{aligned}\tag{122}$$

the conditions that we impose read:

- $A_1+k^2A_2\neq 0$: well defined π field equation;
- No fast exponential growing of π field perturbations:
  - if $B^2-4(A_1+k^2A_2)(C+k^2D_1+k^4D_2)>0$ then:

$$\frac{\left[-B_1-k^2B_2\pm\sqrt{B^2-4(A_1+k^2A_2)(C+k^2D_1+k^4D_2)}\right]}{[2(A_1+k^2A_2)]}<H_0\tag{123}$$

  - if $B^2-4(A_1+k^2A_2)(C+k^2D_1+k^4D_2)<0$ then:

$$-\left[B_1+k^2B_2\right]/\left[2(A_1+k^2A_2)\right]<H_0\tag{124}$$

- $A_T\neq 0$: well defined tensor perturbations equation;

Let us notice that all the conditions based on scale dependent relations are enforced from $k=0$ up to $k=k_{max}$, where k_{max} is the maximum wavenumber that CAMB evolves.

Furthermore, we impose some additional priors on cosmological parameters. These are not related to the EFT framework and are used to help the code deal with very complicated models.

- *Cosmic acceleration prior*: the standard dark matter prior excludes $\Omega_{\rm dm}=0$ and dark matter is supposed to behave as a matter fluid. Dark energy is supposed to source cosmic acceleration. In this case we can safely impose that $w_{\rm DE}\leq -1/3$ at all times.
- *Dark Energy prior*: we impose the additional prior that $\Omega_{\rm DE}\geq 0$.

The EFTCAMB code allows the user to have full control over the prior that are enforced by means of a set of flags contained in the parameter file `params_EFT.ini` that will do the following:

- `EFT_mathematical_stability`: decides whether to enforce requirements of mathematical stability;
- `EFT_physical_stability`: establishes whether to use physical viability conditions;
- `EFTAdditionalPriors`: determines whether to use the additional priors on cosmological parameters;
- `MinkowskyPriors`: for some theories stability on Minkowsky background is known and leads to constraints on theory parameters. This flag decides whether to enforce them or not;

.2.8 Initial Conditions

We assume that DE perturbations are sourced by matter perturbations at a sufficiently early time so that the theory is close to GR and initial conditions can be taken to be:

$$\begin{aligned}\pi\left(\tau_\pi\right) &= -H_0\frac{E(\tau_\pi)}{C(\tau_\pi)+k^2D(\tau_\pi)}\,,\\ \dot{\pi}\left(\tau_\pi\right) &= H_0\left[\frac{E(\tau_\pi)}{(C(\tau_\pi)+k^2D(\tau_\pi))^2}(\dot{C}(\tau_\pi)+k^2\dot{D}(\tau_\pi))-\frac{\dot{E}(\tau_\pi)}{C(\tau_\pi)+k^2D(\tau_\pi)}\right],\end{aligned} \tag{125}$$

where τ_π is the time at which the code is switching from GR to DE/MG. This scheme is enforced here to speed up models that are too close to GR at early times.

Studying early DE/MG models requires the user to modify the flag `EFTturnonpiInitial` in `EFT_main.f90` to a suitable value. Its default value is set to be EFTturnonpiInitial=0.01. The initial conditions for matter components and curvature perturbations are set in the radiation dominated epoch ($a \sim 10^{-8}$).

.2.9 Pure EFT Models

In the *pure* EFT procedure once the background expansion history has been fixed, one has to specify the functional forms for the EFT functions. EFTCAMB allows to choose among several models. We write them here just for Ω but the same time dependence can be assumed for any other EFT function $\gamma_1, \ldots, \gamma_6$.

Constant models: $\Omega(a) = \Omega_0$;

Linear models: $\Omega(a) = \Omega_0 a$;

Power law models: $\Omega(a) = \Omega_0 a^s$;

Exponential models: $\Omega(a) = \exp(\Omega_0 a^s) - 1$.

The first option includes the minimal coupling, corresponding to $\Omega = 0$; the linear model can be thought of as a first order approximation of a Taylor expansion; while the power law is inspired by $f(R)$. There is also the possibility for the user to choose an arbitrary form of Ω/γ_i according to any ansätz the user wants to investigate, defining them as a function of the scale factor and by specifying their derivatives with respect to the scale factor. Of course the possibility to set all/some second order EFT functions to zero is included.

In the code we implemented a slot for user defined forms which can be easily spotted inside the file `EFT_main.f90`. Once the user defined form has been specified no other modifications to the code are required but numerical stability is not guaranteed. Notice also that due to the structure of our modification it is possible to use, inside the definition of the EFT functions, cosmological parameters like Ω_Λ and Ω_m.

Code notation for pure EFT models:

- Ω_0 = `EFTOmega0`, s = `EFTOmegaExp`;
- γ_1^0 = `EFTGamma10`, s = `EFTGamma1Exp`;
- γ_2^0 = `EFTGamma20`, s = `EFTGamma2Exp`;
- γ_3^0 = `EFTGamma30`, s = `EFTGamma3Exp`;
- γ_4^0 = `EFTGamma40`, s = `EFTGamma4Exp`;
- γ_5^0 = `EFTGamma50`, s = `EFTGamma5Exp`;
- γ_6^0 = `EFTGamma60`, s = `EFTGamma6Exp`.

Horndeski implementation into EFTCAMB

The Horndeski gravity [192] or Generalized Galileons (GG) [333] correspond to the most general scalar tensor theory with second order derivatives in the equations. As discussed in [173, 174] they are a subset of the models encompassed by the EFT framework which corresponds to the following conditions on the EFT functions (in terms of our convention):

$$2\gamma_5 = \gamma_3 = -\gamma_4\,, \quad \gamma_6 = 0 \tag{126}$$

Models belonging to this class can be implemented into EFTCAMB following three different procedures as we discuss in what follows.

- Pure EFT: if one is interested in investigating the general Horndeski class, rather than implementing a specific model within it, then one can opt to work directly with the four EFT functions that describe the Horndeski class in the EFT framework [174], i.e. $\{\Omega(a), \gamma_1(a), \gamma_2(a), \gamma_3(a)\}$, after an expansion history has been chosen ($w_{\rm DE}$). In this case one has to parametrize the dependence of the EFT functions on time instead of specifying the functions (K, G_i). The limit of this procedure is that the user loses information about the corresponding theory as an inverse machinery to reconstruct the Horndeski functions $(K, G_i)[\phi, X]$ is not possible to implement.

- EFT implementation of the parametrization proposed in [160]; the latter is a parametrization of Horndeski theory in terms of five functions of time which are chosen to correspond to specific physical properties of the scalar d.o.f.. Let us notice that it is equivalent to the pure EFT approach, and hence it shares the same limit mentioned above, while perhaps being closer to the phenomenology and the observables in the specific choice of the five functions. See Section .2.11 for details.

- Full/designer Mapping approaches: one starts from a specific Horndeski/GG model, i.e. from a choice of the 4 unknown functions $(K, G_i)[\phi, X]$ (where $i = 3, 4, 5$ and $x \equiv -\partial_\mu\phi\partial^\mu\phi/2$) and in the case of designer mapping by specifying also the expansion history, i.e. $w_{\rm DE}$; proceeds solving the background field equations for this model and then, through the mapping described in [173, 174], reconstructs the corresponding EFT functions. At this point EFTCAMB has all the ingredients to evolve linear perturbations. This approach emphasizes the choice of a specific theory and its implementation in EFTCAMB is work in progress.

Here we will focus on the pure EFT approach leaving the other options to the specific Sections. To use the code using the EFT approach restricted to Horndeski case, the user has to change the flag `PureEFTHorndeski` setting it to true. Once this has been done, the code will automatically restrict the number of the involved second order EFT functions according to eq. (126). This condition will internally fix the behaviour of the EFT functions γ_4, γ_5 and γ_6 so that the corresponding choices and parameters for these functions will be ignored. At this point the user can choose according to the model he/she wants to investigate, the behaviours of the three remaining EFT functions $\{\gamma_1, \gamma_2, \gamma_3\}$ and $\{\Omega, w_{DE}\}$ to fix the background. Built-in models for these functions are already present in the code, see Section .2.9, as well as the possibility to implement the user own model.

.2.10 Designer Mapping EFT Models

The EFT framework allows to study a specific single field DE/MG model once the mapping into the EFT language is known. We refer the reader to [162, 163, 173, 174] for a complete list of the theories that can be cast in the EFT framework and for an exhaustive theoretical treatment of models already mapped in this language.

Once the user chooses the model of interest, a model-dependent flag solves the corresponding background equations for a given expansion history (ΛCDM, wCDM or CPL). Then, using the mapping into the EFT formalism, it reconstructs the corresponding EFT functions and, finally, has all the ingredients to evolve the full dynamical EFT perturbed equations. Notice that in this case all the EFT functions are completely specified by the choice of the model and once the background equations are solved. In the current version, EFTCAMB includes flags for $f(R)$ models and minimally coupled quintessence. The background equations are solved through the use of the designer approach specific to $f(R)$ [249, 251] (see the following Subsection for implementation details). In the future, new flags implementing the background equations and the mapping for

other DE/MG models of interest that are included in the EFT formalism will be added. A detailed diagram of the *mapping* EFT case is shown in Figure 10.

Designer $f(R)$

We consider the following action in Jordan frame

$$S = \int d^4x\sqrt{-g}\,(R + f(R)) + S_m, \tag{127}$$

where f is a generic function of the Ricci scalar, R, and S_m indicates the action for matter fields which, in this frame, are minimally coupled to gravity. $f(R)$ models can be mapped into the EFT language via the following relations [162]:

$$\Lambda(t) = \frac{m_0^2}{2}\left[f - Rf_R\right] \quad ; \quad c(t) = 0 \quad ; \quad \Omega(t) = f_R, \tag{128}$$

where $f_R \equiv \frac{df}{dR}$.

It is well known that given the higher order nature of $f(R)$ gravity, there is enough freedom to reproduce any desired expansion history. When dealing with perturbations, it is common to adopt the *designer* approach which consists in fixing the expansion history and solving the Friedman equation as a second order differential equation in $\ln a$ for the function $f[R(a)]$ [249, 251]. This procedure yields, for each chosen background, a family of $f(R)$ models that can be labelled by the value of $f_R \equiv df/dR$ today, or analogously, by the present value of the mass scale of the scalaron

$$B \equiv \frac{f_{RR}}{1 + f_R}\frac{\mathcal{H}\dot{R}}{\dot{\mathcal{H}} - \mathcal{H}^2}, \tag{129}$$

One further needs to impose certain viability conditions on the resulting models in order to have stable and viable cosmologies [251]. We refer the reader to [249, 251] for the details of the designer approach to $f(R)$ models. In the following Subsection we shall present some of the technical aspects of its implementation in EFTCAMB.

Following [251], let us define the dimensionless quantities:

$$y \equiv \frac{f(R)}{H_0^2}, \qquad E \equiv \frac{H^2}{H_0^2}, \qquad \frac{R}{H_0^2} \equiv 3\left(4E + E'\right), \qquad E_{m,r} \equiv \frac{\rho_{m,r}}{\rho_c^0}, \tag{130}$$

where $\rho_c^0 \equiv 3H_0^2M_P^2$ is the critical density today and, *in this Section only, primes indicate derivation with respect to* $\ln a$ (to be not confused with the primes indicating derivatives with respect to a in the previous Sections).

Furthermore, let us introduce an effective energy density, $E_{\rm eff}$, and an effective equation of state, $w_{\rm eff}$, which allow one to set the desired expansion history:

$$\begin{aligned} E &\equiv E_m + E_r + E_{\rm eff} \\ E_{\rm eff} &= \Omega_{DE}\exp\left[-3x + 3\int_a^1 w_{\rm eff}(\tilde{a})d\ln\tilde{a}\right]. \end{aligned} \tag{131}$$

In terms of these dimensionless quantities the scalaron mass scale reads:

$$B = \frac{2}{3(1+f_R)}\frac{1}{4E'+E''}\frac{E}{E'}\left(y'' - y'\frac{4E''+E'''}{4E'+E''}\right) . \tag{132}$$

The designer approach will then consist in choosing one of the expansion histories in Section .2.5 and solving the following equation for $y(x)$

$$y'' - \left(1 + \frac{E'}{2E} + \frac{R''}{R'}\right)y' + \frac{R'}{6H_0^2 E}y = -\frac{R'}{H_0^2 E}E_{\rm eff} , \tag{133}$$

with appropriate boundary conditions that allow us to select the growing mode, as described in [251]. The outcome will be a family of models labelled by the present day value, B_0, of (132).
In order to implement eq. (133) in the code we need to define the following quantities:

$$\begin{aligned} E_{\rm eff} \equiv \Omega_\Lambda e^{-3g(x)} \;\Rightarrow\; g(x) &= \int_1^{e^x} \frac{1+w_{\rm DE}(\tilde{a})}{\tilde{a}} d\tilde{a} , \\ g'(x) &= 1 + w_{\rm DE} , \\ g''(x) &= e^x \frac{dw_{\rm DE}}{da} , \\ g^{(3)}(x) &= e^x \frac{dw_{\rm DE}}{da} + e^{2x}\frac{d^2 w_{\rm DE}}{da^2} , \end{aligned} \tag{134}$$

where we have introduced the variable $x \equiv \ln a$. These definitions allow us to rewrite $E(x)$ and its derivatives as follows:

$$\begin{aligned} E' =& -3\Omega_m e^{-3x} - 4\Omega_r e^{-4x} - 3\Omega_\Lambda e^{-3g(x)} g'(x) , \\ E'' =& 9\Omega_m e^{-3x} + 16\Omega_r e^{-4x} - 3\Omega_\Lambda e^{-3g(x)}\left(g''(x) - 3g'(x)^2\right) , \\ E''' =& -27\Omega_m e^{-3x} - 64\Omega_r e^{-4x} - 3\Omega_\Lambda e^{-3g(x)}\left(g^{(3)}(x) - 9g'(x)g''(x) + 9g'(x)^3\right) . \end{aligned} \tag{135}$$

Let us notice that massive neutrinos are consistently implemented in the designer approach. For a detailed treatment of their inclusion in the above equations we refer the user to [5] and references therein for an historical background. Once we have solved the background according to the above procedure, there remains only to map the solution into the EFT language. To this extent we have:

$$\Omega(a) \equiv f_R(a) = \frac{y'}{3(4E'+E'')} . \tag{136}$$

For the code purposes we need also the derivatives of this function with respect to a, and it turns useful to input their analytical expressions directly in the code, rather than having the code evaluate them numerically. We have:

$$
\begin{aligned}
\frac{d\Omega}{da} =& \frac{e^{-x}\left(-E''(6E_{\rm eff}+y)+E'\left(y'-4(6E_{\rm eff}+y)\right)+2Ey'\right)}{6E\left(E''+4E'\right)}\,,\\
\frac{d^2\Omega}{da^2} =& \frac{e^{-2x}}{12E^2\left(E''+4E'\right)}\Bigg(E'\left(E'\left(24E_{\rm eff}-y'+4y\right)-6E\left(8E'_{\rm eff}+y'\right)\right)\\
&+E''\left(E'(6E_{\rm eff}+y)-12EE'_{\rm eff}\right)\Bigg)\,,\\
\frac{d^3\Omega}{da^3} =& \frac{e^{-3x}}{24E^3\left(E''+4E'\right)}\Bigg[2E\Bigg(E''^{\,2}(6E_{\rm eff}+y)+4E'^{\,2}\left(18E'_{\rm eff}+6E_{\rm eff}+2y'+y\right)\\
&+E'E''\left(18E'_{\rm eff}+30E_{\rm eff}-y'+5y\right)\Bigg)+12E^2\Bigg(E''\left(-2E''_{\rm eff}+4E'_{\rm eff}-y'\right)\\
&+E'\left(-8E''_{\rm eff}+16E'_{\rm eff}+y'\right)\Bigg)\\
&+3E'^{\,2}\left(E'\left(y'-4(6E_{\rm eff}+y)\right)-E''(6E_{\rm eff}+y)\right)\Bigg]\,.
\end{aligned}
\tag{137}
$$

At this point, having $H(a)$ and $\Omega(a)$ at hand, one can go back to the general treatment of the background in the EFT formalism (setting $w_{\rm DE}=w_{\rm eff}$), and use the designer EFT described in Section .2.10 to determine c and Λ. However, for a matter of numerical accuracy, it is better to determine these functions via the mapping too. We have:

$$
\begin{aligned}
\frac{ca^2}{m_0^2} =& 0, \qquad \frac{\dot{c}a^2}{m_0^2}=0\,,\\
\frac{\Lambda a^2}{m_0^2} =& a^2\frac{\mathcal{H}_0^2}{2}\left[y-3f_R\left(4E+E'\right)\right]\,, \qquad \frac{\dot{\Lambda}a^2}{m_0^2}=-\frac{3}{2}\mathcal{H}_0^2\,\mathcal{H}\left[a^3\frac{d\Omega}{da}\left(4E+E'\right)\right]\,.
\end{aligned}
\tag{138}
$$

The user can select the designer-f(R) model by setting `mappingEFTmodel=1` in the designer flag (`EFTflag=2`) as described earlier (see Section .2.4).

Designer minimally coupled quintessence models

Minimally coupled quintessence models correspond to setting all the EFT functions Ω and γ's to zero, while using an effective dark energy equation of state different from -1.
These models are specified by the action:

$$
S=\int d^4x\sqrt{-g}\left[\frac{m_0^2}{2}R-\frac{(\nabla\phi)^2}{2}-V(\phi)\right]\,,
\tag{139}
$$

and can be mapped into the EFT framework by [162, 163]:

$$
\begin{aligned}
c(\tau) =& \frac{1}{2a^2}\dot{\phi}_0^2\,,\\
\Lambda(\tau) =& \frac{1}{2a^2}\dot{\phi}_0^2-V\left(\phi_0(\tau)\right)\,,
\end{aligned}
\tag{140}
$$

where ϕ_0 is the background value of the quintessence field and $V(\phi_0)$ is the quintessence potential.
It can be shown that fixing the background expansion history by a designer approach results in:

$$\begin{aligned} \frac{ca^2}{m_0^2} &= \frac{1}{2}\frac{a^2\rho_{\rm DE}}{m_0^2}(1+w_{\rm DE})\,, & [{\rm Mpc}^{-2}] \\ \frac{\Lambda a^2}{m_0^2} &= w_{\rm DE}\frac{a^2\rho_{\rm DE}}{m_0^2}\,, & [{\rm Mpc}^{-2}] \end{aligned} \tag{141}$$

and their time derivatives can be read from equation (77).

The user can select the minimally coupled quintessence models by setting `mappingEFTmodel=2` in the designer flag (`EFTflag=2`) as described earlier (see Section .2.4). Once this has been done, the user has to choose only the behaviour of $w_{\rm DE}$.

.2.11 Alternative Parametrizations

Besides the EFT approach, in literature there are several alternative model-independent parametrizations which allow to describe possible departures from General Relativity which come from a modification at the level of the action or directly by parametrizing the field equations by introducing new functions or parameters. Due to the versatility of the EFT approach and to the large number of DE/MG models that can be described within this framework, it is possible to completely cast most of these model-independent parametrizations in terms of EFT functions. In this Section we will gradually implement the technical details of such alternative parametrizations.

RPH: ReParametrized Horndeski

As already discussed, there are three ways to implement the Horndeski/GG theory in EFTCAMB (See Section .2.9). In the following we want to focus on the implementation of the parametrization proposed in [160], which is a built-in feature of the latest release (v2.0). Hereafter we will refer to this parametrization as ReParametrized Horndeski (RPH) as it is a model-independent parametrization of Horndeski theory in terms of five functions of time defined in such a way that they correspond to specific physical properties of the scalar d.o.f.. They correspond to the expansion history (in terms of $w(a)$) and four functions of time $\{\tilde{M}, \alpha_K, \alpha_B, \alpha_T\}$. There is a fifth function, which is not independent but can be derived from $\tilde{M}$ and whose expression reads $\alpha_M = a\tilde{M}'/(1+\tilde{M})$. As it will be clear in the following, RPH is equivalent to the pure EFT approach.

As described in [160] the correspondence between these functions and the EFT ones is (in our convention):

$$\begin{aligned} \frac{M_*^2}{m_0^2} = 1+\tilde{M} &= 1+\Omega+\gamma_3\,, \\ \alpha_K &= \frac{\frac{2ca^2}{m_0^2}+4H_0^2\gamma_1 a^2}{(1+\Omega+\gamma_3)\mathcal{H}^2}\,, \end{aligned}$$

$$\begin{aligned}\alpha_B &= +\frac{1}{2}\frac{a\gamma_2 H_0 + a\mathcal{H}\Omega'}{\mathcal{H}(1+\Omega+\gamma_3)}\,,\\ \alpha_T &= -\frac{\gamma_3}{1+\Omega+\gamma_3}\,.\end{aligned} \tag{142}$$

Notice that we have redefined $\frac{M_*^2}{m_0^2} = 1+\tilde{M}$ for numerical reasons.
To implement this parametrization into EFTCAMB we need first to invert the previous definitions in order to calculate $\{\Omega, \gamma_1\gamma_2, \gamma_3\}$ as functions of $\{\tilde{M}, \alpha_K, \alpha_B, \alpha_T\}$:

$$\begin{aligned}\Omega(a) &= (1+\tilde{M})\alpha_T + \tilde{M}\,,\\ \gamma_1(a) &= \frac{1}{4H_0^2a^2}\left[\alpha_K(1+\tilde{M})\mathcal{H}^2 - \frac{2ca^2}{m_0^2}\right]\,,\\ \gamma_2(a) &= \frac{1}{aH_0}\left[+2\alpha_B\mathcal{H}(1+\tilde{M}) - a\mathcal{H}\Omega'\right]\,,\\ \gamma_3(a) &= -\alpha_T(1+\tilde{M})\,,\\ \gamma_4(a) &= -\gamma_3\,.\end{aligned} \tag{143}$$

Then we can compute the following derived quantities that are needed for the equations in the code:

$$\begin{aligned}\Omega'(a) &= \tilde{M}\alpha_T' + \tilde{M}'(\alpha_T+1)\,,\\ \Omega''(a) &= 2\tilde{M}'\alpha_T' + \tilde{M}\alpha_T'' + \tilde{M}''(\alpha_T+1)\,,\\ \Omega'''(a) &= 3\tilde{M}''\alpha_T' + 3\tilde{M}'\alpha_T'' + \tilde{M}\alpha_T''' + \tilde{M}'''(\alpha_T+1)\,,\\ \gamma_1'(a) &= -\frac{2}{a}\gamma_1 + \frac{1}{4H_0^2a^2}\left[\alpha_K'(1+\tilde{M})\mathcal{H}^2 + \alpha_K\tilde{M}'\mathcal{H}^2 + 2\alpha_K(1+\tilde{M})\frac{\dot{\mathcal{H}}}{a} - \frac{2c'a^2}{m_0^2} - \frac{4ca}{m_0^2}\right]\,,\\ \gamma_2'(a) &= -\frac{\gamma_2}{2} - \frac{1}{aH_0}\left[-2(1+\tilde{M})(\alpha_B'\mathcal{H} + \alpha_B\frac{\dot{\mathcal{H}}}{a\mathcal{H}}) - 2\alpha_B\mathcal{H}\tilde{M}' + \mathcal{H}\Omega' + \frac{\dot{\mathcal{H}}}{\mathcal{H}}\Omega' + a\mathcal{H}\Omega''\right]\,,\\ \gamma_3'(a) &= -(1+\tilde{M})\alpha_T' - \alpha_T\tilde{M}'\,,\\ \gamma_4(a) &= -\gamma_3\,,\\ \gamma_4'(a) &= -\gamma_3'\,,\\ \gamma_4''(a) &= -\gamma_3'' = (1+\tilde{M})\alpha_T'' + 2\alpha_T'\tilde{M}' + \alpha_T\tilde{M}''\,,\\ \gamma_5(a) &= \frac{\gamma_3}{2}\,,\\ \gamma_5'(a) &= \frac{\gamma_3'}{2}\,,\\ \gamma_6(a) &= 0\,,\\ \gamma_6'(a) &= 0\,.\end{aligned} \tag{144}$$

To use the RPH parametrization of Horndeski models, one has to set `EFTflag=3` as described earlier (see Section .2.4) and then choose `AltParEFTmodel=1`. Once this has been done, the user has to choose the behaviour for the four RPH functions of time $\{\tilde{M}, \alpha_K, \alpha_B, \alpha_T\}$ by acting on the `RPHmassPmodel`, `RPHkineticitymodel`, `RPHbraidingmodel` and `RPHtensormodel` flags and for the expansion history by choosing w_{DE}. The built-in models allow to choose a constant (e.g.: $\alpha_K = \alpha_K^0$) and power law (e.g.: $\alpha_K = \alpha_K^0\, a^s$), or the user can define by him/herself the

behaviours for the respective functions according to the model he/she wants to investigate. The name of the parameters are then specified by:

- $\tilde{M}_0 =$ `RPHmassP0`, $s =$ `RPHmassPexp`;
- $\alpha_K^0 =$ `RPHkineticity0`, $s =$ `RPHkineticityexp`;
- $\alpha_B^0 =$ `RPHbraiding0`, $s =$ `RPHbraidingexp`;
- $\alpha_T^0 =$ `RPHtensor0`, $s =$ `RPHtensorexp`;

By running parameter space explorations of these models we noticed that the viability priors [160] are particularly aggressive so we suggest to have some ideas of the parameter space of these models before studying them.

.2.12 Full EFT Mapping

As already discussed, the EFT framework offers a unifying language for all single field models of DE and MG; once a given model is mapped into the EFT language, i.e. the corresponding EFT functions are determined, one does not need to derive lengthy perturbation equations specific for that model. Rather, the general perturbation equations for the EFT action, which are implemented in EFTCAMB, can be used. All the necessary input are the background evolution and the EFT functions as functions of the scale factor. There are two ways in which the latter can be determined: via the designer approach discussed in the previous Section, or solving for the background evolution of the given model, determining the Hubble parameter and the time evolution of the EFT functions. Once these are worked out, they are passed to the main code which solves the full perturbative equations.

The users can choose this branch by setting `EFTflag=4`. The current built-in model is low-energy Hořava gravity, implemented as described in [3], which can be selected by choosing `FullMappingEFTmodel=1`.

Low-energy Hořava gravity

A thorough discussion of the theory considered and analysis of its cosmological implications via EFTCAMB can be found in [3]. Here we will report the action and few important details about its implementation in the code. The action that we consider corresponds to the low-energy Hořava gravity [310]

$$\mathcal{S} = \frac{m_0^2}{(2\xi - \eta)} \int d^4x \sqrt{-g} \left[K_{ij} K^{ij} - \lambda K^2 - 2\xi \bar{\Lambda} + \xi \mathcal{R} + \eta a_i a^i \right] \tag{145}$$

where K_{ij} and K are the extrinsic curvature and its trace and $\mathcal{R}$ is the Ricci scalar of the three-dimensional space-like hypersurfaces. The coefficients λ, η, ξ are running coupling constants, while $\bar{\Lambda}$ is the "bare" cosmological constant, $a_i \equiv \partial_i \ln N$ being N the lapse function in the ADM formalism. Let us now introduce the following definitions useful for numerical computations

$$\tilde{\xi} = \xi - 1 \quad ; \quad \tilde{\lambda} = \lambda - 1 \tag{146}$$

Action (145) can be mapped in EFT formalism as follows [3]

$$
\begin{aligned}
&\Omega = \frac{\eta}{2+2\tilde{\xi}-\eta} \ ; \ \Omega' = \Omega'' = \Omega''' = 0, \\
&\gamma_1 = \frac{1}{2H_0^2 a^2}\frac{2\tilde{\xi}-3\tilde{\lambda}}{(2+2\tilde{\xi}-\eta)}\left(\dot{\mathcal{H}}-\mathcal{H}^2\right) \ , \\
&\gamma_1' = \frac{1}{2H_0^2 a^3}\frac{2\tilde{\xi}-3\tilde{\lambda}}{(2+2\tilde{\xi}-\eta)}\left(\frac{\ddot{\mathcal{H}}}{\mathcal{H}}-4\dot{\mathcal{H}}+2\mathcal{H}^2\right), \\
&\gamma_2 = 0 \ ; \ \gamma_2' = \gamma_2'' = 0, \\
&\gamma_3 = 2\frac{\tilde{\lambda}-\tilde{\xi}}{(2+2\tilde{\xi}-\eta)} \ ; \ \gamma_3' = \gamma_3'' = 0, \\
&\gamma_4 = \frac{2\tilde{\xi}}{(2+2\tilde{\xi}-\eta)} \ ; \ \gamma_4' = \gamma_4'' = 0, \\
&\gamma_5 = 0 \ ; \ \gamma_5' = \gamma_5'' = 0, \\
&\gamma_6 = \frac{\eta}{4(2+2\tilde{\xi}-\eta)} \ ; \ \gamma_6' = \gamma_6'' = 0, \\
&\frac{ca^2}{m_0^2} = -\frac{2\tilde{\xi}-3\tilde{\lambda}}{(2+2\tilde{\xi}-\eta)}\left(\dot{\mathcal{H}}-\mathcal{H}^2\right), \\
&\frac{\dot{c}a^2}{m_0^2} = -\frac{2\tilde{\xi}-3\tilde{\lambda}}{(2+2\tilde{\xi}-\eta)}\left(\ddot{\mathcal{H}}-4\mathcal{H}\dot{\mathcal{H}}+2\mathcal{H}^3\right), \\
&\frac{\Lambda a^2}{m_0^2} = -3\left(\Omega_{DE}^0-1+\frac{3\tilde{\lambda}+2}{2\tilde{\xi}+2-\eta}\right)H_0^2a^2 - 2\frac{2\tilde{\xi}-3\tilde{\lambda}}{(2+2\tilde{\xi}-\eta)}\left(\frac{\mathcal{H}^2}{2}+\dot{\mathcal{H}}\right), \\
&\frac{\dot{\Lambda}a^2}{m_0^2} = -2\frac{2\tilde{\xi}-3\tilde{\lambda}}{(2+2\tilde{\xi}-\eta)}\left(\ddot{\mathcal{H}}-\mathcal{H}\dot{\mathcal{H}}-\mathcal{H}^3\right).
\end{aligned}
\tag{147}
$$

The background of Hořava gravity is fully solved without imposing *a priori* any condition. In detail, we implemented in EFTCAMB and solved the following equation which describes the background evolution:

$$
\mathcal{H}^2 = \frac{(2\tilde{\xi}+2-\eta)}{3\tilde{\lambda}+2}a^2\left\{\frac{8\pi G_N}{3}(\rho_m+\rho_\nu)+\left[\Omega_{DE}^0-1+\frac{3\tilde{\lambda}+2}{2\tilde{\xi}+2-\eta}\right]H_0^2\right\} \tag{148}
$$

where we have used the following relation

$$
\bar{\Lambda} = 3\frac{2\xi-\eta}{2\xi}\left[\Omega_{DE}^0-1+\frac{3\lambda-1}{2\xi-\eta}\right]H_0^2, \tag{149}
$$

to eliminate the $\bar{\Lambda}$ parameter from the evolution equation in favour of Ω_{DE}^0. As usual the density of the massive neutrinos is implemented as explained in [5]. Moreover, we also computed the derivatives of the Hubble function:

$$
\begin{aligned}
\mathcal{H}^2 =& \frac{(2\tilde{\xi}+2-\eta)}{3\tilde{\lambda}+2}a^2\left\{\frac{8\pi G_N}{3}(\rho_m+\rho_\nu)+\left[\Omega_{DE}^0-1+\frac{3\tilde{\lambda}+2}{2\tilde{\xi}+2-\eta}\right]H_0^2\right\} \\
\dot{\mathcal{H}} =& -\frac{(2\tilde{\xi}+2-\eta)}{3\tilde{\lambda}+2}a^2\Bigg[-\left(\Omega_{DE}^0-1+\frac{3\tilde{\lambda}+2}{2\tilde{\xi}+2-\eta}\right)H_0^2
\end{aligned}
$$

$$+\frac{4\pi G_N}{3}(3P_\nu+\rho_\nu)+\frac{4\pi G_N}{3}(1+3w_m)\rho_m\Bigg]$$
$$\ddot{\mathcal{H}}=-\frac{(2\tilde{\xi}+2-\eta)}{3\tilde{\lambda}+2}a^2\Bigg[-2\left(\Omega^0_{DE}-1+\frac{3\tilde{\lambda}+2}{2\tilde{\xi}+2-\eta}\right)H_0^2\mathcal{H}$$
$$+\frac{8\pi G_N}{3}\left(\frac{3}{2}P_\nu\mathcal{H}-\frac{1}{2}\rho_\nu\mathcal{H}+\frac{3}{2}\dot{P}_\nu\right)-\frac{4\pi G_N\mathcal{H}}{3}(1+6w_m+9w_m^2)\rho_m\Bigg]. \tag{150}$$

Hořava gravity belongs to the class of theory for which EFTCAMB has not yet the appropriate general stability conditions, therefore for this model we implemented the stability conditions found in [3] which, in code notation, read:

$$\tilde{\lambda}>0 \qquad 0<\eta<2\tilde{\xi}+2. \tag{151}$$

These conditions are imposed by default and they become viability priors when using EFTCosmoMC.

To investigate the low-energy Hořava gravity, the user has to set `EFTflag=4` as described earlier (see Section .2.4) and then choose `FullmappingEFTmodel=1`. At this point the user can study the model for which all the three parameters appearing in the action can vary. If one is interested in investigating the case for which the theory evades the Solar System constraints the user has to set `HoravaSolarSystem=2`. For details about the physics of the two models see [3].

Point	$[x_c, y_c, u_c, \alpha_{0,c}, \alpha_{1,c}]$	Stability	$\Omega_{\rm DE}$	$w_{\rm eff}$
P_{1a}	$[0,0,0,0,0]$	**Saddle point:** $\lambda_0 \neq 3 \wedge \alpha_2 \neq \frac{3}{2}$	0	0
P_{1b}	$\left[0,0,0,0,\alpha_2-\frac{3}{2}\right]$	**Saddle point:** $\lambda_0 \neq 3 \wedge \alpha_2 \neq \frac{3}{2} \wedge \alpha_2 \neq 3$	0	0
P_{2a}	$[1,0,0,0,0]$	**Unstable node:** $\alpha_2 < 3 \wedge \lambda_0 < 6$ **Saddle point:** otherwise	1	1
P_{2b}	$[1,0,0,0,-3+\alpha_2]$	**Unstable node:** $3 < \alpha_2 < 6 \wedge \lambda_0 < 6$ **Saddle point:** otherwise	1	1
P_{3a}	$\left[\frac{\lambda_0}{6}, 1-\frac{\lambda_0}{6}, 0, 0, 0\right]$	**Stable node:** $(\alpha_2 \geq 0 \wedge \lambda_0 < 0) \vee (\alpha_2 < 0 \wedge \lambda_0 < 2\alpha_2)$, **Unstable node:** $(\lambda_0 > 6 \wedge \alpha_2 < 3) \vee (\lambda_0 > 2\alpha_2 \wedge \alpha_2 \geq 3)$, **Saddle point:** otherwise	1	$\frac{1}{3}(\lambda_0 - 3)$
P_{3b}	$\left[\frac{\lambda_0}{6}, 1-\frac{\lambda_0}{6}, 0, 0, \alpha_2-\frac{\lambda_0}{2}\right]$	**Stable node:** $\alpha_2 < 0 \wedge 2\alpha_2 < \lambda_0 \wedge \lambda_0 < \alpha_2$, **Unstable node:** $(\alpha_2 \geq 6 \wedge \alpha_2 < \lambda_0 \wedge \lambda_0 < 2\alpha_2) \vee (\alpha_2 > 3 \wedge \lambda_0 > 6 \wedge \alpha_2 < 6 \wedge \lambda_0 < 2\alpha_2)$, **Saddle point:** otherwise	1	$\frac{1}{3}(\lambda_0 - 3)$
P_{4a}	$[-1,0,0,2,0]$	**Stable node:** $\alpha_2 > 2 \wedge \lambda_0 > -2$ **Saddle point:** otherwise	1	$-\frac{7}{3}$
P_{4b}	$\left[-1,0,0,2,1+\frac{\alpha_2}{2}\right]$	**Stable node:** $\alpha_2 < -2 \wedge \lambda_0 > \alpha_2$, **Unstable node:** $\alpha_2 > 4 \wedge \lambda_0 < \alpha_2$ **Saddle point:** otherwise	1	$\frac{1}{3}(-5+\alpha_2)$
P_5	$[-1,0,0,-3,0]$	**Stable node:** $\alpha_2 > 3 \wedge \lambda_0 > 3$, **Saddle point:** otherwise	-4	1
P_6	$\left[\frac{\lambda_0}{2}, 1+\frac{\lambda_0}{2}, 0, -\lambda_0, 0\right]$	**See Fig. 7.5**	1	$-1+\frac{2\lambda_0}{3}$
P_{7a}	$[0,0,1,0,0]$	**Saddle point:** $\lambda_0 \neq 4 \wedge \alpha_2 \neq \frac{3}{2}$	0	$\frac{1}{3}$
P_{7b}	$\left[0,0,1,0,-\frac{3}{2}+\alpha_2\right]$	**Saddle point:** $\lambda_0 \neq 4 \wedge \alpha_2 \neq \frac{7}{2} \wedge \alpha_2 \neq \frac{3}{2}$	0	$\frac{1}{3}$
P_8	$[-4,0,9,-4,0]$	**Saddle point:** $\lambda_0 \neq 4 \wedge \alpha_2 \neq -\frac{1}{2}$	-8	$\frac{5}{3}$
P_9	$[\alpha_2-5,0,0,6-\alpha_2,3]$	**See Fig. 7.5**	1	$-3+\frac{2\alpha_2}{3}$
P_{10}	$\left[-9+2\sqrt{8-2\alpha_2}+2\alpha_2, 0, 8-2\alpha_2, 2-2\sqrt{8-2\alpha_2}, 3-\sqrt{8-2\alpha_2}\right]$	**See Sec. 7.5**	$-7+2\alpha_2$	$\frac{1}{3}\left(-1+2\sqrt{8-2\alpha_2}\right)$
P_{11}	$\left[-9-2\sqrt{8-2\alpha_2}+2\alpha_2, 0, 8-2\alpha_2, 2+2\sqrt{8-2\alpha_2}, 3+\sqrt{8-2\alpha_2}\right]$	**See Appendix .1.1**	$-7+2\alpha_2$	$\frac{1}{3}\left(-1-2\sqrt{8-2\alpha_2}\right)$

Table 3: Hyperbolic critical points for the second order system with $\alpha_2, \lambda_0 =$ constant. Taking into account also the additional constraints $\Omega_{\rm m} \geq 0$ and $\Omega_{\rm r} \geq 0$, the domain for last two critical points is $\mathcal{D} \equiv \{\alpha_2 < 4, \lambda_0 \in \mathbb{R}\}$, while all other points have $\mathcal{D} \equiv \{\alpha_2, \lambda_0 \in \mathbb{R}\}$.

.3 The Hořava L_4 and L_6 Lagrangians

The original action considered in ref. [163], and implemented in the public version of EFTCAMB, contains all Horndeski and some of the extensions like GLPV [311, 176, 337], but does not have all the operators necessary to study Hořava gravity.

The L_4 and L_6 Lagrangians contain, respectively, all the operators up to fourth and sixth order spatial derivatives, which are compatible with the symmetry of Hořava gravity and guarantee its power-counting renormalizability. The number of those operators is very large, but given that we are interested in an effective field theory description of linear scalar perturbations, only the ones which are second order in perturbations have to be considered in the action. The latter have been identified in ref. [310] and they are given by suitably contracting the three-dimensional Ricci tensor and scalar, the acceleration a_i, and their spatial derivatives. In detail, the HE part of action (12.3) can be written as

$$\begin{aligned}\mathcal{S}_{H,HE} &= \frac{1}{16\pi G_H}\int d^4x\sqrt{-g}\left(g_1\mathcal{R}^2+g_2\mathcal{R}_{ij}\mathcal{R}^{ij}+g_3\mathcal{R}\nabla_i a^i+g_4 a_i\nabla^2 a^i\right.\\ &\left.+g_5\mathcal{R}\nabla^2\mathcal{R}+g_6\nabla_i\mathcal{R}_{jk}\nabla^i\mathcal{R}^{jk}+g_7 a_i\nabla^4 a^i+g_8\nabla^2\mathcal{R}\nabla_i a^i\right) \quad (152)\end{aligned}$$

where $\nabla^2=\nabla^i\nabla_i$ and $\nabla^4=\nabla^i\nabla_i\nabla^j\nabla_j$, and the coefficients g_i are running coupling constants of suitable dimensions. The first and second lines contain respectively the contributions from L_4 and L_6.

We expand now the above action up to second order in perturbations by considering that on a flat FRLW background the components of $\mathcal{R}$ and $\mathcal{R}_{ij}$ identically vanish. Then we map it into the language at the basis of the EFT formalism by using the relation (12.18) for a_i. With these recipes, it is straightforward to show that the operators in action (152) up to second order can be written as

$$g_1\frac{m_0^2}{(2\xi-\eta)}\mathcal{R}^2=g_1\frac{m_0^2}{(2\xi-\eta)}(\delta\mathcal{R})^2, \quad (153a)$$

$$g_2\frac{m_0^2}{(2\xi-\eta)}\mathcal{R}_{ij}\mathcal{R}^{ij}=g_2\frac{m_0^2}{(2\xi-\eta)}\delta\mathcal{R}_{ij}\delta\mathcal{R}^{ij}, \quad (153b)$$

$$g_3\frac{m_0^2}{(2\xi-\eta)}\mathcal{R}\nabla_i a^i=g_3\frac{m_0^2}{2(2\xi-\eta)}\delta\mathcal{R}\nabla^2(a^2\delta g^{00}), \quad (153c)$$

$$g_4\frac{m_0^2}{(2\xi-\eta)}a_i\nabla^2 a^i=g_4\frac{m_0^2}{4(2\xi-\eta)}\partial_i(a^2g^{00})\nabla^2\partial^i(a^2g^{00}), \quad (153d)$$

$$g_5\frac{m_0^2}{(2\xi-\eta)}\mathcal{R}\nabla^2\mathcal{R}=g_5\frac{m_0^2}{(2\xi-\eta)}\delta\mathcal{R}\nabla^2\delta\mathcal{R}, \quad (153e)$$

$$g_6\frac{m_0^2}{(2\xi-\eta)}\nabla_i\mathcal{R}_{jk}\nabla^i\mathcal{R}^{jk}=g_6\frac{m_0^2}{(2\xi-\eta)}\nabla_i\delta\mathcal{R}_{jk}\nabla^i\delta\mathcal{R}^{jk}, \quad (153f)$$

$$g_7\frac{m_0^2}{(2\xi-\eta)}a_i\nabla^4 a^i=g_7\frac{m_0^2}{4(2\xi-\eta)}\partial_i(a^2\delta g^{00})\nabla^4(\partial^i(a^2\delta g^{00})), \quad (153g)$$

$$g_8\frac{m_0^2}{(2\xi-\eta)}\nabla^2\mathcal{R}\nabla_i a^i=g_8\frac{m_0^2}{2(2\xi-\eta)}\nabla^2\delta\mathcal{R}\nabla^2(a^2\delta g^{00}). \quad (153h)$$

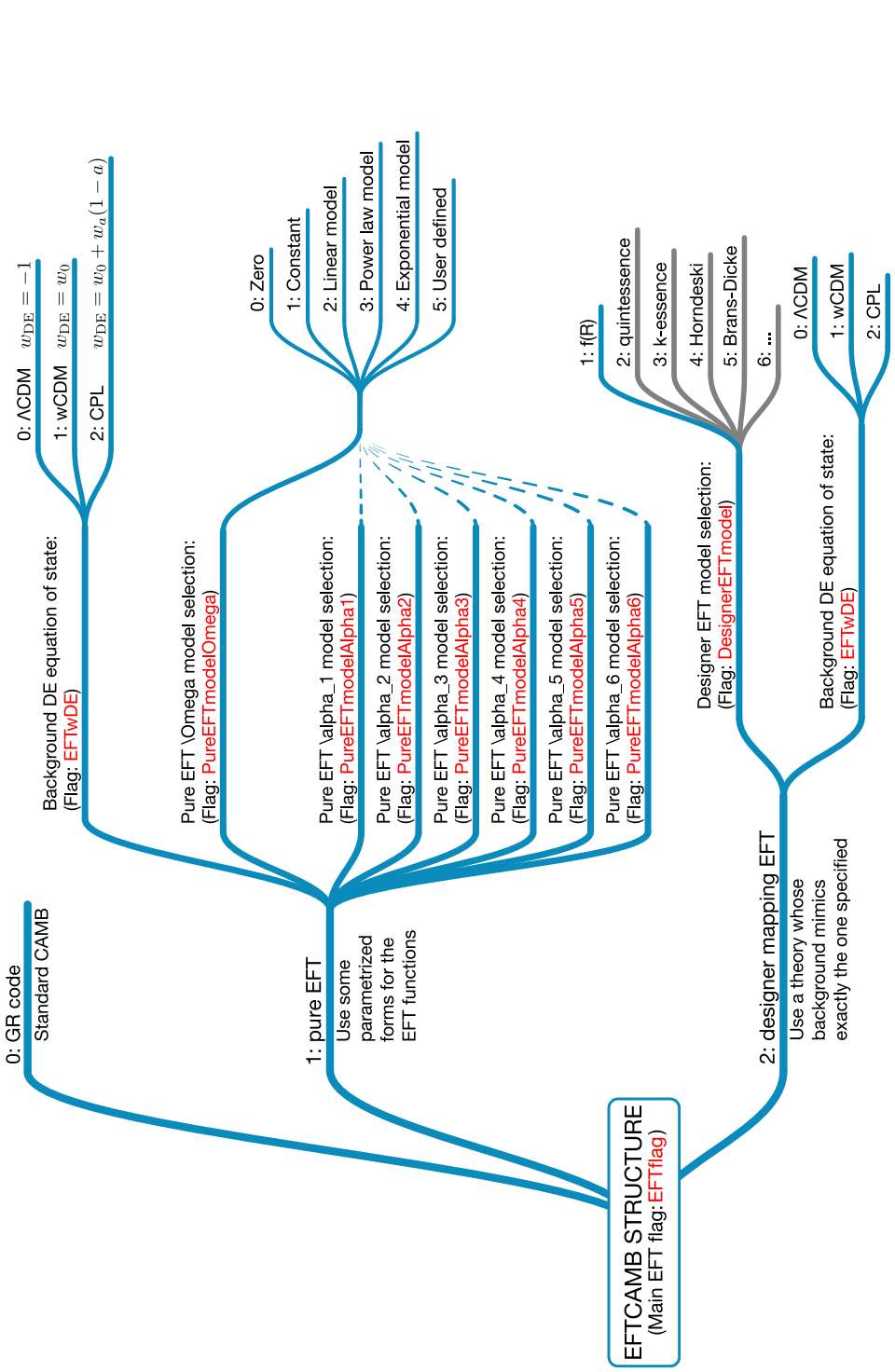

Figure 8: Flowchart of the structure of EFTCAMB V1.0: blue lines correspond to flags that are already present in the code, while grey lines are a sample of the models that will be implemented gradually in future code releases.

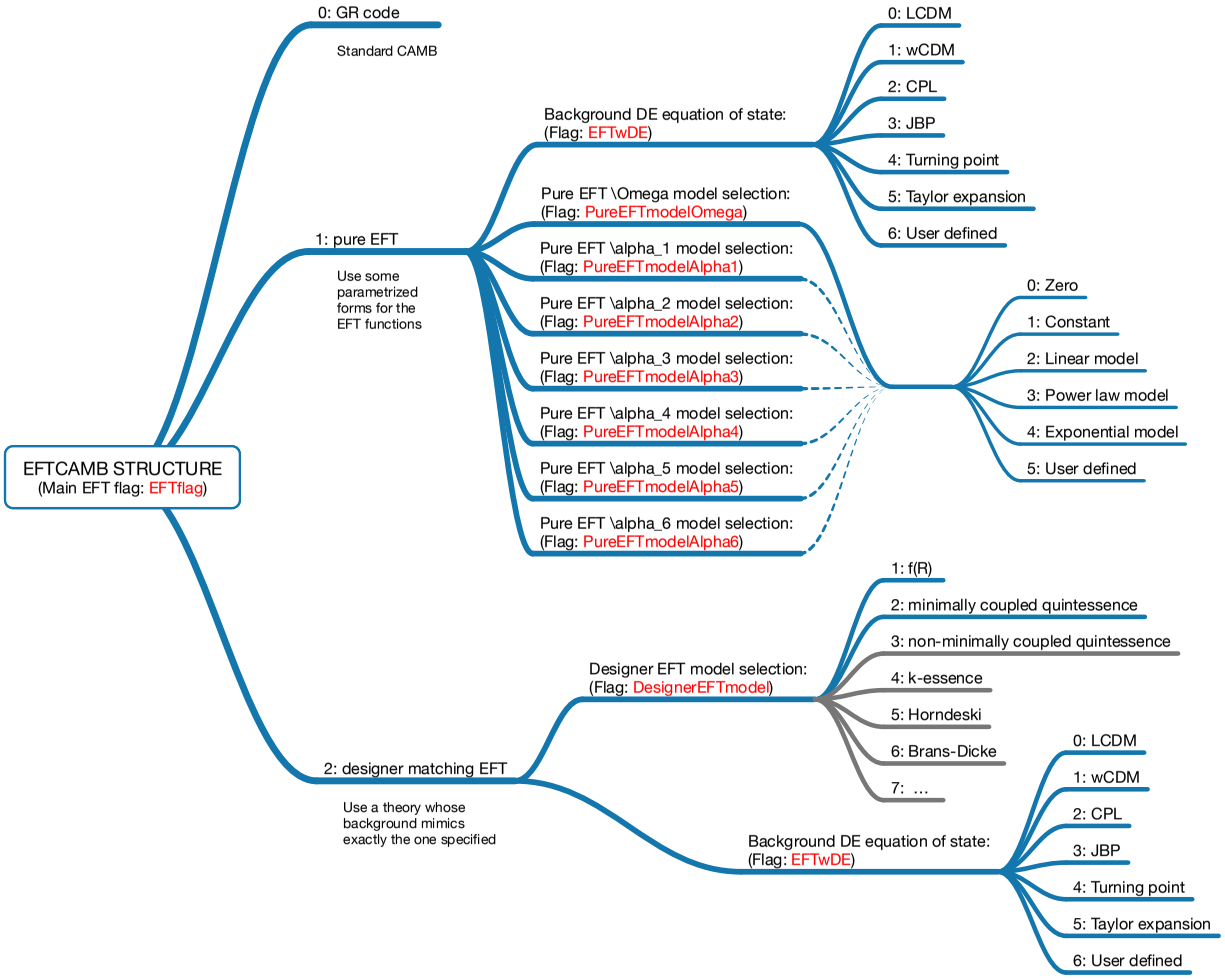

Figure 9: Flowchart of the structure of EFTCAMB V1.1: blue lines correspond to flags that are already present in the code, while grey lines are a sample of the models that will be implemented gradually in future code releases.

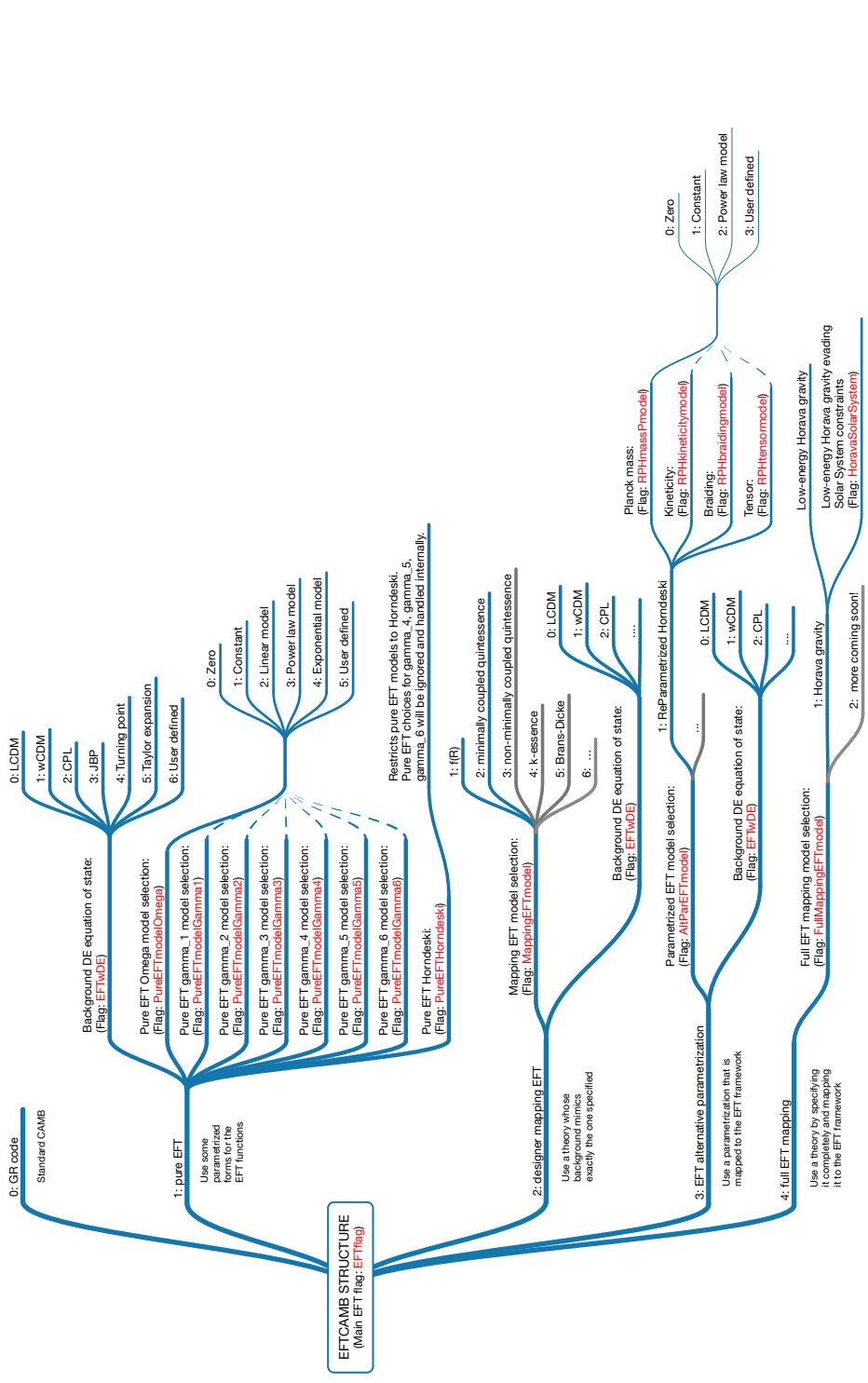

Figure 10: Flowchart of the structure of EFTCAMB V2.0: blue lines correspond to flags that are already present in the code, while grey lines are a sample of the models that will be implemented gradually in future code releases.

We notice immediately that the EFT action (6.1) is incomplete if one wants to treat the full version of Hořava gravity (which includes the operators in action (152)), then we need to add to it all the operators in eqs. (153). This suggests to extend the EFT action to a more general one by adding the following part:

$$\begin{aligned}\mathcal{S}_{EFT,2} = \int d^4x\sqrt{-g}\Big[&\lambda_1(\tau)(\delta\mathcal{R})^2 + \lambda_2(\tau)\delta\mathcal{R}_{ij}\delta\mathcal{R}^{ij} + \lambda_3(\tau)\delta\mathcal{R}\nabla^2(a^2\delta g^{00}) \\ &+ \lambda_4(\tau)\partial_i(a^2g^{00})\nabla^2\partial^i(a^2g^{00}) + \lambda_5(\tau)\delta\mathcal{R}\nabla^2\delta\mathcal{R} \\ &+ \lambda_6(\tau)\nabla_i\delta\mathcal{R}_{jk}\nabla^i\delta\mathcal{R}^{jk} \\ &+ \lambda_7(\tau)\partial_i(a^2\delta g^{00})\nabla^4(\partial^i(a^2\delta g^{00})) \\ &+ \lambda_8(\tau)\nabla^2\delta\mathcal{R}\nabla^2(a^2\delta g^{00})\Big]. \end{aligned} \tag{154}$$

In the Hořava gravity case the EFT functions λ_i's reduce to the constant coefficients in eqs. (153), e.g. $\lambda_1 = g_1 m_0^2/(2\xi - \eta)$.

Notice that the first two operators in the action (154) have already been considered in ref. [173], while the remaining operators have been considered in refs. [176, 309]. However, in these latter works an explicit EFT action (in the form of the action (154)) has not been emphasized as well as an explicit mapping between these operators and a specific theory has not been worked out. In this respect our finding corresponds to new results. Finally, let us mention that although we wrote the operators in eqs. (153) in terms of 3D quantities, following the 3+1 formalism employed in Hořava gravity, one can always express them by means of 4D quantities by using the Gauss-Codazzi relation [322].

It would be of interest to implement the contributions of these new operators in the equations for the perturbations evolved in EFTCAMB, in order to investigate their cosmological effects. We expect that their contribution becomes more important as the cosmological scale becomes smaller.

.4 Hořava Cosmological Parameters

In this appendix we report the 99.7% C.L. constraints on the derived cosmological parameters: $\Omega_b^0 h^2$ the present day density parameter of baryons; $\Omega_c^0 h^2$ the present day value of the cold dark matter density parameter; $100\theta_{MC}$ which measures the sound horizon at last scattering; τ is the Thomson scattering optical depth due to reionization; n_s the power law index of the scalar spectrum; $\ln(10^{10}A_s)$ the log power of the primordial curvature perturbation, H_0 (km/s/Mpc) the present time value of the Hubble rate, and Ω_m^0 the dark matter density parameter today. We found that the constraints on these parameters for H2 are the same as in ΛCDM as reported in the following table. The reason for this is that, in H2 case, the Hořava gravity parameters are constrained to be very close to the GR limit so that the cosmological parameters fall back to their ΛCDM values.

	Bounds on cosmological parameters for ΛCDM and H2 cases				
Parameters	PLC	PLC+BG	PLC+CMBL	PLC+WiggleZ	all combined
$\Omega_b^0 h^2$	0.02202 ± 0.008	0.02216 ± 0.0007	0.02210 ± 0.0008	0.02182 ± 0.0008	$0.02213^{+0.0008}_{-0.0007}$
$\Omega_c^0 h^2$	0.120 ± 0.008	0.118 ± 0.004	$0.119^{+0.007}_{-0.006}$	0.123 ± 0.008	$0.119^{+0.004}_{-0.003}$
$100\theta_{MC}$	1.041 ± 0.002	1.041 ± 0.002	1.041 ± 0.002	1.041 ± 0.002	1.041 ± 0.002
τ	$0.089^{+0.047}_{-0.036}$	$0.092^{+0.040}_{-0.034}$	$0.089^{+0.041}_{-0.036}$	$0.085^{+0.037}_{-0.033}$	$0.090^{+0.037}_{-0.032}$
n_s	$0.959^{+0.021}_{-0.020}$	0.963 ± 0.015	$0.961^{+0.022}_{-0.021}$	0.953 ± 0.021	0.963 ± 0.015
$\ln(10^{10} A_s)$	$3.088^{+0.085}_{-0.069}$	$3.090^{+0.078}_{-0.069}$	$3.085^{+0.073}_{-0.064}$	$3.087^{+0.072}_{-0.063}$	$3.087^{+0.071}_{-0.065}$
H_0	$67.2^{+3.5}_{-3.4}$	$68.0^{+1.9}_{-1.6}$	$67.7^{+3.1}_{-2.9}$	$65.8^{+3.3}_{-3.1}$	$67.7^{+1.8}_{-1.6}$
Ω_m^0	$0.316^{+0.052}_{-0.044}$	$0.305^{+0.022}_{-0.024}$	$0.309^{+0.042}_{-0.039}$	$0.337^{+0.051}_{-0.046}$	$0.309^{+0.022}_{-0.021}$

Table 4: Mean values and 99.7% C.L. bounds on several cosmological parameters. Notice that these bounds do not change for the ΛCDM and H2 cases.

	Bounds on cosmological parameters for H3 case				
Parameters	PLC	PLC+BG	PLC+CMBL	PLC+WiggleZ	all combined
$\Omega_b^0 h^2$	$0.021^{+0.001}_{-0.001}$	$0.0218^{+0.0009}_{-0.0010}$	$0.0218^{+0.0010}_{-0.0009}$	0.021 ± 0.001	$0.0218^{+0.0008}_{-0.0009}$
$\Omega_c^0 h^2$	$0.12^{+0.01}_{-0.01}$	$0.119^{+0.005}_{-0.004}$	0.118 ± 0.007	$0.123^{+0.008}_{-0.010}$	$0.119^{+0.004}_{-0.003}$
$100\theta_{MC}$	$1.043^{+0.007}_{-0.004}$	$1.043^{+0.005}_{-0.003}$	$1.043^{+0.006}_{-0.004}$	$1.043^{+0.007}_{-0.004}$	$1.044^{+0.004}_{-0.003}$
τ	$0.08^{+0.05}_{-0.04}$	0.08 ± 0.04	0.08 ± 0.04	$0.08^{+0.04}_{-0.03}$	$0.08^{+0.04}_{-0.03}$
n_s	0.96 ± 0.03	0.96 ± 0.02	0.96 ± 0.02	0.96 ± 0.03	0.96 ± 0.02
$\ln(10^{10} A_s)$	$3.09^{+0.09}_{-0.08}$	$3.09^{+0.09}_{-0.08}$	$3.08^{+0.08}_{-0.07}$	3.10 ± 0.08	$3.07^{+0.08}_{-0.06}$
H_0	67 ± 5	67 ± 2	68^{+4}_{-3}	65^{+5}_{-4}	67^{+1}_{-2}
Ω_m^0	$0.31^{+0.07}_{-0.05}$	0.31 ± 0.02	$0.30^{+0.05}_{-0.04}$	0.33 ± 0.06	0.30 ± 0.02

Table 5: Mean values and 99.7% C.L. bounds on several cosmological parameters in H3 case.

Acknowledgments

I wish to thank...

...my supervisors Carlo Baccigalupi and Alessandra Silvestri for wisely guiding me these years, for nurturing my interests and pushing me to purse my ideas. I have learned a great deal about physics, cosmology, research, scientific and academic life from you and I will be forever grateful.

...Sabino Matarrese for introducing me, during my master studies, to cosmology and its beauty as a physical science.

...my collaborators Carlo Baccigalupi, Noemi Frusciante, Bin Hu, Matteo Rizzato, Alessandra Silvestri, Daniele Vernieri, Shuang-Yong Zhou for their constant support and the great amount of work that we did together. None of this would have been possible without you.

...my fellows Ph.D. student in Sissa for making these years enjoyable and for making SISSA a lively and interesting environment.

I wish to thank Enrico Barausse, Nicola Bartolo, Diego Blas, Jolyon Bloomfield, Matteo Calabrese, Stefano Camera, Paolo Creminelli, Antonio J. Cuesta, Antonio De Felice, Jérôme Gleyzes, Tamara Grava, Alan Heavens, Luca Heltai, Alireza Hojjati, Wayne Hu, Mikhail Ivanov, Martin Kunz, Julien Lesgourgues, Stefano Liberati, Michele Liguori, Stefano Luzzatto, Matteo Martinelli, Sabino Matarrese, Ali Narimani, Laurence Perotto, Valeria Pettorino, Federico Piazza, Levon Pogosian, Thomas Sotiriou, Sergey Sibiryakov, Licia Verde, Riccardo Valdarnini, Wessel Valkenburg, Filippo Vernizzi, Matteo Viel, Massimo Viola, Bo Yu and Gong-Bo Zhao for useful conversations, discussions, comments and feedback that contributed to the development of my research.

Finally, my deepest gratitude goes to all the important people in my life outside physics.

Bibliography

[1] Bin Hu, Marco Raveri, Matteo Rizzato, and Alessandra Silvestri. Testing Hu-Sawicki f(R) gravity with the Effective Field Theory approach. 2016.

[2] Marco Raveri. Are cosmological data sets consistent with each other within the Λ cold dark matter model? *Phys. Rev.*, D93(4):043522, 2016.

[3] Noemi Frusciante, Marco Raveri, Daniele Vernieri, Bin Hu, and Alessandra Silvestri. Hoava Gravity in the Effective Field Theory formalism: From cosmology to observational constraints. *Phys. Dark Univ.*, 13:7–24, 2016.

[4] Bin Hu and Marco Raveri. Can modified gravity models reconcile the tension between the CMB anisotropy and lensing maps in Planck-like observations? *Phys. Rev.*, D91(12):123515, 2015.

[5] Bin Hu, Marco Raveri, Alessandra Silvestri, and Noemi Frusciante. Exploring massive neutrinos in dark cosmologies with $EFTCAMB/$ EFTCosmoMC. *Phys. Rev.*, D91(6):063524, 2015.

[6] Marco Raveri, Carlo Baccigalupi, Alessandra Silvestri, and Shuang-Yong Zhou. Measuring the speed of cosmological gravitational waves. *Phys. Rev.*, D91(6):061501, 2015.

[7] Marco Raveri, Bin Hu, Noemi Frusciante, and Alessandra Silvestri. Effective Field Theory of Cosmic Acceleration: constraining dark energy with CMB data. *Phys. Rev.*, D90(4):043513, 2014.

[8] Bin Hu, Marco Raveri, Noemi Frusciante, and Alessandra Silvestri. Effective Field Theory of Cosmic Acceleration: an implementation in CAMB. *Phys. Rev.*, D89(10):103530, 2014.

[9] Noemi Frusciante, Marco Raveri, and Alessandra Silvestri. Effective Field Theory of Dark Energy: a Dynamical Analysis. *JCAP*, 1402:026, 2014.

[10] Bin Hu, Marco Raveri, Noemi Frusciante, and Alessandra Silvestri. EFTCAMB/EFTCosmoMC: Numerical Notes v2.0. 2014.

[11] S. Perlmutter et al. Measurements of Omega and Lambda from 42 high redshift supernovae. *Astrophys. J.*, 517:565–586, 1999.

[12] Adam G. Riess et al. Observational evidence from supernovae for an accelerating universe and a cosmological constant. *Astron. J.*, 116:1009–1038, 1998.

[13] D. N. Spergel et al. First year Wilkinson Microwave Anisotropy Probe (WMAP) observations: Determination of cosmological parameters. *Astrophys. J. Suppl.*, 148:175–194, 2003.

[14] G. Hinshaw et al. Nine-Year Wilkinson Microwave Anisotropy Probe (WMAP) Observations: Cosmological Parameter Results. *Astrophys. J. Suppl.*, 208:19, 2013.

[15] R. Adam et al. Planck 2015 results. I. Overview of products and scientific results. 2015.

[16] P. A. R. Ade et al. Planck 2015 results. XIII. Cosmological parameters. 2015.

[17] Sdss web-page. `http://www.sdss.org`.

[18] Wigglez web-page. `http://wigglez.swin.edu.au/site/`.

[19] Cfhtlens web-page. `http://www.cfhtlens.org`.

[20] Des web-page. `http://www.darkenergysurvey.org`.

[21] Simons array web-page. `http://cosmology.ucsd.edu/simonsarray.html`.

[22] Euclid web-page. `http://sci.esa.int/euclid/`.

[23] Wfirst web-page. `http://wfirst.gsfc.nasa.gov`.

[24] Lsst web-page. `http://www.lsst.org`.

[25] Ska web-page. `https://www.skatelescope.org`.

[26] G. F. R. Ellis. Issues in the philosophy of cosmology. In *Philosophy of Physics*, volume B of *Handbook of the Philosophy of Science*. North-Holland, 2007.

[27] P. J. E. Peebles. *The Large-Scale Structure of the Universe*. Princeton Series in Physics. Princeton University Press, New Jersey, 1980.

[28] Steven Weinberg. *Gravitation and Cosmology: Principles and Applications of the General Theory of Relativity*. Wiley, New York, NY, 1972.

[29] David W. Hogg. Distance measures in cosmology. 1999.

[30] S. Perlmutter et al. Measurements of the cosmological parameters Omega and Lambda from the first 7 supernovae at z¿=0.35. *Astrophys. J.*, 483:565, 1997.

[31] S. Perlmutter et al. Discovery of a supernova explosion at half the age of the Universe and its cosmological implications. *Nature*, 391:51–54, 1998.

[32] Peter M. Garnavich et al. Constraints on cosmological models from Hubble Space Telescope observations of high z supernovae. *Astrophys. J.*, 493:L53–57, 1998.

[33] John L. Tonry et al. Cosmological results from high-z supernovae. *Astrophys. J.*, 594:1–24, 2003.

[34] Adam G. Riess et al. New Hubble Space Telescope Discoveries of Type Ia Supernovae at z¿=1: Narrowing Constraints on the Early Behavior of Dark Energy. *Astrophys. J.*, 659:98–121, 2007.

[35] Pierre Astier et al. The Supernova legacy survey: Measurement of omega(m), omega(lambda) and W from the first year data set. *Astron. Astrophys.*, 447:31–48, 2006.

[36] Jerome Martin. Everything You Always Wanted To Know About The Cosmological Constant Problem (But Were Afraid To Ask). *Comptes Rendus Physique*, 13:566–665, 2012.

[37] C. Wetterich. Cosmology and the Fate of Dilatation Symmetry. *Nucl. Phys.*, B302:668, 1988.

[38] Bharat Ratra and P. J. E. Peebles. Cosmological Consequences of a Rolling Homogeneous Scalar Field. *Phys. Rev.*, D37:3406, 1988.

[39] P. J. E. Peebles and Bharat Ratra. Cosmology with a Time Variable Cosmological Constant. *Astrophys. J.*, 325:L17, 1988.

[40] Joshua A. Frieman, Christopher T. Hill, and Richard Watkins. Late time cosmological phase transitions. 1. Particle physics models and cosmic evolution. *Phys. Rev.*, D46:1226–1238, 1992.

[41] R. R. Caldwell, Rahul Dave, and Paul J. Steinhardt. Cosmological imprint of an energy component with general equation of state. *Phys. Rev. Lett.*, 80:1582–1585, 1998.

[42] Greg Huey, Li-Min Wang, Rahul Dave, R. R. Caldwell, and Paul J. Steinhardt. Resolving the cosmological missing energy problem. *Phys. Rev.*, D59:063005, 1999.

[43] Timothy Clifton, Pedro G. Ferreira, Antonio Padilla, and Constantinos Skordis. Modified Gravity and Cosmology. *Phys. Rept.*, 513:1–189, 2012.

[44] Syksy Rasanen. Backreaction of linear perturbations and dark energy. In *39th Rencontres de Moriond Workshop on Exploring the Universe: Contents and Structures of the Universe La Thuile, Italy, March 28-April 4, 2004*, 2004.

[45] Syksy Rasanen. Backreaction in the Lemaitre-Tolman-Bondi model. *JCAP*, 0411:010, 2004.

[46] Alessio Notari. Late time failure of Friedmann equation. *Mod. Phys. Lett.*, A21:2997–3001, 2006.

[47] Edward W. Kolb, Sabino Matarrese, Alessio Notari, and Antonio Riotto. The Effect of inhomogeneities on the expansion rate of the universe. *Phys. Rev.*, D71:023524, 2005.

[48] Edward W. Kolb, S. Matarrese, and A. Riotto. On cosmic acceleration without dark energy. *New J. Phys.*, 8:322, 2006.

[49] Tirthabir Biswas, Reza Mansouri, and Alessio Notari. Nonlinear Structure Formation and Apparent Acceleration: An Investigation. *JCAP*, 0712:017, 2007.

[50] Tirthabir Biswas and Alessio Notari. Swiss-Cheese Inhomogeneous Cosmology and the Dark Energy Problem. *JCAP*, 0806:021, 2008.

[51] R. Ali Vanderveld, Eanna E. Flanagan, and Ira Wasserman. Systematic corrections to the measured cosmological constant as a result of local inhomogeneity. *Phys. Rev.*, D76:083504, 2007.

[52] *George F. Smoot - Nobel Lecture: Cosmic Microwave Background Radiation Anisotropies: Their Discovery and Utilization*, 2006.

[53] *John C. Mather - Nobel Lecture: From the Big Bang to the Nobel Prize and Beyond*, 2006.

[54] D. Larson, J. Dunkley, G. Hinshaw, E. Komatsu, M. R. Nolta, C. L. Bennett, B. Gold, M. Halpern, R. S. Hill, N. Jarosik, A. Kogut, M. Limon, S. S. Meyer, N. Odegard, L. Page, K. M. Smith, D. N. Spergel, G. S. Tucker, J. L. Weiland, E. Wollack, and E. L. Wright. Seven-year Wilkinson Microwave Anisotropy Probe (WMAP) Observations: Power Spectra and WMAP-derived Parameters. *Astrophysical Journal Supplement Series*, 192:16, February 2011.

[55] James M. Bardeen. Gauge Invariant Cosmological Perturbations. *Phys. Rev.*, D22:1882–1905, 1980.

[56] Hideo Kodama and Misao Sasaki. Cosmological Perturbation Theory. *Prog. Theor. Phys. Suppl.*, 78:1–166, 1984.

[57] J. A. Peacock. *Cosmological physics*. 1999.

[58] Viatcheslav F. Mukhanov, H. A. Feldman, and Robert H. Brandenberger. Theory of cosmological perturbations. Part 1. Classical perturbations. Part 2. Quantum theory of perturbations. Part 3. Extensions. *Phys. Rept.*, 215:203–333, 1992.

[59] Chung-Pei Ma and Edmund Bertschinger. Cosmological perturbation theory in the synchronous and conformal Newtonian gauges. *Astrophys. J.*, 455:7–25, 1995.

[60] Scott Dodelson. *Modern Cosmology*. Academic Press, Amsterdam, 2003.

[61] Alexei A. Starobinsky. Dynamics of Phase Transition in the New Inflationary Universe Scenario and Generation of Perturbations. *Phys. Lett.*, B117:175–178, 1982.

[62] Alan H. Guth and S. Y. Pi. Fluctuations in the New Inflationary Universe. *Phys. Rev. Lett.*, 49:1110–1113, 1982.

[63] S. W. Hawking and I. G. Moss. Fluctuations in the Inflationary Universe. *Nucl. Phys.*, B224:180, 1983.

[64] James M. Bardeen, Paul J. Steinhardt, and Michael S. Turner. Spontaneous Creation of Almost Scale - Free Density Perturbations in an Inflationary Universe. *Phys. Rev.*, D28:679, 1983.

[65] Robert H. Brandenberger, Ronald Kahn, and William H. Press. Cosmological Perturbations in the Early Universe. *Phys. Rev.*, D28:1809, 1983.

[66] Alan H. Guth and So-Young Pi. The Quantum Mechanics of the Scalar Field in the New Inflationary Universe. *Phys. Rev.*, D32:1899–1920, 1985.

[67] P. A. R. Ade et al. Planck 2015 results. XX. Constraints on inflation. 2015.

[68] M. Betoule et al. Improved cosmological constraints from a joint analysis of the SDSS-II and SNLS supernova samples. *Astron. Astrophys.*, 568:A22, 2014.

[69] Michael J. Drinkwater et al. The WiggleZ Dark Energy Survey: Survey Design and First Data Release. *Mon. Not. Roy. Astron. Soc.*, 401:1429–1452, 2010.

[70] David Parkinson et al. The WiggleZ Dark Energy Survey: Final data release and cosmological results. *Phys. Rev.*, D86:103518, 2012.

[71] Chris Blake et al. The WiggleZ Dark Energy Survey: the selection function and z=0.6 galaxy power spectrum. *Mon. Not. Roy. Astron. Soc.*, 406:803–821, 2010.

[72] Jason Dossett, Bin Hu, and David Parkinson. Constraining models of f(R) gravity with Planck and WiggleZ power spectrum data. *JCAP*, 1403:046, 2014.

[73] Catherine Heymans et al. CFHTLenS tomographic weak lensing cosmological parameter constraints: Mitigating the impact of intrinsic galaxy alignments. *Mon. Not. Roy. Astron. Soc.*, 432:2433, 2013.

[74] P. A. R. Ade et al. Planck 2015 results. XIV. Dark energy and modified gravity. 2015.

[75] Adam G. Riess, Lucas Macri, Stefano Casertano, Hubert Lampeitl, Henry C. Ferguson, Alexei V. Filippenko, Saurabh W. Jha, Weidong Li, and Ryan Chornock. A 3% Solution: Determination of the Hubble Constant with the Hubble Space Telescope and Wide Field Camera 3. *Astrophys. J.*, 730:119, 2011. [Erratum: Astrophys. J.732,129(2011)].

[76] N. Aghanim et al. Planck 2015 results. XI. CMB power spectra, likelihoods, and robustness of parameters. *Submitted to: Astron. Astrophys.*, 2015.

[77] P. A. R. Ade et al. Planck 2013 results. XV. CMB power spectra and likelihood. *Astron. Astrophys.*, 571:A15, 2014.

[78] P. A. R. Ade et al. Planck 2013 results. XVI. Cosmological parameters. *Astron. Astrophys.*, 571:A16, 2014.

[79] P. A. R. Ade et al. Planck 2015 results. XV. Gravitational lensing. 2015.

[80] Wayne Hu and Takemi Okamoto. Mass reconstruction with cmb polarization. *Astrophys. J.*, 574:566–574, 2002.

[81] P. A. R. Ade et al. Planck 2013 results. XVII. Gravitational lensing by large-scale structure. *Astron. Astrophys.*, 571:A17, 2014.

[82] Ashley J. Ross, Lado Samushia, Cullan Howlett, Will J. Percival, Angela Burden, and Marc Manera. The clustering of the SDSS DR7 main Galaxy sample I. A 4 per cent distance measure at $z = 0.15$. *Mon. Not. Roy. Astron. Soc.*, 449(1):835–847, 2015.

[83] Lauren Anderson et al. The clustering of galaxies in the SDSS-III Baryon Oscillation Spectroscopic Survey: baryon acoustic oscillations in the Data Releases 10 and 11 Galaxy samples. *Mon. Not. Roy. Astron. Soc.*, 441(1):24–62, 2014.

[84] Florian Beutler, Chris Blake, Matthew Colless, D. Heath Jones, Lister Staveley-Smith, Lachlan Campbell, Quentin Parker, Will Saunders, and Fred Watson. The 6dF Galaxy Survey: Baryon Acoustic Oscillations and the Local Hubble Constant. *Mon. Not. Roy. Astron. Soc.*, 416:3017–3032, 2011.

[85] Florian Beutler et al. The clustering of galaxies in the SDSS-III Baryon Oscillation Spectroscopic Survey: Testing gravity with redshift-space distortions using the power spectrum multipoles. *Mon. Not. Roy. Astron. Soc.*, 443(2):1065–1089, 2014.

[86] Lado Samushia et al. The clustering of galaxies in the SDSS-III Baryon Oscillation Spectroscopic Survey: measuring growth rate and geometry with anisotropic clustering. *Mon. Not. Roy. Astron. Soc.*, 439(4):3504–3519, 2014.

[87] P. A. R. Ade et al. Detection of B-Mode Polarization at Degree Angular Scales by BICEP2. *Phys. Rev. Lett.*, 112(24):241101, 2014.

[88] P.A.R. Ade et al. Joint Analysis of BICEP2/$KeckArray$ and $Planck$ Data. *Phys. Rev. Lett.*, 114:101301, 2015.

[89] ric Aubourg et al. Cosmological implications of baryon acoustic oscillation measurements. *Phys. Rev.*, D92(12):123516, 2015.

[90] T. Abbott et al. Cosmology from Cosmic Shear with DES Science Verification Data. 2015.

[91] Mark Wyman, Douglas H. Rudd, R. Ali Vanderveld, and Wayne Hu. Neutrinos Help Reconcile Planck Measurements with the Local Universe. *Phys. Rev. Lett.*, 112(5):051302, 2014.

[92] Jan Hamann and Jasper Hasenkamp. A new life for sterile neutrinos: resolving inconsistencies using hot dark matter. *JCAP*, 1310:044, 2013.

[93] Matteo Costanzi, Barbara Sartoris, Matteo Viel, and Stefano Borgani. Neutrino constraints: what large-scale structure and CMB data are telling us? *JCAP*, 1410(10):081, 2014.

[94] Eleonora Di Valentino, Alessandro Melchiorri, and Joseph Silk. Beyond six parameters: extending ΛCDM. *Phys. Rev.*, D92(12):121302, 2015.

[95] Phil Marshall, Nutan Rajguru, and Anze Slosar. Bayesian evidence as a tool for comparing datasets. *Phys. Rev.*, D73:067302, 2006.

[96] Farhan Feroz, Benjamin C. Allanach, Mike Hobson, Shehu S. Abdus-Salam, Roberto Trotta, and Arne M. Weber. Bayesian Selection of sign(mu) within mSUGRA in Global Fits Including WMAP5 Results. *JHEP*, 10:064, 2008.

[97] M. C. March, R. Trotta, L. Amendola, and D. Huterer. Robustness to systematics for future dark energy probes. *Mon. Not. Roy. Astron. Soc.*, 415:143–152, 2011.

[98] Luca Amendola, Valerio Marra, and Miguel Quartin. Internal Robustness: systematic search for systematic bias in SN Ia data. *Mon. Not. Roy. Astron. Soc.*, 430:1867–1879, 2013.

[99] Licia Verde, Pavlos Protopapas, and Raul Jimenez. Planck and the local Universe: Quantifying the tension. *Phys. Dark Univ.*, 2:166–175, 2013.

[100] Jerome Martin, Christophe Ringeval, Roberto Trotta, and Vincent Vennin. Compatibility of Planck and BICEP2 in the Light of Inflation. *Phys. Rev.*, D90(6):063501, 2014.

[101] N. V. Karpenka, F. Feroz, and M. P. Hobson. Testing the mutual consistency of different supernovae surveys. *Mon. Not. Roy. Astron. Soc.*, 449(3):2405–2412, 2015.

[102] R. E. Smith, J. A. Peacock, A. Jenkins, S. D. M. White, C. S. Frenk, F. R. Pearce, P. A. Thomas, G. Efstathiou, and H. M. P. Couchmann. Stable clustering, the halo model and nonlinear cosmological power spectra. *Mon. Not. Roy. Astron. Soc.*, 341:1311, 2003.

[103] Ryuichi Takahashi, Masanori Sato, Takahiro Nishimichi, Atsushi Taruya, and Masamune Oguri. Revising the Halofit Model for the Nonlinear Matter Power Spectrum. *Astrophys. J.*, 761:152, 2012.

[104] Antony Lewis, Anthony Challinor, and Anthony Lasenby. Efficient computation of CMB anisotropies in closed FRW models. *Astrophys. J.*, 538:473–476, 2000.

[105] Antony Lewis and Sarah Bridle. Cosmological parameters from CMB and other data: A Monte Carlo approach. *Phys. Rev.*, D66:103511, 2002.

[106] W. J. Handley, M. P. Hobson, and A. N. Lasenby. PolyChord: nested sampling for cosmology. *Mon. Not. Roy. Astron. Soc.*, 450(1):L61–L65, 2015.

[107] Niall MacCrann, Joe Zuntz, Sarah Bridle, Bhuvnesh Jain, and Matthew R. Becker. Cosmic Discordance: Are Planck CMB and CFHTLenS weak lensing measurements out of tune? *Mon. Not. Roy. Astron. Soc.*, 451(3):2877–2888, 2015.

[108] Jia Liu and J. Colin Hill. Cross-correlation of Planck CMB Lensing and CFHTLenS Galaxy Weak Lensing Maps. *Phys. Rev.*, D92(6):063517, 2015.

[109] Marcel M. Schmittfull, Anthony Challinor, Duncan Hanson, and Antony Lewis. Joint analysis of CMB temperature and lensing-reconstruction power spectra. *Phys. Rev.*, D88(6):063012, 2013.

[110] Richard A. Battye and Adam Moss. Evidence for Massive Neutrinos from Cosmic Microwave Background and Lensing Observations. *Phys. Rev. Lett.*, 112(5):051303, 2014.

[111] Jason N. Dossett, Mustapha Ishak, David Parkinson, and Tamara Davis. Constraints and tensions in testing general relativity from Planck and CFHTLenS data including intrinsic alignment systematics. *Phys. Rev.*, D92(2):023003, 2015.

[112] Jia Liu, Alvaro Ortiz-Vazquez, and J. Colin Hill. Constraining Multiplicative Bias in CFHTLenS Weak Lensing Shear Data. 2016.

[113] Shahab Joudaki et al. CFHTLenS revisited: assessing concordance with Planck including astrophysical systematics. 2016.

[114] Marika Asgari, Catherine Heymans, Chris Blake, Joachim Harnois-Deraps, Peter Schneider, and Ludovic Van Waerbeke. Revisiting CFHTLenS cosmic shear: Optimal E/B mode decomposition using COSEBIs and compressed COSEBIs. 2016.

[115] Edmund Bertschinger. On the Growth of Perturbations as a Test of Dark Energy. *Astrophys. J.*, 648:797–806, 2006.

[116] Eric V. Linder and Robert N. Cahn. Parameterized Beyond-Einstein Growth. *Astropart. Phys.*, 28:481–488, 2007.

[117] Luca Amendola, Martin Kunz, and Domenico Sapone. Measuring the dark side (with weak lensing). *JCAP*, 0804:013, 2008.

[118] Pengjie Zhang, Michele Liguori, Rachel Bean, and Scott Dodelson. Probing Gravity at Cosmological Scales by Measurements which Test the Relationship between Gravitational Lensing and Matter Overdensity. *Phys. Rev. Lett.*, 99:141302, 2007.

[119] Wayne Hu and Ignacy Sawicki. A Parameterized Post-Friedmann Framework for Modified Gravity. *Phys. Rev.*, D76:104043, 2007.

[120] Edmund Bertschinger and Phillip Zukin. Distinguishing Modified Gravity from Dark Energy. *Phys. Rev.*, D78:024015, 2008.

[121] Scott F. Daniel, Robert R. Caldwell, Asantha Cooray, and Alessandro Melchiorri. Large Scale Structure as a Probe of Gravitational Slip. *Phys. Rev.*, D77:103513, 2008.

[122] Yong-Seon Song and Kazuya Koyama. Consistency test of general relativity from large scale structure of the Universe. *JCAP*, 0901:048, 2009.

[123] Constantinos Skordis. Consistent cosmological modifications to the Einstein equations. *Phys. Rev.*, D79:123527, 2009.

[124] Yong-Seon Song and Olivier Dore. A step towards testing general relativity using weak gravitational lensing and redshift surveys. *JCAP*, 0903:025, 2009.

[125] Gong-Bo Zhao, Levon Pogosian, Alessandra Silvestri, and Joel Zylberberg. Cosmological Tests of General Relativity with Future Tomographic Surveys. *Phys. Rev. Lett.*, 103:241301, 2009.

[126] Gong-Bo Zhao, Tommaso Giannantonio, Levon Pogosian, Alessandra Silvestri, David J. Bacon, Kazuya Koyama, Robert C. Nichol, and Yong-Seon Song. Probing modifications of General Relativity using current cosmological observations. *Phys. Rev.*, D81:103510, 2010.

[127] Jason Dossett, Mustapha Ishak, Jacob Moldenhauer, Yungui Gong, Anzhong Wang, and Yungui Gong. Constraints on growth index parameters from current and future observations. *JCAP*, 1004:022, 2010.

[128] Yong-Seon Song, Lukas Hollenstein, Gabriela Caldera-Cabral, and Kazuya Koyama. Theoretical Priors On Modified Growth Parametrisations. *JCAP*, 1004:018, 2010.

[129] Scott F. Daniel, Eric V. Linder, Tristan L. Smith, Robert R. Caldwell, Asantha Cooray, Alexie Leauthaud, and Lucas Lombriser. Testing General Relativity with Current Cosmological Data. *Phys. Rev.*, D81:123508, 2010.

[130] Levon Pogosian, Alessandra Silvestri, Kazuya Koyama, and Gong-Bo Zhao. How to optimally parametrize deviations from General Relativity in the evolution of cosmological perturbations? *Phys. Rev.*, D81:104023, 2010.

[131] Rachel Bean and Matipon Tangmatitham. Current constraints on the cosmic growth history. *Phys. Rev.*, D81:083534, 2010.

[132] Shaun A. Thomas, Stephen A. Appleby, and Jochen Weller. Modified Gravity: the CMB, Weak Lensing and General Parameterisations. *JCAP*, 1103:036, 2011.

[133] Tessa Baker, Pedro G. Ferreira, Constantinos Skordis, and Joe Zuntz. Towards a fully consistent parameterization of modified gravity. *Phys. Rev.*, D84:124018, 2011.

[134] Daniel B. Thomas and Carlo R. Contaldi. Testing model independent modified gravity with future large scale surveys. *JCAP*, 1112:013, 2011.

[135] Jason N. Dossett, Mustapha Ishak, and Jacob Moldenhauer. Testing General Relativity at Cosmological Scales: Implementation and Parameter Correlations. *Phys. Rev.*, D84:123001, 2011.

[136] Gong-Bo Zhao, Hong Li, Eric V. Linder, Kazuya Koyama, David J. Bacon, and Xinmin Zhang. Testing Einstein Gravity with Cosmic Growth and Expansion. *Phys. Rev.*, D85:123546, 2012.

[137] Alireza Hojjati, Gong-Bo Zhao, Levon Pogosian, Alessandra Silvestri, Robert Crittenden, and Kazuya Koyama. Cosmological tests of General Relativity: a principal component analysis. *Phys. Rev.*, D85:043508, 2012.

[138] Philippe Brax, Anne-Christine Davis, and Baojiu Li. Modified Gravity Tomography. *Phys. Lett.*, B715:38–43, 2012.

[139] Jason Dossett and Mustapha Ishak. Spatial Curvature and Cosmological Tests of General Relativity. *Phys. Rev.*, D86:103008, 2012.

[140] Philippe Brax, Anne-Christine Davis, Baojiu Li, and Hans A. Winther. A Unified Description of Screened Modified Gravity. *Phys. Rev.*, D86:044015, 2012.

[141] Ignacy Sawicki, Ippocratis D. Saltas, Luca Amendola, and Martin Kunz. Consistent perturbations in an imperfect fluid. *JCAP*, 1301:004, 2013.

[142] Tessa Baker, Pedro G. Ferreira, and Constantinos Skordis. The Parameterized Post-Friedmann framework for theories of modified gravity: concepts, formalism and examples. *Phys. Rev.*, D87(2):024015, 2013.

[143] Luca Amendola, Martin Kunz, Mariele Motta, Ippocratis D. Saltas, and Ignacy Sawicki. Observables and unobservables in dark energy cosmologies. *Phys. Rev.*, D87(2):023501, 2013.

[144] Alireza Hojjati. Degeneracies in parametrized modified gravity models. *JCAP*, 1301:009, 2013.

[145] Alessandra Silvestri, Levon Pogosian, and Roman V. Buniy. Practical approach to cosmological perturbations in modified gravity. *Phys. Rev.*, D87(10):104015, 2013.

[146] Mariele Motta, Ignacy Sawicki, Ippocratis D. Saltas, Luca Amendola, and Martin Kunz. Probing Dark Energy through Scale Dependence. *Phys. Rev.*, D88(12):124035, 2013.

[147] Shinsuke Asaba, Chiaki Hikage, Kazuya Koyama, Gong-Bo Zhao, Alireza Hojjati, and Levon Pogosian. Principal Component Analysis of Modified Gravity using Weak Lensing and Peculiar Velocity Measurements. *JCAP*, 1308:029, 2013.

[148] Tessa Baker, Pedro G. Ferreira, and Constantinos Skordis. A Fast Route to Modified Gravitational Growth. *Phys. Rev.*, D89(2):024026, 2014.

[149] Jason Dossett and Mustapha Ishak. Effects of Dark Energy Perturbations on Cosmological Tests of General Relativity. *Phys. Rev.*, D88(10):103008, 2013.

[150] Ayumu Terukina, Lucas Lombriser, Kazuhiro Yamamoto, David Bacon, Kazuya Koyama, and Robert C. Nichol. Testing chameleon gravity with the Coma cluster. *JCAP*, 1404:013, 2014.

[151] Federico Piazza, Heinrich Steigerwald, and Christian Marinoni. Phenomenology of dark energy: exploring the space of theories with future redshift surveys. *JCAP*, 1405:043, 2014.

[152] Lszl . Gergely and Shinji Tsujikawa. Effective field theory of modified gravity with two scalar fields: dark energy and dark matter. *Phys. Rev.*, D89(6):064059, 2014.

[153] Bin Hu, Michele Liguori, Nicola Bartolo, and Sabino Matarrese. Future CMB integrated-Sachs-Wolfe-lensing bispectrum constraints on modified gravity in the parametrized post-Friedmann formalism. *Phys. Rev.*, D88(2):024012, 2013.

[154] D. Munshi, B. Hu, A. Renzi, A. Heavens, and P. Coles. Probing Modified Gravity Theories with ISW and CMB Lensing. *Mon. Not. Roy. Astron. Soc.*, 442(1):821–837, 2014.

[155] Bin Hu, Michele Liguori, Nicola Bartolo, and Sabino Matarrese. Parametrized modified gravity constraints after Planck. *Phys. Rev.*, D88(12):123514, 2013.

[156] Heinrich Steigerwald, Julien Bel, and Christian Marinoni. Probing non-standard gravity with the growth index: a background independent analysis. *JCAP*, 1405:042, 2014.

[157] Qing-Guo Huang. An analytic calculation of the growth index for $f(R)$ dark energy model. *Eur. Phys. J.*, C74:2964, 2014.

[158] Lucas Lombriser. Constraining chameleon models with cosmology. *Annalen Phys.*, 526:259–282, 2014.

[159] Shinji Tsujikawa. The effective field theory of inflation/dark energy and the Horndeski theory. *Lect. Notes Phys.*, 892:97–136, 2015.

[160] Emilio Bellini and Ignacy Sawicki. Maximal freedom at minimum cost: linear large-scale structure in general modifications of gravity. *JCAP*, 1407:050, 2014.

[161] Richard A. Battye and Jonathan A. Pearson. Effective action approach to cosmological perturbations in dark energy and modified gravity. *JCAP*, 1207:019, 2012.

[162] Giulia Gubitosi, Federico Piazza, and Filippo Vernizzi. The Effective Field Theory of Dark Energy. *JCAP*, 1302:032, 2013. [JCAP1302,032(2013)].

[163] Jolyon K. Bloomfield, anna . Flanagan, Minjoon Park, and Scott Watson. Dark energy or modified gravity? An effective field theory approach. *JCAP*, 1308:010, 2013.

[164] Federico Piazza and Filippo Vernizzi. Effective Field Theory of Cosmological Perturbations. *Class. Quant. Grav.*, 30:214007, 2013.

[165] Paolo Creminelli, Markus A. Luty, Alberto Nicolis, and Leonardo Senatore. Starting the Universe: Stable Violation of the Null Energy Condition and Non-standard Cosmologies. *JHEP*, 12:080, 2006.

[166] Paolo Creminelli, Guido D'Amico, Jorge Norena, and Filippo Vernizzi. The Effective Theory of Quintessence: the w¡-1 Side Unveiled. *JCAP*, 0902:018, 2009.

[167] Minjoon Park, Kathryn M. Zurek, and Scott Watson. A Unified Approach to Cosmic Acceleration. *Phys. Rev.*, D81:124008, 2010.

[168] Clifford Cheung, Paolo Creminelli, A. Liam Fitzpatrick, Jared Kaplan, and Leonardo Senatore. The Effective Field Theory of Inflation. *JHEP*, 03:014, 2008.

[169] Steven Weinberg. Effective Field Theory for Inflation. *Phys. Rev.*, D77:123541, 2008.

[170] Raul Jimenez, P. Talavera, and Licia Verde. An effective theory of accelerated expansion. *Int. J. Mod. Phys.*, A27:1250174, 2012.

[171] John Joseph M. Carrasco, Mark P. Hertzberg, and Leonardo Senatore. The Effective Field Theory of Cosmological Large Scale Structures. *JHEP*, 09:082, 2012.

[172] Mark P. Hertzberg. Effective field theory of dark matter and structure formation: Semianalytical results. *Phys. Rev.*, D89(4):043521, 2014.

[173] Jerome Gleyzes, David Langlois, Federico Piazza, and Filippo Vernizzi. Essential Building Blocks of Dark Energy. *JCAP*, 1308:025, 2013.

[174] Jolyon Bloomfield. A Simplified Approach to General Scalar-Tensor Theories. *JCAP*, 1312:044, 2013.

[175] Alberto Nicolis, Riccardo Rattazzi, and Enrico Trincherini. The Galileon as a local modification of gravity. *Phys. Rev.*, D79:064036, 2009.

[176] Ryotaro Kase and Shinji Tsujikawa. Effective field theory approach to modified gravity including Horndeski theory and HoavaLifshitz gravity. *Int. J. Mod. Phys.*, D23(13):1443008, 2015.

[177] Noemi Frusciante, Georgios Papadomanolakis, and Alessandra Silvestri. An Extended action for the effective field theory of dark energy: a stability analysis and a complete guide to the mapping at the basis of EFTCAMB. 2016.

[178] H. Nariai. Gravitational instability of regular model-universes in a modified theory of general relativity. *Prog. Theor. Phys.*, 49:165–180, 1973.

[179] V. Ts. Gurovich and Alexei A. Starobinsky. QUANTUM EFFECTS AND REGULAR COSMOLOGICAL MODELS. *Sov. Phys. JETP*, 50:844–852, 1979. [Zh. Eksp. Teor. Fiz.77,1683(1979)].

[180] Alvaro Nunez and Slava Solganik. The Content of f(R) gravity. 2004.

[181] James M. Cline, Sangyong Jeon, and Guy D. Moore. The Phantom menaced: Constraints on low-energy effective ghosts. *Phys. Rev.*, D70:043543, 2004.

[182] Stefano Liberati. Tests of Lorentz invariance: a 2013 update. *Class. Quant. Grav.*, 30:133001, 2013.

[183] A. Emir Gmrkolu, Kurt Hinterbichler, Chunshan Lin, Shinji Mukohyama, and Mark Trodden. Cosmological Perturbations in Extended Massive Gravity. *Phys. Rev.*, D88(2):024023, 2013.

[184] D. Blas and S. Sibiryakov. Technically natural dark energy from Lorentz breaking. *JCAP*, 1107:026, 2011.

[185] B. Audren, D. Blas, J. Lesgourgues, and S. Sibiryakov. Cosmological constraints on Lorentz violating dark energy. *JCAP*, 1308:039, 2013.

[186] T. Padmanabhan. Accelerated expansion of the universe driven by tachyonic matter. *Phys. Rev.*, D66:021301, 2002.

[187] J. S. Bagla, Harvinder Kaur Jassal, and T. Padmanabhan. Cosmology with tachyon field as dark energy. *Phys. Rev.*, D67:063504, 2003.

[188] L. Raul W. Abramo and Fabio Finelli. Cosmological dynamics of the tachyon with an inverse power-law potential. *Phys. Lett.*, B575:165–171, 2003.

[189] J. M. Aguirregabiria and Ruth Lazkoz. Tracking solutions in tachyon cosmology. *Phys. Rev.*, D69:123502, 2004.

[190] Edmund J. Copeland, M. Sami, and Shinji Tsujikawa. Dynamics of dark energy. *Int. J. Mod. Phys.*, D15:1753–1936, 2006.

[191] Luca Amendola, Radouane Gannouji, David Polarski, and Shinji Tsujikawa. Conditions for the cosmological viability of f(R) dark energy models. *Phys. Rev.*, D75:083504, 2007.

[192] Gregory Walter Horndeski. Second-order scalar-tensor field equations in a four-dimensional space. *Int. J. Theor. Phys.*, 10:363–384, 1974.

[193] Carlo Baccigalupi, Sabino Matarrese, and Francesca Perrotta. Tracking extended quintessence. *Phys. Rev.*, D62:123510, 2000.

[194] Edmund J. Copeland, Andrew R Liddle, and David Wands. Exponential potentials and cosmological scaling solutions. *Phys. Rev.*, D57:4686–4690, 1998.

[195] Alireza Hojjati, Levon Pogosian, Alessandra Silvestri, and Starla Talbot. Practical solutions for perturbed f(R) gravity. *Phys. Rev.*, D86:123503, 2012.

[196] Lucas Lombriser, Jaiyul Yoo, and Kazuya Koyama. Relativistic effects in galaxy clustering in a parametrized post-Friedmann universe. *Phys. Rev.*, D87:104019, 2013.

[197] Johannes Noller, Francesca von Braun-Bates, and Pedro G. Ferreira. Relativistic scalar fields and the quasistatic approximation in theories of modified gravity. *Phys. Rev.*, D89(2):023521, 2014.

[198] Wenjuan Fang, Wayne Hu, and Antony Lewis. Crossing the Phantom Divide with Parameterized Post-Friedmann Dark Energy. *Phys. Rev.*, D78:087303, 2008.

[199] Gong-Bo Zhao, Levon Pogosian, Alessandra Silvestri, and Joel Zylberberg. Searching for modified growth patterns with tomographic surveys. *Phys. Rev.*, D79:083513, 2009.

[200] Alireza Hojjati, Levon Pogosian, and Gong-Bo Zhao. Testing gravity with CAMB and CosmoMC. *JCAP*, 1108:005, 2011.

[201] Jolyon Bloomfield and Jonathon Pearson. Simple implementation of general dark energy models. *JCAP*, 1403:017, 2014.

[202] Richard A. Battye and Jonathan A. Pearson. Computing model independent perturbations in dark energy and modified gravity. *JCAP*, 1403:051, 2014.

[203] Michel Chevallier and David Polarski. Accelerating universes with scaling dark matter. *Int. J. Mod. Phys.*, D10:213–224, 2001.

[204] Eric V. Linder. Exploring the expansion history of the universe. *Phys. Rev. Lett.*, 90:091301, 2003.

[205] Uros Seljak and Matias Zaldarriaga. A Line of sight integration approach to cosmic microwave background anisotropies. *Astrophys. J.*, 469:437–444, 1996.

[206] Antony Lewis and Anthony Challinor. Weak gravitational lensing of the cmb. *Phys. Rept.*, 429:1–65, 2006.

[207] Wayne Hu. Weak lensing of the CMB: A harmonic approach. *Phys. Rev.*, D62:043007, 2000.

[208] Daniel J. Eisenstein and Wayne Hu. Baryonic features in the matter transfer function. *Astrophys. J.*, 496:605, 1998.

[209] Ivaylo Zlatev, Li-Min Wang, and Paul J. Steinhardt. Quintessence, cosmic coincidence, and the cosmological constant. *Phys. Rev. Lett.*, 82:896–899, 1999.

[210] M. Maltoni, T. Schwetz, M. A. Tortola, and J. W. F. Valle. Status of global fits to neutrino oscillations. *New J. Phys.*, 6:122, 2004.

[211] G. L. Fogli, E. Lisi, A. Marrone, and A. Palazzo. Global analysis of three-flavor neutrino masses and mixings. *Prog. Part. Nucl. Phys.*, 57:742–795, 2006.

[212] Julien Lesgourgues and Sergio Pastor. Massive neutrinos and cosmology. *Phys. Rept.*, 429:307–379, 2006.

[213] Yvonne Y. Y. Wong. Neutrino mass in cosmology: status and prospects. *Ann. Rev. Nucl. Part. Sci.*, 61:69–98, 2011.

[214] Antony Lewis and Anthony Challinor. Evolution of cosmological dark matter perturbations. *Phys. Rev.*, D66:023531, 2002.

[215] Alessandra Silvestri and Mark Trodden. Approaches to Understanding Cosmic Acceleration. *Rept. Prog. Phys.*, 72:096901, 2009.

[216] Bhuvnesh Jain and Justin Khoury. Cosmological Tests of Gravity. *Annals Phys.*, 325:1479–1516, 2010.

[217] Bhuvnesh Jain et al. Novel Probes of Gravity and Dark Energy. 2013.

[218] Hayato Motohashi, Alexei A. Starobinsky, and Jun'ichi Yokoyama. Cosmology Based on f(R) Gravity Admits 1 eV Sterile Neutrinos. *Phys. Rev. Lett.*, 110(12):121302, 2013.

[219] Marco Baldi, Francisco Villaescusa-Navarro, Matteo Viel, Ewald Puchwein, Volker Springel, and Lauro Moscardini. Cosmic degeneracies I. Joint N-body simulations of modified gravity and massive neutrinos. *Mon. Not. Roy. Astron. Soc.*, 440(1):75–88, 2014.

[220] Jian-hua He. Weighing Neutrinos in $f(R)$ gravity. *Phys. Rev.*, D88(10):103523, 2013. [Phys. Rev.D88,103523(2013)].

[221] Laurence Perotto, Julien Lesgourgues, Steen Hannestad, Huitzu Tu, and Yvonne Y. Y. Wong. Probing cosmological parameters with the CMB: Forecasts from full Monte Carlo simulations. *JCAP*, 0610:013, 2006.

[222] Max Tegmark, Andy Taylor, and Alan Heavens. Karhunen-Loeve eigenvalue problems in cosmology: How should we tackle large data sets? *Astrophys. J.*, 480:22, 1997.

[223] Antony Lewis. Lensed CMB simulation and parameter estimation. *Phys. Rev.*, D71:083008, 2005.

[224] J. Tauber, M. Bersanelli, J. M. Lamarre, G. Efstathiou, C. Lawrence, F. Bouchet, E. Martinez-Gonzalez, S. Matarrese, D. Scott, M. White, et al. The Scientific programme of Planck. 2006.

[225] Erminia Calabrese, Anze Slosar, Alessandro Melchiorri, George F. Smoot, and Oliver Zahn. Cosmic Microwave Weak lensing data as a test for the dark universe. *Phys. Rev.*, D77:123531, 2008.

[226] P. A. R. Ade et al. A Measurement of the Cosmic Microwave Background B-Mode Polarization Power Spectrum at Sub-Degree Scales with POLARBEAR. *Astrophys. J.*, 794(2):171, 2014.

[227] Matias Zaldarriaga and Uros Seljak. An all sky analysis of polarization in the microwave background. *Phys. Rev.*, D55:1830–1840, 1997.

[228] Petr Horava. Quantum Gravity at a Lifshitz Point. *Phys. Rev.*, D79:084008, 2009.

[229] Charalampos Bogdanos and Emmanuel N. Saridakis. Perturbative instabilities in Horava gravity. *Class. Quant. Grav.*, 27:075005, 2010.

[230] V. A. Rubakov. Lorentz-violating graviton masses: Getting around ghosts, low strong coupling scale and VDVZ discontinuity. 2004.

[231] S. L. Dubovsky. Phases of massive gravity. *JHEP*, 10:076, 2004.

[232] C. Deffayet, Xian Gao, D. A. Steer, and G. Zahariade. From k-essence to generalised Galileons. *Phys. Rev.*, D84:064039, 2011.

[233] Luca Amendola. Cosmology with nonminimal derivative couplings. *Phys. Lett.*, B301:175–182, 1993.

[234] Tsutomu Kobayashi, Masahide Yamaguchi, and Jun'ichi Yokoyama. Generalized G-inflation: Inflation with the most general second-order field equations. *Prog. Theor. Phys.*, 126:511–529, 2011.

[235] Xian Gao and Daniele A. Steer. Inflation and primordial non-Gaussianities of 'generalized Galileons'. *JCAP*, 1112:019, 2011.

[236] Antonio De Felice and Shinji Tsujikawa. Inflationary non-Gaussianities in the most general second-order scalar-tensor theories. *Phys. Rev.*, D84:083504, 2011.

[237] Yi-Fu Cai and Yi Wang. Testing quantum gravity effects with latest CMB observations. *Phys. Lett.*, B735:108–111, 2014.

[238] Sergei Dubovsky, Raphael Flauger, Alexei Starobinsky, and Igor Tkachev. Signatures of a Graviton Mass in the Cosmic Microwave Background. *Phys. Rev.*, D81:023523, 2010.

[239] A. Emir Gumrukcuoglu, Sachiko Kuroyanagi, Chunshan Lin, Shinji Mukohyama, and Norihiro Tanahashi. Gravitational wave signal from massive gravity. *Class. Quant. Grav.*, 29:235026, 2012.

[240] Clifford M. Will. The Confrontation between General Relativity and Experiment. *Living Rev. Rel.*, 17:4, 2014.

[241] Alessandra Silvestri. Scalar radiation from Chameleon-shielded regions. *Phys. Rev. Lett.*, 106:251101, 2011.

[242] Claudia de Rham, Andrew Matas, and Andrew J. Tolley. Galileon Radiation from Binary Systems. *Phys. Rev.*, D87(6):064024, 2013.

[243] Philippe Brax, Anne-Christine Davis, and Jeremy Sakstein. Pulsar Constraints on Screened Modified Gravity. *Class. Quant. Grav.*, 31:225001, 2014.

[244] Clifford M. Will. The Confrontation between general relativity and experiment. *Living Rev. Rel.*, 9:3, 2006.

[245] Claudia Antolini, Matteo Martinelli, Yabebal Fantaye, and Carlo Baccigalupi. Measuring primordial gravitational waves from CMB B-modes in cosmologies with generalized expansion histories. *JCAP*, 1302:024, 2013.

[246] Andrew R. Liddle and David H. Lyth. COBE, gravitational waves, inflation and extended inflation. *Phys. Lett.*, B291:391–398, 1992.

[247] F. R. Bouchet et al. COrE (Cosmic Origins Explorer) A White Paper. 2011.

[248] Philippe Andr et al. PRISM (Polarized Radiation Imaging and Spectroscopy Mission): An Extended White Paper. *JCAP*, 1402:006, 2014.

[249] Yong-Seon Song, Wayne Hu, and Ignacy Sawicki. The Large Scale Structure of f(R) Gravity. *Phys. Rev.*, D75:044004, 2007.

[250] Rachel Bean, David Bernat, Levon Pogosian, Alessandra Silvestri, and Mark Trodden. Dynamics of Linear Perturbations in f(R) Gravity. *Phys. Rev.*, D75:064020, 2007.

[251] Levon Pogosian and Alessandra Silvestri. The pattern of growth in viable f(R) cosmologies. *Phys. Rev.*, D77:023503, 2008. [Erratum: Phys. Rev.D81,049901(2010)].

[252] Antonio De Felice and Shinji Tsujikawa. f(R) theories. *Living Rev. Rel.*, 13:3, 2010.

[253] Alexei A. Starobinsky. Disappearing cosmological constant in f(R) gravity. *JETP Lett.*, 86:157–163, 2007.

[254] Tommaso Giannantonio, Matteo Martinelli, Alessandra Silvestri, and Alessandro Melchiorri. New constraints on parametrised modified gravity from correlations of the CMB with large scale structure. *JCAP*, 1004:030, 2010.

[255] Lucas Lombriser, Anze Slosar, Uros Seljak, and Wayne Hu. Constraints on f(R) gravity from probing the large-scale structure. *Phys. Rev.*, D85:124038, 2012.

[256] Andrea Marchini and Valentina Salvatelli. Updated constraints from the PLANCK experiment on modified gravity. *Phys. Rev.*, D88(2):027502, 2013.

[257] Andrea Marchini, Alessandro Melchiorri, Valentina Salvatelli, and Luca Pagano. Constraints on modified gravity from the Atacama Cosmology Telescope and the South Pole Telescope. *Phys. Rev.*, D87(8):083527, 2013.

[258] Erminia Calabrese, Asantha Cooray, Matteo Martinelli, Alessandro Melchiorri, Luca Pagano, Anze Slosar, and George F. Smoot. CMB Lensing Constraints on Dark Energy and Modified Gravity Scenarios. *Phys. Rev.*, D80:103516, 2009.

[259] Sudeep Das et al. The Atacama Cosmology Telescope: temperature and gravitational lensing power spectrum measurements from three seasons of data. *JCAP*, 1404:014, 2014.

[260] A. van Engelen et al. A measurement of gravitational lensing of the microwave background using South Pole Telescope data. *Astrophys. J.*, 756:142, 2012.

[261] Catherine Heymans et al. CFHTLenS: The Canada-France-Hawaii Telescope Lensing Survey. *Mon. Not. Roy. Astron. Soc.*, 427:146, 2012.

[262] T. Erben et al. CFHTLenS: The Canada-France-Hawaii Telescope Lensing Survey - Imaging Data and Catalogue Products. *Mon. Not. Roy. Astron. Soc.*, 433:2545, 2013.

[263] Wayne Hu and Ignacy Sawicki. Models of f(R) Cosmic Acceleration that Evade Solar-System Tests. *Phys. Rev.*, D76:064004, 2007.

[264] Gong-Bo Zhao, Baojiu Li, and Kazuya Koyama. N-body Simulations for f(R) Gravity using a Self-adaptive Particle-Mesh Code. *Phys. Rev.*, D83:044007, 2011.

[265] Claudio Llinares, David F. Mota, and Hans A. Winther. ISIS: a new N-body cosmological code with scalar fields based on RAMSES. Code presentation and application to the shapes of clusters. *Astron. Astrophys.*, 562:A78, 2014.

[266] Lucas Lombriser, Kazuya Koyama, and Baojiu Li. Halo modelling in chameleon theories. *JCAP*, 1403:021, 2014.

[267] Hans A. Winther et al. Modified Gravity N-body Code Comparison Project. *Mon. Not. Roy. Astron. Soc.*, 454(4):4208–4234, 2015.

[268] Junpu Wang, Lam Hui, and Justin Khoury. No-Go Theorems for Generalized Chameleon Field Theories. *Phys. Rev. Lett.*, 109:241301, 2012.

[269] Florian Beutler, Chris Blake, Matthew Colless, D. Heath Jones, Lister Staveley-Smith, Gregory B. Poole, Lachlan Campbell, Quentin Parker, Will Saunders, and Fred Watson. The 6dF Galaxy Survey: $z \approx 0$ measurement of the growth rate and σ_8. *Mon. Not. Roy. Astron. Soc.*, 423:3430–3444, 2012.

[270] Will J. Percival et al. The 2dF Galaxy Redshift Survey: Spherical harmonics analysis of fluctuations in the final catalogue. *Mon. Not. Roy. Astron. Soc.*, 353:1201, 2004.

[271] Chris Blake et al. The WiggleZ Dark Energy Survey: the growth rate of cosmic structure since redshift z=0.9. *Mon. Not. Roy. Astron. Soc.*, 415:2876, 2011.

[272] Lado Samushia, Will J. Percival, and Alvise Raccanelli. Interpreting large-scale redshift-space distortion measurements. *Mon. Not. Roy. Astron. Soc.*, 420:2102–2119, 2012.

[273] Beth A. Reid et al. The clustering of galaxies in the SDSS-III Baryon Oscillation Spectroscopic Survey: measurements of the growth of structure and expansion rate at z=0.57 from anisotropic clustering. *Mon. Not. Roy. Astron. Soc.*, 426:2719, 2012.

[274] S. de la Torre et al. The VIMOS Public Extragalactic Redshift Survey (VIPERS). Galaxy clustering and redshift-space distortions at z=0.8 in the first data release. *Astron. Astrophys.*, 557:A54, 2013.

[275] Anthony R. Pullen, Shadab Alam, Siyu He, and Shirley Ho. Constraining Gravity at the Largest Scales through CMB Lensing and Galaxy Velocities. 2015.

[276] Federico Bianchini and Alessandra Silvestri. Kinetic Sunyaev-Zeldovich effect in modified gravity. *Phys. Rev.*, D93(6):064026, 2016.

[277] C. Danielle Leonard, Pedro G. Ferreira, and Catherine Heymans. Testing gravity with E_G: mapping theory onto observations. *JCAP*, 1512(12):051, 2015.

[278] Anthony R. Pullen, Shadab Alam, and Shirley Ho. Probing gravity at large scales through CMB lensing. *Mon. Not. Roy. Astron. Soc.*, 449(4):4326–4335, 2015.

[279] Andreu Font-Ribera, Patrick McDonald, Nick Mostek, Beth A. Reid, Hee-Jong Seo, and An Slosar. DESI and other dark energy experiments in the era of neutrino mass measurements. *JCAP*, 1405:023, 2014.

[280] Lucas Lombriser, Fabian Schmidt, Tobias Baldauf, Rachel Mandelbaum, Uros Seljak, and Robert E. Smith. Cluster Density Profiles as a Test of Modified Gravity. *Phys. Rev.*, D85:102001, 2012.

[281] Lucas Lombriser, Kazuya Koyama, Gong-Bo Zhao, and Baojiu Li. Chameleon f(R) gravity in the virialized cluster. *Phys. Rev.*, D85:124054, 2012.

[282] Lucas Lombriser, Baojiu Li, Kazuya Koyama, and Gong-Bo Zhao. Modeling halo mass functions in chameleon f(R) gravity. *Phys. Rev.*, D87(12):123511, 2013.

[283] Lixin Xu. FRCAMB: An $f(R)$ Code for Anisotropies in the Microwave Background. 2015.

[284] Alireza Hojjati, Aaron Plahn, Alex Zucca, Levon Pogosian, Philippe Brax, Anne-Christine Davis, and Gong-Bo Zhao. Searching for scalar gravitational interactions in current and future cosmological data. *Phys. Rev.*, D93(4):043531, 2016.

[285] Kazuya Koyama. Cosmological Tests of Modified Gravity. *Rept. Prog. Phys.*, 79(4):046902, 2016.

[286] V. Alan Kostelecky and Neil Russell. Data Tables for Lorentz and CPT Violation. *Rev. Mod. Phys.*, 83:11–31, 2011.

[287] Don Colladay and V. Alan Kostelecky. CPT violation and the standard model. *Phys. Rev.*, D55:6760–6774, 1997.

[288] Don Colladay and V. Alan Kostelecky. Lorentz violating extension of the standard model. *Phys. Rev.*, D58:116002, 1998.

[289] Kent Yagi, Diego Blas, Nicols Yunes, and Enrico Barausse. Strong Binary Pulsar Constraints on Lorentz Violation in Gravity. *Phys. Rev. Lett.*, 112(16):161101, 2014.

[290] Kent Yagi, Diego Blas, Enrico Barausse, and Nicols Yunes. Constraints on Einstein-ther theory and Hoava gravity from binary pulsar observations. *Phys. Rev.*, D89(8):084067, 2014. [Erratum: Phys. Rev.D90,no.6,069901(2014)].

[291] Sean M. Carroll and Eugene A. Lim. Lorentz-violating vector fields slow the universe down. *Phys. Rev.*, D70:123525, 2004.

[292] Joseph A. Zuntz, P. G. Ferreira, and T. G. Zlosnik. Constraining Lorentz violation with cosmology. *Phys. Rev. Lett.*, 101:261102, 2008.

[293] Diego Blas, Mikhail M. Ivanov, and Sergey Sibiryakov. Testing Lorentz invariance of dark matter. *JCAP*, 1210:057, 2012.

[294] B. Audren, D. Blas, M. M. Ivanov, J. Lesgourgues, and S. Sibiryakov. Cosmological constraints on deviations from Lorentz invariance in gravity and dark matter. *JCAP*, 1503(03):016, 2015.

[295] Petr Horava. Membranes at Quantum Criticality. *JHEP*, 03:020, 2009.

[296] Gianluca Calcagni. Cosmology of the Lifshitz universe. *JHEP*, 09:112, 2009.

[297] Elias Kiritsis and Georgios Kofinas. Horava-Lifshitz Cosmology. *Nucl. Phys.*, B821:467–480, 2009.

[298] Robert Brandenberger. Matter Bounce in Horava-Lifshitz Cosmology. *Phys. Rev.*, D80:043516, 2009.

[299] Shinji Mukohyama. Scale-invariant cosmological perturbations from Horava-Lifshitz gravity without inflation. *JCAP*, 0906:001, 2009.

[300] Rong-Gen Cai, Bin Hu, and Hong-Bo Zhang. Dynamical Scalar Degree of Freedom in Horava-Lifshitz Gravity. *Phys. Rev.*, D80:041501, 2009.

[301] Bin Chen, Shi Pi, and Jin-Zhang Tang. Scale Invariant Power Spectrum in Horava-Lifshitz Cosmology without Matter. *JCAP*, 0908:007, 2009.

[302] Rong-Gen Cai, Bin Hu, and Hong-Bo Zhang. Scalar graviton in the healthy extension of Hořava-Lifshitz theory. *Phys. Rev.*, D83:084009, 2011.

[303] Xian Gao, Yi Wang, R. Brandenberger, and A. Riotto. Cosmological Perturbations in Horava-Lifshitz Gravity. *Phys. Rev.*, D81:083508, 2010.

[304] Anzhong Wang and Roy Maartens. Linear perturbations of cosmological models in the Horava-Lifshitz theory of gravity without detailed balance. *Phys. Rev.*, D81:024009, 2010.

[305] Tsutomu Kobayashi, Yuko Urakawa, and Masahide Yamaguchi. Large scale evolution of the curvature perturbation in Horava-Lifshitz cosmology. *JCAP*, 0911:015, 2009.

[306] Tsutomu Kobayashi, Yuko Urakawa, and Masahide Yamaguchi. Cosmological perturbations in a healthy extension of Horava gravity. *JCAP*, 1004:025, 2010.

[307] Sourish Dutta and Emmanuel N. Saridakis. Observational constraints on Horava-Lifshitz cosmology. *JCAP*, 1001:013, 2010.

[308] Sourish Dutta and Emmanuel N. Saridakis. Overall observational constraints on the running parameter λ of Horava-Lifshitz gravity. *JCAP*, 1005:013, 2010.

[309] Xian Gao. Unifying framework for scalar-tensor theories of gravity. *Phys. Rev.*, D90:081501, 2014.

[310] D. Blas, O. Pujolas, and S. Sibiryakov. Consistent Extension of Horava Gravity. *Phys. Rev. Lett.*, 104:181302, 2010.

[311] Jrme Gleyzes, David Langlois, and Filippo Vernizzi. A unifying description of dark energy. *Int. J. Mod. Phys.*, D23(13):1443010, 2015.

[312] M. Ostrogradski. *Mem. Ac. St. Petersburg.*, VI 4:385, 1850.

[313] Matt Visser. Lorentz symmetry breaking as a quantum field theory regulator. *Phys. Rev.*, D80:025011, 2009.

[314] Matt Visser. Power-counting renormalizability of generalized Horava gravity. 2009.

[315] Thomas P. Sotiriou, Matt Visser, and Silke Weinfurtner. Phenomenologically viable Lorentz-violating quantum gravity. *Phys. Rev. Lett.*, 102:251601, 2009.

[316] Thomas P. Sotiriou, Matt Visser, and Silke Weinfurtner. Quantum gravity without Lorentz invariance. *JHEP*, 10:033, 2009.

[317] Thomas P. Sotiriou. Horava-Lifshitz gravity: a status report. *J. Phys. Conf. Ser.*, 283:012034, 2011.

[318] Matt Visser. Status of Horava gravity: A personal perspective. *J. Phys. Conf. Ser.*, 314:012002, 2011.

[319] Daniele Vernieri and Thomas P. Sotiriou. Horava-Lifshitz Gravity: Detailed Balance Revisited. *Phys. Rev.*, D85:064003, 2012.

[320] Daniele Vernieri and Thomas P. Sotiriou. Hoava-Lifshitz gravity with detailed balance. *J. Phys. Conf. Ser.*, 453:012022, 2013.

[321] Daniele Vernieri. On power-counting renormalizability of Hoava gravity with detailed balance. *Phys. Rev.*, D91(12):124029, 2015.

[322] Eric Gourgoulhon. 3+1 formalism and bases of numerical relativity. 2007.

[323] J. F. Bell, F. Camilo, and T. Damour. A Tighter test of local Lorentz invariance of gravity using PSR-2317+1439. *Astrophys. J.*, 464:857, 1996.

[324] Diego Blas, Oriol Pujolas, and Sergey Sibiryakov. Models of non-relativistic quantum gravity: The Good, the bad and the healthy. *JHEP*, 04:018, 2011.

[325] Diego Blas and Hillary Sanctuary. Gravitational Radiation in Horava Gravity. *Phys. Rev.*, D84:064004, 2011.

[326] Matteo Bonetti and Enrico Barausse. Post-Newtonian constraints on Lorentz-violating gravity theories with a MOND phenomenology. *Phys. Rev.*, D91:084053, 2015. [Erratum: Phys. Rev.D93,029901(2016)].

[327] Joshua W. Elliott, Guy D. Moore, and Horace Stoica. Constraining the new Aether: Gravitational Cerenkov radiation. *JHEP*, 08:066, 2005.

[328] Guy D. Moore and Ann E. Nelson. Lower bound on the propagation speed of gravity from gravitational Cherenkov radiation. *JHEP*, 09:023, 2001.

[329] R. K. Sachs and A. M. Wolfe. Perturbations of a cosmological model and angular variations of the microwave background. *Astrophys. J.*, 147:73–90, 1967. [Gen. Rel. Grav.39,1929(2007)].

[330] Luca Amendola, Guillermo Ballesteros, and Valeria Pettorino. Effects of modified gravity on B-mode polarization. *Phys. Rev.*, D90:043009, 2014.

[331] Shinji Tsujikawa and M. Sami. A Unified approach to scaling solutions in a general cosmological background. *Phys. Lett.*, B603:113–123, 2004.

[332] A. R. Gomes and Luca Amendola. Towards scaling cosmological solutions with full coupled Horndeski Lagrangian: the KGB model. *JCAP*, 1403:041, 2014.

[333] C. Deffayet, S. Deser, and G. Esposito-Farese. Generalized Galileons: All scalar models whose curved background extensions maintain second-order field equations and stress-tensors. *Phys. Rev.*, D80:064015, 2009.

[334] H. K. Jassal, J. S. Bagla, and T. Padmanabhan. WMAP constraints on low redshift evolution of dark energy. *Mon. Not. Roy. Astron. Soc.*, 356:L11–L16, 2005.

[335] Harvinder K. Jassal, J. S. Bagla, and T. Padmanabhan. Understanding the origin of CMB constraints on Dark Energy. *Mon. Not. Roy. Astron. Soc.*, 405:2639–2650, 2010.

[336] Yazhou Hu, Miao Li, Xiao-Dong Li, and Zhenhui Zhang. Investigating the Possibility of a Turning Point in the Dark Energy Equation of State. *Sci. China Phys. Mech. Astron.*, 57:1607–1612, 2014.

[337] Jrme Gleyzes, David Langlois, Federico Piazza, and Filippo Vernizzi. Healthy theories beyond Horndeski. *Phys. Rev. Lett.*, 114(21):211101, 2015.